On Effects of Hydrodynamic Interaction in Active and Passive Suspensions - Multi Particle Simulations

Von der Universität Bayreuth
zur Erlangung des Grades eines
Doktors der Naturwissenschaften (Dr. rer. nat.)
genehmigte Abhandlung

von

Johannes Greber

aus Münster in Westfalen

1. Gutachter: Prof. Dr. Walter Zimmermann
2. Gutachter: Prof. Dr. Philippe Peyla

Tag der Einreichung: 01. Dezember 2016
Tag des Kolloquiums: 31. März 2017

Kurzfassung

In der vorliegenden Dissertation wird die überdämpfte Dynamik einer Vielzahl hydrodynamisch wechselwirkender kolloidaler Teilchen untersucht. Diese Teilchen werden entweder durch Kugel-Feder Modelle beschrieben oder üben selbst Antriebskräfte aus, die ihnen eine selbstgesteuerte Bewegung ermöglicht und werden passiv oder aktiv genannt.

Der erste Teil dieser Arbeit widmet sich dem Nachweis einer turbulenten Strömung in gescherten Systemen elastischer Hanteln. Als passive Teilchen führen diese nur Bewegungen aus, sofern sie von einer äußeren Strömung, z. B. einer Scherströmung angetrieben werden. In Bewegung versetzt erzeugen die suspendierten Kugeln eine langreichweitige Störung des Strömungsfeldes, das hydrodynamische Interaktion genannt wird und so die Dynamik aller anderen Kugeln beeinflusst. Im Falle einer Hantel, bestehend aus zwei Kugeln mit einer Federkraft verbunden sind, führt dessen Bewegung im Zusammenspiel aus Scherströmung, Federkräften und hydrodynamischer Wechselwirkung zu einer Rotationsbewegung, die als *Taumeln* bezeichnet wird.

In einem Strömungskanal sind zusätzllich zu der Wechselwirkung zwischen den Kugeln noch Wechselwirkungen mit den Kanalwänden zu berücksichtigen. Eine systematische Untersuchung der Bewegung in Abhängigkeit der Kanalgröße und der Elastizität der Hantel zeigt eine homoklinische Bifurkation, an deren kritischen Punkt ein zweiter Bewegungszustand auftritt, der im Englischen als *vacillating breathing* bezeichnet wird. Dieser Zustand zeichnet sich durch eine schräge Orientierung der Hantel gegenüber der Richtung der Scherströmung aus, in der sich die hydrodynamische Wechselwirkung zwischen den beiden Hantelkugeln, die Federkräfte, der Scherfluss und Wandwechselwirkungen ausgleichen.

Ein dimensionsloser Parameter, die Weissenbergzahl, gibt vor, in welchem Maße die Federkräfte in der Lage sind, äußere Störungen durch die Scherströ-

mung auszugleichen. Rheologische Untersuchungen, die zeigen sowohl durch die direkte Bestimmung der effektiven Viskosität, als auch durch die so genannte Kramer-Kirkwood Formel, dass in bestimmten Konfigurationen einer weichen Hantel negative Beiträge zur effectiven Viskosität liefert. Dieses scheinbar ungewöhnliche Ergebnis lässt sich durch geometrische Überlegungen erklären.

Das Phänomen der Turbulenz ist aus dem Alltag wohlbekannt, das z. B. in der Atmosphäre aufgrund von Trägheitseffekten hervorgerufen wird. Seit den vierziger Jahren des letzten Jahrhunderts haben sich verschiedene Analysewerkzeuge für Strömungen entwickelt, die eine Beschreibung turbulenter Strukturen mit Hilfe von stochastischen Methoden ermöglicht. Erstaunlicher ist, dass sich ähnliche turbulente Strömungsmuster selbst im überdämpften Fall gezeigt haben, wenn der Flüssigkeit weiche Teilchen hinzugefügt werden. Im Falle vieler gelöster, wechselwirkender Teilchen zeigt sich auch im Rahmen der hier vorgestellten Ergebnisse chaotisches Verhalten. Es stellt sich heraus, dass sich die hydrodynamische Wechselwirkung zwischen den Teichen die notwendige Störung der Scherströmung ist, um eine turbulente Strömung zu erzeugen. Das Auftreten turbulenten Verhaltens wird hier systematisch in Abhängigkeit der Teilchenzahl, aber auch der Deformierbarkeit der Hanteln und deren Länge untersucht.

Der zweite Teil der Arbeit widmet sich der kollektiven Dynamik schwimmender Mikroorganismen, wie Bakterien oder Algen, die effektive Mechanismen ausgebildelt haben, um sich in einer überdämpften Umgebung fortzubewegen. Durch den Antrieb erzeugt ein sogenannter Mikroschwimmer langreichweitige Strömungsfelder, mit denen er, ähnlich wie die Hanteln im ersten Teil, andere Schwimmer in seiner Umgebung beeinflusst. In der Natur kommen solche Schwimmer als sogenannte Pusher und Puller vor, die sich durch das einfaches Modell eines Kraftdipols beschreiben lassen. Die kollektive Dynamik von Pullern und Pushern unterscheiden sich grundlegend voneinander, als dass Pusher dazu tendieren, Gruppen von mehreren Schwimmern zu bilden, wohingegen Puller sich gegenseitig abstoßen.

Darüber hinaus haben biologische Schwimmer Sensoren zur Detektion von äußeren Lichtquellen oder chemischer Gradienten entwickelt, um Nahrung zu suchen, was entsprechend als Photo- bzw. Chemotaxis bezeichnet wird. Schwimmer tendieren dazu, sich in Richtung hoher Nahrungskonzentrationen

oder einer äußeren Lichtquelle zu bewegen, haben jedoch nur einen stochastischen Zugriff auf die eingeschlagene Bewegungsrichtung. Über einen längeren Zeitraum beobachtet entspricht ihre Bewegung einem *biased Random-Walk* und die Bewegung der Mikroschwimmer lässt sich durch einen Diffusions-prozess beschreiben. Die Verteilung der Positionen einer höheren Anzahl von Schwimmern, die nicht durch Wände begrenzt ist, läuft demnach auseinander, was man als Dispersion bezeichnet.

Diese Arbeit behandelt entsprechend die Dispersion der Wahrscheinlichkeitsverteilung von Schwimmern, wenn diese hydrodynamisch wechselwirken unter der Bedingung, dass die eingeschlagenen Bewegungsrichtungen gleichverteilt sind. Um den Effekt der hydrodynamischer Wechselwirkung zu analysieren, wird der Diffusions-Koeffizient in Abhängigkeit des Volumenanteils bestimmt, der innerhalb eines Referrenzvolumens von den Schwimmern eingenommen wird, das an die Standardabweichung der Verteilung gekoppelt ist. Die Dispersion un-terscheidet sich grundlegend im Fall von Pushern und Pullern. So sorgt beispielsweise die hydrodynamische Wechselwirkung immer für eine Erhöhung des Diffusions-Koeffizienten der Schwimmerverteilung, jedoch bleibt dieser im Fall von Pushern konstant, wohingegen er im Falle von Pullern abnimmt. Die auftretenden Skalengesetze mit Exponenten proportional zu $\frac{1}{3}$ tauchen auch im Falle von ungleich verteilten Bewegungsrichtungen auf, wie sie im Rahmen der Beschreibung von Photo- oder Chemotaxis vorkommen. Dies scheint ein universelles Ergebnis für hydrodynamisch wechselwirkende Teilchen zu sein.

Abstract

In this thesis, the overdamped dynamics of multiple hydrodynamically interacting colloidal particles is investigated. These particles are described either by bead-spring models or exert their own propulsion, which allows them a self-controlled movement. The partices are called passive or active.

The first part of this work is devoted to the proof of a turbulent flow in sheared systems of elastic dumbbells. Being passive particles, they only move as long as they are driven by an external flow, e. g., a shear flow. In motion, the suspended beads induce a long-range perturbation field, called hydrodynamic interaction, influencing the dynamics of all other beads. In the case of a suspended dumbbell, the particle performs a rotational movement called *tumbling*, as a result of the interplay of the shear flow, spring force, and hydrodynamic interaction.

In a flow channel, the interaction with the channel walls has to be considered in addition to the particle-particle interaction. A systematic investigation of the motion in dependence of the channel size and the dumbbell elasticity shows a homoclinic bifurcation, where at the critical point a second state of motion, called *vacillation breathing*, occurs. This condition is characterized by a skew position of the dumbbell against the shear flow in which the hydrodynamic interaction between the two dumbbell beads is balanced by the spring forces, shear flow, and interactions with the wall.

A dimensionless parameter, the Weissenberg number, specifies the ability of the spring forces to equilibrate external stresses generated by the shear flow. Rheological investigations, determining the effective viscosity, as well as the spring contribution via the so-called Kramer-Kirkwood formula reveal a negative contribution to the effective viscosity for soft dumbbells. This result seems unusual, but can be explained by geometrical considerations.

The phenomenon of turbulence is well-known from everyday life caused by

inertial effects, e. g., in the atmosphere. Therefore, since the forties of the last century various analysis tools for flows have been developed, which allow to describe turbulent structures within a stochastic methodology. More astonishing has been the observation that by adding elastic particles turbulence occurs in the overdamped regime. Simulations of many suspended, interacting particles also have shown a chaotic behavior. It turns out that the hydrodynamic interaction between the dumbbells are required to induce perturbations of the shear flow and thus to generate a turbulent flow. Here, the occurrence of turbulent characteristics is systematically examined as a function of the number of particles, but also the deformability of the dumbbells, and their length.

The second part of the work is devoted to the collective dynamics of swimming micro-organisms such as bacteria or algae, which have developed effective mechanisms to move in the overdamped regime. The propulsion of these micro-swimmers generates long-ranged flow fields influencing other swimmers in the surrounding, similar as in the case of dumbbells in the first part. In nature there exist two types of swimmers, namely *pushers* and *pullers*, which can be described via a the simple model of a force dipole. The collective dynamics of pullers and pushers are fundamentally different from each other, in so far as pushers tend to form clusters of several swimmers, wheras pullers repel each other.

In addition, biological swimmers have developed sensors for the detection of external light sources or chemical gradients and utilized in the process of forage referred to as *photo-* or *chemotaxis*. Swimmers tend to move in the direction of high nutrient concentrations or an external light source. However, they have only access to the direction of motion via a stocahstic reorientation. Over a longer period of time, their movement corresponds to a *biased random-walk* and the movement of the micro-swimmer can be described within a diffusion process. Therefore, the distribution of the positions of a higher number of swimmers, which is not bounded by walls denoted as *dispersion*.

This thesis takes a closer look at the dispersion of this probability distribution of swimmers when they interact hydrodynamically, under the condition of a uniform distribution of the chosen directions of motion. The effect of hydrodynamic interaction is analysed in terms of the diffusion-coefficient depending on the volume-fraction, with reference to a spherical volume of a radius equal

to the standard deviation of the distribution. This reference volume accords to the volume occupied by the swimmers. The dispersion differs fundamentally in the case of pushers and pullers. The hydrodynamic interaction ensures an increase of the diffusion coefficient in both cases, but this coefficient remains constant in the case of pushers, whereas for pullers it decreases with decreasing volume fraction. The scaling laws with their exponents being proportional to $\frac{1}{3}$ also appear in the case of unequally distributed directions of motion, as considered for the description of photo- or chemotaxis. The scaling seems to be a universal result for hydrodynamically interacting particles.

Contents

1. Introduction

1.1. Dynamics in passive and active suspensions

The photography of Dexter Gordon, which was made by the photographer Herman Leonard in the year 1948 (Cf. Figure 1.1), does not only illustrates a famous musician, but is also a good example for the esthetics inherent to turbulent flows, visualized by the small particles inside the cigarette smoke. It is speculative how the celebrity of this picture was influenced by the illustrated smoke. A fact is that the investigation of turbulent flows is a fascinating and classical discipline going back to drawings of flowing water made by Leonardo da Vinci in the early 16th century, which illustrate the main characteristics of turbulent flows displaying astonishing details (Cf. Figure 1.2).

General features of turbulence

Turbulence with its vortex structures at different scales is a phenomenon occurring in everyday life. It can occur by thermally driven fluctuations in a room as on the stage, where the photo was taken in 1948. However, the wide occurrence in different areas leads to a broad physical interest in this topic. On large scales this includes meteorological phenomena and weather prediction [108], where hurricanes represent atmospheric vortices, stable for a couple of days, or even the clouds consisting of small droplets following the wind represent a visualization of turbulent structures [51]. But even on microscopic scales turbulent flows occur in suspensions of bacteria [42, 92, 106, 142, 143, 144, 171] or polymers caused by *elastic* instabilities [67, 68, 69, 112], which show some differences compared to classical turbulence, e. g., the transfer of energy does not play an essential role. In between these scales the flow around the wing of an aircraft or rotor blades of a wind turbine [114] as well as many combustion or mixing processes [50, 77] elevate the problem of turbulence to the area of

Figure 1.1.: Photography of Dexter Gordon from the year 1948 [1].

technical applications.

Despite the breadth of phenomena a full understanding, even a precise definition of the term *turbulence* is still missing. The name *turbulence* is based on the Latin verb *turbare*, meaning "to disturb" or "to entangle". Therefore, in the common understanding every flow of a liquid or gas which is disturbed from a laminar stream is called turbulent, if it fulfills some characteristics [14] as enumerated below:

1. Each turbulent flow requires forces that bring the unperturbed system out of equilibrium and keep it there. This may be thermal fluctuations as in Figure 1.1, or gravitational forces of a water jet, as in the image of da Vinci.

2. The applied energy is dissipated in a cascade via structures of various length scales before it is converted into thermal energy beyond a critical length. The most famous representative of such a cascade consists in the Kolmogorov 5/3 law [97, 98], coupling the energy dissipation to inner flow wave numbers. Tools to determine both the longest and the smallest length scales are given by evaluating particular correlation functions of

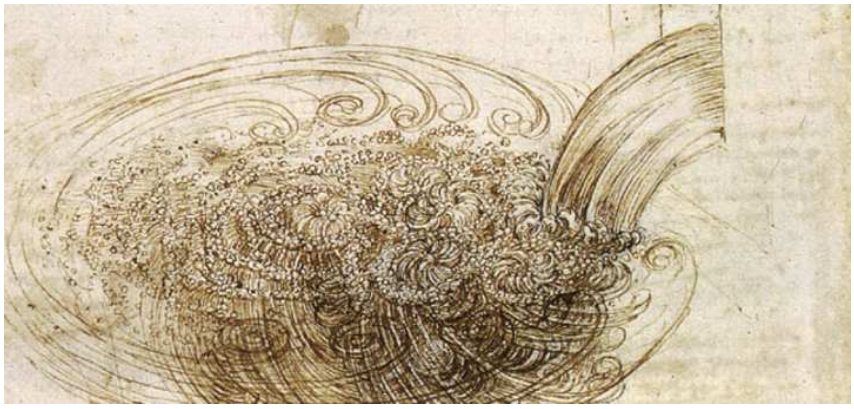

Figure 1.2.: Drawing of water made by Leonardo da Vinci in the early 16th century [2].

the flow field [157]. And indeed in Figure 1.1 the vortices arising near Dexter's mouth remain small at first, but grow with increasing distance from the smoke source, before they dissappear. The energy cascade does not occur along orders of magnitude in polymeric or bacterial suspension, rather the energy fed into the system is dissipated via flow structures induced by the motion of the suspended particles at different velocities.

3. Turbulent flow structures are time-dependent perturbations of a laminar flow. A dynamical description requires nonlinear instabilities in the set of dynamical equations. A mixing process is inherent to hydrodynamic instabilities [50, 52, 67, 68, 77, 86, 118, 139, 141, 162, 170].

4. The perturbations induce irregular, unpredictable dynamics of physical observables. Therefore, it is convenient to proceed using a statistical description. Within the statistical analysis of the velocity field,e. g., the phenomenon of intermittency characteristic for turbulent flows is visible [18, 55, 56, 139]. Turbulent flows at different monitoring parameters appear similar along several legnth scales per se, what is called *self-similarity*. In polymer or bacterial suspensions the significant parameter is the concentration of suspended particles [149]. Self-similarity is not given for all ranges of the considered parameter, what is referred to as a break of the self-similarity or *intermittence*.

Turbulence consists of the interaction between stochastic flow perturbations

and smoothing mechanisms driven by the viscosity. Parts of the theoretical work focus on understanding the occurrence of turbulence with the increase of perturbations [81, 102, 108, 118, 155]. The common view is that instabilities stemming from the presence of the convective term $\boldsymbol{u} \cdot \nabla \boldsymbol{u}$ of the Navier-Stokes equation are promoted within an increase of the so called Reynolds number (Cf. Chapter 4), measuring the strength of inertial against viscous effects. The onset of fully developed turbulence can be classified via numerous bifurcation points, where the flow changes the dynamical behavior [81, 102, 108, 118, 155].

Turbulence in pipe-flows and drag reduction

In experiments homogeneous, isotropic turbulence is often generated in wind channels [17], where the characteristics without wall interactions can be analyzed. However, the subject of wall interaction changing turbulent flows in essential ways should not be omitted in the treatment of turbulent flows. So the stability and characteristics of turbulent flows in shear-flows [105] and pipe-flows [16, 46, 79, 139] have been investigated, where it has been shown that additional back flows from walls in curved geometries amplify the instabilities [83].

The interest of dealing with turbulent flows in pipes may be motivated, for instance, medically or technologically, where every flow through a blood vessel or a pipeline is a transport process whose efficiency is inhibited by each occurrence of turbulences. The question for ways of stabilizing pipe flows by reducing the drag with additives [70, 115] plays an important role in research, which is reviewed in [167]. However, with the addition of deformable objects like polymers or vesicles the dynamics inside the channel becomes increasingly complex, so that an amplification of turbulent characteristics may occur [140] in the sense that turbulent structures arise at comparatively small Reynolds numbers.

With the addition of suspended particles a complex fluid arises, in which a variety of phenomena like crystallization or shear thinning occur, as reviewed in [26, 103]. The flow properties are characterized, among others, by the shear viscosity. Already in suspensions of beads the viscosity increases linearly with the concentration of suspended particles [47, 48]. Nonlinear effects like the

particle-particle interaction leads to a quadratic increase in the semi-dilute regime [27, 35, 28]. Simulations of bead suspensions in confined channels have shown that this law is universal, but the linear as well as quadratic pre-factor depend on the wall interaction [37]. Strongly deformable particles such as polymers or vesicles stimulate even a much bigger number of dynamic degrees of freedom, changing the macroscopic flow properties in essential ways especially, when the particle relaxation is not able to equilibrate the outer stresses as a result of an outer shear flow, measured in terms of the Weissenberg number [166] (Cf. Chapter 5). Within the description of shear thinning phenomena it has been shown that elastic particles execute dynamics called *tumbling* [25, 31, 62, 89, 111, 99, 132, 136, 146, 148, 159], where the wall interaction leads to a second state called *vacillating breathing*. This state occurs in dynamical simulations of a sheared elastic dumbbell, where the particle aligns along the streamlines with brief oscillations around this equilibrium state [123]. An overview, especially on the dynamics of vesicles, is given in the reviews [163, 174], where a phase diagram of the vesicle dynamics is presented.

Elastic turbulence in suspensions of deformable solutes

While tumbling or vacillating breathing are states of the single-particle dynamics, they represent the basis for even more complex dynamics in multi-particle dynamics including particle-particle interactions. In suspensions at low Reynolds numbers therefore the phenomenon of mixing [67] occurs and is associated with elastic instabilities [68, 69, 112]. Initially it was assumed that the onset of *elastic turbulence* requires curved streamlines in addition, but [120] has shown that the elastic instability also occurs in plane shear flows, so that back-flows in curved geometries can be identified as merely a turbulence amplifier.

The theoretical modeling of macroscopic flows in suspensions of deformable particles is often based on constitutive dynamical equations like the Navier-Stokes equations [103] (Cf. Chapter 4). In the range of small Weissenberg numbers with implied small particle deformations and in systems with a small particle concentration and thus weak nonlinear hydrodynamic particle-particle interaction these models are quite common. Especially the long-ranged hydrodynamic interaction yields intricate dynamics inside the suspension, where

effects of walls may even increase the complexity. To identify the hierarchy of stimulated degrees of freedom it is common to simulate polymers as bead-spring chains [5, 28, 38, 54, 164, 168]. So the appropriate simulation method enables the observation of individual dumbbells in the flow field created by all other solute particles to estimate effects of hydrodynamic interaction. Common simulation methods are Brownian dynamics methods [88, 100, 129] based on a numerical treatment of Langevin equations, where hydrodynamic interaction is taken into account via the Oseen-, Rotne-Prager-tensor, or Stokeslets, multi-particle collision dynamics [29, 99, 109], Lattice-Boltzmann methods [95], and the Fluid-Particle-Dynamics methods [90, 123, 156], which is described in Chapter 4. The advantage of the latter two simulation methods consists in a description, which includes directly the hydrodynamic interaction. Deformations of a dumbbell in a stochastic but smooth field were investigated in [10, 30]. Whereas stochastic fields are related to mixing processes, the dumbbell characteristics like extension, asymmetry, and elasticity can be used in separation processes [19, 20, 145].

Bacterial turbulence due to active swimmers

A second effect, which is coined turbulent due to its similarities, is called *bacterial turbulence* [42, 92, 113, 171]. Here, the turbulent structures are driven by propelling motions of the swimming bacteria, what implies the time-dependency of instabilities, as a forward moving swimmer moves the generated interactive flow field. The evoked collective patterns range across several swimmer diameters and resemble patterns as they can be found in convective flows [13, 65, 66, 151]. Also bacterial turbulence can be inhibited by adding additives [106].

The understanding of collective dynamics in bacterial suspensions starts at biological effects inside the cell ranging from sensor systems for and concepts of foraging to the function of the motor protein driving the propelling flexible rods called *flagella* or *cilia* and ranges to observations of swimmer suspensions with studies on the rheology of the suspension [53, 85, 71, 134, 138, 150, 152], characterizations of the hydrodynamic flow field via tracer diffusion [86, 113, 162], or direct effects on the swimmers like clustering [34, 58, 142, 173]. In [133] it has been shown that one swimmer is sufficient to mix its surrounding fluid

due to the curved generated streamlines. Detailed overviews containing the single-cell dynamics and collective effects are given in the reviews [49, 87, 104]. One might think that the research on collective dynamics in micro-swimmer suspension is pure basic research, but the work increasingly advances to the task of imitating biological swimmers to recreate and use them, e. g., in medical technology as a reliable means of transport [32, 59].

In any case a bacterium poses a small object moving in a highly viscous surounding, which damps inertial effects. Therefore, concepts for an effective propagation in a high Reynolds number regime based on the rebound have to be replaced by mechanisms using viscous effects like asymmetries in drag coefficients. Moreover, the occurence of turbulent flow patterns is a surprise in collective cell dynamics. The basis for a hydrodynamic understanding of swimming processes at low Reynolds numbers was laid by observation by G. I. Taylor [158] completed by investigations of E. M. Purcell [131] who presented some concepts like the turning corkscrew and highlighted breaking the time-reciprocal symmetry of the underlying Stokes equation technically. The problem of this symmetry consists in no propulsion as long as the backward motion equals the reciprocal forward motion in one stroke. The symmetry ranges that far that it does not matter that forward and backward motion are executed at different velocities. An object consisting of two sub-components will not propagate autonomously in all cases.

The simplest swimming object moving on its own consists of three elements, e. g., spheres whose respective distances change with a phase difference of π [116]. The stroke pattern of the three spheres generates a characteristic backflow around the swimmer with attractive and repulsive parts, leading to configurational dependent hydrodynamic attraction or repulsion between two swimmers [128]. This research is accompanied by a description of the collective dynamics of two interacting, sinusoidal striking dumbbells. If these objects apply a phase difference in their beating pattern they show an effective orientation dependent collective propagation althoug one single object would not move to a certain extent [8, 7, 9].

In the biological world two kinds of swimmers occur denoted as *pushers* and *pullers*. A pusher like the bacteria *Escherichia coli*, illustrated on the right of Figure 1.3 or *Bacillus subtilis* consist of a spherical or rodlike body,

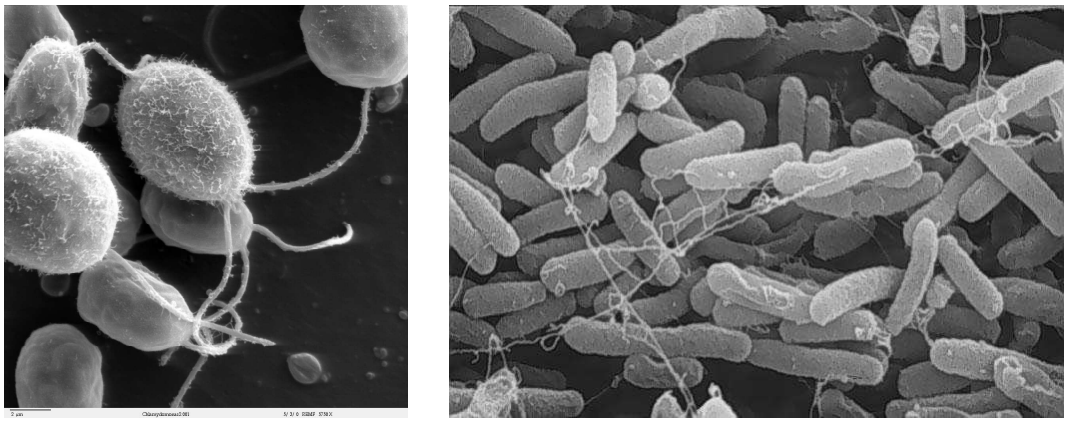

Figure 1.3.: Left: Illustration of *Chlamydomonas reinhardtii* cells with the two cilia [3]. Right: Illustration of a colony of *Escherichia coli* bacteria with a couple of flagella anchored at the cell surface [4].

which is pushed through the surrounding liquid by a bundle of counterclockwise rotating long thin rods called *flagella* [24]. The geometrical shape of the surface is numerically calculated in [84], where this model is taken to investigate the collective dynamics of two swimmers. The propagation and hydrodynamic interaction of two spheres with a rotating helical rod have been analysed by simulation considering sophisticated geometric reproduction of the complete surface of the swimmer [84] containing important states on the configurational dependencies of the hydrodynamic interaction.

A puller like the alga *Chlamydomonas reinhardtii*, illustrated on the feft of Figure 1.3 pulls itself with two flagella fulfilling a motion, similar to a human breaststroke. The executed forces during one stroke are analysed in [21]. Also multicellular algae like *Volvox* executes strokes with flagella similar to the puller type [43]. A third groundlaying swimmer type is the so called *squirmer*. This swimmer consists of a body covered by rods called *cilia*. These execute periodic motions synchronized in waves, propagating over the body and propell the swimmer forward with prescribed tangential surface velocity [64]. Precised numerical investigations of the collective dynamics in a two-body system are presented in [64, 107]. Also squirmer suspensions have been treated, where hydrodynamic attraction leads to spontaneous aggregation [6, 85, 86].

In questions including the hydrodynamic particle-particle interaction in sus-

pensions of swimmers as well as wall effects it is common to average the propelling forces, forming a force-dipole. One force acts at a certain point in front or behind the spherical swimmer body. The second force is the friction, acting on the cell-body equilibrating the first force in opposite direction. Only the directions of these two forces pointing towards or away from each other decide on the described swimmer type. For pushers [45] as well as for pullers [44] the modeled flow field depicts the experimentally determined flow field arround an E. coli bacterium and a C. reinhardtii alga. This seemingly little difference in sign decides whether a suspension of swimmers tends to build clusters spontaneously [34, 173] in confined systems or not. The cell body can be modified by replacing the sphere by dumbbells [76] or even more complex shapes taking into account possible deformations of the cell body [101].

Orientational stochasticity: Diffusion by tumbling

The self-propulsion together with the induced flow-fields are only one aspect in the full dynamics of micro-swimmers. It has been shown that synchronization and desynchronization processes within the flagella beating patterns lead to re-orientations of *E. coli* dynamics [36] as well as *C. reinhardtii* cells [127] inducing *run-and-tumble* dynamics of each individual swimmer. Two facts are important in the following:

1. The change of the direction of motion claims only short times compared to the runs.
2. The resulting direction of motion is not predistined, but a stochastic quantity within a certain angle range.

Therefore, observed swimmer trajectories resemble random-walks [61] so that the description of the dynamics requires stochastic (diffusive) tools [12, 22]. Re-orientations are the result of inner-cellular decisions to be taken by the cell for successful foraging. Biological micro-organisms exhibit sensor systems to track gradients in chemical concentrations of nutrients, light intensity, or a magnetic field. The executed movement patterns are therefore summed up to terms *chemotaxis* [23, 147, 96], *phototaxis* [169], and *magnetotaxis* [39]. The decision on taking a new direction actually runs in the same way. After a run the cell detects the increase or decrease of, e. g., the intensity of light. An increase

means a good region for the intake of food and the traveling direction remains more or less. A decrease of intensity means traveling towards regions poor in nutrients, which can be harmful for the cell. Then the direction of motion may be strongly varied. Hence, the swimmer dynamics underlies a stochastic process with biased directions. By turning on a light source, the orientation of a micro-swimmer can be controlled. This can be used to stabilize the actually unstable dynamics of Chlamydomonas suspensions in outer streams called *self-focusing* [60, 110, 91] or set to outer forces [117].

1.2. Structure of this work

In this work the complex dynamics in suspensions of passive particles driven by an outer shear flow and active, self-propelled particles are investigated. Therefore, this work is organized in two parts, where both parts have in common a particle-based description of the underlying solutes, while they differ in the chosen simulation methods. The first part treats turbulent structures occurring due to particle-induced perturbations. These structures are investigated by means of the Fluid-Particle-Dynamics method (FPD) [90, 123, 156], where the complex hydrodynamic particle-particle interaction and wall-effects are naturally taken into account.

Before getting into the subject on rotating dumbbells, an overview of local bifurcations is given in Chapter 2. In Chapter 3 the Lorenz system is introduced. This three-component nonlinear system was stated by E. N. Lorenz in 1963 to model meteorological systems [108]. Within some steps it can be derived from the Navier-Stokes equation and thus shows the way into chaotic, turbulent dynamics increasing the perturbations in terms of one of the three system parameters. This way via period doubling is traced. Due to its detailed knowledge, the Lorenz system can be handled as a reference for the introduction of Lyapunov exponents, which characterize the stability along trajectories. The algorithm yielding the whole spectrum of Lyapunov exponents is presented and applied to the Lorenz system in this chapter.

In Chapter 4 the idea of the simulation method is explained. The structure of the MAC-grid (*Marker-And-Cell*) is discussed as well as the consideration of boundary conditions. Moreover, the method is improved within a comparison

of the simulated dynamics of a rotating sphere, where the analytical expression of the surrounding flow field is known. The effect of hydrodynamic particle-particle interaction is analyzed for a collision between two beads.

The FENE-dumbbell (*Finitely Extensible Nonlinear Elastic*) is introduced as two connected beads in Chapter 5. First the tumbling dynamics of this object is discussed under the increasing impact of backflows from the walls, causing a separation between the two dynamic states *tumbling* and *vacillating breathing*. A study that takes into account the dumbbell extension compared to the channel size and elastic effects is carried out with the aim to draw a bifurcation diagram. Furthermore, the structure of backflows is presented containing information about the stability along the dumbbell trajectory. Moreover, the rheological behavior of the rotating dumbbell in dependency of the elasticity is investigated by calculating the orientation-dependent shear viscosity and comparing it with the contribution of potential forces calculated by the commonly applied Kramers-Kirkwood formula [26, 40].

In Chapter 6 the concentration of suspended particles is systematically increased by enhancing the number of dumbbells to concentrations around 12 per cent. Thereby, the impact of synchronization and desynchronization will be pointed out in the power spectrum until a chaotic spectrum occurs, where a broad band of frequencies is stimulated and the dumbbell dynamics occurs in an unpredictable manner. The stability analysis is provided by means of the Lyapunov spectrum and the hydrodynamically induced diffusion of tracer particles indicating the turbulent mixing process. These investigations are provided for bead and dumbbell suspensions to point out the influence of the particle deformability and extension. The chapter is closed with the study of rheological behaviors in dependence of the same parameter and a short view on the statistical behavior of the flow field within the increase of concentration is presented.

The second part of this work addresses the dispersion of a distribution of micro-swimmers called *cloud* via particle based simulations. The dispersion is influenced by two effects

1. The hydrodynamic interaction between the swimmers with its attractive and repulsive parts.

2. The stochasticity of the reorientations a swimmer undergoes within forag.

In which way these two effects are modeled is described in Chapter 7.

Finally, in Chapter 8 the dispersion of a cloud is analysed by means of a diffusion process. In this chapter the reference case of free dispersion, i. e., only reorientations of the swimmers are considered without hydrodynamic interaction. Furthermore, the influence of pushers and pullers on the dispersion is investigated. The chapter closes with the description of the dispersion of interacting particles, which execute a biased random-walk.

Part I.

Turbulence in sheared dumbbell suspensions

2. Local Bifurcations

Dynamical systems are determined by the trajectories of an observable $(x, \dot{x})$ in the phase-space. The system behavior is determined primarily by the so-called *control parameter* μ. If a system is described by a set of nonlinear equations of motion

$$\dot{\boldsymbol{x}} = f(\boldsymbol{x}, \mu) \tag{2.1}$$

it usually happens that variations in the control parameter lead to completely new dynamical patterns. Transformations of the dynamic behavior as a function of the control parameter are called *bifurcation* and the parameter value μ_c at which the transition takes place is called critical point. The task of the bifurcation analysis is to determine these values μ_c and to construct the phase space for $\mu > \mu_c$.

For systems that depend on one control parameter μ there are four types of a *local bifurcation*. It is spoken of such kind of a bifurcation if the behavior of the system beyond the critical point arises entirely from an analysis of phase trajectories in the immediate surrounding of the fixed points or orbits. In addition to local bifurcations, there are *global bifurcations* that result from qualitative changes at the critical point μ_c, which can not be determined from the local information around steady states.

In this chapter the *pitchfork-* and the *Hopf-bifurcation* are presented with their characteristics after a short classification of occuring *attractors*. While for systems depending on one parameter μ a systematization of transitions between several attractor types at a certain crtical point μ_c is possible, this task may be complicated for higher dimensional systems depending on a couple of parameter, such as in the present work. An overview of all bifurcations can be found in [14].

2.1. Classification of attractors

Each dynamic system is based on a system of partial differential equations in the form represented in Eq. (2.1). In the simplest case, the mapping rule $\boldsymbol{f}(\boldsymbol{x}, \mu)$ is linear and the dynamical system is solvable. In the nonlinear case, the unique solvability of Eq. (2.1) is often only possible for a couple of special cases. Nevertheless, there is a considerable physical interest to estimate the dynamical behavior of a system especially in the nonlinear case. To determine the long-term dynamics, there are recipes that are briefly introduced at this point.

The first physical interest consists in the determination of the equilibrium states $\boldsymbol{x}_s$, which are the stationary solutions $\dot{\boldsymbol{x}}_s = 0$ in which the evolution of the system does not change. For a characterisation of the stationary state the surrounding environment of the equilibrium state is crucial, where one differentiates between *asymptotically stable* or *unstable* equilibria, if all trajectories in the immediate surounding are attracted or repelled from the steady state $\boldsymbol{x}_s$.

The assymptotic behavior of a trajectory in the surrounding of a stationary solution is characterized by the eigenvalues λ_i of the mapping rule $\boldsymbol{f}(\boldsymbol{x}, \mu)_{\boldsymbol{x}_s}$. The asymptotic behavior is reproduced here for two-dimensional systems $\dot{\boldsymbol{x}} = \boldsymbol{L}\boldsymbol{x}$ with the two eigenvalues λ_1 and λ_2. With the eigenbasis $\{\boldsymbol{y}_1, \boldsymbol{y}_2\}$ the system can be transformed to

$$\dot{\tilde{\boldsymbol{x}}} = (\dot{\tilde{x}}_1, \dot{\tilde{x}}_2) = \tilde{\boldsymbol{L}}\tilde{\boldsymbol{x}}, \tag{2.2}$$

with the diagonalized matrix $\tilde{\boldsymbol{L}}$. The solution of Eq. (2.2) for $\lambda_1 \neq \lambda_2$ yields finally:

$$\tilde{x}_2 = C\tilde{x}_1^{\lambda_2/\lambda_1}. \tag{2.3}$$

Considering the case of non-degenerate eigenvalues $\lambda_1 \neq \lambda_2$ is quite suficient. Four dynamical states can occur, which are illustrated in Figure 2.1:

a) $\operatorname{sign}\lambda_1 = \operatorname{sign}\lambda_2$:
   If the two eigenvalues have the same sign, the solution Eq. (2.3) describes parabolic curves of order λ_2/λ_1, which all have one common tangent at the origin. This situation is called *node*. A stable node is given if the two eigenvalues λ_i are negative, otherwise the node is unstable.

b) $\operatorname{sign}\lambda_1 \neq \operatorname{sign}\lambda_2$:
If the signs differ, the dynamics is unstable in one direction. The trajectories then describe hyperboles and the stationary solution $\boldsymbol{x}_S$ is called *saddle node*.

The cases a) and b) assume purely real eigenvalues. The two values may be conjugated complex $\lambda_{1,2} = \alpha \pm i\omega$ with the real and imaginary parts α and ω. This is, when oscillatory solutions in the form of

$$\tilde{x}_{1,2} = C_{1,2} \exp\{(\alpha \pm i\omega)t\} \tag{2.4}$$

occur. Again two different situations are known:

c) $\alpha \neq 0$:
In this case Eq. (2.4) can be transposed to polar coordinates with a radius $r = r_0 \exp\{\alpha t\}$ and phase $\phi = \omega t + \phi_0$. The trajectories form spirals that rotate into the stable equilibrium state $\boldsymbol{x}_s$ called stable *focus* if $\alpha < 0$ is negative. Otherwise the focus is unstable and the trajectories diverge from $\boldsymbol{x}_s$.

d) $\alpha = 0$:
The case of a vanishing real part $\alpha = 0$ is a special case, where Eq. (2.4) describes elliptic trajectories, whose center point is $\boldsymbol{x}_s$.

At least the first three examples illustrate situations where changes in the long-term behavior of a system do not occur. Thus, the above list enumerates possible motions that result in a fixed point. In linear systems, all long-term solutions are considered by this list. The special feature of nonlinear systems, however, is that the long-term dynamics does not contract to a fixed point, but remains time-dependent. In that case, there is by definition no stationary solution $\dot{\boldsymbol{x}}_s = 0$, so that the stability analysis of a time-dependent long-term solution requires an extension of the term *asymptotic stability* to time-dependent trajectories.

It is purely intuitive to say that a reference trajectory passing through the point $\boldsymbol{x}_r(t_0)$ is stable, if all trajectories starting in the vicinity of $\boldsymbol{x}(t) \approx \boldsymbol{x}_r(t_0)$ stay close to $\boldsymbol{x}_r(t)$ for all following times $t > t_0$. *Asymptotical stability* is given, if $\boldsymbol{x}(t)$ converges to $\boldsymbol{x}_r(t)$ [14]:

$$\lim_{t\to\infty} |\boldsymbol{x}(t) - \boldsymbol{x}_r(t)| = 0. \tag{2.5}$$

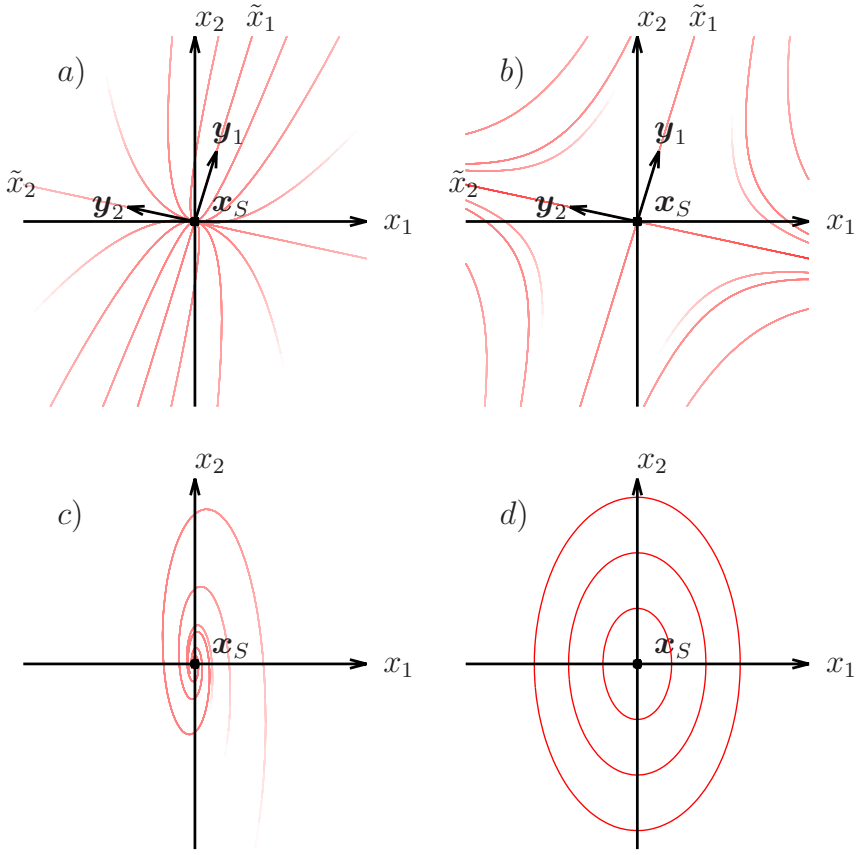

Figure 2.1.: The four different steady states. In a) all trajectories converge to a stable *node* with $\lambda_1/\lambda_2 = 2$. b) illustrates a *saddle node* with stable dynamics in $\boldsymbol{y}_1$-direction, but unstable dynamics in $\boldsymbol{y}_2$ direction. In c) all trajectories converge in spirals towards the stable *focus* $\boldsymbol{x}_s$, where d) presents the concentrical dynamics around the center $\boldsymbol{x}_s$.

This condition provides a hard criterion for the stability analysis, which is in general only applicable for small perturbations of the equilibrium state. Much more common is the use of an attenuated stability definition called Lyapunov stability, which assumes that neighboring trajectories remain adjacent for all times $t > t_0$. Expressed mathematically this means that for an arbitrary deviation $\varepsilon > 0$ there exists a $\delta(\varepsilon) > 0$ so that the initial condition $|\boldsymbol{x}(t_0) - \boldsymbol{x}_r(t_0)| < \delta(\varepsilon)$ yields

$$|\boldsymbol{x}(t) - \boldsymbol{x}_r(t)| < \varepsilon \tag{2.6}$$

for all $t > t_0$ [14]. This definition may seem unwieldy, but, it allows to make statements about the stability behavior under significantly more pronounced disturbances resulting in an analysis tool that is based on the exponential growth of ε with time t:

$$\varepsilon \propto \exp\{\sigma t\}, \tag{2.7}$$

where σ denotes the so-called *Lyapunov exponent*. The sign of σ decides about the stability of $\boldsymbol{x}(t)$, where

$\sigma \leq 0$ means $\boldsymbol{x}$ is stable
$\sigma < 0$ means $\boldsymbol{x}$ is asymtotic stable
$\sigma > 0$ means $\boldsymbol{x}$ is unstable.

The method for determining the Lyapunov exponent is presented in Section 3.3. A strong tool for the visualisation of the behavior of time-dependent flows is the *Poincaré map*. This map depicts the n-dimensional phase-trajectories $\boldsymbol{x}(t)$ on the intersections with a transversal $n-1$-dimensional hypersurface using the idea of a *periodic* trajectory crossing the hypersurface after one circulation [126], as illustrated in Figure 2.2 for a trajectory obtained numerically from the Lorenz system [108]. In the illustrated example, a three-dimensional periodic trajectory breaks through the surface at four intersections P_1 to P_4 (Cf. Figure 2.2*a*). The occurrence of only a few points shows that the trajectory is not subjected to large perturbations and is thus stable. A different picture emerges for an unstable trajectory in Figure 2.2*b*), where the perturbed trajectory penetrates the surface in wide bands. Although the Poincaré map is no suitable quantitive tool, but nevertheless, this method represents a reduction of dimension without losing any essential information on the stability, which is quite important for illustrative purposes.From Figure 2.2*b*) one can

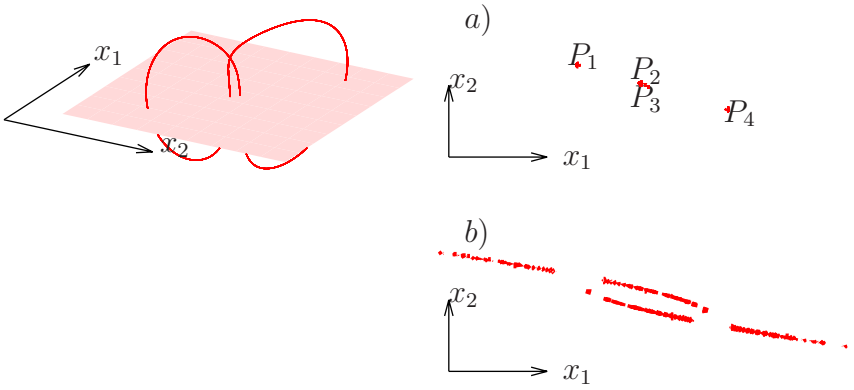

Figure 2.2.: Illustration of a Poincaré map of the trajectory of the Lorentz attractor with $\sigma = 10$, $b = 0.5$ and $r = 28$. The red area corresponds to $z = r - 1$. Under these special parameters a stable dynamics is indicated by four cluster points P_1 to P_4 in a). Unstable dynamics as in b) for $b = 8/3$ lead to broad bands of intersections.

make two important observations on the stability:

1. Although the illustrated trajectory depicts an unstable state, the range of penetration points is limited. Therefore, the term *instability* should not be confused with the divergence of trajectories to infinity.

2. The unstable trajectories are periodic trajectories.

The trajectory illustrated in Figure 2.2 indicates a periodic stable state arising in the long-term behavior, which does not vary its characteristics. This stable *limit cicle* is a further type of attractor, which the dynamic of the system can adopt. In contrast to the previously described fixed points, the occurence of limit cycles requires a nonlinear equation of motion $\dot{\boldsymbol{x}} = \boldsymbol{f}(\boldsymbol{x})$, where at least one pair of complex conjugate eigenvalues $\lambda_{1,2}$ drives the dynamics into oscillations. Then, also the corresponding eigenvectors $\boldsymbol{y}_1 = \boldsymbol{y}_2^*$ of the subspace are also complex conjugate. If the oscillation is determined by such a pair, it is called a one-dimensional orbit or T^1-orbit. Every further pair of complex conjugate eigenvalues increases the dimension of the orbit by one. The dimension n of an orbit allows the categorization of attractors in T^n-orbits, as illustrated in Figure 2.1. Thus, a T^2 orbit with two linearly independent frequencies ω_1 and ω_2 forms a torus.

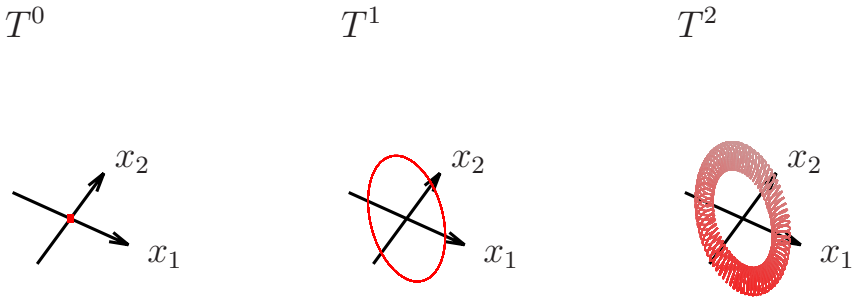

Figure 2.3.: Classification of stationary solutions based on the involved period T. A T^0-orbit represents a fixed point, whereby T^1 and T^2 denote an orbit and a torus, respectively. Depending on the number n of fundamental frequencies this categorization can be continued to T^n.

The stability analysis of the presented attractors arises from purely local properties around the reference trajectories $\boldsymbol{x}_r$ or stationary solution given by $\dot{\boldsymbol{x}}_s = 0$. There may occur situations in which this local understanding, e. g., around the saddle node $\boldsymbol{x}_{s1}$, which repells the trajectory in a certain direction in Figure 2.4 is not sufficient for a global understanding of the dynamics. In Figure 2.4 a half-turn around a rotation axis through the point $\boldsymbol{x}_{s0}$ drives the trajectory back into the saddle node. This kind of dynamics is called *structurally unstable* because the direction of small perturbations can decide about the long-term behavior of the dynamics. The illustrated orbit is called *homoclinic orbit*. A further type of attractor that does not fit into the category of T^n-orbits is the so-called *strange attractor* as a quasi-stationary state for chaotic dynamics. The equations of motion yielding this attractor were derived as a model for the weather prediction in [108]. This attractor will be introduced in more detail as the reference system for turbulent characteristics in Chapter 3.

Knowing the different types of attractors one might ask, if a transition from one attractor to another is possible? The answer is yes. To describe these transitions, a parameter μ is introduced ocurring in the dynamical equation via $\dot{\boldsymbol{x}} = \boldsymbol{f}(\boldsymbol{x}, \mu)$. This parameter μ is called *system parameter* and the system may esentially change the dynamical behavior in dependence of μ via *bifurcations*. In the following, the two important bifurcation types for this work are

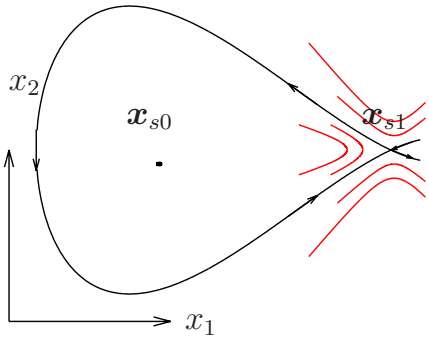

Figure 2.4.: Homoclinic orbit starting and ending in the saddle node $\boldsymbol{x}_{s1}$. The dynamics can not be understood only from local considerations in the immediate surounding of $\boldsymbol{x}_{s1}$.

introduced

2.2. The pitchfork-bifurcation

One of the four fundamental bifurcation patterns is the pitchfork-bifuraction. For its illustration a system is assumed that follows the one-dimensional dynamical equation

$$\dot{x} = f(x, \mu) = \mu x - x^3. \tag{2.8}$$

The stationary solutions x_0 of Eq. (2.8) are given by

$$0 = \mu x_s - x_s^3, \tag{2.9}$$

where besides the trivial solution $x_{s,0} = 0$ regardless of μ, the pair of solutions

$$x_{s,1,2} = \pm\sqrt{\mu} \tag{2.10}$$

is obtained for $\mu > 0$.

All three solutions are illustrated in the bifurcation diagram Figure 2.5. The solution $x_{s,0}$ is a solution for all parameters μ, whereas the two solutions $x_{s,1,2}$ branch off for positve $\mu > 0$.

The question now is how the system behaves if the solutions x_s are perturbed within a small displacement ε? To analyze the motions in the phase

space, equation Eq. (2.8) is extended to a two dimensional de-coupled system of equations $\dot{\boldsymbol{x}} = \boldsymbol{f}(\boldsymbol{x}, \mu)$, which does not affect the characteristics of the bifurcation:

$$\begin{aligned} \dot{x} &= \mu x - x^3 \\ \dot{y} &= -y \end{aligned} \tag{2.11}$$

From $\boldsymbol{f}(\boldsymbol{x}_s, \mu) = 0$ the stationary solutions yield

$$\boldsymbol{x}_{s,0} = (0,0) \qquad \text{and} \qquad \boldsymbol{x}_{s,1,2} = (\pm\sqrt{\mu}, 0) \tag{2.12}$$

with the coresponding Jacobian matrix

$$\left.\frac{\partial \boldsymbol{f}}{\partial \boldsymbol{x}}\right|_{\boldsymbol{x}_s} = \begin{bmatrix} -3x^2 + \mu & 0 \\ 0 & -1 \end{bmatrix}_{\boldsymbol{x}_s}. \tag{2.13}$$

The eigenvalues of this matrix are given by $\lambda_1 = -3x_s + \mu$ and λ_2. For the stationary solutions $\boldsymbol{x}_{s,0} = (0,0)$ both eigenvalues are negative and one stable fixed point can be found. Within the change of sign to positive parameters μ the eigenvalue λ_1 becomes positive, whereby the solution $\boldsymbol{x}_{s,0} = (0,0)$ loses its stability in x-direction. The eigenvalues for the solutions $\boldsymbol{x}_{s,1,2}$ are $\lambda_1 = -2\mu$ and $\lambda_2 = -1$, which due to $\mu > 0$ remain negative. Thus, at the critical point $\mu_c = 0$ two stable branches split up from a once stable solution similar to a pitchfork. Hence this name was given.

The equation Eq. (2.8) is an illustrative example for a pitchfork bifurcation. Investigating an unknown system, identifying the bifurcation with the aim of deriving Eq. (2.8) from the system properties can be difficult if not impossible. Nevertheless, this equation and Figure 2.5 illustrate the properties a bifurcation point at the origin $(x, \mu) = (0,0)$ have to show, namely:

1. The two graphs $x = 0$ and $x^2 = \mu$ intersect in the origin.
2. The fixed point $x = 0$ exists for all μ, where the curve $x^2 = \mu$ stays on one side of $\mu = 0$.
3. The solution $x = 0$ changes its stability within the passage of $\mu = 0$, where $x^2 = \mu$ keeps its stability.

These three conditions are fullfilled within the equation

$$\dot{x} = \mu x + a x^3 + \mathcal{O}(x^5) \tag{2.14}$$

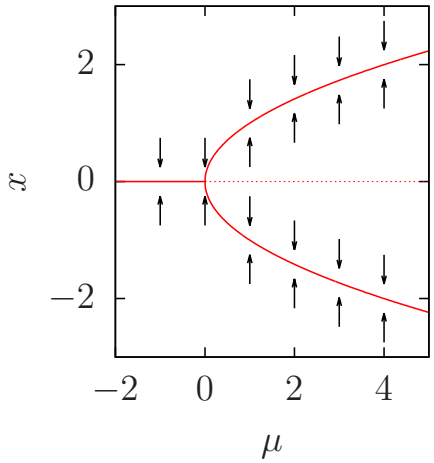

Figure 2.5.: Stationary solutions of the pitchfork bifurcation. The arrows indicate the growth direction of perturbations.

with the real coefficient a determining the stability of the branching fixed points. In Figure 2.5 the stable solution branches into two stable and one unstable solution for a positive value $a = 1$. The opposite case is given for $a < 0$.

2.3. The Hopf-bifurcation

The pitchfork-bifurcation exists if the eigenvalues λ_1 and λ_2 of the Jacobian matrix (Cf. Eq. (2.13)) remain real. Therefore, a pitchfork-bifurcation is not able to describe the transition from a stable fixed point to an oscillatory dynamics on a stable orbit, as this requires complex eigenvalues. This kind of transition occurs frequently in nature, but only occurs in the case of complex conjugate eigenvalues. The transition is illustrated by the dynamical system, which was stated in [80]

$$\begin{aligned} \dot{x} &= -y + x(\mu - r^2) \\ \dot{y} &= x + y(\mu - r^2) \end{aligned} \tag{2.15}$$

with $r^2 = x^2 + y^2$. For all values of μ the only stationary solution is given by $x_0 = y_0 = 0$. The Jacobian matrix

$$\left.\frac{\partial \boldsymbol{f}}{\partial \boldsymbol{x}}\right|_0 = \begin{bmatrix} \mu & -1 \\ 1 & \mu \end{bmatrix} \tag{2.16}$$

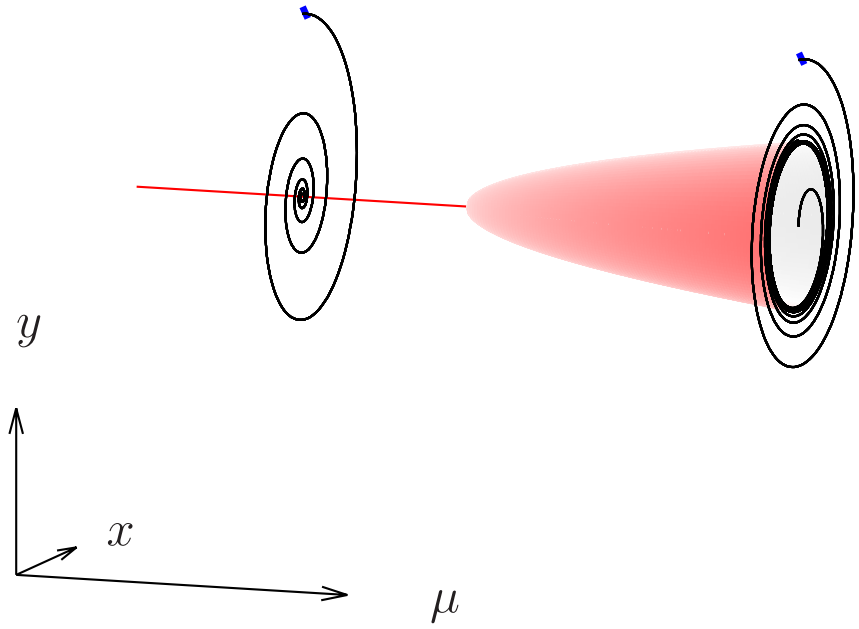

Figure 2.6.: Normal form of a Hopf bifurcation with converging phase trajectories to the orbit. The blue marks indicate the initial positions. At $\mu = \mu_c$ the dynamics towards a stable fixpoint transiates towards a stable orbit.

yields the eigenvalues $\lambda_{1,2} = \mu \pm i$. For $\mu < 0$, the real part $\mathrm{Re}(\lambda_{1,2}) < 0$ is negative und the stationary state is denoted as stable focus. At the critical point $\mu = 0$, the real part changes the sign $\mathrm{Re}(\lambda_{1,2}) > 0$ and the point attractor $\boldsymbol{x}_s = (0, 0)$ becomes unstable.

Which state the trajectories approach for $t \to \infty$, when they leave the unstable focus is not cleared so far. To answer this question the dynamical system Eq. (2.15) is transformed using polar coordinates

$$x = r\cos\phi, y = \sin\phi \tag{2.17}$$

and after some steps one findes the decoupled equation

$$\begin{aligned} \dot{r} &= -r^3 + \mu r \\ \dot{\phi} &= 1. \end{aligned} \tag{2.18}$$

Note that the structure of the equation for r is equivalent to Eq. (2.8). The stationary solutions are $r_{s,0} = 0$ and $r_{s,1} = \sqrt{\mu}$ (radii are defined positively).

Thus, the solution $r_{s,1}$ leads to closed orbits, whose amplitude grows with $\sqrt{\mu}$. The stability of the orbit can also be estimated directly from the temporal derivative of r (Cf. Eq. (2.18)):

$$\begin{aligned} \dot{r} > 0, \quad \text{if} \quad r < \sqrt{\mu} \quad \text{inside the orbit} \\ \dot{r} < 0, \quad \text{if} \quad r > \sqrt{\mu} \quad \text{outside the orbit} \end{aligned} \tag{2.19}$$

driving the dynamics towards the stable orbit for $\mu > 0$. The phase space with the stable fixed point for $\mu < 0$ from where the stable orbit arises is ilustrated in Figure 2.6, where for the chosen values of μ the trajactories converge in spirals to the stable configurations, as shown.

Also equation Eq. (2.15) is only illustrative. The normal case is that variations of the amplitude r and the phase ϕ depend on μ

$$\begin{aligned} \dot{r} &= a_1(\mu)r + a_3(\mu)r^3 + \mathcal{O}(r^5) \\ \dot{\phi} &= b_1(\mu) = \omega(\mu) + br^2 + \mathcal{O}(r^4). \end{aligned} \tag{2.20}$$

Again the real prefactors a_1, a_3, and b decide on the stability of the branching fix point and orbit. In general a Hopf-bifurcation can be defined as a transition between a focus and an orbit, where the amplitude of the appearing orbit grows continuously with μ.

3. The Lorenz system

First investigations on the onset of turbulent flows have been done in the fourties of the last century [81, 102], where the postulate was put forward that a laminar flow $\boldsymbol{u}(\boldsymbol{x})$ splits into a chaotic behavior via an infinite sequence of instabilities under the influence of time-dependent perturbations $\tilde{\boldsymbol{u}}(t)$. The strength of these perturbations is related to the Reynolds number Re, defined as the ratio of viscous to inertial effects. This number represents the key system parameter in the description of inertial turbulence. The underlying question is, when a perturbed flow may be called *turbulent* and which tools are required to describe their behavior in a satisfying manner.

By the transition from a T^n- to a T^{n+1}-orbit, one additional degree of freedom is excited at each bifurcation point one additional degree of freedom is excited, i. e., in the description of turbulent, chaotic dynamics an enormous number of dynamical degrees of freedom should be considered. Ultimately, the introduction of a three-dimensional nonlinear system in the sixties [108] has refuted this requirement by showing the existence of irregular dynamics in a low dimensional system in certain ranges of system parameters. In works from the seventies [118, 155] the *Feigenbaum route* to chaos has been established as one of the commonly accepted ways to chaos following a cascade of Hopf-bifurcations inducing period doubling. In this scenario, the assumption is made that the first transitions from a fixed point along a T^1-orbit to a torus (T^2-orbit) with two intrinsic frequencies via two bifurcations are *generic transitions*, i. e., the new state is stable under small perturbations, and at each bifurcation point a new mode is excited. The modes are assumed to be weakly coupled and it has been shown that the dynamics on a T^3-orbit may disintegrate to the *strange attractor* via unstable modes.

Besides the influence of emerging modes, their stability has been mentioned as being an important ingredient on the way to turbulent dynamics. In this

section, the Lorenz-system [108] with the meaning of its system parameters on the Feigenbaum route to chaos on the one hand and the loss of stability on the other is introduced to make the readeer familiar to important analysis tools characterizing irregular dynamics, which are employed in the course of this work.

3.1. Dynamical equiations and system parameters

The Lorenz system is defined by the three nonlinear equations of motion for the three dimensionless modes x,y, and z, combined to the state $\boldsymbol{x} = (x, y, z)$:

$$\dot{x} = -\sigma x + \sigma y, \tag{3.1a}$$

$$\dot{y} = rx - y - xz, \tag{3.1b}$$

$$\dot{z} = -bz + xz. \tag{3.1c}$$

Since the Lorenz system has been derived as a model for Rayleigh-Bénard convection and weather prediction it is one of the prime examples for a *dissipative system*. Eq. (3.1) are used to describe convective flow patterns and thus the quantity x originally represented flow velocities, where the other two variables stand for temperature differences between upstreaming and downstreaming flows (y) and in vertical direction (z). The pursued trajectories $\boldsymbol{x}(t)$ strongly depend on the choice of the system parameters σ,r, and b. σ is the so-called Prandtl number, measures the amplitude of flow cells, and is set to $\sigma = 10$. The nonlinearities enter via the relative Rayleigh number r related to the strength of perturbations and the quantity b related to the geometry of the flow [108]. The famous *strange attractor* (Cf. Figure 3.1 describing unpredictable dynamics, is obtained with the choice $b = \frac{8}{3}$ and $r = 28$.

3.2. Stability of the Lorenz system

The stability of the Lorenz system is mainly influenced by the relative Rayleigh number r. Therefore, a short discussion of the stability behavior of the Lorenz system Eq. (3.1) within an increase of r trajectories is introduced here.

For $r < 1$, the only stationary state of Eq. (3.1) is given by $\boldsymbol{x}_0 = (0, 0, 0)$,

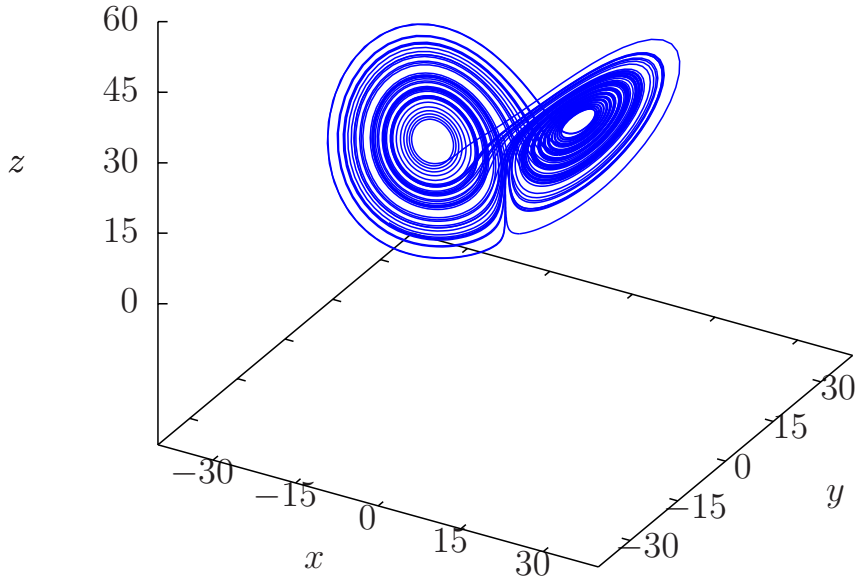

Figure 3.1.: Trajectory on the strange attractor for $\sigma = 10$, $r = 28$ and $b = \frac{8}{3}$.

where a stability analysis yields one stable node, from where two stable nodes

$$\boldsymbol{x}_{1,2} = (\pm\sqrt{b(r-1)}, \pm\sqrt{b(r-1)}, r-1) \tag{3.2}$$

branch off at the first critical point $r_c = 1$ via a pitchfork bifurcation. The trivial solution forms a saddle node, which becomes unstable in the $(1, 1, 0)$ direction and trajectories starting with a little perturbation $(\pm\delta, \pm\delta, r-1)$ in the stability range of $\boldsymbol{x}_1$ or $\boldsymbol{x}_2$ move towards the coresponding fixed point. The characteristic polynomial

$$P(\lambda) = \lambda^3 + (\sigma + b + 1)\lambda^2 + b(\sigma + r)\lambda + 2\sigma b(r-1) = 0 \tag{3.3}$$

shows that all eigenvalues corresponding to $\boldsymbol{x}_1$ and $\boldsymbol{x}_2$ are negative for $1 < r < r_1 \approx 1.346$, where for $r > r_1$ two complex conjugate eigenvalues (Cf. Figure 3.2 occur, and the nodes at $\boldsymbol{x}_{1,2}$ transform to stable foci.

Whether a trajectory converges to $\boldsymbol{x}_1$ or $\boldsymbol{x}_2$ depends on the initial conditions. Perturbations in the positive hemisphere remain in the stability range of $\boldsymbol{x}_1$ and vice versa, while negative perturbations move in spirals towards $\boldsymbol{x}_2$. For comparatively small vaues of $r > r_1$, the spirals curl very fast towards the corresponding fixed point. Looking carefully at the projections to the x, y-plane for $r = 5$ and $r = 10$, as illustrated in Figure 3.3, one can identify that the ability of trapping a trajectory diminishes when r is increased. Roughly

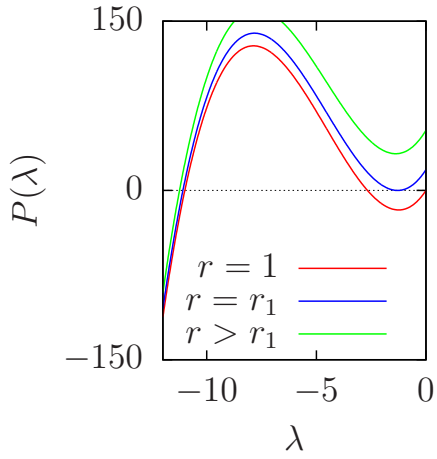

Figure 3.2.: The characteristic polynomial $P(\lambda)$ for increasing values of r illustrates the emerging pair of conjugate-complex eigenvalues when $r > r_1 \approx 1.346$.

speaking, this corresponds to the increasing destablising effects around $\boldsymbol{x}_0$. In the extreme case, when $r = r_2 = 13.926$ a trajectory that starts at the origin rotates around one of the two points $\boldsymbol{x}_1$ or $\boldsymbol{x}_2$ before returning to the origin. This is an example for a homoclinic orbit and the coresponding global bifurcation. Within passing r_2 an unstable limit cycle occurs and suddenly a trajectory, starting in the negative hemisphere, is repelled from $\boldsymbol{x}_2$ until the stability range of $\boldsymbol{x}_1$ attracts the trajectory. Note that the stability of $\boldsymbol{x}_{1,2}$ is not affected within this bifurcation (Cf. Figure 3.3: curves for $r = 15$ and $r = 20$). This happens for much larger values of r. The real part of the conjugate-complex eigenvalues $\lambda_{1,2}$ vanishes for $r = r_c \approx 24.74$ for $\sigma = 10$ and $b = \frac{8}{3}$ and become positive when r is enhanced further. The two stable foci $\boldsymbol{x}_{1,2}$ change to saddle foci with one stable direction and two unstable directions. The *Lorenz attractor*, as illustrated in Figure 3.1, appears via a subcritical Hopf-bifurcation.

This attractor is one example for a chaotic, unpredictable dynamics, described by a low dimensional set of equations of motion. The irregularity arises as follows:

The trajectory starting in the surounding of the origin starts with spirals around one of the two points $\boldsymbol{x}_{1,2}$. While the trajectory is repelled from the respective fixed point, e. g., $\boldsymbol{x}_1$ it approaches simultaneously towards the sta-

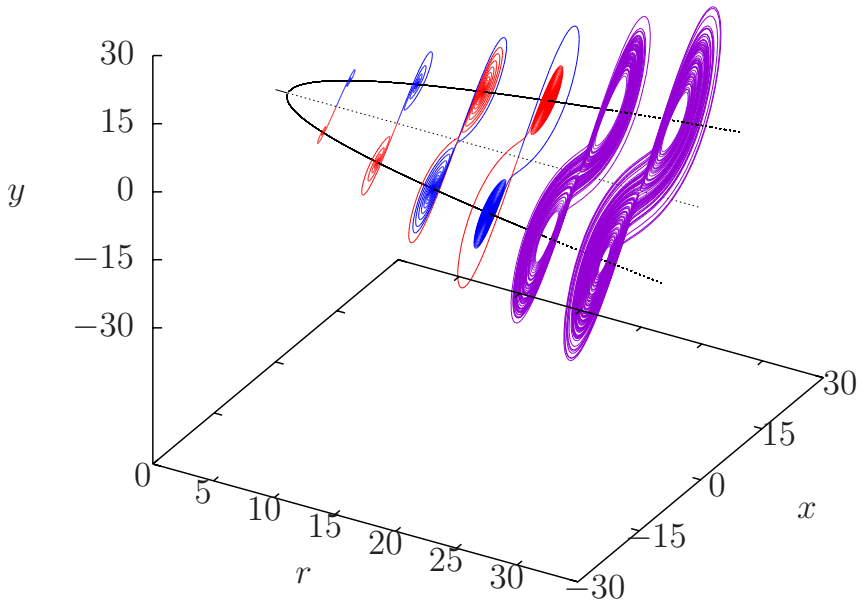

Figure 3.3.: Bifurcation diagram for the Lorenz system Eq. (3.1) with the projection of the trajectories starting at $(\pm\delta, \pm\delta, 0)$ around the origin to the x, y-plane for selected values of r.

bility range of the second fixed point $\boldsymbol{x}_2$. At an unpredictable time, the trajectory leaves the influence $\boldsymbol{x}_1$ and changes to loops around $\boldsymbol{x}_2$ initialzing the same behavior again. The result is an indeed oscillatory, but unpredictable dynamics around the two fixed points with both, stabilizing and destabilizing contributions.

3.3. The Lyapunov spectrum

In the last section, the way to a chaotic dynamical behavior within two bifurcations, where stable fixed points change their local stability characteristics along a trajectory. An experiment often reveals a set of trajectories and the question arises whether their stability behavior can be reconstructed without an exact knowledge of the dynamic equations.

The answer is yes and there are lots of works concentrating on the question of determining the stability of time series considering directional differences in the stability [63, 141, 170, 172]. All concepts have in common that they

determine a spectrum of values, which is called *Lyapunov spectrum*. By means of this spectrum one can obtain important information about the stability of a system and in connection to the ability of mixing. Since this property is associated with the signs of the occuring values, the attractor type can be identified. Based on [14] a method for the determination of the spectrum is presented in the following.

The concept of Lyapunov exponents works with a reference trajectory $\boldsymbol{x}_r(t)$, where the exponent σ measures the sensitivity of the trajectory with respect to small perturbations $\boldsymbol{\varepsilon}(0)$ of the initial conditions.

It may be assumed that the reference trajectory fulfills the dynamical equations, e. g., Eq. (3.1) or Eq. (4.1), where the information on the executed dynamics is contained in the tensor $\mathcal{F}$, so that

$$\dot{\boldsymbol{x}}_r = \mathcal{F}(\boldsymbol{x}_r). \tag{3.4}$$

This formulation is in principle valid for any dynamical system.

To analyze the stability of $\boldsymbol{x}_r$, a second, neighboring trajectory $\tilde{\boldsymbol{x}}(t) = \boldsymbol{x}_r(t) + \boldsymbol{\varepsilon}(t)$ is defined, which corresponds to a small perturbation $\boldsymbol{\varepsilon}(t_0)$. An expansion for small $\boldsymbol{\varepsilon}$ yields

$$\dot{\boldsymbol{x}} = \dot{\boldsymbol{x}}_r + \dot{\boldsymbol{\varepsilon}} = \mathcal{F}(\boldsymbol{x}_r) + \nabla\mathcal{F}|_{\boldsymbol{x}_r}\boldsymbol{\varepsilon} + \mathcal{O}(\boldsymbol{\varepsilon}^2) \tag{3.5}$$

By taking into account only the linear terms one can show that a matrix $\mathcal{L}(t, t_0)$ exists [15], which contains the information how the perturbation $\boldsymbol{\varepsilon}$ at t_0

$$\boldsymbol{\varepsilon}(t) = \mathcal{L}(t, t_0)\boldsymbol{\varepsilon}(t_0). \tag{3.6}$$

The matrix $\mathcal{L}$ may be either linear or nonlinear. Especially in nonlinear systems, it is rare that the eigenvalues λ_i of this matrix can be determined. However, the stability criterion can be related to exponential growth-rates in all dimensions. Then, the *Lyapunov exponent* $\sigma_{\boldsymbol{x}_r}$ is defined with respect to the reference trajectory as exponential convergence or divergence of neighboring trajectories [14]

$$\boldsymbol{\varepsilon}(t) = \boldsymbol{\varepsilon}_0 \exp\{\sigma_{\boldsymbol{x}_r} t\}. \tag{3.7}$$

For $t \to \infty$, the Lyapunov exponent is given by

$$\sigma_{\boldsymbol{x}_r} = \limsup_{t\to\infty} \frac{1}{t} \ln \frac{|\boldsymbol{\varepsilon}(t)|}{|\boldsymbol{\varepsilon}(0)|}. \tag{3.8}$$

While in one dimension this definition is satisfactory, it has to be refined in higher dimensional systems. The main problem is that the directional information on the evolution of the disturbance gets lost with time. The second point concerns the occuring "lim sup", which still may be subject to oscillations even in the long-term behavior.

Additionally, the Lyapunov exponent depends on the choice of the reference $\boldsymbol{x}_r$ itself, but in a stable as well as unstable regime the convergence or divergence of trajectories does not depend on the chosen ergodic reference trajectory, i. e., after a sufficiently long time, the reference trajectory has sampled enough points in the phase space for a robust statement on the system stability. Especially in unstable systems a trajectory $\boldsymbol{x}_r$ covers the entire range of the allowed phase-space volume $\{\boldsymbol{x}(\mu), \dot{\boldsymbol{x}}(\mu)\}$, regardless of the initial conditions, where μ denotes the system parameter. Such a loss of initial conditions is an essential part of an effective mixing process where a small initial volume of a reference substance is smeared out on the entire volume of a considered system. In summary, the Lyapunov exponent is of significance throughout the entire system, so that the initial dependence of the reference trajectory $\boldsymbol{x}_r$ is negligible and hence the index is omitted from hereon.

Flux of an n-dimensional perturbation and Gram-Schmidt method

To obtain information about the Lyapunov spectrum, the initial perturbation $\boldsymbol{\varepsilon}(0)$ of an n-dimensional trajectory is described by an orthonormal basis $\{\boldsymbol{e}_i\}$, spanning the unity volume V^n. Initially, the arbitrarry perturbation $\boldsymbol{\varepsilon}(0)$ may be given by

$$\boldsymbol{\varepsilon}(0) = c_1\boldsymbol{e}_1 + ... + c_n\boldsymbol{e}_n \tag{3.9}$$

with real pre-factors c_i. Note that each individual component $c_i\boldsymbol{e}_i$ itself represents a perturbation $\tilde{\boldsymbol{x}} = \boldsymbol{x}_r + c_i\boldsymbol{e}_i$ of the reference trajectory $\boldsymbol{x}_r$, which propagates independently from the reference trajectory following $\dot{\tilde{\boldsymbol{x}}} = \mathcal{F}(\tilde{\boldsymbol{x}})$. Thus the perturbation $\boldsymbol{\varepsilon}(t)$ grows in each direction $\boldsymbol{e}_i$ with increasing time t with the corresponding growth-rate σ_i

$$\boldsymbol{\varepsilon}(t) = c_1e^{\sigma_1 t}\boldsymbol{e}_1 + c_2e^{\sigma_2 t}\boldsymbol{e}_2 + ... + c_ne^{\sigma_n t}\boldsymbol{e}_n. \tag{3.10}$$

Assuming that $\boldsymbol{e}_1$ with $c_1 \neq 1$ denotes the direction with the highest Lyapunov exponent σ_1, reflecting the largest perturbation, Eq. (3.10) converges to the

component $\boldsymbol{e}_1$ for $t \to \infty$

$$\boldsymbol{\varepsilon}(t) = c_1 e^{\sigma_1 t} \left(\boldsymbol{e}_1 + \underbrace{\frac{c_2}{c_1} e^{(\sigma_2 - \sigma 1)t} \boldsymbol{e}_2}_{\to 0} + ... + \underbrace{\frac{c_n}{c_1} e^{(\sigma_n - \sigma 1)t} \boldsymbol{e}_2}_{\to 0} \right). \tag{3.11}$$

Even when if the pre-factor $c_1 = 0$ initially vanishes, numerical uncertainties lead to an increase of this component in particular.

To prevent the loss of information about one component, the time-line is departed in a sequence t_k, where t_k and t_{k+1} are separated by a small time interval Δt. Within Δt the system and thus the perturbation basis $\{\boldsymbol{e}_1(t_k), ..., \boldsymbol{e}_n(t_k)\}$ evolves to a new basis $\{\boldsymbol{a}_1(t_{k+1}), ..., \boldsymbol{a}_n(t_{k+1})\}$, where this basis is no longer normalized or orthogonal. This basis $\{\boldsymbol{a}_i\}$ has to be converted in a new orthonormal basis $\{\boldsymbol{e}_i\}$ at every time step t_k. For this purpose, the Gram-Schmidt method is used, as illustrated in the sketch in Figure 3.4. The first vector $\boldsymbol{e}_1'$ is given by $\boldsymbol{e}_1' = \boldsymbol{a}_1$. The normalized vector is obtained by $\boldsymbol{e}_1 = \frac{\boldsymbol{a}_1}{|\boldsymbol{a}_1|}$. The second vector $\boldsymbol{e}_2$ is obtained by $\boldsymbol{e}_2' = \boldsymbol{a}_2 - \boldsymbol{a}_2 \cdot \boldsymbol{e}_1 \, \boldsymbol{e}_1$ and $\boldsymbol{e}_2 = \frac{\boldsymbol{e}_2'}{|\boldsymbol{e}_w'|}$. For each following component i this leads to the recursion

$$\boldsymbol{e}_i' = \boldsymbol{a}_i - \sum_{j=1}^{i-1} \boldsymbol{a}_i \cdot \boldsymbol{e}_j \, \boldsymbol{e}_j \qquad \text{with} \quad \boldsymbol{e}_i = \frac{\boldsymbol{e}_i'}{|\boldsymbol{e}_i'|}. \tag{3.12}$$

Determination of the Lyapunov spectrum

While using the Gram-Schmidt method the growth of the unit vector $\boldsymbol{e}_1$ is directly measured by determining the length of the vector $\boldsymbol{a}_{1j} = |\boldsymbol{a}_1(t_j)|$. It can be shown that the $\boldsymbol{\varepsilon}(t_k)$ can be calculated by the product of a_{1j} at all times-steps $j \leqq k$ [15]

$$|\boldsymbol{\varepsilon}(t_k)| = \prod_{j=1}^{k} a_{1,j}. \tag{3.13}$$

For the first Lyapunov exponent this means

$$\sigma_1 = \lim_{k \to \infty} \frac{1}{k \Delta t} \ln \sum_{j=1}^{k} a_{1j}. \tag{3.14}$$

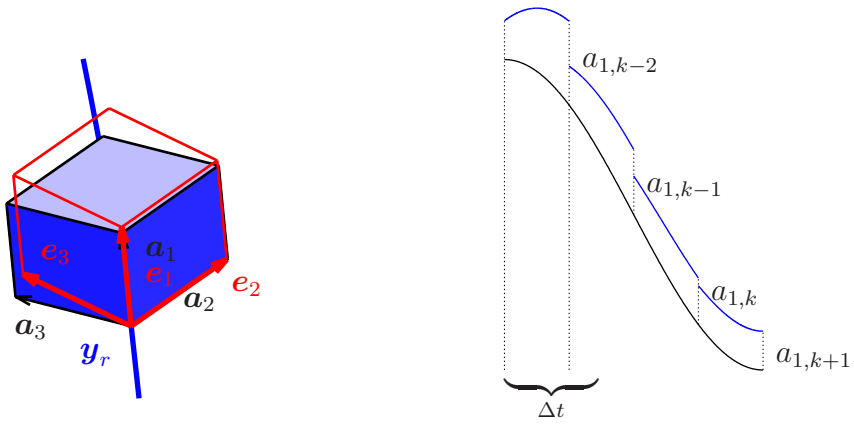

Figure 3.4.: Left: Reference trajectory $\boldsymbol{x}_r$ with a cubic perturbation corresponding to an orthonormal basis $\{\boldsymbol{e}_i(t)\}$. After a certain Δt the $\{\boldsymbol{e}_i(t)\}$ has dispersed to the new basis $\{\boldsymbol{a}_i(t+\Delta t)\}$, where the Gram-Schmidt method is used to recalculate a perturbation with the orthonormal basis $\{\boldsymbol{e}_i(t+\Delta t)\}$. Right: The method yields a piecewise choice of perturbed trajectories, which propagate in a similar direction like the reference trajectory. By summing the lengths $a_{1,k}$ determined after time intervals $k\Delta t$ the Lyapunov exponent is calculated.

The recursive formula, which can be extracted from Eq. (3.14) is used to obtain the convergent sequence $\sigma_{1,k}$ to approximate $\sigma_{1,k+1}$:

$$\sigma_{1,k+1} = \frac{k}{k+1}\sigma_{1,k} + \frac{1}{k+1}\ln a_{1,k+1}. \tag{3.15}$$

This definition is true not only for $\boldsymbol{a}_1$, but for each of the three vectors $\boldsymbol{a}_1, \boldsymbol{a}_2$ and $\boldsymbol{a}_3$, where the Lyapunov exponent converges to the same (highest) value σ_1. To determine the total spectrum of n exponents, the Lyapunov exponent of order p is defined, where $p < n$. Instead of taking the length $a_{1,k}$ the p-dimensional volume V_k^p of the parallelepiped is introduced, which is spanned by the vectors $\boldsymbol{a}_1, ..., \boldsymbol{a}_p$ at $t = t_k$ (Cf. Figure 3.4). Then, if $a_{1,k+1}$ in Eq. (3.15) is replaced by V_{k+1}^p, the spectrum of exponents of order p is given as

$$\sigma_{k+1}^p = \frac{k}{k+1}\sigma_k^p + \frac{1}{k+1}\ln V_{j+1}^p, \tag{3.16}$$

where $\sigma_1 = \sigma^1$ is the Lyapunov exponent of first order and for $p = 2$ and $p = 3$ the volume V^p is given by

$$V^2 = |\boldsymbol{a}_1 \times \boldsymbol{a}_2| \qquad \text{and} \qquad V^3 = |\det(\mathcal{A})|. \tag{3.17}$$

$\mathcal{A}$ denotes the matrix consisting of the vectors $\boldsymbol{a}_i$. By replacing the basis $\{\boldsymbol{a}_i\}$ after the time interval Δt, the trajectories coresponding to the perturbation are piecewise replaced by trajectories, which propagate in similar directions as the reference trajectory (Cf. Figure 3.4). By summing the volume V_k^p according to Eq. (3.16), sequences for σ_k^p are gradually generated, which all converge to the Lyapunov exponent σ^k for $k \to \infty$.

The aim now is to determine all Lyapunov exponents of first order $\sigma_{1,2,3}$. Looking at the order of 2 the Lyapunov exponent

$$\sigma^2 = \sigma(\boldsymbol{e}_1) + \sigma(\boldsymbol{e}_2) = \sigma_1 + \sigma_2 \tag{3.18}$$

is observed, where in principle the second order Lyapunov exponent could be one of the values $\sigma_1+\sigma_2, \sigma_1+\sigma_3$, or $\sigma_2+\sigma_3$. In analogy to the first order value, the sequence tends to the highest growth rate. Determining the Lyapunov exponent of second order enables to calculate the second first order exponent by solving $\sigma^2 = \sigma_1 + \sigma_2$. For any exponent of higher order n the recursive rule fto determine the total spectrum yields $\sigma^n = \sigma_{n-1} + \sigma_n$, resulting in the

recursive mapping rule

$$\begin{aligned} \sigma^1 &= \sigma_1 \\ \sigma^2 &= \sigma_1 + \sigma_2 \qquad \Rightarrow \qquad \sigma_2 = \sigma^2 - \sigma^1, \\ \sigma^n &= \sigma_1 + ... + \sigma_{n-1} + \sigma_n \qquad \Rightarrow \qquad \sigma_n = \sigma^n - \sigma^{n-1}, \end{aligned} \tag{3.19}$$

so that the total spectrum of Lyapunov exponents follows automatically, if one calculates the Lyapunov exponents to n-th order.

Meaning of the Lyapunov spectrum

Note that the determination of Lyapunov exponents depends on a chosen trajectory and not directly on the equations of motion. One goal of using such a spectrum is to identify dynamical changes from one attractor to another within the variation of a system parameter μ, as illustrated in Figure 3.4, when the parameter r in the Lorenz system Eq. (3.1) is increased. In the illustrated parameter range from $r = 5$ to $r = 30$, the spectrum only changes its qualitative behavior, quantified within the signs of σ_1, σ_2, and σ_3 at the critical point $r_c = 24.74$ from $(-,-,-)$ to $(-,0,+)$, shown by the small inlay of Figure 3.5, which besides the negative sign of the highest value, illustrates that the arising unstable limit cycles at $r_2 \approx 13.96$ do not change the stability of the system. This is no accidential trend, but coupled to the arising new dynamical regime at a critical point.

The stability of the system is classified within the highest Lyapunov exponent σ. If this value is negative and the corresponding spectrum reads $(-,-,-)$, neighboring trajectories converge referred to an asymptotic stable system converging to a fixed point. It can be shown that at each bifurcation point at least one exponent becomes 0, e. g., the transition to a stable limit cycle via a Hopf-bifurcation is connected to a variation of the spectrum from $(-,-,-)$ to $(0,-,-)$, where the next Hopf-bifurcation to a torus would lead to $(0,0,-)$ [170], as illustrated in Figure 3.6. The resulting unstable limit cycle for $r_2 < r < r_c$ only induces the change of influence of the still stable fixed points $\boldsymbol{x}_{1,2}$, but does not change their stability. Hence, the spectrum does not change the quantitative behavior at r_2.

In case of a positive highest value, the system is unstable. In general, it is sufficient that one exponent of the spectrum is positive, to change the stability

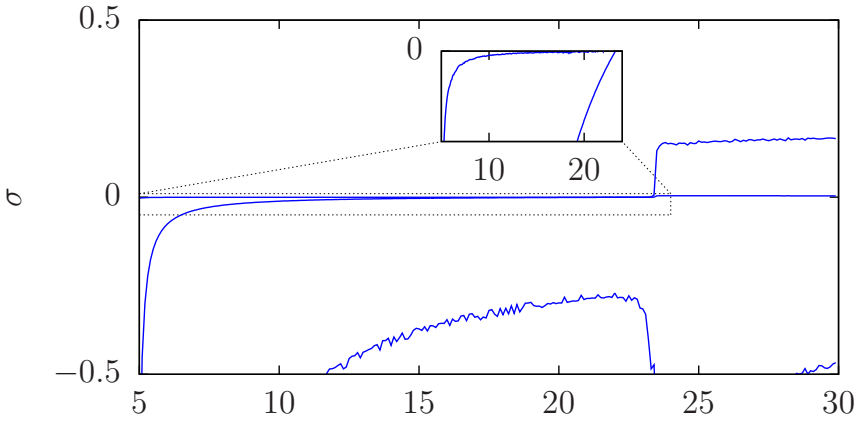

Figure 3.5.: The Lyapunov spectrum σ_1, σ_2, and σ_3 in dependence of the system parameter r. The critical point $r_c \approx 24.74$, where the dynamics changes to a chaotic behavior, as characterized by the change of the spectrum from $(-,-,-)$ to $(-,0,+)$, where the negative sign of the highest value can be seen in the inlay.

of the system from stable to unstable. If all the exponents of the spectrum are positive, two neighboring trajectories will diverge in all directions. Although this is also an unstable dynamics, however, this is not a property of temporally unpredictable trajectories on a strange attractor. These are characterized by stable and unstable parts expressed in a spectrum of the form $(+,0,-)$ as it arises for $r_c > 24.74$ passing from the two stable foci with $(-,-,-)$ via a subcritical Hopf-bifurcation.

The previous considerations on the stability of the Lorenz system have only

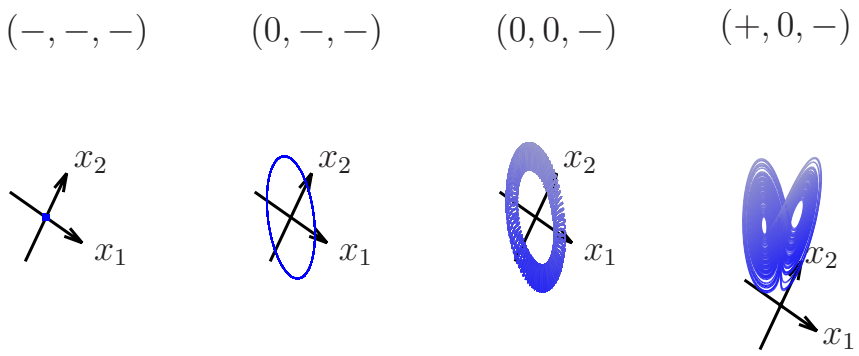

Figure 3.6.: Classification of limit cycles with the Lyapunov spectrum.

served as a reference system to improve the determination method of the Lyapunov spectrum applied here to sheared dumbbell suspensions in Chapter 6 to prove the ability of mixing by rotating dumbbells. In order to assess the specific Lyapunov spectrum determined later, the following statement is made here: If the sum of Lyapunov exponents vanishes, i. e.,

$$\sum_i \sigma_i = 0 \tag{3.20}$$

the underlying system is called *conservative*. In this special case, a considered process runs symmetrically in an inversed direction. A look at Figure 3.5 reveals that the sum $\sum \sigma_i < 0$ for the Lorenz system is negative indicating a *dissipative system*. For flows in the overdamped case, for which a time reversal symmetry is valid, this sum can disappear.

3.4. The Feigenbaum route to chaos

A second way to display a chaotic characteristics is the so-called *Feigenbaum route* to chaos. Based on the Lorenz system this way can be pursued within a variation of the system parameter b in Eq. (3.1), if the other two parameters $\sigma = 10$ and $r = 30$ are fixed [11]. This parameter represents the geometric characteristics of flow cells.

The parameter b is varied between $b = 0.3$ and $b = \frac{8}{3}$. The low parameter regime is characterized by a periodic movement, in symmetrical loops around the first $\boldsymbol{x}_1$ and second fixed point $\boldsymbol{x}_2$. Thus, in Figure 3.10*a*) the projection of the trajectory to the R, z plane with $R = \sqrt{x^2 + y^2}$ shows a periodic limit cycle, so that it can be Fourier transformed

$$\chi(\omega) = \int_0^T x(t) \exp(\pm i\omega t). \tag{3.21}$$

It is sufficient to transform only the x component without a loss of information and to determine the power-spectrum $P(\omega)$ from $\chi(\omega)$

$$P(\omega) = \lim_{T\to\infty} \frac{1}{T} |\chi(\omega)|^2 \tag{3.22}$$

to extract the involved modes ω.

In contrast to Eq. (3.21), the general case does not consist in the Fourier transform of a continuous function $x(t)$. Rather, $x(t)$ is given by a discrete

sequence x_n of $N = 2^\alpha$ data points tracked at the time steps t_n and departed by the constant time interval Δt. In its discrete form, Eq. (3.21) is given by

$$\chi(\omega_k) = \chi_k = \sum_{n=0}^{N-1} x_n \exp(i\omega_k t_n) = \sum_{n=0}^{N-1} x_n \exp(2\pi ikn/N) \tag{3.23}$$

with entries at the discrete frequencies ω_k

$$\omega_k = 2\pi \frac{k}{N\Delta t} \tag{3.24}$$

running from $k = -\frac{N}{2}, ..., \frac{N}{2}$. There are lots of implemented algorithms calculating the discrete Fourier transform, e. g., the fast Fourier transform (FFT) described in [130]. It is common to all that they yield a symmetric spectrum χ_k around $k = 0$. The discrete power spectrum for $k = 0, ..., \frac{N}{2}$ results from averaging the two sides

$$\begin{aligned} P(\omega_0) &= \frac{1}{N^2}|\chi_0|^2, \\ P(\omega_k) &= \frac{1}{N^2}(|\chi_k|^2 + |\chi_{N-k}|^2), \\ P(\omega_{N/2}) &= \frac{1}{N^2}|\chi_{N/2}|^2 \end{aligned} \tag{3.25}$$

for the zero and positive frequencies ω_k. Actually one might think that the power spectrum results after the simple application of a FFT and some rearrangements. This is only partially true, since the finiteness of the data set causes the spectrum to be smeared out to several adjacent frequencies, as shown in Figure 3.7. In this figure, the sine function $f(n) = sin(n)$ is illustrated which analytical Fourier spectrum contains two sharp peaks $\delta\left(\pm\frac{2\ pi}{N\ Deltat}\right)$ at the frequencies $\omega = \pm 2\pi/N\Delta t$. It can be seen that a maximum appears at both frequencies, but the spectrum has also contributions at very large and small frequencies, which can distort the power spectrum.

This phenomenon is called *leakage* and can not be avoided. However, it is possible to filter the leaked frequencies, especially the extreme small and large ones by applying a window function w_n, to the data x_n so that instead of x_n the filtered data $\tilde{x}_n = w_n x_n$ is Fourier transformed to obtain the windowed power spectrum $\tilde{P}(\omega_k)$. Due to its linearity, the Fourier transform of $x_n w_n$ is obtained from the product of the individual Fourier transforms χ_k and W_k

$$\tilde{\chi}_k = W_k \, \chi_k. \tag{3.26}$$

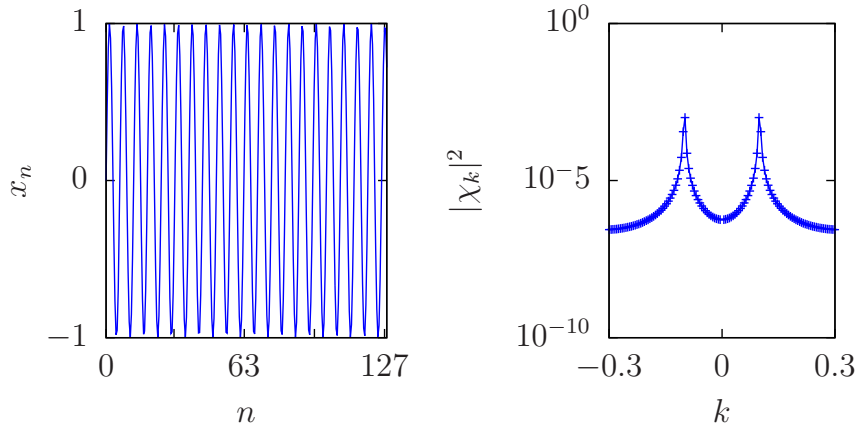

Figure 3.7.: A sine function is numerically Fourier transformed. The resulting δ-peaks leak at small and large frequencies.

There is a variety of windows, where a few are listed in [130]. For this work the Hamming-window, as illustrated in Figure 3.8, is used. The corresponding function w_n is given by

$$w_n = a_0 - a_1 \cos\left(\frac{2\pi n}{N-1}\right) \tag{3.27}$$

with the pre-factors $a_0 = 0.54$ and $a_1 = 0.46$.

The Fourier transform W_k of the window function W_n is shown on the right side of Figure 3.8. Here, the influence of the windowing on the original Fourier transform is clarified, where frequencies with large distances from the main maximum are attenuated.

To calculate the windowed power spectrum $\tilde{P}(\omega_k)$, a data set of the length N_g is subdivided into K sub-segments of length $N = 2M$, which are Fourier transformed and finally averaged. It has been shown that an overlapping generation of segments provides the most effective attenuation of secondary frequencies [130]. The first segment ranges from $n = 0$ to $n = 2M - 1$. The second half of the first segment simultaneously forms the first half of the second segment ranging from $n = M$ to $n = 3M - 1$ and so on. In the following, only the filtered power spectrum is calculated, so that an identification with $\tilde{}$ is omitted in the further parts of the work.

The power spectrum obtained for an orbit of the Lorenz system, as illustrated in Figure 3.10*a*), reveals peaks at a ground mode ω_0 and its harmonics

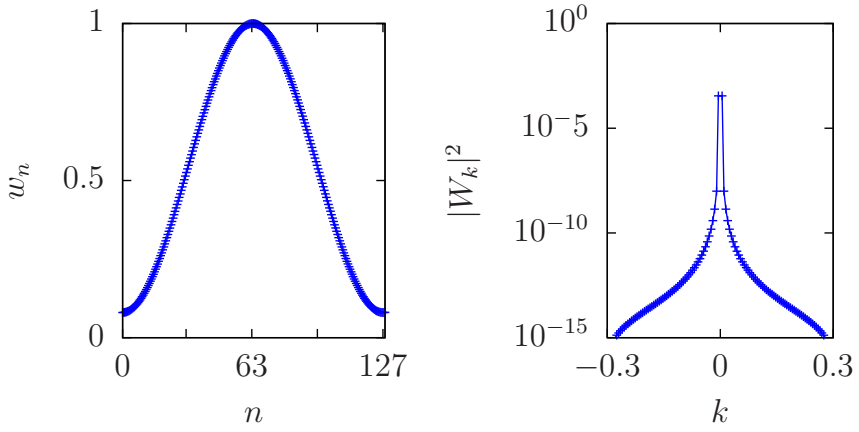

Figure 3.8.: Left: The window function w_n. Right: The Fourier transform W_n of the window function.

$\omega_n = n\omega_0$ due to the nonlinearities in Eq. (3.1). The dependence on one frequency holds until $b_1 \approx 0.44$, where two additional intersections of R appear in the Poincaré section through the reference plane $z = r - 1$ (Cf. Figure 3.9). This point is a classical Hopf-bifurcation at which a new frequency ω emerges in the power-spectrum Figure 3.10*b*) and thus in the dynamical behavior. In the last section, it was mentioned that the transition from a T^1-orbit with one intrinsic frequency ω_0 to a T^2-orbit with two frequencies ω_1 and ω_2 should cause a trajectory moving on a torus. This does not happen, rather, a synchronization mechanism between the weakly coupled modes x, y, and z ensures that the dynamics transiates to a loop with *periodicity* 2. In a cascade of such bifurcations, new frequencies enter the dynamics gradually, where the periodicity of the limit cycle doubles at each bifurcation point. Limit cycles of periodicity 4 arise after $b_2 \approx 0.554$ (Cf. Figure 3.10*d*) and even the periodicity 8 cycles arising at $b_3 \approx 0.572$ are resolvable. The density of bifurcation points with respect to the parameter b increases and the next critical point at $b_c \approx 0.576$ is coupled to the excitation of a continuous band of frequencies ω. The dynamics changes on the strange attractor and becomes chaotic, as shown in Figure 3.10*d*) for $b = 2.666$. Although the stimulated band is continuous, the power-spectrum is not uniformly distributed preferring the low frequence range. This property reaffirms the dissipative characteristics of the Lorenz system.

Not the entire range between $b = 0.576$ and $b = 2.666$ is marked by a chaotic

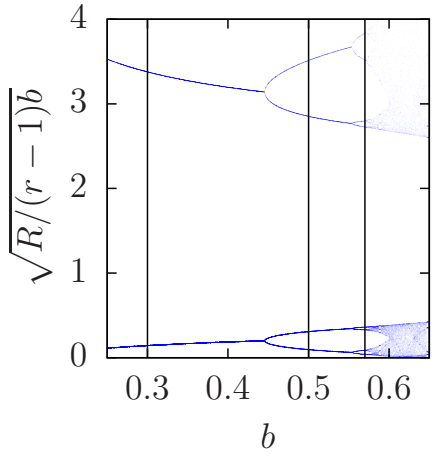

Figure 3.9.: Poincaré section of the Lorenz system in dependence of b. The three black lines indicate the parameters of the measured trajectories and power-spectrum illustrated in Figure 3.10

dynamics, e. g., at $b \approx 0.684$ the dynamics stabilizes again and the periodicity 2 orbits re-emerge and within the next cascade of bifurcations a new chaotic regime emerges at $b \approx 0.76$. The phenomenon of the continuous replacement of a chaotic dynamics by a regular dynamics is called *intermittency*, meaning that the self-similar occurence of a system in certain parameter ranges can be broken in other ranges.

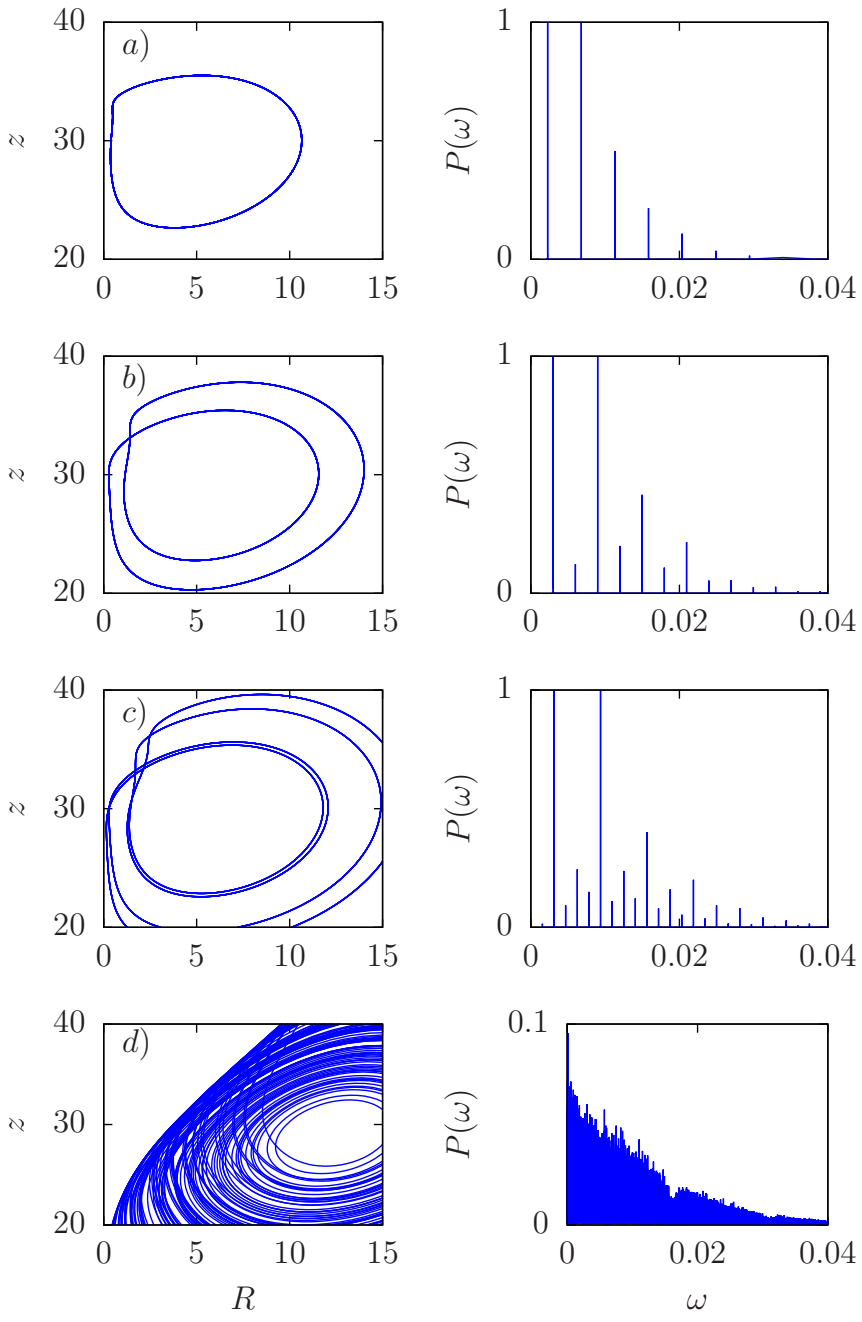

Figure 3.10.: Trajectories of the Lorenz system projected to the R, z plane, where $R = \sqrt{x^2 + y^2}$ for *a)* $b = 0.3$, *b)* $b = 0.5$, *c)* $b = 0.57$, and *d)* $b = 2.666$.

4. Fluid Particle Dynamics

To get a feeling for the properties of dynamical systems, Chapter 2 and Chapter 3 provided an insight into the theory of bifurcations introducing the Lorenz system as a reference system for turbulence. The aim of this chapter is to introduce the simulation technique *Fluid Particle Dynamics* [90, 123, 156].

For the numerical description of elastic multi-particle systems this simulation method is the tool of choice despite the comperatively time consuming effort. The idea of the method consists in a direct solution of the Navier-Stokes equation on a special grid called *MAC-grid (Marker-and-Cell)* [125] so that the hydrodynamic interaction between suspended particles is directly included. The boundary-condition on a moving particle, especially, if several particles are considered, poses a further problem, which is circumvented by assuming the extended particles being part of the solvent liquid with the only difference that they are considered as highly viscous areas in the liquid. A two-component liquid actually is replaced by a quasi-Newtonian fluid. The concept of the method enables an easy consideration of boundary conditions and thus it was used for the investigation of the rheology in bead suspensions [37]. In addition, the method has been used to describe the coil-globule transition in connection with polymers [93].

In Chapter 5 the method first is applied to the dynamics of a confined dumbbell to investigate the transition between *vacillating breathing*, a configuration, where the dumbbell rests in a position parallel to the streamlines, and *tumbling*, where the elastic dumbbell rotates. Further, the contribution of elastic spring forces on the dumbbell rheology is investigated before this method is used in Chapter 6 to prove turbulent characteristics in overdamped dumbbell suspensions.

4.1. Numerical method

The Fluid Particle Dynamics [123, 156] approach (FPD) is used to describe the dynamics of suspended colloidal particles in the low Reynolds number regime confined in a box of size $L_x \times L_y \times L_z$. $L_y = L_z = 60\delta$ are fixed and only the channel width L_x is varied with $L_x \in [18\delta; 66\delta]$. Inside this box, a grid with an equidistant mesh-size of $\delta = 1$ is applied in all three dimensions. The suspension inside this box consists of a Newtonian liquid described by the incompressible Navier-Stokes equation

$$\rho_0 \left[\partial_t \boldsymbol{u}(\boldsymbol{x},t) + \boldsymbol{u}(\boldsymbol{x},t) \cdot \nabla \boldsymbol{u}(\boldsymbol{x},t)\right] = \nabla \cdot \boldsymbol{\sigma}(\boldsymbol{x},t) + \boldsymbol{f}(\boldsymbol{x},t) \tag{4.1}$$

$$0 = \nabla \cdot \boldsymbol{u}(\boldsymbol{x},t) \tag{4.2}$$

with the local flow-field $\boldsymbol{u}(\boldsymbol{x},t)$, and direct internal and external force-field $\boldsymbol{f}(\boldsymbol{x},t)$ per volume element, e. g., executed by direct couplings between two suspended particles. ρ_0 denotes the fluid density, which is assumed to be constant and of the same value for the liquid solvent and suspended particles. The stress tensor $\boldsymbol{\sigma}$ is given by

$$\boldsymbol{\sigma}(\boldsymbol{x},t) = -p(\boldsymbol{x},t)\mathcal{I} + \eta(\boldsymbol{x})[\nabla \boldsymbol{u} + \nabla \boldsymbol{u}^T] \tag{4.3}$$

with $p(\boldsymbol{x},t)$ and $\eta(\boldsymbol{x})$ representing the local pressure-field and viscosity-profile respectively.

The main idea of the FPD method is to circumvent the problem of constructing moving boundaries between the liquid and colloidal particles. This is executed by domains of an effective radius $a = 3\delta$ placed at position $\boldsymbol{x}_i$. Within an inner radius of $\alpha = 2\delta$ the viscosity η_1 is enhanced by a factor of $100\eta_0$ to mimic a solid particle around the bead position $\boldsymbol{x}_i$, where a particle interface of size $2\beta = \delta$ is assumed. In this transition region the viscosity decays from η_1 to η_0 yielding the viscosity-profile $\eta(\boldsymbol{x})$ of m suspended beads Figure 4.1:

$$\eta(\boldsymbol{x}) = \eta_0 + \frac{\eta_1 - \eta_0}{2} \sum_i^m \tanh\left\{\frac{\alpha - |\boldsymbol{x}_i - \boldsymbol{x}|}{\beta}\right\}. \tag{4.4}$$

This viscosity-profile enters the stress tensor given in Eq. (4.3), where the resulting equations of motion Eq. (4.1) and Eq. (4.2) are solved numerically using the projection method on a three dimensional MAC-grid [125].

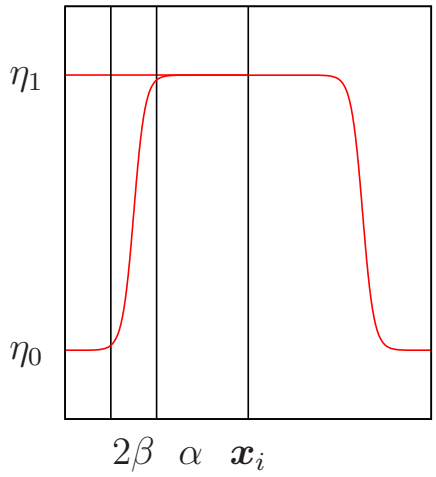

Figure 4.1.: Viscosity-profile around the center $\boldsymbol{x}_i$ of one bead.

Note that the full Navier-Stokes equation Eq. (4.1) is solved instead of the Stokes equation, which neglects all inertial effects. Therefore, although the described dynamics remains in the small Reynolds number regime, the FPD method is able to handle flows at small, but finite Reynolds numbers $\mathrm{Re} < 1$. For the present work the particle Reynolds number is given by the characteristic radius $a = 3\delta$ and the constant gradient $\dot{\gamma}$

$$\dot{\gamma} = \frac{2U_0}{L_x}. \tag{4.5}$$

of a shear-flow, which is induced by moving the upper wall at $x = L_x$ with the constant velocity U_0 and the lower plate at $x = 0$ with $-U_0$ in the opposite direction. The velocity U_0 is chosen such that $\dot{\gamma} = 2 \cdot 0.5/60 \approx 0.01724$ remains small. The particle Reynolds number

$$\mathrm{Re} = \frac{2\rho_0}{\eta_0} a\dot{\gamma}\delta \approx 0.1, \tag{4.6}$$

so that inertial effects can be safely discarded.

To solve the incompressible Navier-Stokes equation numerically the projection method as proposed in [125] is used. Eq. (4.1) with the incompressibility condition Eq. (4.2) is rewritten in a finite-difference scheme on the so called MAC-grid in three dimensions. Actually, this grid consists of two grids, where the viscosity $\eta_{i,j,k}$ and stress tensor $\sigma_{i,j,k}$ are defined at the center of the cell (i, j, k), where the fluid velocity $\boldsymbol{u} = (u, v, w)$ is defined at the boundaries of

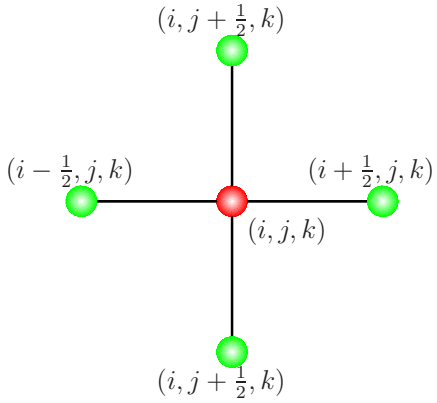

Figure 4.2.: Illustration of the MAC-mesh: Pressure p and viscosity η are defined at the mesh center (red), where the velocity components (u, v, w) are defined at the edge (green).

the cell in x-direction at $i \pm \frac{1}{2}$, y-direction at $j \pm \frac{1}{2}$ and z-direction at $k \pm \frac{1}{2}$ (Cf. Figure 4.2). This definition has some practical advantages, e. g., the stress tensor $\sigma_{i,j,k}$ at the cell (i, j, k) is characterized by the spatial derivatives

$$\partial_x u_{i,j,k} = \frac{u_{i+1/2,j,k} - u_{i-1/2,j,k}}{\delta} \tag{4.7}$$

with an equivalent expression in the y- and z-directions, which are defined at the cell center.

The grid width δ is chosen to be much smaller than the bead radius a. In order to obtain a reasonable resolution of a suspended particle on the grid, one particle consists of around one hundred inner grid points. Thus $a = 3\delta$ represents a lower limit for the choice of the bead radius a. In the y- and z-direction $N_y = N_z = 61$ grid points are implemented, where according to the variations of the box width L_x a number of $N_z \in [19; 67]$ leads to an entire number of grid points $N = N_x N_y N_z$ between $N = 60,000$ and $N = 300,000$. The box size is limited by the moving solid walls, where no-slip boundary conditions are applied with velocities $w(0, L_x) = \pm U_0 \hat{\boldsymbol{e}}_z$ in the x-direction and $w(0, L_y) = \dot{\gamma}(x - \frac{L_x}{2})\, \hat{\boldsymbol{e}}_z$ in the y-direction. Furthermore, periodic boundaries are applied in the z-direction.

The integration of Eq. (4.1) and Eq. (4.2) via the projection method can be split into three steps. The starting point consists of a forward discretization

of Eq. (4.1) in time:

$$\frac{\boldsymbol{u}^{n+1}-\boldsymbol{u}^{n}}{\delta t}+(\boldsymbol{u}\cdot\nabla\boldsymbol{u}^{n})=\frac{1}{\rho_0}[-\nabla p^{n+1}+\nabla\epsilon^{n}+\boldsymbol{f}^{n}] \tag{4.8}$$

with $\epsilon=\eta(\boldsymbol{x})[\nabla\boldsymbol{u}+(\nabla\boldsymbol{u})^{T}]$. Superscripts indicate the time-step, i. e., $u^{n}=u(t_n)$. The pressure p can be considered as Lagrange multiplier ensuring the incompressibility of the fluid. That is why at the initial step only an intermediate 'wrong' velocity $\boldsymbol{u}*$ is calculated, where the pressure p is neglected in Eq. (4.8):

$$\begin{aligned}\frac{\boldsymbol{u}^{*}-\boldsymbol{u}^{n}}{\delta t} &= \frac{1}{\rho_0}[\nabla\sigma^{n}+\boldsymbol{f}^{n}]-(\boldsymbol{u}\cdot\nabla\boldsymbol{u}^{n})\\ \Rightarrow \boldsymbol{u}* &= \boldsymbol{u}^{n}+\frac{\delta t}{\rho_0}[\nabla\sigma^{n}+\boldsymbol{f}^{n}-\rho_0(\boldsymbol{u}\cdot\nabla\boldsymbol{u}^{n})].\end{aligned} \tag{4.9}$$

The velocity $\boldsymbol{u}^{*}$ violates the incompressibility condition Eq. (4.2). Nevertheless, within this step the outer shear-flow is imposed. To obtain the 'real' velocity-field $\boldsymbol{u}^{n+1}$ the equation

$$\frac{\boldsymbol{u}^{n+1}-\boldsymbol{u}^{*}}{\delta t}+\frac{1}{\rho_0}\nabla p^{n+1}=0 \tag{4.10}$$

has to be solved, where Eq. (4.9) and Eq. (4.10) result in Eq. (4.8). Taking the divergence of this equation under the condition that $\boldsymbol{u}^{n+1}$ fulfills the incompressibility condition one finds the Poisson equation, coupling the flow- and pressure-field:

$$\nabla^2 p^{n+1}=\frac{\rho_0}{\delta t}\nabla\boldsymbol{u}^{*}. \tag{4.11}$$

The calculation of the solution of Eq. (4.11) is the time consuming limitation of the simulation method. Without taking any numerical libraries Eq. (4.11) can be solved with relaxation methods. Then the equation

$$\frac{\partial p}{\partial q}=\nabla^2 p-\frac{\rho_0}{\delta t}\nabla\boldsymbol{u}^{*} \tag{4.12}$$

whith the time q representing an artificial variable with no physical meaning is solved iteratively until the residual on the left of Eq. (4.12) is smaller than the error ε. Within this second step the periodic boundary conditions in z-direction are realized, where an applied pressure-gradient generates a Poiseuille flow. After the calculation of the pressure-field p one uses Eq. (4.10) to determine $\boldsymbol{u}^{n+1}$. This is the last step of the method.

$$\boldsymbol{u}^{n+1}=\boldsymbol{u}^{*}-\frac{\delta t}{\rho_0}\nabla p^{n+1}. \tag{4.13}$$

After the determination of the flow field $\boldsymbol{u}$ within the entire domain, the velocity $\boldsymbol{u}_i(t)$ of the i-th bead is calculated by averaging the flow inside the bead volume $V_i = \frac{4}{3}\pi a^3$ located at $\boldsymbol{x}_i$, where the viscosity $\eta(\boldsymbol{x})$ is enhanced. Further, at the considered grid point (i, j, k) a pre-factor $w_{i,j,k}$

$$w_{i,j,k} = \frac{\eta_{i,j,k} - \eta_0}{\eta_1 - \eta_0} \tag{4.14}$$

is introduced to smear out the velocity $\boldsymbol{u}(\boldsymbol{x})$:

$$\boldsymbol{u}_i(t) = \frac{\sum_V w(\boldsymbol{x})\boldsymbol{u}^{n+1}(\boldsymbol{x}, t)}{\sum_V w(\boldsymbol{x})}. \tag{4.15}$$

The position $\boldsymbol{x}_i(t)$ of each bead is then updated by integrating this velocity via an Euler-step to the new position

$$\boldsymbol{x}_i(t + \delta t) = \boldsymbol{x}_i(t) + \delta t \boldsymbol{u}_i, \tag{4.16}$$

where $\boldsymbol{u}_i(t)$ is the effective velocity of the i-th bead with all forces included due to potentials or hydrodynamic interaction (HI). Note that the averaging causes a decoupling of the particle position $\boldsymbol{x}_i$ from the grid.

4.2. Rotation of one bead and generation of vortices

The shearing of one extended bead no matter at which position leads to a bead rotation due to the torque, generated by the different flow velocities at the top respectively bottom of the bead. Of interest is the structure of that flow field, which is formed around the sphere, which is illustrated in Figure 4.3 on the left. This flow field represents the irregular perturbation of a regular motion, each turbulent flow pattern is based on. Already in predictable, regular states perturbations, caused by the extension a of the suspended beads, influence the dynamics, so that an analysis of perturbing flow structures is helpful for the understanding of complex multi-particle dynamics.

In the simplest case of a flow perturbation one bead causes a feedback on the driving shear flow resulting in a fast decaying vortex around the suspended sphere. This vortex contributes to the hydrodynamic particle-particle interaction in multi-particle suspensions. However, before the dynamics of several beads is discussed, the question is, how the perturbed rotational component

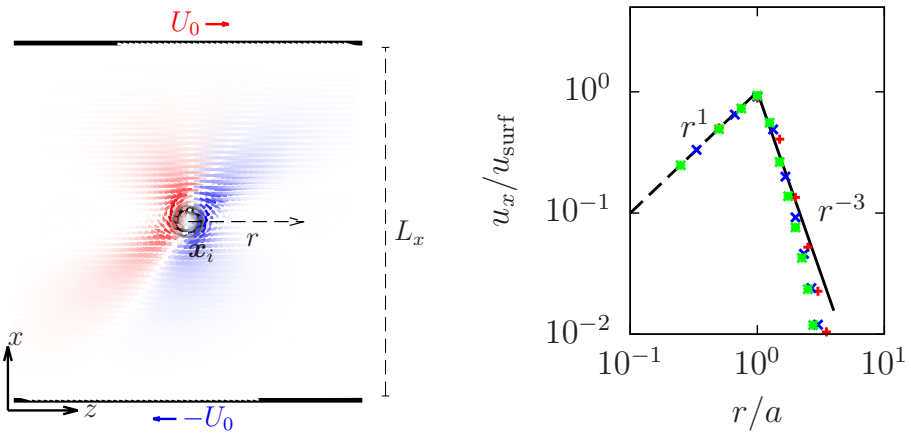

Figure 4.3.: Left: Sketch of a rotating bead in the centerline of a linear shear flow with shear rate $\dot{\gamma} = 2U_0/L_x$. The surrounding flow field is illustrated by the small vectors, where the direction of the x-component is plotted color-coded. The black arrow indicates the direction in which r is varied to obtain the tangential flow. Right: Tangential flow-component u_x with respect to the velocity on the bead surface $u_{\mathrm{surf}} = -\frac{1}{2}\dot{\gamma}a$ illustrated for $a = 2$ (red), $a = 3$ (blue) and $a = 4$ (green).

of the flow profile can be extracted from the total flow field $\boldsymbol{u}(\boldsymbol{x}, t)$ containing all flow effects.

As the left of Figure 4.3 shows, the bead induced perturbations of a laminar flow occur symmetric around the centerline of the channel at $x = L_x/2$. In addition, this figure shows that the perturbations of the laminar flow along the centerline are given by the perpendicular u_x component of the flow field. This enables an illustration of flow contributions due to the so-called *hydrodynamic interaction*. On the right of Figure 4.3 the numerically determined flow u_x in dependece of the distance $r = |\boldsymbol{x} - \boldsymbol{x}_i|$ is illustrated for different radii a.

Due to the shear the bead starts to rotate with the angular velocity $\dot{\theta} = -\dot{\gamma}$, so that the velocity increases linearly inside the bead ($r < a$) until at the bead surface the velocity

$$u_{\text{surf}} = -\frac{1}{2}\dot{\gamma}a \tag{4.17}$$

is reached. A very strong decay with r^{-3} can be observed for $r > a$, deviations from this law for large ratios r/a can be explained in terms of wall-induced back flows. The vortex flow $u_\perp$ is given by

$$\boldsymbol{u}_\perp = \begin{cases} -\frac{1}{2}\dot{\gamma} r \, \hat{\boldsymbol{e}}_y \times \frac{\boldsymbol{r}}{r} & \text{for } r \leq a \\ -\frac{1}{2}\dot{\gamma} a \cdot \left(\frac{a}{r}\right)^3 \hat{\boldsymbol{e}}_y \times \frac{\boldsymbol{r}}{r} & \text{for } r > a. \end{cases} \tag{4.18}$$

The negative sign of $u_\perp$ indicates the sense of bead and vortex rotation, which changes if the system is sheared in the opposite direction. The perturbations scale with the shear-rate $\dot{\gamma}$ and the radius a, so that the shear-rate next to the driving is connected with the degree of irregularity in the system at the same time. Beyond a distance $\lambda \approx 5a$ around the bead there is no contribution to the total flow due to the vortex. Hence, the length λ may be considered as a correlation length for the flow inside a vortex and will play a role as characteristic length scale especially in the turbulent regime, as we will show later.

4.3. Collision of two beads

The numerically determined flow in Eq. (4.18) represents the reproduction of the analytic solution of a *rotlet* [33], which is used to calculate hydrodynamic impacts at a certain position $\boldsymbol{x}$ as a result of torques acting at $\boldsymbol{x}_i$. Considering

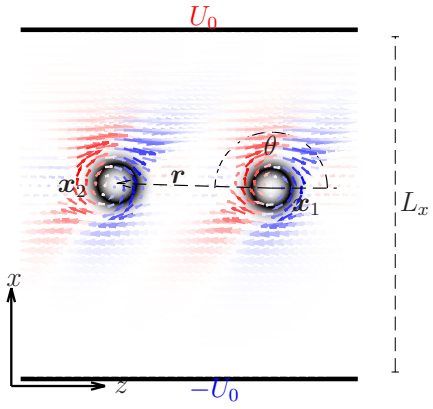

Figure 4.4.: Sketch of two colliding beads in a linear shear flow.

the dynamics of two suspended rotating beads a rotlet causes a small asymmetry, prefering a clockwise rotation, in the otherwise time-reversible dynamics in low Reynolds number regimes. The temporal reversibility implies a configurational symmetry of any bead motion due to hydrodynamic flows. To check the good agreement of the simulated processes, a collision of two spheres is simulated with the FPD method. The two colliding beads are initially located at

$$x_{1,2}(t=0) = L_x/2 \pm \varepsilon_0 \qquad z_{1,2} = L_z/2 \pm r_{12}(t) \tag{4.19}$$

with a small deflection from the centerline, ensuring the approach of both beads with the relative velocity $\boldsymbol{v} = \boldsymbol{u}_2 - \boldsymbol{u}_1 = \dot{\gamma}\boldsymbol{e}_z$ (Cf. Figure 4.4).

The distance $r(t)$ between both spheres is plotted in dependence of the enclosed angle $\theta(t)$ between the z-axis and the connection vector between the two beads (Cf. Figure 4.4). This angle is defined as

$$\theta(t) = \tan^{-1}\left(\frac{x_2(t) - x_1(t)}{z_2(t) - z_1(t)}\right) \tag{4.20}$$

and replaces the time t as parameter. Note that this angle evolves in negative direction due to the negative sense of rotation.

The time reciprocal symmetry also implies a symmetry of the dynamics around $\theta = -\frac{\pi}{2}$, which is re-found in the numerical data illustrated in Figure 4.5. The two particles approach each other following the streamlines in z-direction without a considerable variation of $\theta(t)$ until for small distances r, but still bigger than the contact distance $r = 2a$, the hydrodynamic interaction kicks in pushing each bead towards the outer channel regions, increasing

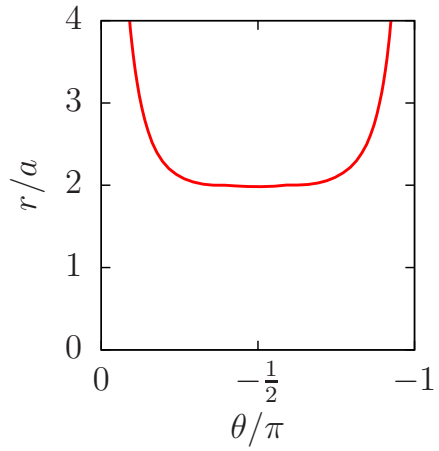

Figure 4.5.: The distance $r > 2a$ between the two beads during the collision process. The collision starts at a configuration when $\theta \approx 0$ passes through the range of allowed angles in negative direction and ends with $\theta \approx -\pi$.

velocity difference v until they reach the configuration $\theta = -\frac{\pi}{2}$, where they touch moving in a comparatively fast half-turn around each other before they diverge in the reciprocal hydrodynamically induced way. To characterize the velocity of the rotation the angular velocity $\dot{\theta}$ can be defined:

$$\dot{\theta}(t) = \frac{\boldsymbol{r} \times \boldsymbol{v}}{r^2} \cdot \hat{\boldsymbol{e}}_y. \tag{4.21}$$

Due to the clockwise rotation, even the angular velocity has a negative sign.

5. Dynamics of a suspended FENE-dumbbell

Chapter 4 described the simulation technique called Fluid-Particle-Dynamics, which is used to simulate the dynamics of suspended beads. In this chapter the dynamics of a dumbbell is considered, which is generated by the direct coupling of the two beads via a potential force. This deformable particle forms the basis for the particle-induced turbulence described in the next chapter.

Even the single-particle case reveals astonishing results on the stability and rheology of the dumbbell dynamics in dependence of its elasticity and expansion relative to the bead radius, but also to the channel width. Therefore, this part of the work is strictly limited to the case of one dumbbell, before the multi-particle case is systematically described in Chapter 6.

5.1. Direct coupling of two beads and definition of the Weissenberg number

In Eq. (4.1) a term $\boldsymbol{f}(\boldsymbol{x})$ occurs representing the force-density of outer forces such as gravity, electric fields, or the coupling potential forces between the suspended beads. Such forces $\boldsymbol{f}^k = f(r)\boldsymbol{e}_r$ couple two beads at an equilibrium length r_0 acting respectively at their center coordinates $\boldsymbol{x}_1$ and $\boldsymbol{x}_2$ along the connection vector $\boldsymbol{e}_r = \frac{\boldsymbol{r(t)}}{r(t)}$ with

$$\boldsymbol{R}(t) = \boldsymbol{x}_1(t) - \boldsymbol{x}_2(t). \tag{5.1}$$

The pre-factor $f(r)$ may, e. g., be determined by the harmonic pre-factor $f(R) = k_0(R(t) - R_0)$, but for weak spring constants k_0 this force has the disadvantage that the coupled beads may be apart on a distance. Due to the periodic boundary conditions assumed in the simulation method, self-interaction between the beads may occur. To prevent this situation the range of distance

between the two beads is restricted to $R_{\max} = 2R_0$ by using a *FENE*-potential (*Finitely Extensible Nonlinear Elastic*), yielding the pre-factor [54]

$$\boldsymbol{f}^k(\boldsymbol{R}) = k_0 \frac{(R(t) - R_0)}{1 + \frac{(R(t)-R_0)^2}{(R(t)-R_{\max})^2}} \frac{\boldsymbol{R}}{R}. \tag{5.2}$$

Note that these forces face the stress forces $\boldsymbol{f}^\sigma$ coming from the linear shear flow resulting from the stress tensor via

$$\boldsymbol{f}^\sigma = \nabla \cdot \boldsymbol{\sigma}, \tag{5.3}$$

which are directly coupled to translational motions of a sphere with the velocity $\boldsymbol{u}_i$ via the Stokes friction:

$$\boldsymbol{f}^\sigma = 6\pi\eta_0 a \boldsymbol{u}_i. \tag{5.4}$$

The dumbbell does not react instantaneously to the outer shear flow. To characterize its reaction on outer stresses, a relaxation time τ is defined, which is related to the time a stretched or compressed dumbbell needs to relax to its equilibrium length. This time τ depends on k_0 as well as on the Stokes friction ζ. Outer stress occurs only through friction forces and thus scales with the shear-gradient $\dot{\gamma}$, so that the dimensionless product of τ and $\dot{\gamma}$ determines a system parameter for the dumbbell elasticity, called *Weissenberg number* W:

$$\tau = \frac{6\pi\eta_0 a}{k} \qquad W = \dot{\gamma}\tau. \tag{5.5}$$

The Weissenberg number relates the inner reaction of the dumbbell expressed in terms of k_0, a, and η_0 to outer stimuli due to the shear flow with rate $\dot{\gamma}$. W can be seen as an outer system parameter, when a dumbbell with a certain, but constant set of inner parameters is exposed to shear flows with different $\dot{\gamma}$. This variation of W is certainly viable in an easy experimental way. In this work W is varied in dependence of k_0 for constant $\dot{\gamma}$, so that the variation of W becomes characteristic for the material.

5.2. A tumbling dumbbell in shear flow

A sheared dumbbell is stretched or compressed depending on its position with respect to the shearlines. The relative deformation in dependence of the angle θ, enclosed by the z-direction and the conection vector $\boldsymbol{e}_R$, is defined as

$$\Delta(\theta) = \frac{R(\theta) - R_0}{R_0}. \tag{5.6}$$

These deformations and thus the dumbbell dynamics is determined by three effects which are listed here together with the corresponding parameter:

- The stretching and compressing is driven by friction forces due to the shear flow acting against coupling forces. The shape of deformation is determined by the time a dumbbell needs to equilibrate the stresses in terms of the Weissenberg number.

- The trajectories of two colliding beads in Chapter 4 have shown that the particle-particle interaction increases for short distances R between both beads. Especially, when the dumbbell is equilibrated parallel to the streamlines at $\theta = -\alpha\pi$ with $\alpha \in \mathbb{Z}$ the dumbbell rotation is sustained by this interaction. The dimensionless dumbbell length $\hat{R}$

$$\hat{R} = \frac{R_0}{a} \tag{5.7}$$

  is defined as corresponding system parameter.

- The last effect acting on the dumbbell is the backflow, induced by the wall-particle interaction. Important contributions on the motion of the bead arise especially in small channels, measured in terms of

$$\hat{L} = \frac{L_x}{R_0}. \tag{5.8}$$

  Because the wall-induced backflow from the walls may be seen as a reflection of the flow arriving at the wall, also the wall-interaction should follow the r^{-3} dependence of the vortex flow in Eq. (4.18).

The initial condition for the equilibrated dumbbell is considered in the symmetric arrangement around the centerline given in Eq. (4.19) (Cf. Figure 5.1), where a small destinction ϵ, corresponding to a slightly negative angle $\theta < 0$, accelarates the onset of the dumbbell rotation called *tumbling*. The velocity of the dumbbell is defined as the angular velocity $\dot{\theta}$ given in Eq. (4.21) and compared with the shear rate $\dot{\gamma}$.

Initially, the dynamics of the dumbbell is investigated in a box of size $\hat{L} = 6$, what is sufficiently large so that wall effects are negligible. The dumbbell can perform a continuous rotation with angular velocity $\dot{\theta}$ and deformation Δ, depending on the configuration, as illustrated in Figure 5.2a) and Figure 5.2b) for several Weissenberg numbers W.

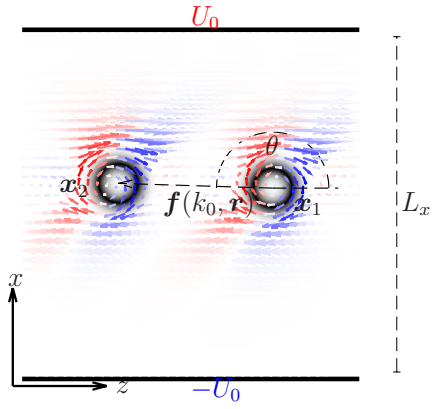

Figure 5.1.: One dumbbell is modeled by to beads at positions $\boldsymbol{r}_1$ and $\boldsymbol{r}_2$ defining areas of enhanced viscosity. The gray values indicate the spatial change $\nabla\eta(\boldsymbol{x})$. Along the connection vector $\boldsymbol{R}$, a FENE-force couples the two beads. The applied shear flow with shear rate $\dot{\gamma} = 2U_0/L_x$ is color-coded blue and red. One can identify the rotational parts with $\boldsymbol{\omega}_0$ of the flow-field around the spheres.

For values $W \ll 1$ (red curve), the deformations remain small, but also the dumbbell equilibrates rather quickly since the relaxation time τ is small. During the first quarter turn the dumbbell is compressed until $\theta = -\frac{\pi}{2}$. In this configuration it is equilibrated for a short time, but is then tressed during the second quarter turn. This pattern appears quite symmetric with

$$\Delta(\theta) = \Delta_0 \sin(2\theta)\,, \tag{5.9}$$

where the angular velocity can be approximated by

$$\dot{\theta} = -\frac{\gamma}{2}\left(1 + \cos(2\theta)\right). \tag{5.10}$$

For increasing Weissenberg numbers in the range of $W \approx 1$ (blue curve) and beyond (green curve) the relative extension Δ increases, accompanied with an increase of the relaxation time τ. The response of the coupling forces to the driving friction forces is delayed, leading to a symmetry breaking in the rotation. The dumbbell is strongly compressed during the first quarter-turn, where at $\theta = -\frac{\pi}{2}$ the maximum angular velocity $\dot{\theta} \approx -\dot{\gamma}$ is adopted. The inner forces do not suffice for an immediate compensation of the stress forces, so that the dumbbell passes this configuration compressed. The equilibration

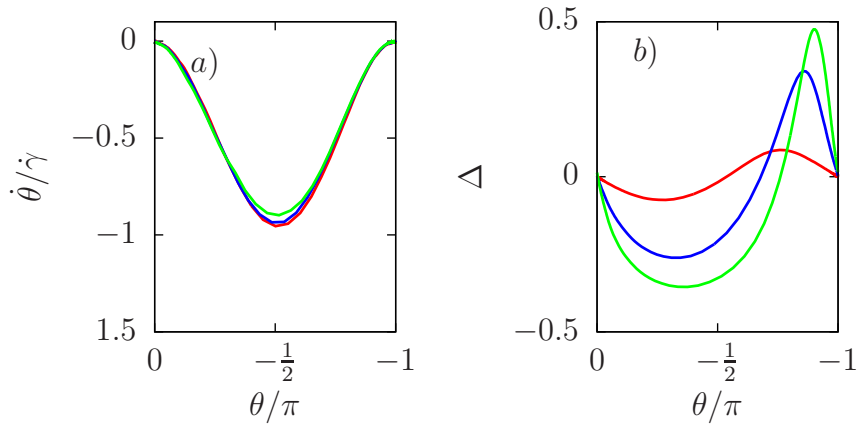

Figure 5.2.: *a)* Plot of the angular velocity $\dot{\theta}$ within one half-turn for Weissenberg numbers $W = 0.2$ (red), $W = 1$ (blue), and $W = 2$ (green). *b)* illustrates the relative deformations Δ for the same springs. Both graphs illustrate the configurational dependence towards the streamlines measured in terms of the angle θ.

happens at a certain point $\theta_0 < -\frac{\pi}{2}$. Furthermore, the increasingly compressed configuration of soft dumbbells with $W \gg 1$ is responsible for the reduction of the angular velocity $\dot{\theta}$ at $\theta = -\frac{\pi}{2}$.

Besides the decay of the rotational frequency with increasing Weissenberg number W, Figure 5.3 illustrates the direct influence of the hydrodynamic bead-bead interaction on the tumbling orbit for dumbbells of relative length $\hat{R} = 3.33$ (red) to $\hat{R} = 4.33$. A longer dumbbell length R_0 means a reduction of the flow contribution from the two vortices around the beads, driving them away from the equilibrium state at $\theta = \alpha\pi$. For dumbbells longer than $R_0 = 4.33a$ the bead-bead interaction does not show considerable contributions, so that the rotation comes to a halt in a parallel alignment with respect to the streamlines. In this configuration, the velocity difference $\boldsymbol{v}$ in Eq. (4.21) only consists of the two vortices around the beads, so that $\boldsymbol{u}_1$ and $\boldsymbol{u}_2$ are given by

$$\boldsymbol{u}_{1,2} = \mp\frac{1}{2}\dot{\gamma}\frac{a^4}{(R_0 - a)^3}\hat{\boldsymbol{e}}_x \tag{5.11}$$

for small $\hat{R}$ with Eq. (4.18), so that the offset $\dot{\theta}_0$ yields

$$\dot{\theta}_0 = \omega_R = -\dot{\gamma}\frac{a^4}{(R_0 - a)^4}, \tag{5.12}$$

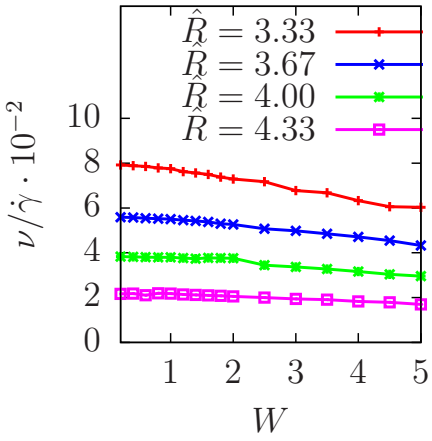

Figure 5.3.: Numerical study on the dumbbell rotational frequency ν showing a decrease for increasing W as well as increasing dumbbell-length $\hat{R}$.

taking into account that the vortex is generated at the bead surface and thus the relevant distance is $R = R_0 - a$.

5.3. Bifurcation from tumbling to vacilating breathing

The tumbling dynamics has been investigated in a box with $\hat{L} = 6$, where the dumbbell is able to rotate without being affected by wall effects. By reducing the channel width $\hat{L}$ from $\hat{L} = 6$ to $\hat{L} = 2$ Figure 5.4a) shows the slowdown of the tumbling until at a critical point $L_c(\hat{R})$ the tumbling stops, and the dumbbell enters into a state called *vacillating breathing* [123]. The plot of $\hat{L}_c$ against the Weissenberg number W in Figure 5.5 shows a slight increase of the critical ratio for large W. In addition, the critical point depends on the dumbbell length $\hat{R}$, where for the shown data sets $\hat{L}_c(\hat{R} = 3) \approx 3.55$, $\hat{L}_c(\hat{R} = 3) \approx 3.8$, and $\hat{L}_c(\hat{R} = 3.67) \approx 3.91$ were determined. These values are a hint that this transition via a bifurcation may be attributed to the hydrodynamic wall-interaction inhibiting the effects of bead-bead-interaction, both of which equilibrate at the critical point, where below $\hat{L}_c$ the repulsion from the wall-interaction generates effects that can only be compensated by the coupling FENE-forces with $\Delta > 0$ lifting the dumbbell in a slight skew orientation depending on $\hat{L}$ at $\theta > 0$ (Cf. Figure 5.4b)).

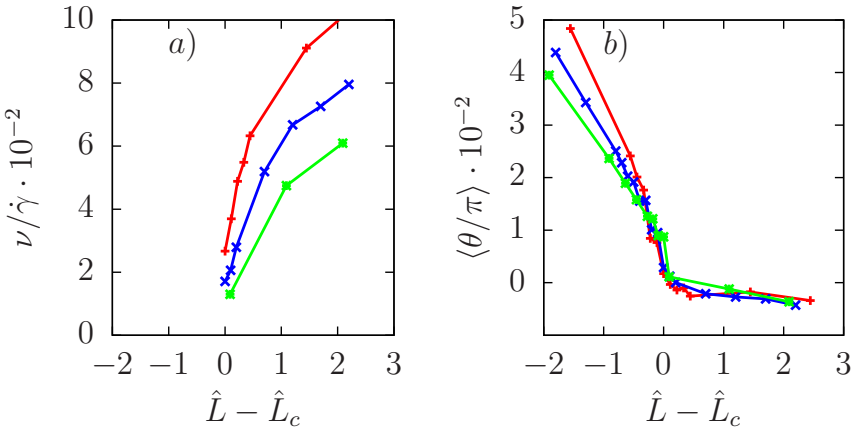

Figure 5.4.: *a*) The frequency ν of rotations and *b*) the angle $\overline{\theta}$ as function of the channel-width $\hat{L}$ for dummbells with $W = 0.2$ corresponding to the dumbbell length $\hat{R} = 3$ (red), $\hat{R} = 3.33$ (red), and $\hat{R} = 3.67$ (green). Below a critical ratio $\hat{L}_c$ the rotation of the dumbbell stops. The dumbbell reaches an elongated, but stable configuration with $\hat{\theta} > 0$ and $\nu = 0$.

The only difference between tumbling and vacillating breathing seems to be that either the angular velocity reaches zero or the forces do not balance at any point, and therefore the angular velocity remains always negative (or positive: depending on the shear direction). This difference allows the definition of a frequency ω in the stationary states ω_S as follows:

$$\omega_S = \begin{cases} |\dot{\theta}_0| & \text{if } \dot{\theta} \neq 0 \\ 0 & \text{if } \dot{\theta} = 0. \end{cases} \tag{5.13}$$

Then, especially in those cases where $\omega_S \neq 0$, ω_S can be split up into those parts originating from the bead-bead-interaction $\omega_S(\hat{R})$ and those $\omega_S(\hat{L})$ due to the wall-interaction. From Eq. (5.12) follows $\omega_S(\hat{R}) = \omega_R$ and thus the normalized equilibrium states $\hat{\omega}_S = \omega_S/\omega_R$ yield

$$\hat{\omega}_S = 1 + \hat{\omega}(\hat{L}). \tag{5.14}$$

$\hat{\omega_S}$ may adopt values between 0 and ± 1 and from Figure 5.5 one can see the coincidence of curves for different dumbbell sizes $\hat{R}$. In the investigated range of the channel widths $\hat{L}$ it seems as if the numerically determined frequences ω branch off the anciently stable $\omega = 0$ for $\hat{L} < \hat{L}_c$ increasing with $\sqrt{\hat{L}_c}$. The

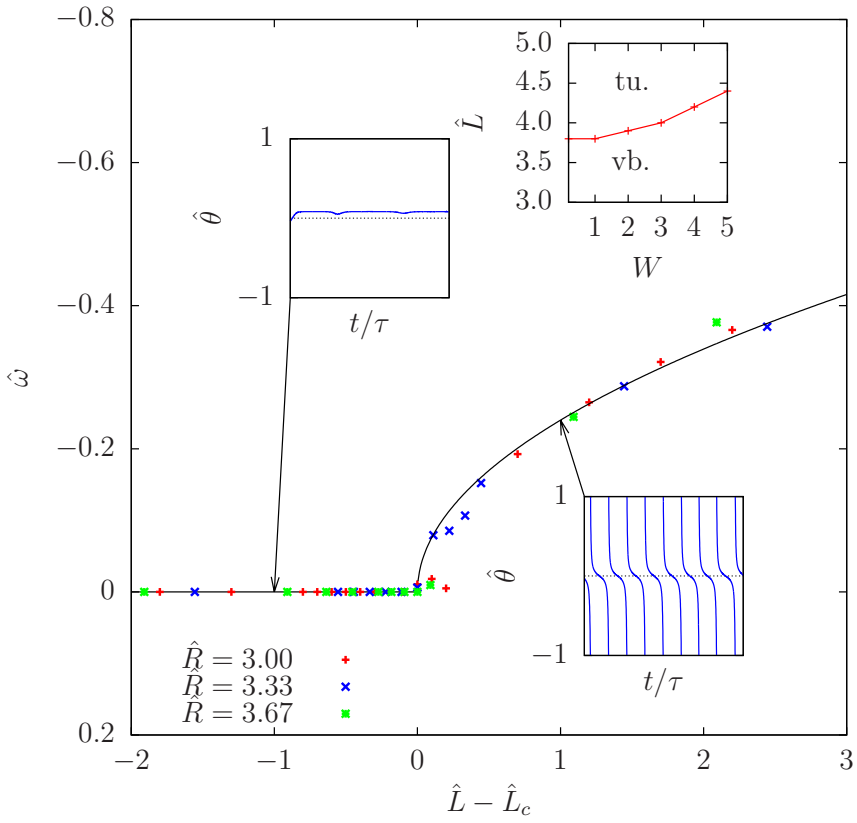

Figure 5.5.: Bifurcation diagram for the transition between *tumbling* (tu) and *vacillating breathing* (vb). With decrease of the system parameter $\hat{L}$ the stationary solutions ω_s/ω_R converge to zero at the critical point. Below the critical value $\hat{L}_c$ the angular velocity remains zero.

order parameter ω thus fullfills the equation Eq. (2.8) of a pitchfork-bifurcation with

$$\dot{\omega} = \omega - \mu\omega^3, \tag{5.15}$$

with the stable solutions $\omega_{S,1} = 0$ for $\hat{L} < \hat{L}_c$ and $\omega_{S,2} = -\sqrt{\mu}$ for $\hat{L} < \hat{L}_c$, where the system parameter μ

$$\mu = \varepsilon(\hat{L} - \hat{L}_c) \tag{5.16}$$

is directly coupled to the channel width $\hat{L}$. The prefactor $\varepsilon \approx 0.06$ is numerically determined from the illustrated data in Figure 5.5.

Complementary view

The transition from a steady solution to an oscillatory dynamics on a limit circle within the increase of the channel width $\hat{L}$ with contunious branching of the frequencies, as illustrated in Figure 5.5 and Eq. (5.15), leads to the suspicion that a Hopf-bifurcation Eq. (2.20) at the critical point $L_c(W_c)$ is responsible for the transition between different attractors. However, the described transition shows some unusual properties that differ from a Hopf bifurcation. E. g., it is striking that the frequency ω_s transiates continuously and not the amplitude measured in terms of the deformation Δ. Δ depends only on the Weissenberg number W. Therefore, the transition to the limit cycle appears within a jump of the amplitude. Note that Figure 5.5 does not depict the phase space. The following considerations are made to complete the picture of the bifurcation.

The wall-interaction repels or attracts the beads in perpendicular direction to the walls. Therefore, it is assumed that the main effects appear in the x-component of the total flow containing the information about flows towards the walls or away from them as a result of flow reflections. The only flow parts showing characteristics in this direction are the bead induced backflows around $\boldsymbol{x}_1$ and $\boldsymbol{x}_2$. By superposing the bead-bead interaction and the wall-interaction, the remaining component is the pure wall-induced flow $u_{\mathrm{WI}}(\boldsymbol{x})$. At the position $\boldsymbol{x}$ inside the channel this flow is obtained by subtracting the flows $u_{\perp}(\boldsymbol{x}, \boldsymbol{x}_i)$ around the spheres (cf. Eq. (4.18)) from the total flow $\boldsymbol{u}(\boldsymbol{x})$:

$$u_{\mathrm{WI}}(\boldsymbol{x}) = u_x(\boldsymbol{x}) - \sum_i^2 u_{\perp}(\boldsymbol{x}, \boldsymbol{x}_i). \tag{5.17}$$

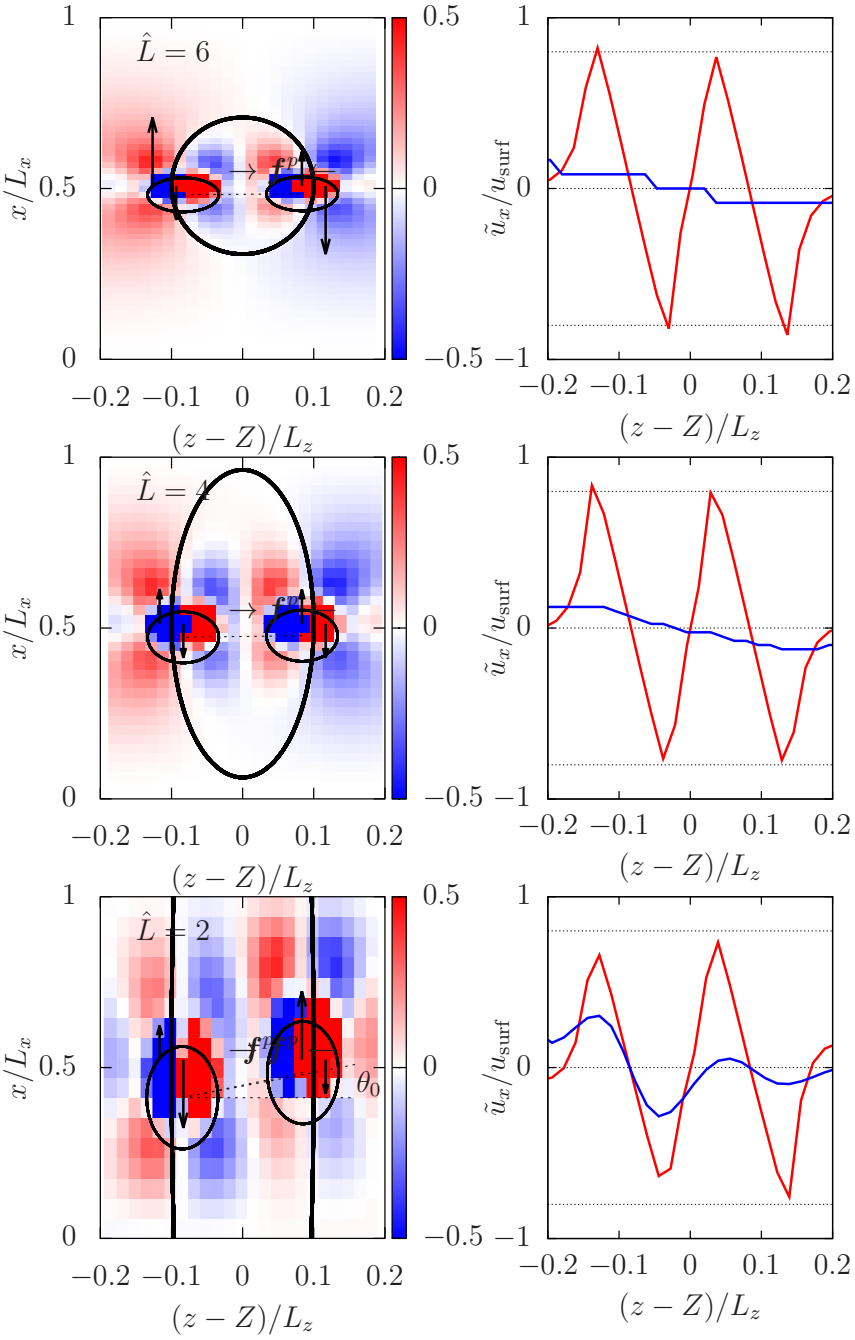

Figure 5.6.: Flow at the walls for various channel widths $\hat{L}$. The flow reflctions at the walls induce two vortices with opposite rotational sense. The approach of the inner vortex to the walls, prevents the dumbbell rotation for small $\hat{L}$.

This flow is visualized in Figure 5.6 on the left for the three cases of $\hat{L} \ll \hat{L}_c$, $\hat{L} \gg \hat{L}_c$ and $\hat{L} \gg \hat{L}_c$. The incompressibility condition together with the no-slip boundaries require

$$\int_0^{L_z} u_x(z)\,\mathrm{d}z = 0, \tag{5.18}$$

at the two walls at $x = 0$ and $x = L_x$, where the contributions at any position along the z-direction do not vanish as the blue lines in Figure 5.6 illustrate, showing the backflows at the wall $x = 0$. Especially around the bead positions $\boldsymbol{x}_1$ and $\boldsymbol{x}_2$ backflows arise at the walls as a result of the bead rotation. These flows are not reflected directly, rather flows that are pressed towards the walls in large channels ($\hat{L} = 6$) around the first bead position $\boldsymbol{x}_1$ are reflected towards the inner channel at position $\boldsymbol{x}_2$, so that a large vortex rotating in the same sense as the suspended dumbbell is formed, surrounding the whole dumbbell. On the other hand a counter-rotating vortex around the dumbbell center is formed fullfilling the incompressibility condition in inner regions of the channel. The deviding line between the two wall induced vortices is marked by black circles in Figure 5.6.

It is the impact of these two vortices on the two beads that inhibits the dumbbell rotation. The relative size of the inner vortex inside the channel grows when $\hat{L}$ is reduced and leads to an increase of swirled flows. The x-components at the centerline for dumbbell constellations parallel to the centerlines are illustrated in red in Figure 5.6 on the right. Two maxima can be identified with a small difference in the maximal values $\Delta\tilde{u}_x$, which maintain the rotational dynamics. This difference corresponds to $\omega_S(\hat{L})$. At the critical point, where the dumbbell rotation stops, the inner vortex reaches the wall indicated by the increase of zero crossings of the blue curve from one ($\hat{L} > \hat{L}_c$) to three ($\hat{L} > \hat{L}_c$). The outer vortex formerly covering the entire channel outside the dumbbell is broken by the inner vortex. Now two vortices are generated respectively around the beads bringing the dumbbell rotation to a halt. The difference $\Delta\tilde{u}_x$ changes the sign, so that the dumbbell is driven into the opposite tumbling direction until the coupling forces set the equilibrium state.

What do these considerations contribute to the understanding of the transition at the critical point $\hat{L}_c$? A lot, if one takes into account that the periodicity of the dynamics depend on the stability of the surounding of the parallel constelation at $\theta = \alpha\pi$. In Figure 5.8 the stationary position $\hat{x}_s = \hat{R}\sin(\bar{\theta})$ as a

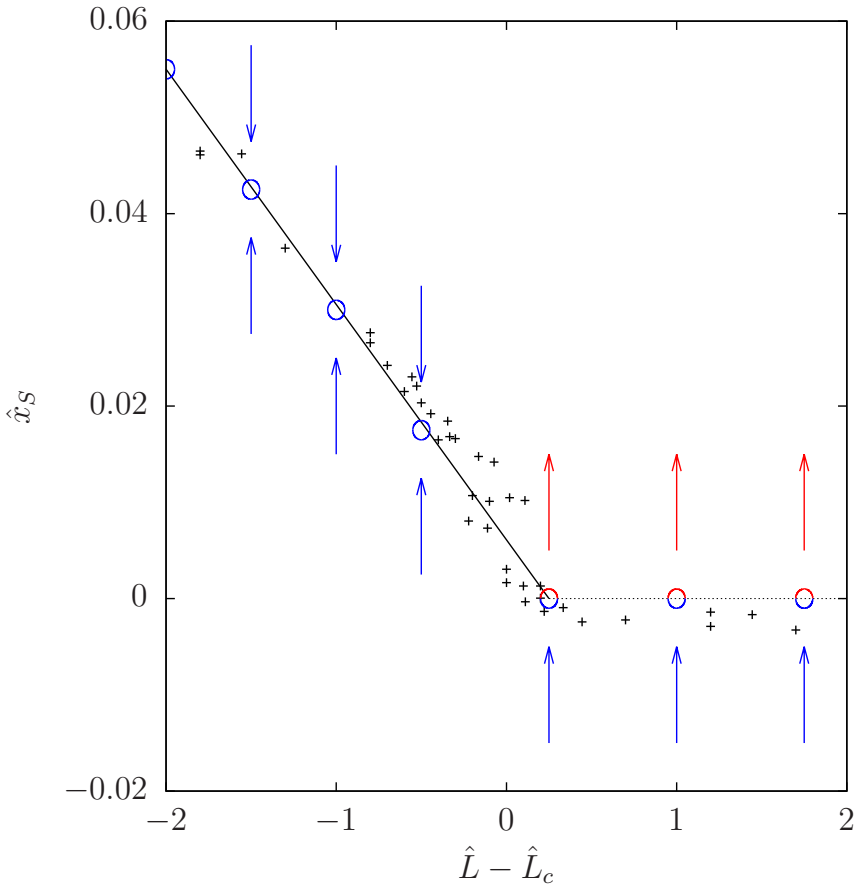

Figure 5.7.: Stability of the stationary state $\dot{\theta} = 0$. For $\hat{L} < \hat{L}_c$ the stationary solution adapts independently of the direction of perturbations. For $\hat{L} > \hat{L}_c$ the fixed point loses its stability, but only in one direction. A perturbed trajectory in the upper regions is closed within a half-turn approaching the fixed-point from bellow.

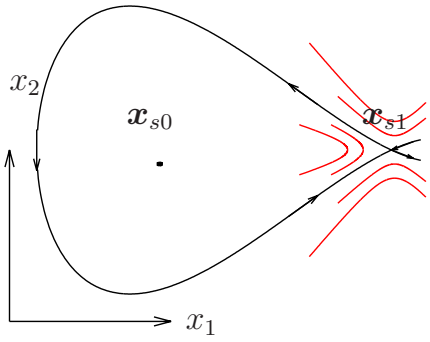

Figure 5.8.: Replot of the homoclinic orbit in Figure 2.4.

time average of all positions in the steady state is illustrated. For $\hat{L} < \hat{L}_c$ all perturbations are reset to the stable fixed point at $x_s > 0$ within the interplay of hydrodynamic interaction and coupling forces. For increasing values $\hat{L}$ the stable fixed point approaches towards $x_s = 0$ and with the reaching of this configuration something strange happens: The stable stationary solution keeps its stability for all perturbations in negative direction, where perturbations in positive x-directions grow. The dumbbell starts a half-turn, which is generated by the interplay of coupling forces and shear flow. It is important to mention that the rotation not only results from the local information about the stability around x_s. Thus, the identified bifurcation is a global bifurcation from a stable fixed point to a homoclinic orbit.

The present results are obtained for a dumbbell at constant Weissenberg number W, where the channel width $\hat{L}$ is varied. This enables a controlled change of the wall effects without a simultaneous change of the dumbbell deformation. There remains the question, what happens if the channel width is kept constant and the Weissenberg number is varied, whereby this situation is more easily accessible experimentally. The plot of the critical point $\hat{L}_c(W)$ as function of the Weissenberg number illustrates that the same transition between tumbling and vacillating breathing is re-found within a exchange of the parameters W and $\hat{L}$, where the quantitative relationships like the continuous frequency variation at the critical point W_c stays. In this situation, the initially strong coupling forces are decreased to the critical value W_c, where the semi-stability of the position x_S changes to a global stability, where the coupling forces do not suffice any more to equilibrate the wall-effects.

5.4. Rheology of a suspended dumbbell

In a stationary shear flow $\boldsymbol{u} = \dot{\gamma}(x - L_x/2)\hat{\boldsymbol{e}}_z$, the local effective viscosity $\eta^{\text{eff}}(\boldsymbol{x}, t)$ is defined via the xz-component of the stress-tensor $\sigma(\boldsymbol{x}, t)$ from Eq. (4.3) [40]:

$$\eta^{\text{eff}}(\boldsymbol{x}, t) = \frac{\sigma_{xz}}{\dot{\gamma}}. \tag{5.19}$$

By averaging the contributions to the stress tensor at the upper and lower wall, the effective viscosity $\eta^{\text{eff}}(t)$ of the suspension at a given time t is given by:

$$\eta^{\text{eff}}(t) = \frac{1}{2\dot{\gamma}}(\langle\sigma_{xz}\rangle_{x=L_x} + \langle\sigma_{xz}\rangle_{x=0}). \tag{5.20}$$

The viscosity of a suspension of beads will deviate from the viscosity of the solvent liquid η_0 due to the force contributions exerted by the rotating flows around the suspended beads. According to the bead motion the effective viscosity is time-dependent and thus depends on the orientation θ, as can be seen in Figure 5.9 and Figure 5.11, where the relative change of the viscosity induced by the suspended beads $\Delta\hat{\eta}(t)$ defined as

$$\Delta\hat{\eta}(t) = \frac{\eta^{\text{eff}}(t) - \eta_0}{\eta_0} \tag{5.21}$$

is illustrated.

Einstein has derived the linear dependence of the viscosity η^{eff} on the volume fraction Φ in the dilute regime [47, 48], which has been extended to a quadratic dependence on Φ^2 by Batchelor and Green [27] as well as Felderhoff and Cichocki [35] for the semi-dilute regime taking into account the non-negligible bead-bead interaction

$$\eta^{\text{eff}} = \eta_0 \left[1 + w_1\Phi + w_2\Phi^2 + \mathcal{O}(\Phi^3)\right]. \tag{5.22}$$

The pre-factors have been determined to $w_1 = 2.5$ [47, 48] and $w_2 = 5.0$ [35] or $w_2 = 5.2$ [27], but it has been shown that in strongly confined suspensions of onconnected beads these pre-factors change [37]. Also the effect of different object shapes on the viscosity has been analysed [75].

The total viscosity can be split in contributions η_0^{eff}, which act through the solvent and the contribution χ containing the elastic non-hydrodynamic forces acting between the suspended particles. The latter contribution is calculated

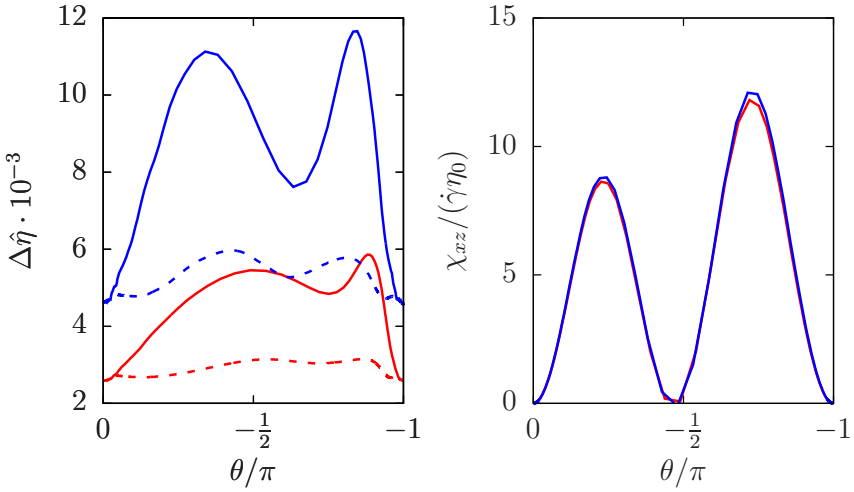

Figure 5.9.: The effective viscosity change $\Delta\hat{\eta}$ and the distribution of coupling forces χ_{xz} to the viscosity during one half-turn for dumbbells with $W = 0.2$ at $\hat{L} = 4$ (blue) and $\hat{L} = 6$ (red). Solid lines represent the dynamics of beads coupled to a dumbbell and the dashed line refer to uncoupled beads.

by the so called Kramers-Kirkwood formula [26, 40], where the component-by-component product $r_i f_j$ of the forces $\boldsymbol{f}^p(t) = (f_{mx}, f_{my}, f_{mz})$ and the dumbbell length $\boldsymbol{r}(t) = (r_{mx}, r_{my}, r_{mz})$ are summed up over the suspended particles indexed by m:

$$\chi_{ij} = -\frac{1}{V} \sum_m f_{mi} r_{mj} \tag{5.23}$$

with the bead volume $V = \frac{4}{3}\pi a^3$. Technically speaking, this formula is derived under the assumption of point-like particles at the two endpoints of the dumbbell, i. e., the bead radii should be much smaller than the dumbbell length $a \ll r_0$. In the present case, the viscosity contribution of dumbbells is obtained by taking the xz-component of this tensor. For comparison $\Delta\hat{\eta}_W$ and the Kramers-Kirkwood χ contribution are calculated numerically in the configurations θ within one half-turn for different Weissenberg numbers $W = 0.2$ and $W = 1.5$. To compare the pure particle contribution obtained with the Kramers-Kirkwood formula χ_{xz} with direct measured viscosity contributions $\Delta\hat{\eta}_W$, effects of the particle extension have to be taken into account. Therefore, the collision described in Section 4.3 is simulated to determine the viscosity change $\Delta\hat{\eta}_\infty(\theta)$ of two uncoupled particles. Despite a pre-factor the

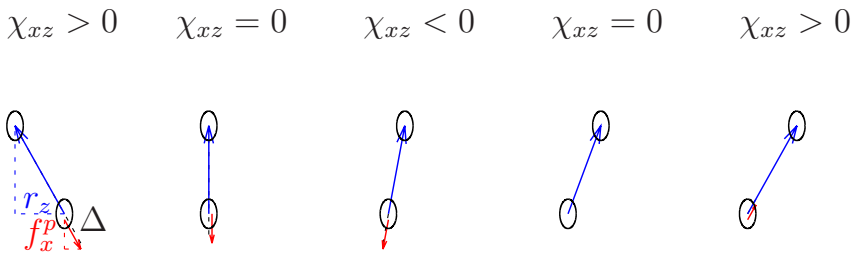

Figure 5.10.: Sketch of the tumbling motion at high Weissenberg number with directions of $\boldsymbol{r}$ and $\boldsymbol{f}^p$ illustrate the connection to χ_{xz}.

Kramers-Kirkwood contribution χ_{xz} behave similarly to the difference between $\Delta\hat{\eta}_W - \Delta\hat{\eta}_\infty$ [40]:

$$\chi_{xz} \propto \Delta\hat{\eta}_W - \Delta\hat{\eta}_\infty. \tag{5.24}$$

The dumbbell length $r_{mj}(t)$ as well as the coupling force $f^p_{mi}(t)$ depend on the configuration θ. This can be shown by numerical simulations, where the dumbbell contributions to $\Delta\hat{\eta}$ and χ in different confinements $\hat{L}$ are illustrated for a small Weissenberg number $W = 0.2$ (Figure 5.9) and for $W = 1.5$ (Figure 5.11).

Both at high as well as low Weissenberg number χ_{xz} is independent of the channel size $\hat{L}$, as long as the dynamics occurs within the tumbling regime, but nevertheless a dependence of χ on W is obtained. The component $\chi_{xz}(t)$ from Eq. (5.23) can be rewritten in the following form [40]:

$$\chi_{xz}(r,\theta) = -f^p(r)\frac{r}{2}\sin(2\theta) \tag{5.25}$$

and depends on the deformation $r(t) - r_0$ via $f(r)$ and also on the orientation $\theta(t)$.

For small values of W the two functions $\sin(-2\theta)$ and $r(t) - r_0$ pass zero near the perpendicular dumbbell orientation, i. e., for $\theta \approx -\pi/2$. Therefore $\chi_{xz}(\theta \approx -\pi/2)$ vanishes as illustrated on the right in Figure 5.9, where for large W, as pointed out in Section 5.2, the deformation $r(t) - r_0$ passes zero at $\theta < -\pi/2$ (cf. Figure 5.2) and $\chi_{xz}(\theta)$ becomes negative (Cf. Figure 5.10) in the range between $f(r) = 0$ and $\theta = -\frac{\pi}{2}$. On a first sight this range of a negative χ_{xz}-value contradicts all expectations to a quantity that represents a viscosity.

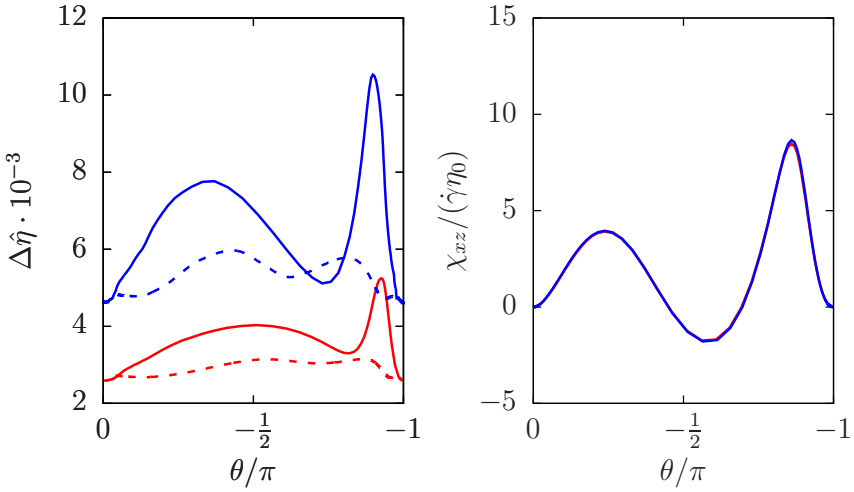

Figure 5.11.: The effective viscosity change $\Delta\hat{\eta}$ and the distribution of coupling forces χ_{xz} to the viscosity during one half-turn for dumbbells with $W = 0.2$ at $\hat{L} = 4$ (blue) and $\hat{L} = 6$ (red). As in Figure 5.9, solid lines represent the dynamics of beads coupled to a dumbbell, where the dashed line indicates $\Delta\hat{\eta}$ obtained for uncoupled beads.

Indeed, the effective viscosity change, which contains all effects of hydrodynamic as well as elastic nature, remains positive in all configurations as shown in Figure 5.11. As one would expect, due to the increasing wall effects, the effective viscosity grows in small channels, but the main point is that the illustrated measured data indicates the limitation of the Kramers-Kirkwood formula as a tool for the computation of the shear viscosity of dumbbell suspensions for not too high Weissenberg numbers W under strong confinement, when $\hat{L}$ is small.

At $\theta \approx 0$ and $\theta \approx -1$ the dumbbell axis is nearly parallel to the streamlines. In this range the dumbbell contribution to $\Delta\hat{\eta}$ is similar to the contribution of two unconnected beads. The dashed and solid lines on the left in Figure 5.9 and Figure 5.11 have the same initial and end point. The solid lines represent the dumbbell viscosity for $\hat{L} = 4$ (red) and $\hat{L} = 6$ (blue). Thus, in these configurations the contribution to $\Delta\hat{\eta}$ is only caused by flows, i. e., the ones around rotating beads. The increase of the offset in $\Delta\hat{\eta}$ with decreasing $\hat{L}$ is related to the stronger impact of flows at the walls, if we chose a small confinement.

The dashed lines correspond to the viscosity change $\Delta\hat{\eta}(\theta)$ of uncoupled beads, where only "real" hydrodynamic interaction affects $\Delta\hat{\eta}$. "Real" indicates the fact that also in the case of a dumbbell $\Delta\hat{\eta}$ represents a method of measurement, which is only related to the flow field $\boldsymbol{u}$, but not to the forces $\boldsymbol{f}^p$. The curves show two maxima, one in the first quarter-turn separated by an intermediate minimum at $\theta = -\frac{\pi}{2}$ from the second in the second quarter-turn.

During the first quarter-turn the beads push each other towards the walls, one at the top and the second at the bottom. Not only the spheres, but also the surrounding fluid is pressed towards the corresponding wall. As a result, at the other wall an eddy is formed, which has the same impact on the effective viscosity. In addition to the vortices, which impact on $\Delta\hat{\eta}$ also increases as the dumbbell beads approach the walls, the bead motion itself increases the vorticity until the beads reach the perpendicular orientation $\theta = -\frac{\pi}{2}$ within the closest distance to the walls. Again only the bead induced flow field contributes to $\Delta\hat{\eta}$, where the appearing minimum is above the offset in the parallel constellation because of the smaller distance of beads to the walls so that the hydrodynamic interaction with the walls is stronger.

The curve of $\Delta\hat{\eta}$ for hard dumbbells $W = 0.2$ (cf. Figure 5.9) and weak dumbbells $W = 1.5$ (cf. Figure 5.9) qualitatively show the same characteristics. Where for vanishing coupling forces the pushing or pulling of the suspended particles towards or away from the walls leads to an increase of the viscosity, the effects also drive the viscosity change in the coupled state. The main difference is that the torque in $\boldsymbol{r} \times \boldsymbol{f}^p$ perpendicular to the dumbbell axis accelerates the beads in the direction perpendicular to the shear flow, increasing the viscosity once again. For hard dumbbells the two maxima show a factor of roughly two for the shown data. Certainly, the maxima depend on the ratio $\hat{R}$ between the dumbbell length and bead radius a showing an increase, if the dynamics of a shorter dumbbell is investigated with its enhanced bead-bead interaction. In contrast, the maximum decreases for increasing Weissenberg number W. Note that the uncoupled case represents $W \to \infty$ and thus is the limit case of increasing the Weissenberg number.

Revisiting the comparison of χ with $\Delta\hat{\eta}$, where it was pointed out that χ becomes negative for high Weissenberg numbers and χ in contrast to $\Delta\hat{\eta}$ does not depend on the confinement, this result still seems astonishing, as the

material parameter viscosity is supposed to be positive. But is the negative sign alone a good criteria for the quality of the Kramers-Kirkwood formula? On its own it does not suffice to answer this question, but combined with the determined viscosity change for coupled and uncoupled beads the following statement can be made:

As long as $\Delta\hat{\eta}_W(\theta)$ represents the total viscosity and $\Delta\hat{\eta}_\infty(\theta)$ stands for the orientation dependent viscosity caused by the pure hydrodynamic bead-bead interaction, the contribution of elastic objects should be recovered at least qualitatively by subtracting $\Delta_W - \Delta_\infty$ according to Eq. (5.25). Looking at Figure 5.11 for weak spring forces one can identify that the negative range of χ corresponds approximatlely to that range, where the viscosity $\Delta\hat{\eta}_\infty$ represented by the dashed lines is enhanced with respect to the solid line of $\Delta\hat{\eta}_W$ in a large channel with $\hat{L} = 6$. In this range the elastic contribution measured via the right hand side of Eq. (5.25) becomes negative at least in large channels. Even in a channel of width $\hat{L} = 4$ the negative range vanishes, revealing a contradiction in Eq. (5.25) for large W and small $\hat{L}$. This quantitative difference in dependence of the confinement does not occur at small Weissenberg numbers (Cf. Figure 5.9) so that the Kramers-Kirkwood formula loses its validity only for high W and low $\hat{L}$.

5.5. Conclusions

The dynamics of a suspended dumbbell in linear shear flows was investigated by simulations with the Fluid-Particle-Dynamics method. The numerical results show a bifurcation of a steady-state, characterized by a orientation of the dumbbell along the streamlines with a little skew. This state loses its global stability via a global bifurcation to a homoclinic orbit, which arises, when a dumbbell starts its dynamics perturbed in the sense of rotation. Then an instability mediated through the bead rotation with its generated vortices in the surrounding drives the dumbbell out of the steady solution. The homoclinic orbit is closed by the interaction of the shear flow and the coupling forces in the ensuing dumbbell half-turn called *tumbling*, where the followed bead trajectories mainly depend on the dumbbell deformability and its ability to compensate outer stresses. The dumbbell moves back to the idle position

which now has a stabilizing effect. At the end of a half-turn the same, initially unstable fixed point shows a stabilizing action, so that the beads periodically approach and move away from the equilibrium position. The transition can not be understood within the context of stability in the surounding of the fixed points so that this bifurcation falls in the class of *global bifurcations*. The limit cycle seems to appear from nowhere and its shape depends only slightly on the channel size. However, it is surprising that the stability, which is directly coupled to the hydrodynamic interaction, provides a continuous branching, similar to a *Pitchfork-bifurcation* of the dumbbell rotational frequencies.

The simulations have shown that the shape of the limit cycle is not influenced by the channel width $\hat{L}$ in the tumbling regime, but certainly depends on the Weissenberg number W. Hence, the dumbbell deformations are increased while slowing down the rotational motion with increasing Weissenberg number. The decelerated dumbbells have a reduced effect on the walls and by comparing the maxima of $\Delta\hat{\eta}_{\text{eff}}$ illustrated in the Figure 5.9 and Figure 5.11 a reduction of the effective viscosity with increasing Weissenberg number can be identified similarly as in the phenomenon of shear thinning.

The contribution of the coupling forces to the effective viscosity in simulations is commonly determined by the Kramers-Kirkwood formula. Within the simulations it has been shown that independent of the channel width $\hat{L}$ this contribution becomes negative, what can be explained based on geometric arguments. Nevertheless, this result seems astonishing since the Kramers-Kirkwood formula addresses a quantity representing friction. Hence, the direct comparison to the determined effective viscosity of the dumbbell apparently seems contradicting a negative dumbbell contribution. Therefore, one has to be careful, since the effective viscosity and the Kramers-Kirkwood formula still do not measure the same quantity because the effective viscosity takes effects of the extended beads of radius a into account. These contributions can easily be determined via simulations of two colliding uncoupled beads (Cf. Section 4.3). The comparison between the Kramers-Kirkwood formula and the directly determined effective shear viscosities reveals that the Kramers-Kirkwood formula represents quite reasonable the elastic contributions even of a dumbbell with extended beads to the shear viscosity with the limitation that the tumbling may not be inhibited by wall effects.

6. Turbulence in dumbbell suspension

Turbulence at high Reynolds numbers is the best-investigated prime example of turbulent flows on the basis of numerous examples from everyday life. Nevertheless, the phenomenon is hardly understood so far [161, 57], the Kolmogorov law [98] is the only analytical result in this field.. It is agreed that vortex structures are described by the nonlinear term $\boldsymbol{u}\nabla \cdot \boldsymbol{u}$ in the Navier-Stokes equation Eq. (4.1). In the course of investigations of turbulent flows, powerful analysis tools, such as the power-spectrum, Lyapunov spectrum and statistical tools such as structure functions and correlation functions have been applied. Partially these tools were presented in Chapter 3. In this chapter these tools are applied to simulations on the overdamped multi-particle dynamics of suspended bead-spring dumbbells.

In overdamped flows at low Reynolds numbers the nonlinear term hardly plays a role, so that laminar flows occur due to the smoothing effect of the viscosity. In the last decade, experiments have shown that turbulent flows can be generated in this regime by the addition of deformable polymers [67, 69, 120]. The transition to the turbulent regime occurs via subcritical bifurcations like the Hof-bifurcation as a function of the Weissenberg number W, similar to the Lorenz system, which changes its dynamical behavior as a function of the relative Rayleigh number r.

From the point of view of the theory, research is limited to the simulation of single dumbbells in stochastic fields [10]. To the best of my knowledge one does not find any publications on the dynamics of multi-particle systems containing the elasticity of suspended particles and their hydrodynamic interaction. The present part of this work aims to close this gap.

In case of one suspended dumbbell, the dynamics is driven by the hydrodynamic interaction between the dumbbell beads and the coupling forces. Each dumbbell undergoes a periodic motion called *tumbling* with a reference fre-

quency ν_0 described in Section 5.2. By adding more dumbbells in the channel, and thus increasing the volume fraction Φ, the dynamics in the suspension becomes necessarily more complex since each dumbbell provides new degrees of freedom, which all interact via the bead-bead interaction.

This chapter will examine in which parameter ranges a dumbbell suspension can be assumed as a turbulent system according to the behavior of the power-spectrum. This is followed by statements on the loss of stability within an increase of the volume fraction Φ. For this, the method by which the Lyapunov exponents are determined in Section 3.3 is applied to trajectories of *tracers* resulting from simulations of the suspension dynamics with the FPD method (Cf. Chapter 4). The loss of stability is coupled to a mixing process, induced by the dumbbell rotations, transporting the surrounding liquid. Since the nonlinearities of Eq. (4.1) give rise to unpredictable time-dependencies the trajectories can be analysed in terms of diffusion processes, describing the penetration of an initially small reference volume into the surrounding channel. This approach, together with a direct determination of the probability distribution of the flow field, allows the description of turbulent behavior not only in dependence of the volume fraction Φ, but also as a function of various dumbbell-parameters such as the length $\hat{R}$ and elasticity measured in terms of the Weissenberg number W. To complete this chapter, investigations of the rheological properties of dumbbell suspensions are presented.

6.1. Onset of turbulent dynamics

Turbulent flows emerge whenever perturbations of a laminar flow profile increase. So far, it has been shown in Chapter 5 that these perturbations are directly linked to the suspended beads within the rapidly decaying vortices (Cf. Eq. (4.18)). The strength of turbulent flows will therefore mainly depend on the number of suspended particles. This number appears in the volume fraction Φ, which sets the volume of all beads in relation to the channel volume. In addition, the spring forces defined in Eq. (5.2) affect the bead dynamics and impact the shape of the turbulent flow structures. Here, the question is addressed how the turbulent flow patterns depend on the dumbbell length $\hat{R}$ and its elasticity, as characterized by the Weissenberg number W.

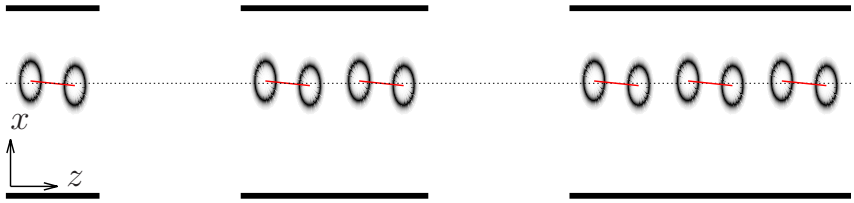

Figure 6.1.: Gradual increase of the number of suspended dumbbells along the centerline.

First, the influence of the volume fraction Φ on the turbulent behavior is examined with the restriction that the dynamics of the suspended dumbbells is considered within the shear plane. For the initial conditions of dumbbells with Weissenberg number $W = 0.1$ and length $\hat{R} = 3.33$, the centerline of the channel length L_z is departed in equidistant parts so that the slightly slanting dumbbells are equally distributed on the centerline (Cf. Figure 6.1). How do the bead-induced perturbations affect the dumbbell dynamics?

To answer this question, the Poincaré section of the connection vectors $\boldsymbol{r}_i = \boldsymbol{x}_{i,1} - \boldsymbol{x}_{i,2}$ through the plane $x = L_x/2$ is considered, as illustrated by the red lines in the Figure 6.1. This plane is cut twice around the section points $r_z = \pm r_0$. For a better visibility of the key changes in the dumbbell dynamics only the intersections around $r_z = r_0$ are illustrated in Figure 6.2. The volume fraction Φ, where $\Phi \approx 0.001$ corresponds to two beads of one suspended dumbbell, is increased in a discrete manner by adding two beads into the channel at each step. Therefore, the volume fraction Φ is no continuously varied parameter.

Figure 6.2 reveals an impressive result. Where the rotation of one dumbbell has one intersection point at $r_z = r_0$, when the dumbbell is equilibrated along the z-direction, this behavior is repeated by each dumbbell in the case of two suspended dumbbells with $\Phi \approx 0.002$. The astonishing thing is that already three dumbbells show a continuous band of intersection points indicating a direct onset of a chaotic dumbbell dynamics. An increase of the number of particles leads to an extension of this band of intersection points, where in Figure 6.2 the numerically obtained data is shown to a number of 9 dumbbells corresponding to $\Phi \approx 0.01$.

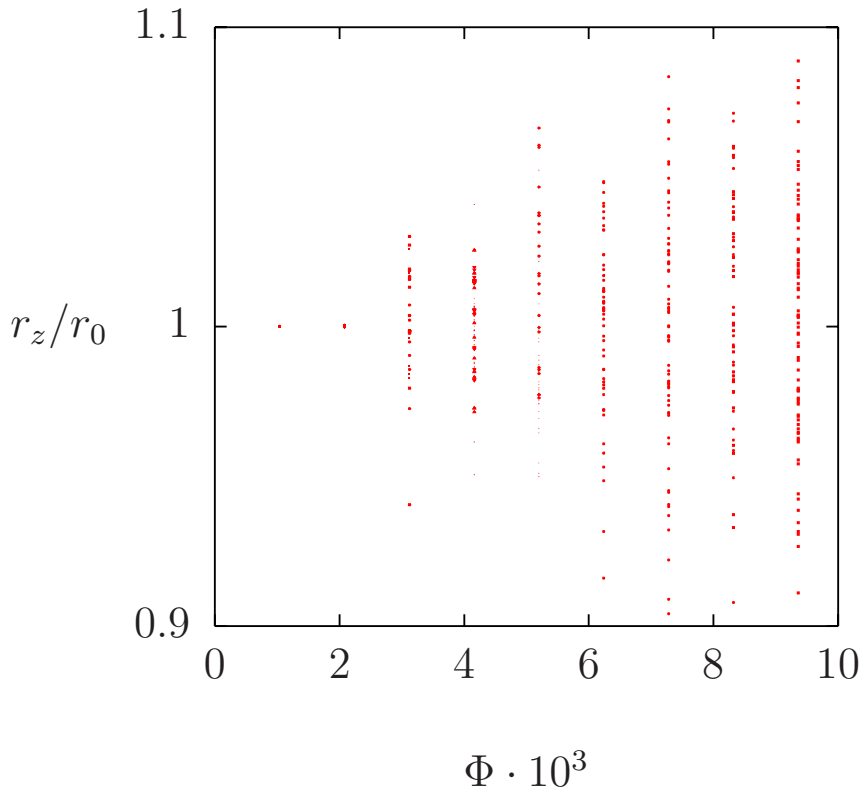

Figure 6.2.: Poincarè map of dumbbell trajectories $\boldsymbol{r}_i = \boldsymbol{x}_{i,1} - \boldsymbol{x}_{i,2}$ with the plane $x = L_x/2$.

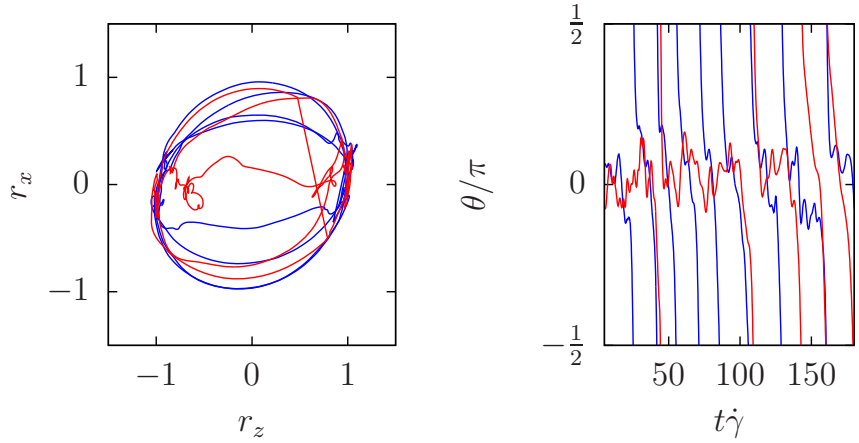

Figure 6.3.: Left: chaotic trajectories of two dumbbells out of a suspension of 60 particles. Right: The time dependence of the angle θ for the two dumbbells.

There seems to be no parameter range of Φ where the dynamics changes to a chaotic behavior along some Hopf bifurcations. Rather, there is only the chance to differ between a regular stable or an irregular unstable dynamical state. Why this happens can be argued as follows:

One main result in Chapter 5 was that the continuous dumbbell rotation depends on the stability around the configuration $\theta = 0$, where the dumbbell is equilibrated. In the phase space (r_x, r_z) this point is represented within the configuration $(0, r_0)$. If the perturbing hydrodynamic interaction with other suspended dumbbells act on a reference dumbbell out of the suspended dumbbells, the dumbbell may pass the point $r_x = 0$ either compressed with $r_z < r_0$ or stretched with $r_z > r_0$ (Cf. Figure 6.2). Both have the consequence that the decisive point for the continuity of dumbbell rotations is circumvented. The dynamics can be considered as *structurally unstable*. Considering a full three-dimensional dynamics in the channel, enhances the possible configurations avoiding this point even more. This leads automatically to a chaotic dumbbell motion, which is illustrated in Figure 6.3, where the phase space (r_x, r_z) and the angle $\theta(t)$ in dependence of time is illustrated for two dumbbells chosen from a suspension of 60 particles.

First, the trajectories in the phase space show that the dumbbell half-turns are retained. Furthermore, the two exemplary trajectories show that the dumb-

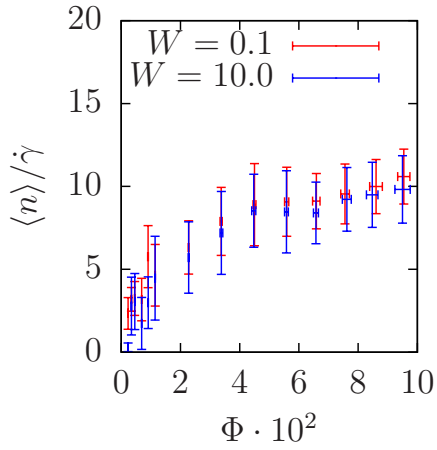

Figure 6.4.: The flip-rate $\langle n \rangle$ per time and particle against the volume fraction Φ.

bells in configurations parallel to the streamlines with $r_x = 0$ underly strong fluctuations induced by the hydrodynamic interaction with the other dumbbells. If the phase space portrait is converted into a plot of the angle θ between the connection vector $\boldsymbol{r}$ and the $\hat{\boldsymbol{e}}_z$-axis versus time, the behavior illustrated on the right of Figure 6.3 appears. It turns out that the dumbbells are oriented fairly parallel most of the time, but within a short period of time the dumbbells execute the well-known half-turns denoted as *flips*.

The average number $\langle n \rangle$ of flips per particle and time is defined as flip-rate. When plotted against the volume-fraction Φ, this quantity illustrates the difference between the dilute and semi-dilute regime, which are departed by a volume-fraction $\Phi^* = 0.05$ (Cf. Figure 6.4). Especially in the dilute regime the number of directly neighboring dumbbells increases continuously so that the dumbbell-dumbbell interaction enhances the flip-rate. However, the space in the immediate vicinity of one dumbbell can not be occupied by other dumbbells without limit due to excluded volume interaction. Since the hydrodynamic interaction between dumbbells is mainly contained in the interaction of nearest neighbors, the flip-rate reaches a maximum plateau, irrespective of the Weissenberg number W and dumbbell length $\hat{R}$ in the semi-dilute regime beyond $\Phi^* = 0.05$.

6.2. Power spectrum

One of the common assumptions on the transition to chaos is discussed by two works of Ruelle and Takens [155] and Newhouse et al. [118], where the first two transitions from a fix-point along an orbit (T^1-torus) to a T^2-torus with two intrinsic frequencies via two Hopf-bifurcations are described as a generic transition, i. e., the new state is stable under small perturbations. During each bifurcation a new mode is stimulated, where the coupling is assumed to be weak. In these works, it is shown that the third bifurcation to a T^3-torus may have unstable modes, enabling the transition of the dynamics to the strange attractor as described in Chapter 3, and thus enabling chaotic dynamics with a broad spectrum of frequencies.

In the last section and also in Chapter 5, there are indications that the onset of a turbulent behavior is not linked to local bifurcation, but depends on a structural instability. In this section the behavior is treated more quantitaively by calculating the power spectrum $P(\nu)$ from the x-component of the normalized dumbbell connection vector $\boldsymbol{e}_r$. Due to the tumbling, this results in a periodic function $r_{x,i}(t)$ from which the single particle power spectra $P_i(\nu)$ for the i-th dumbbell

$$P_i(\nu) = \frac{1}{T}|\chi_i(\nu)|^2, \tag{6.1}$$

can be determined from the windowed Fourier transform

$$\chi_i(\nu) = \frac{1}{N}\sum_{j=0}^{N} r_{x,i}(t)\exp\{i2\pi\nu t_j\}. \tag{6.2}$$

The multi particle power spectrum is assumed to be the superposition of all single particle spectra

$$P(\nu) = \sum_i P_i(\nu). \tag{6.3}$$

The windowing described in Chapter 3 requires the splitting of a total sequence of $N_g = 2^{14} = 16,384$ data points in K sub-segments including N data points, which are Fourier transformed. It has turned out that the most accurate maximum resolution is obtained by dividing the full data set into $K = 3$ segments of length $N = 2^{13} = 8192$.

In the case of one suspended dumbbell, the dynamics is driven by the hydrodynamic interaction and the coupling forces between the two beads. The

dumbbell undergoes a tumbling motion with a reference frequency ν_0. The power spectrum of the dynamics, illustrated at the top of Figure 6.5, shows ν_0, where in addition the corresponding odd harmonics $i\nu_0$ ($i = 1, 3, 5...$) due to the nonlinear dependence of the orientation-vector $\boldsymbol{r}$ on time t.

Within an increase of the number of suspended dumbbells, in addition to the inner dumbbell interaction, each bead moves in the flow field induced by those beads, which are part of other particles. This yields the dynamics of respectively two strictly coupled objects, which are only coupled weakly to all other suspended beads via the hydrodynamic interaction. The dynamics of two dumbbells should include a second frequency ν_1 representing these weak interaction effects. However, there is no period-doubling and thus no second frequency. However, a look at the power spectrum illustrated in the middle of Figure 6.5 reveals that the frequency ν_0 and thus also the harmonic frequencies are shifted to the higher frequency range. This is the expression of a synchronization process where both dumbbells rotate with slightly increased frequency $\tilde{\nu}_0$ with a small phase difference ϕ_0.

The destabilizing effects of the hydrodynamic interaction already occurs in the three dumbbell system, for which the orientation vector r_x and the frequency spectrum is illustrated in the lower part of Figure 6.5. The illustrated trajectories $r_x(t)$ of all three dumbbells show that the particles perform half-turns either synchronized in-phase or anti-phase. However, the synchronization between two dumbbells is broken by the hydrodynamic interaction with the third dumbbell. This results in an unpredictable dumbbell dynamics with very few particles, induced by flows around the suspended beads. This is reflected in the power spectrum, in which the harmonic peaks are replaced by a continuous band of frequencies.

The observation made within the Poincaré section in the last section that an unstable dynamics already occurs for 3 dumbbells is confirmed by the determination of the power spectra. In the following, the power spectra of systems with high dumbbell numbers are discussed, where in Figure 6.6 those for $m = 5$, $m = 10$, and $m = 100$ are illustrated. This figure shows that the high frequency range occurs regardless of the number of suspended dumbbells since it reflects the comparatively fast bead rotation. The rotation of a dumbbells in the sheared channel is dissipative, which means that the fast rotations excite

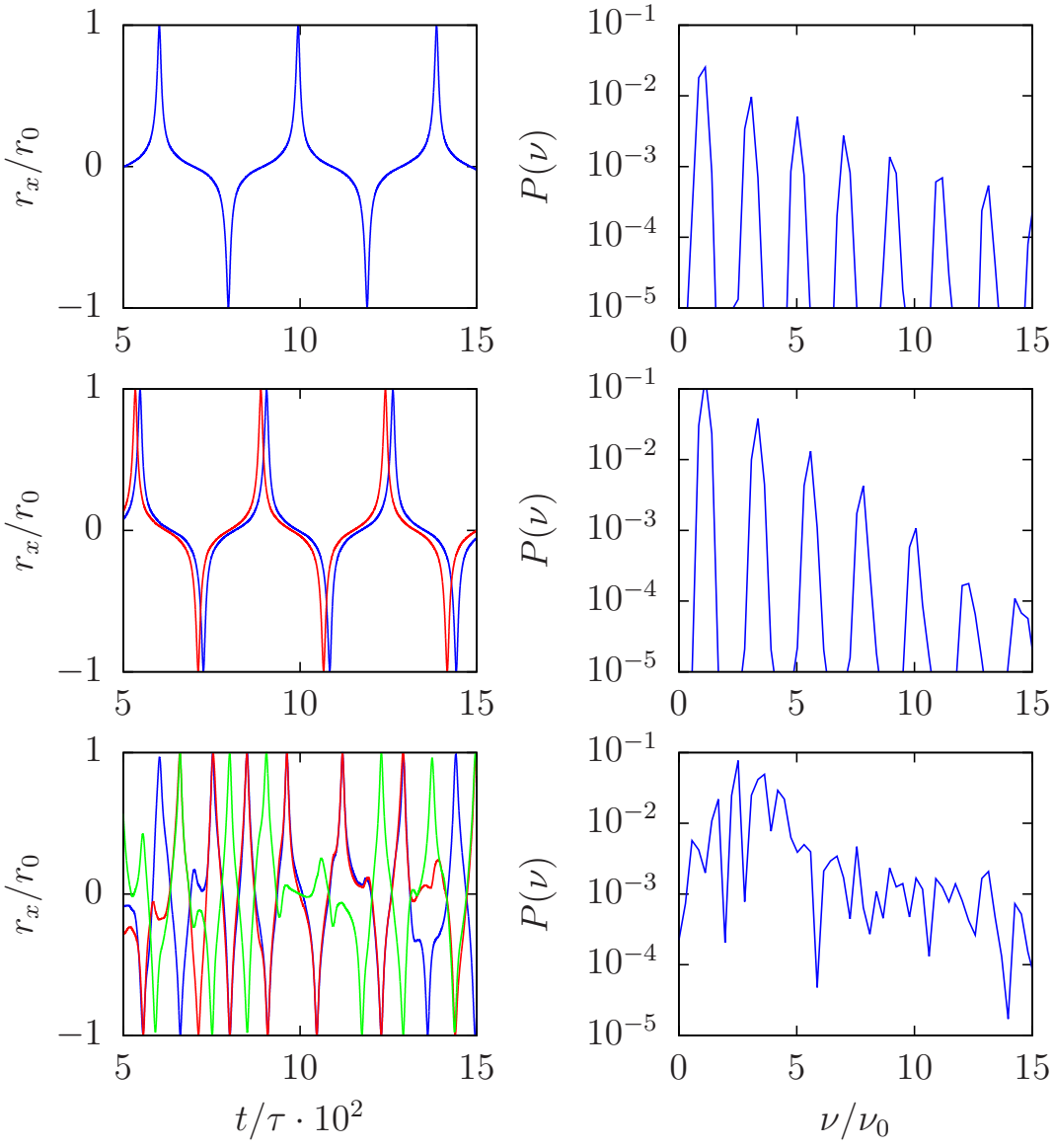

Figure 6.5.: Trajectories $r_x(t)$ and resulting power spectrum $P(\nu)$ of 1, 2 and 3 dumbbells.

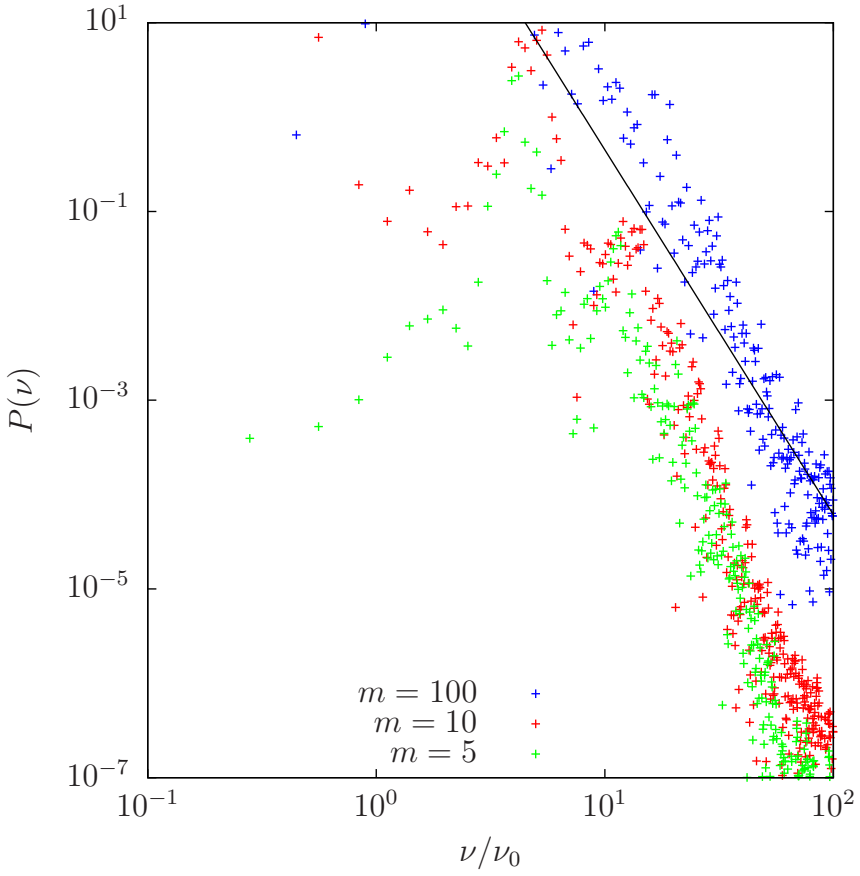

Figure 6.6.: Power spectrum $P(\nu)$ for $m = 5$, $m = 10$, and $m = 100$ suspended dumbbells. The black line indicates the scaling with $P(\nu \propto t^{3.5}$.

slower modes of dumbbell rotations. As Figure 6.6 shows, the intensity of the slow frequencies increases as the number of dumbbells increases. The intensity $P(\nu)$ depends on an universal scale law as a function of the frequencies ν. By fitting the shown data sets with the function

$$P(\nu) = a\nu^b \tag{6.4}$$

the exponent $b = -3.5$ is obtained. This very small value for b expresses very fast damping of movements in a highly viscous system. From this, a cascade can be identified in which the motion of the bead is first stimulated by the shear flow, and then flows into the motion of the dumbbells before it is smoothed by viscous effects converting it, e. g., into heat.

6.3. Statistical description

Executing the experiment of shearing a suspension of a higher number of dumbbells, e. g., $N = 60$, which initially are equally distributed in the channel multiple times denoted by M, one will find M different realisations of this experiment, corresponding to the same particle parameters Φ, W and $\hat{R}$. Therefore, it is unsatisfactory to extract statements about the entire system by consulting the individual particle trajectories. Even more, this applies, when in a box of $N = 61 \times 61 \times 61 = 226981$ grid points $\boldsymbol{x}$ per recorded time-step t_i ($i \in [0:1001]$) each data point, e. g., of the flow field $\boldsymbol{u}(\boldsymbol{x})$ has to be taken into account. For an understanding of the dynamics and structures in the flow it is therefore convenient to switch to a statistical description based on the distribution $\mathcal{P}(x)$ of a considered quantity x. The distribution $\mathcal{P}(x_i)$ is obtained by the average

$$\mathcal{P}(x_i) = \langle \delta(X - x(t_i) \rangle = \langle \delta(X - x_i) \rangle. \tag{6.5}$$

The quantity x may represent the angle θ one dumbbell encloses with the z-direction or the flow field $\boldsymbol{u}$. Numerically, the distribution is determined by counting those states x_i with $x_i \in [X; X + \delta X[$.

The stationary state, in which turbulent flows are fully developed, is characterized by temporally constant probability distributions $\mathcal{P}(x)$ of all considered quantities (angles θ, velocities $\boldsymbol{u}$, effective viscosity η_{eff}, ...). For reasons of ac-

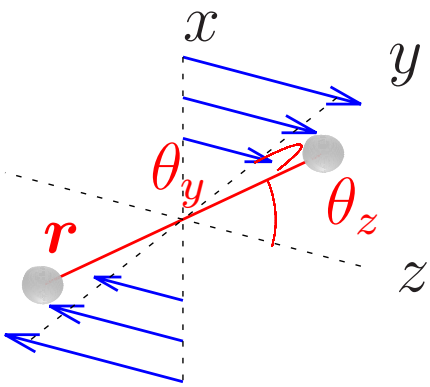

Figure 6.7.: Sketch of a dumbbell in shear flow for the definition of the angles θ_y and θ_z. The shear flow is indicated by the blue vectors.

curacy, the distribution $\mathcal{P}(x)$ is averaged over all snapshots t_i in the stationary state.

An obvious question is, which distribution functions $\mathcal{P}(\theta)$ and $\mathcal{P}(\dot{\theta})$ underly the dumbbell dynamics. For this, the angles θ_z enclosed by the connection vector $\boldsymbol{r}$ and the shear-direction $\hat{\boldsymbol{e}}_z$ and θ_y between $\boldsymbol{r}$ and the y-axis $\hat{\boldsymbol{e}}_y$ perpendicular to the shear-plane are considered (Cf. Figure 6.7). In addition to the angles θ_y and θ_z, the dynamics is defined by the angular velocities $\dot{\theta}_z$ and $\dot{\theta}_y$, which result from the connection vector $\boldsymbol{r}$ and bead velocity $\boldsymbol{v}$ via

$$\dot{\theta}_z = \frac{1}{r^2}(r_x v_y - r_y v_x) \quad \text{and} \quad \dot{\theta}_y = \frac{1}{r^2}(r_z v_x - r_x v_z). \tag{6.6}$$

The determined distributions for $\theta_{y,z}$ and $\dot{\theta}_{y,z}$ are illustrated in Figure 6.8. In the z-direction the fingerprint of the previously described tumbling motion can be identified. Most of the time the dumbbells remain parallel to the streamlines with $\theta_z \approx 0, -\pi$, so that $\mathcal{P}(\theta_z)$ displays two maxima for these configurations. In turn, the minimum at $\theta_z = -\frac{\pi}{2}$ is related to the rather quick dumbbell flips. Looking carefully at the distribution maxima for suspensions with $W = 10$ (dashed line) in Figure 6.8 a difference in the maximum values can be identified. This asymmetry with respect to $\theta_z = -\frac{\pi}{2}$ is related to the asymmetry in $\Delta(\theta)$ shown in Figure 5.2 for high Weissenberg numbers W. The explanation is as follows:

During the first quarter of a turn the dumbbell is compressed, increasing the bead-bead interaction inside one dumbbell, whereas in the second quarter of a

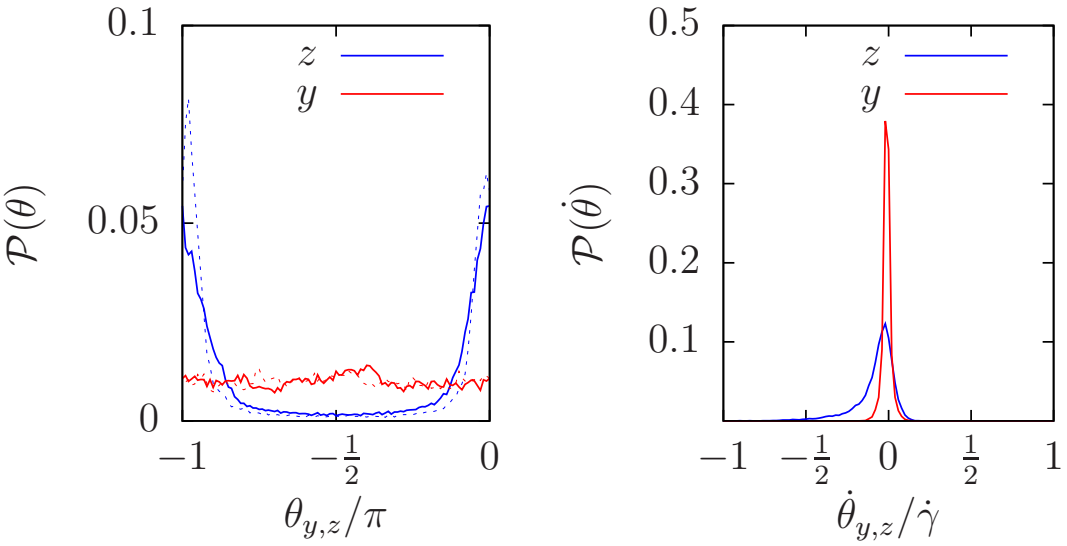

Figure 6.8.: Stationary distribution of the orientation angle θ and the angular velocity $\dot{\theta}$ in y- and z-directions as obtained for a suspension of 50 dumbbells at Weissenberg number $W = 0.1$ (solid lines) and $W = 10$ (dashed lines).

turn the interaction is reduced as the dumbbell gets stretched. Hence, the first quarter turn with angle between $\theta_z = 0$ and $\theta_z = -\frac{\pi}{2}$ happens faster and hence less likely than the part between $\theta_z = -\frac{\pi}{2}$ and $\theta_z = -\pi$. While this effect remains small for hard springs with $W = 0.1$ with only small deformations (solid line in Figure 6.8), for $W = 10$ the impact is quite pronounced.

Also, the distribution of the angular velocities $\dot{\theta}_z$ of the dumbbells is asymmetric in shape. The accumulation of negative rotational velocities is associated with the shear flow. In the present case of an upper plate moving with positive velocity in the z-direction and the lower plate in the exact opposite direction, a bead and dumbbell rotation is generated in clockwise direction, as indicated by negative angular velocities. Nevertheless, the dumbbells move, although rarely, in a positive direction of rotation. This is also a fingerprint of the hydrodynamic bead-bead ineraction and causes the fluctuations in the time dependence of the angles visible in Figure 6.3

In the y-direction no driving force exists, so that the dynamics in this direction is a signature of bead-bead interaction. The corresponding distributions are symmetric around $\theta_y = \dot{\theta}_y = 0$, where the angles θ_y are equally distributed.

This uniform distribution indicates that the dumbbell flips, which always occur in the direction of the shear flow in the z-plane, have equal contributions in the x- and y-direction mediated by the spring forces.

6.4. Turbulent flow structures

Up to this point *turbulent flow patterns* have always been mentioned, which bear the responsibility for the previously described unpredictable dynamics. On the other hand, it has been the *stochasticity* of the flow field that has been used as an explanation aid. What is true now? Is the underlying field a structured or noisy one?

If one likes, both statements are right and the phenomenon of turbulence, no matter what the generating mechanisms are, is a problem of dynamic pattern formation. To make the structures visible, the local vorticity $\boldsymbol{\omega}(\boldsymbol{x})$ is introduced, which is determined from the local flow field $\boldsymbol{u}(\boldsymbol{x})$ by taking the curl

$$\boldsymbol{\omega}(\boldsymbol{x}, t) = \nabla \times \boldsymbol{u}(\boldsymbol{x}, t). \tag{6.7}$$

In four snapshots of the channel cross-section corresponding to the fully developed turbulent state, this quantity is illustrated in Figure 6.9. The vorticity is interpreted as twice the local angular velocity $\dot{\theta}$. Therefore, it indicates extended regions of clockwise (red) and counterclockwise (blue) rotating flow profiles. It stands out that the size of the vortex structures does not vary with propagating time. This is due to the fact that rotational flow patterns caused by the beads can not move far from them before they are damped. Therfore, especially the blue structures are directly linked to the dumbbell dynamics, which is why the position of the vortices in the channel changes very pronounced, namely unpredictable as the last section has shown. This leads to two questions:

1. How does the probability distribution $\mathcal{P}(\boldsymbol{u})$ of the flow field change when the volume fraction Φ is increased and at which point can one speak of *fully developed turbulence*?

2. Is it possible to determine the size of the flow structures, even if the dynamics is subject to a certain stochasticity?

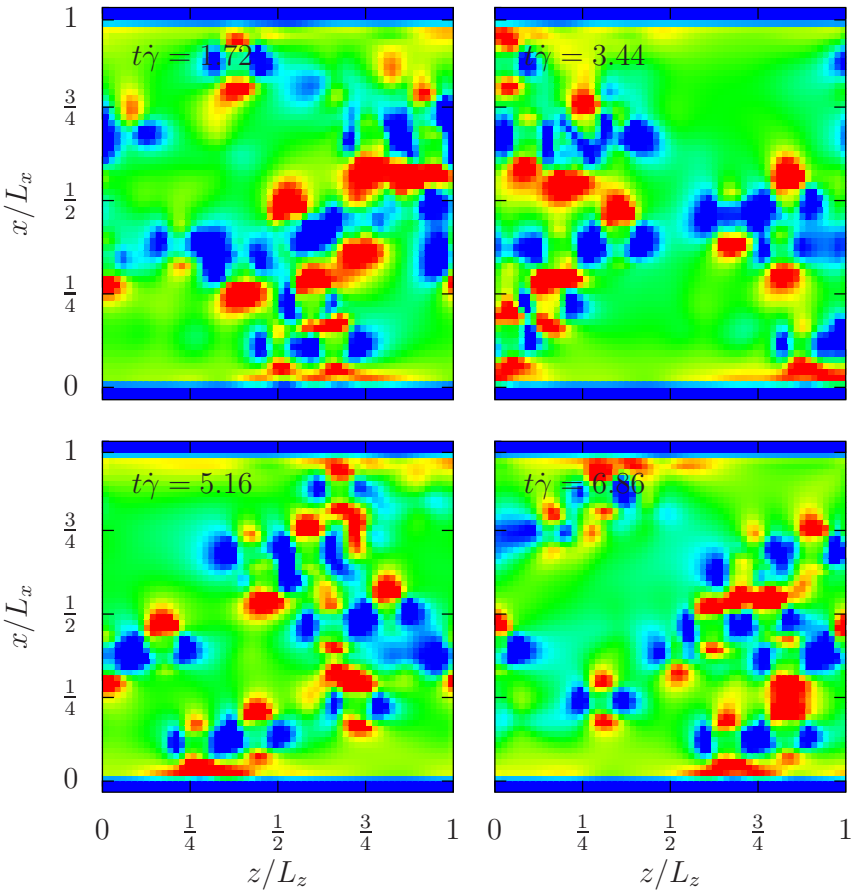

Figure 6.9.: Four snapshots of the vorticity in the channel cross-section in the steady state. Blue areas correspond to negative vorticities, where red areas indicate rotation in the positive sense.

The first question is answered by Figure 6.10. In this Figure the probability distributions $\mathcal{P}(\boldsymbol{u})$ of the flow $\boldsymbol{u}$ are shown, representing the x- and y-components, perpendicular to the driving shear flow. The upper parts a) and b) belong to numerically determined data for uncoupled beads. In the lower parts c) and d) the distributions of dumbbells with Weissenberg number $W = 0.1$ and length $\hat{R} = 3.33$ are illustrated, once for small volume fraction $\Phi \approx 0.002$ corresponding to $m = 4$ suspended beads in blue. In addition, data from the semi-dilute regime with $m = 60$ (red lines), $m = 120$ (green lines) and $m = 180$ (magenta lines) suspended particles, for which the turbulent regime is expected to be fully developed, are illustrated in Figure 6.10. In order to emphasize the influence of comparatively high velocity values at the tails of the distribution, the velocity u_i is normalized by the corresponding standard deviation σ_{ui} given by

$$\sigma_{ui}^2 = \int u_i^2 \mathcal{P}(u_i)\, \mathrm{d}u_i. \tag{6.8}$$

Looking at the dynamics of $m = 4$ suspended beads, whether they are connected by springs or not, one finds that the dynamics are characterized by frequent phases of slow motion, which are occasionally interrupted by half-turns like the flips or particle collisions, as described in Chapter 4. Even if the dynamics in the dilute regime can be described by a probability distribution, the behavior of the individual suspended particles in the velocity distribution can be identified since the distribution is accumulated around $u_i = 0$ and the high velocity at the tails are comparatively rare expressed in the distortions of the distribution at the tails. As the number of particles increases, the incidence of high flow velocities increases as well. The odd probability distribution at low volume fractions Φ changes to a Gaussian distribution, which is plotted in dashed lines as reference to the illustrated distributions in Figure 6.10. It should be mentioned that the tails of the distribution remain enhanced compared to the real Gaussian curve even in the fully developed turbulent state.

To answer the second question about the turbulent length scales, the autocorrelation function $C_{ii}(r)$ of the flow field, which is illustrated for a suspension of $m = 90$ dumbbells in Figure 6.11, is introduced

$$C_{ii} = \langle u_i(\boldsymbol{x}) u_i(\boldsymbol{x} + \boldsymbol{r}) \rangle. \tag{6.9}$$

The brackets $\langle ... \rangle$ have the meaning of a spatial average over the positions $\boldsymbol{x}$,

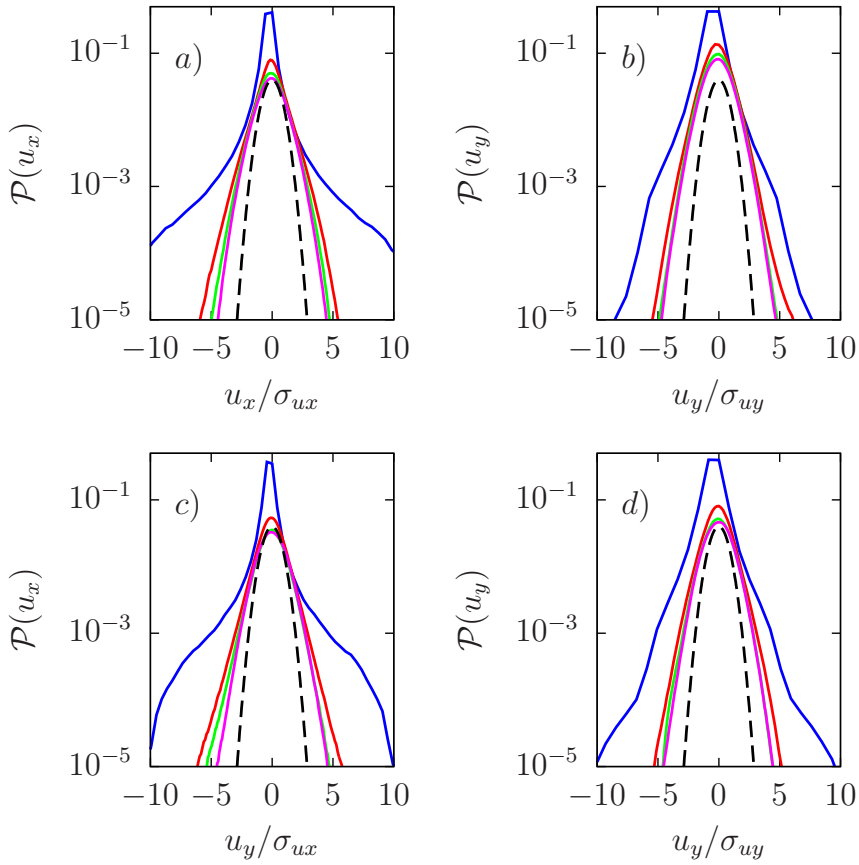

Figure 6.10.: *a*) and b) Probability distribution $\mathcal{P}(u_{x,y})$ for unconnected beads in dependence of the number $m = 4$ (blue), $m = 60$ (red), $m = 120$ (green), and $m = 180$ (magenta) of suspended particles. *c*) and *d*) The same distributions for $m = 2$ (blue), $m = 30$ (red), $m = 60$ (green), $m = 90$ (magenta) suspended dumbbells. To compare the shapes the normalized distributiion u/σ_u with the standard deviation σ_u is illustrated. The dashed line indicates a Gaussian distribution.

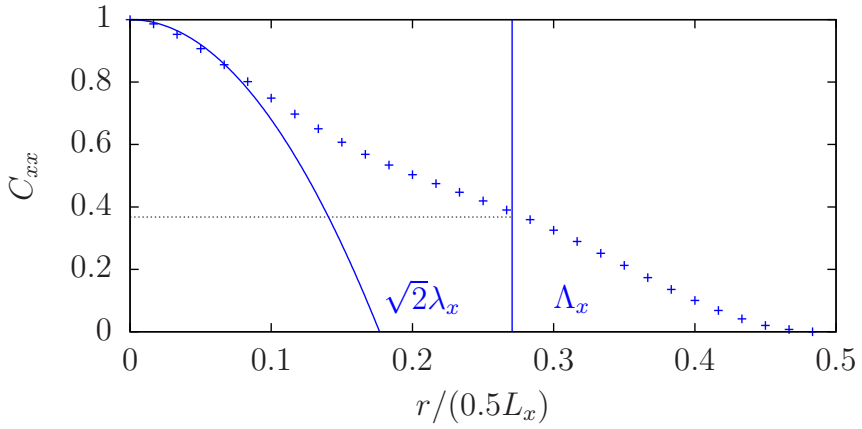

Figure 6.11.: Illustration of the correlation function $C_{xx}(r)$ for a suspension of $m = 90$ dumbbells.

for which the autocorrelation function comparing two grid points separated by the distance $\boldsymbol{r}$ exists within the channel. The autocorrelation function is determined from snapshots of the flow field at equidistant time intervals Δt. Furthermore, C_{ii} is averaged over these number of time steps in the equilibrium state. For simplicity, the distance $\boldsymbol{r}$ is only varied in the direction i whose velocity component is evaluated in the function $C_{ii}(r_i)$. For the definition of the characteristic turbulent length-scales $C_{xx}(r_x)$ and $C_{yy}(r_y)$ are determined from numerical data on the flow field.

The largest flow patterns inside the box cover a length Λ. On larger length-scales the turbulent flows should become statistically independent. This statement can be coupled to the correlation-function $C_{ii}(r)$. Assuming an exponential decay in r, one obtains $C_{ii}(r) = e^{-r/\Lambda} C_{ii}(0)$ and thus, the *integral length-scale* can be defined:

$$\Lambda_i = \int_0^{L_i} \frac{C_{ii}(r)}{C_{ii}(0)} \, \mathrm{d}r. \tag{6.10}$$

Λ_i then denotes the length at which $C_{ii}(\Lambda_i)$ has decayed to $1/e$, as Figure 6.11 illustrates, where C_{xx} for a dumbbell suspension of $m = 60$ dumbbells at $W = 10$ and $\hat{R} = 3.33$ is plotted exemplarily.

This graph also shows that the exponential decay is not valid for small values of the distance r. In this range, the curvature of $C_{ii}(r)$ has a different sign, which can be attributed to the viscosity η_0 and in particular η_1 smoothing the

neighboring velocity-contributions. The changing curvature defines a second length-scale λ_i, called *Taylor length* [157] corresponding to the smallest flow structures. The length λ_i is obtained by a Taylor-expansion to second order

$$C_{ii}(r) = C_{ii}(0) + \frac{\partial}{\partial r} C_{ii}(r)\bigg|_{r=0} r + \frac{1}{2}\frac{\partial^2}{\partial r^2} C_{ii}(r)\bigg|_{r=0} r^2 + \mathcal{O}(r^3). \tag{6.11}$$

The slope of the autocorrelation function vanishes in the origin, smoothed down to zero by the viscosity. Thus, only the second order term remains

$$\frac{C_{ii}(r)}{C_{ii}(0)} = 1 - \frac{1}{2}\frac{r^2}{\lambda_i^2}. \tag{6.12}$$

To show that the numerically determined correlation function can be fitted by this function, it is plotted together with $C_{ii}(r)$. A comparison between Eq. (6.11) and Eq. (6.12) yields

$$\lambda_i = \left[-\frac{\partial^2}{\partial r^2} C_{ii}(r)\bigg|_{r=0} \right]^{-\frac{1}{2}}. \tag{6.13}$$

The second derivative $\frac{\partial^2}{\partial r^2} C_{ii}(r)$ can be expressed via the mean $\langle u_i(x)\rangle_x$ of the local flow and the mean spatial derivatives $\partial_x u_i(x)\rangle_x$ [157], so that one has direct access to the Taylor-length from numerical data:

$$\lambda_i = \sqrt{\frac{\langle u_i(x)\rangle_x}{\langle \partial_x u_i(x)\rangle_x}}. \tag{6.14}$$

The two lengths λ_i and Λ_i play an essential role in the description of inertial turbulence at high Re. In these ranges, λ_i and Λ_i, which measure the smallest and biggest vortex structures, are seperated by decades. In addition, the transfer of energy is coupled to a cascade of structures of lengths between λ_i and Λ_i [97, 98]. This big difference between λ_i and Λ_i does not occur in the case of overdamped dumbbell-driven turbulence. Here, both quantities are coupled to predominating viscous effects. In order to anticipate this, a constant ratio of $\Lambda_i/\lambda_i = 2$ results independently from the parameters Φ, which prescribes the number of vortices and in the semi-dilute regime may induce overlaps between the vortices increasing their size.

On average, the determined lengths increase in the dilute regime, as illustrated in Figure 6.12. This is related to the increasing number of vortices and

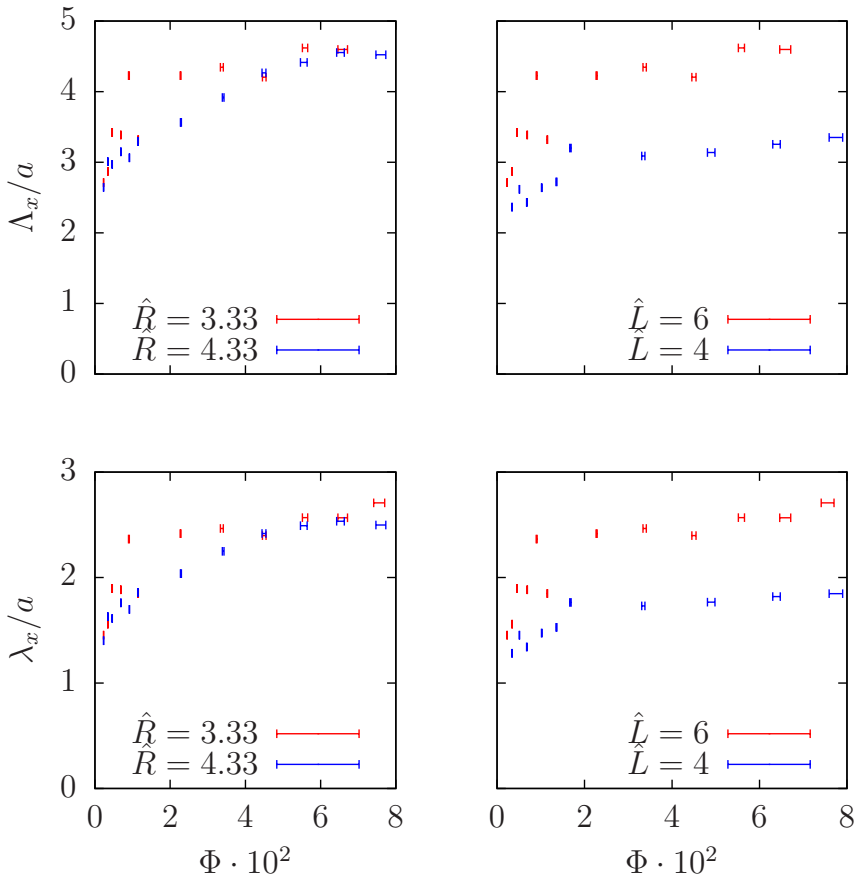

Figure 6.12.: The integral length Λ_x (top) and Taylor-length λ_x (bottom) plotted against the volume fraction Φ for two values of the dumbbell length $\hat{R}$ (left) and channel width $\hat{L}$ (right).

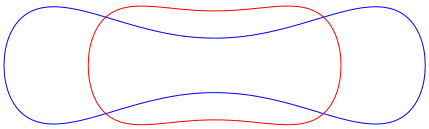

Figure 6.13.: Not true-to-scale mapping of the vortices around a dumbbell of length $\hat{R} = 4.33$ (blue) and $\hat{R} = 3.33$ (red).

their mediated contributions $\boldsymbol{u}(\boldsymbol{x})$ within overlaps, over which is averaged in C_{ii}. In addition, Figure 6.12 illustrates that the two lengths λ_i and Λ_i, set into relation to the bead radius a, change very well in dependence of Φ, $\hat{R}$, and $\hat{L}$. Not surprisingly, a reduction of the channel width $\hat{L}$ leads to a reduction of the vortex size, as illustrated on the right hand side. However, the shrinkage of vortices within the extension of dumbbells in terms of $\hat{R}$ is surprising. Should not the vortex structures become larger?

The answer is no and can be seen in Figure 6.13. In this Figure the boundarries of vortices around a dumbbell of length $\hat{R} = 3.33$ are sketched in red and in blue those structures are illustrated surrounding a dumbbell of length $\hat{R} = 4.33$. Even if the image is not true to scale, it can be seen that a short dumbbell creates a compact swirling in the surrounding with a relatively large vortex size Λ_i. By reducing the overlap by icreasing the distance $\hat{R}$ between the dumbbell beads, the compactness of the surrounding structures reduces and the vortex alters to two independent vorticies with reduced size Λ_i.

Even if the lengths λ_i and Λ_i diverge only by a factor 2, the occurence of structures limited by Λ_i also results in a similarity to the turbulence at high Reynolds numbers called *intermittency*. In Figure 6.10 it was shown that the velocity field $\boldsymbol{u}(\boldsymbol{x})$ follows a Gaussian distribution as if neighboring velocity entries at $\boldsymbol{u}(\boldsymbol{x})$ and $\boldsymbol{r}$) with small $\boldsymbol{r}$ were not correlated. Given a finite correlation length Λ_i, is there always a Gaussian probability distribution for the flow field $\boldsymbol{u}(\boldsymbol{x})$?

To take into account the spatial correlation of flow contributions the flow field $\boldsymbol{u}(\boldsymbol{x}, t)$ is replaced by the velocity increment $\boldsymbol{U}(\boldsymbol{x}, \boldsymbol{r}, t)$, which is defined as

$$\boldsymbol{U}(\boldsymbol{r}) = \boldsymbol{u}(\boldsymbol{x}, t) - \boldsymbol{u}(\boldsymbol{x} + \boldsymbol{r}, t). \tag{6.15}$$

By determinining the probability distribution $\mathcal{P}(\boldsymbol{U}_{\text{norm}}(\boldsymbol{r}))$ of the normalized

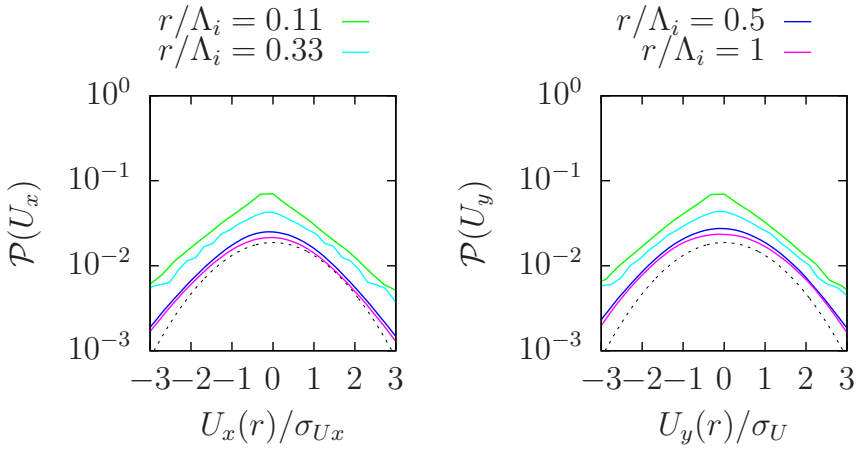

Figure 6.14.: Distribution of velocity increments in x- and y-direction for several distances r. The dashed lines indicate a Gaussian distribution.

increment components $U_{\text{norm}} = U_i/\sigma_i$ for several distances $\boldsymbol{r}$, statements about the *self-similarity* in the dumbbell suspensions are possible. A system is called self similar, if the rescaled field $\tilde{\boldsymbol{U}}$

$$\tilde{\boldsymbol{U}}(\boldsymbol{r}) = \lambda^{\alpha}\boldsymbol{U}(\lambda^{\beta}\boldsymbol{r}, \lambda^{\gamma}t) \tag{6.16}$$

has the same statistical properties for all $\lambda > 0$ and suitable constants α, β, and γ, i. e., the distribution $\mathcal{P}(\boldsymbol{U}_{\text{norm}})$ does not change within a variation of $\boldsymbol{r}$.

For the flow field in the channel, this means that the increment distribution is determined for several values of the distance r in the range $r < \Lambda_i$. The resulting distributions are shown in Figure 6.14. For $r = \Lambda_i$ the two computed values $\boldsymbol{u}(\boldsymbol{x})$ and $\boldsymbol{u}(\boldsymbol{x}+\boldsymbol{r})$ are uncorrelated and the corresponding distribution yields a Gaussian. With a reduction of r, increasingly correlated, i.e., similar, values are compared in Eq. (6.15) thus yielding increasing deviations from the Gaussian distribution. The hat-shaped signatures for very small distances $r \ll \Lambda_i$ is called intermittent distribution since it indicates the break of self similarity. What does this break mean?

Consider a particle that follows the streamlines with the velocity $\boldsymbol{u}(\boldsymbol{x}, t)$ and can detect the velocity field in the neighborhood at a distance r. Due to the detected fluctuations the particle views the flow field as "turbulent".

If this particle reduces the range of view to very short but finite distances $r < \Lambda_i$, the fluctuating parts are blurred and the surrounding field is perceived as "ordered". This difference, which does not depend so much on the system parameters, but rather on the scale at which the system is observed, represents a fraction of the self-similarity in the system and is called *intermittency*. Although this phenomenon is far less pronounced in dumbbell-driven turbulence than in inertial turbulence, this commonality still exists.

6.5. Loss of stability

In Section 6.1 the dumbbell dynamics was directly investigated to illustrate period doubling effects leading to chaotic dynamics in the suspension. This section focuses on the dynamics of tracer particles, following the streamlines within the total box. A rotating dumbbell with the angular momentum $\boldsymbol{L} = \boldsymbol{r} \times \boldsymbol{v}$ can be considered as a shovel, which transports solvent liquid perpendicular to the streamlines from central to peripheral areas inside the channel. The associated questions are whether the dumbbells trigger a mixing process by the entrainment of the surrounding fluid, and how this process is affected by the parameters Φ, W, and $\hat{R}$.

The mixing process inside the whole channel would intuitively be investigated within the consideration of a small reference volume ΔV, penetrating into neighboring liquid layers with increasing time. As long as the conditions in the channel can be assumed isotropic, i. e., the dumbbells are uniformly distributed in the whole channel, the initial position of the volume ΔV does not matter. In addition, the entire channel is covered with liquid, emanating from ΔV after a sufficiently long observation time $t_{\max}$. This loss of the importance of initial conditions is one of the main characteristics of efficient *mixing*. Continuing this idea, one recognizes that the expansion of ΔV to the surounding space is closely linked to the Lyapunov stability (Cf. Chapter 2).

To obtain a reference trajectory $\boldsymbol{y}^0(t)$ and neighboring trajectories $\boldsymbol{y}^p(t)$ a second particle type is defined. In contrast to the beads, these particles are assumed to be point-like without performing any interaction with the surrounding fluid. They only follow the streamlines in a trajectory $\boldsymbol{y}(t) = \int \boldsymbol{u}(\boldsymbol{y}, t')\,\mathrm{d}t'$,

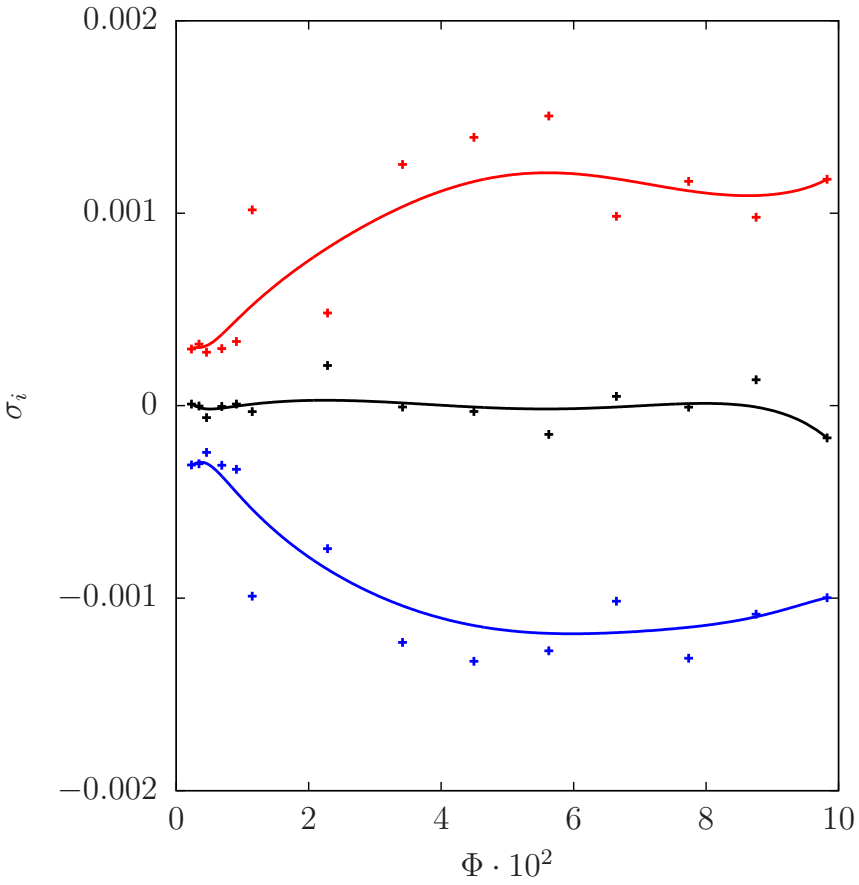

Figure 6.15.: Lyapunov-spectrum for independent beads as function of the volume-fraction Φ.

coupled to the flow field $\boldsymbol{u}(\boldsymbol{x}, t)$ via the discrete delta-function [122]

$$\Delta(\boldsymbol{y}^{0,p} - \boldsymbol{x}) = \frac{1}{64\delta^3} \prod_{d=x,y,z} \left(1 + \cos \frac{\pi(y_d^{0,p} - x_d)}{2\delta}\right), \tag{6.17}$$

where all that grid points are taken into account with $|\boldsymbol{y}^{0,p} - \boldsymbol{x}| < 2\delta$. For all other points $\Delta(\boldsymbol{y} - \boldsymbol{x}) = 0$.

The Lyapunov spectrum σ_1, σ_2, and σ_3 is determined using the technique from Section 3.3. In Figure 6.15 the Lyapunov spectrum of suspensions, consisting of uncoupled, randomly distributed beads, is shown versus the volume fraction Φ. Although the illustrated points seem to underly strong noise, there the spectrum shows tendencies indicated by the smoothened lines.

- The numerically determined spectrum falls into the category $(+, 0, -)$ indicating unstable dynamics.
- The highest as well as the absolute value of the lowest Lyapunov exponent grows in the dilute regime below $\Phi^* \approx 0.05$, indicating the growth of unstable bead-bead interactions in the system. Beyond Φ^* the instabilities do not change up to fluctuations.
- The sum of the three Lyapunov exponents yields $\sum \sigma_i = 0$. This indicates the time-reversal symmetry of the Navier-Stokes equations in the low Reynolds number regime.

Turbulent flows, which appear even at very low volume fractions Φ, are a surprising result. Figure 6.16 shows that the positive Lyapunov exponent can be actually attributed to the flows around the beads and not to numerical uncertainties. This figure illustrates the progress of the reference trajectory perpendicular to the streamlines in the x, y-plane (left) and in parallel direction in the x, z-plane for volume fractions corresponding to $N = 4$, $N = 8$, $N = 12$, and $N = 16$. Although the covered area stays limited and is considerably smaller than the channel cross-section, an unpredictable trajectory occurs. The coupling to back flows around the bead can be clearly identified on the right hand side. Here, the tracer particle is distracted in x-direction, when it follows the back flows around a neighboring bead. Already in the case of four suspended beads, the motion of the tracer particle exhibits an irregular dynamics as a consequence of the superposition the bead-induced flow patterns. The superposition yields the positive Lyapunov exponent. Increasing

the volume fraction Φ by adding further particles, the instabilities increase, as reflected in the growing Lyapunov exponent, but also lead to an increase of the volume covered by the tracer trajectory. However, the destabilizing effects of the hydrodynamic interaction are limited since the perturbing flows are mainly induced by next neighbors. Hence, beyond the volume fraction $\Phi^* \approx 0.05$ in the semi-dilute regime the addition of beads does not increase the bead-bead interaction.

The stability analysis of sheared bead suspensions shows that already extended beads of radius a are sufficient to induce turbulent flow structures. Until here no effects of elastic bead-spring chains have been taken into account in this section. Since a coupling force in addition to the driving shear flow accelerates bead motions perpendicular to the streamlines, one would expect an effect of the dumbbell parameters W and $\hat{R}$ on the mixing characteristics of a suspension. These effects do not appear in the Lyapunov spectrum or they get lost in the fluctuations.

6.6. Diffusion of tracer particles

Mixing denotes a dynamical process in which two distinct areas of a fluid penetrate each other. In the four snapshots of the distribution of tracers $\mathcal{P}(y_x(t), y_y(t))$ in the channel cross-section Figure 6.17, the penetration of tracer particles, initially uniformly distributed in the channel center, can be followed. This penetration can not only be seen by the changing distribution $\mathcal{P}(\boldsymbol{y}(t))$, but also on the left side of Figure 6.17, where two tracer trajectories with similar initial conditions are illustrated. Two regions can be identified. The first, where a particle moves quasi-ballistic in one direction is called *jet*. From time to time these jets are superseded by curved paths, representing the second region. A closer look shows that the radii of these loops may have different sizes.

Under normal conditions, as determined by the unperturbed laminar shear-flow in z-direction, "mixing" takes place in the direction of streamlines due to the shear gradient $\dot{\gamma}$ due to different velocities in neighboring layers. This process does not represent the real meaning of mixing, where the irreversibility of the process leads to inseparability of the two components of the fluid.

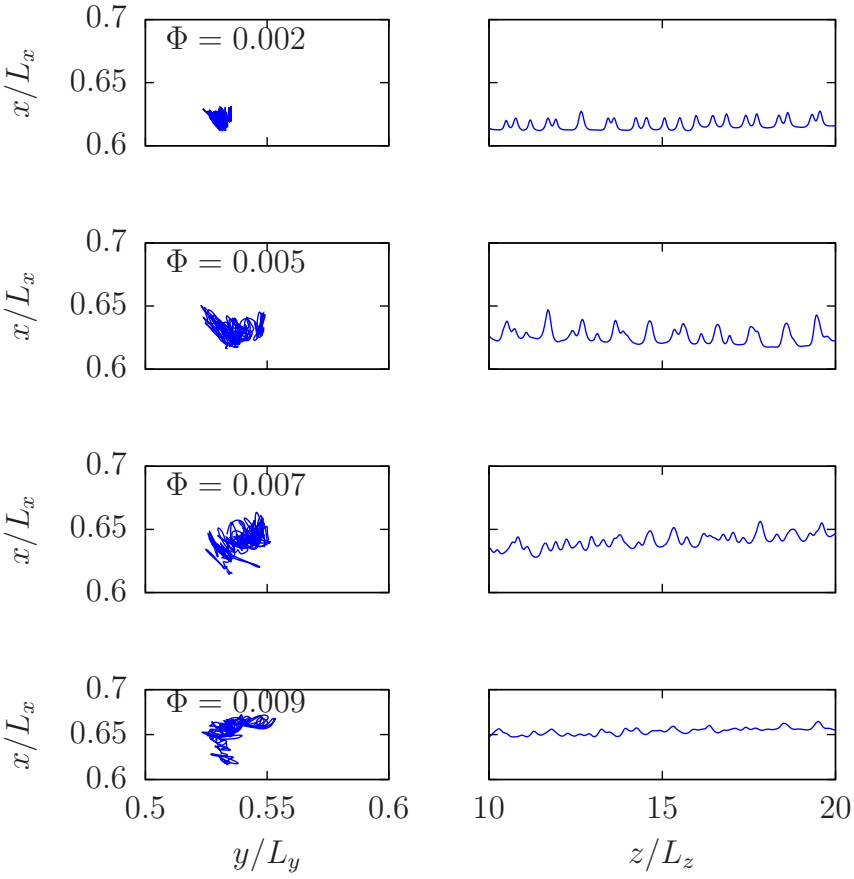

Figure 6.16.: Projections of the reference trajectory in the x, y-plane (left) and x, z-plane (right) for small values of Φ, illustrating the onset of chaotic dynamics due to hydrodynamic interaction.

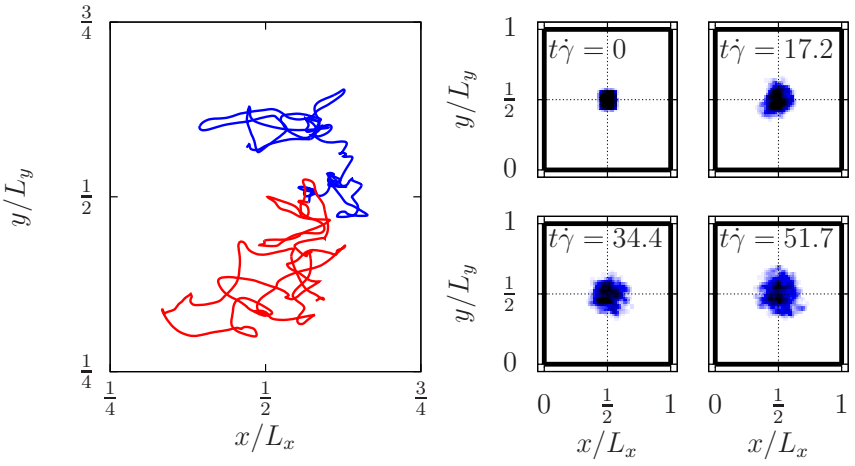

Figure 6.17.: Left: two trajectories from a simulation with $N = 90$ dumbbells in shear flow for a Weissenberg number $W = 0.1$ and $\hat{R} = 4.33$. Both trajectories show the behavior of mixtures, where similar initial conditions may advance to different regions in the fluid. Both curves show zones of jets, where the motion does not change the direction, detached by regions, where this direction is randomly changed in loops. Right: Snapshots of the tracer concentration $\mathcal{P}(x, y)$ at different times t. Initially, only one tenth of the channel is covered by particles, which diffuse to surrounding areas.

Therefore, the following investigations are restricted to the x- and y-direction. Although the Lyapunov exponents have shown the inherent property of mixing in suspensions, but do not depend on the dumbbell-length $\hat{R}$ as well as elasticity in terms of W, the question of the influence of these two parameters remains unanswered.

The definition of $P = 2500$ tracer particles inside the channel center, covering one percent of the channel volume, means a resolution of roughly one particle per grid point, so that a good approximation of the dynamics within the entire channel is guaranteed. We do not save all 2500 trajectories and thus 7500 data-points per tracked time-step. Instead of saving the trajectories of all particles, the distribution of tracers $\mathcal{P}(y_x(t), y_y(t))$ at time t is determined as a histogram with a bin-width equal to the grid size δ. The distribution is continuously tracked after the elapsed time interval Δt. In this manner, the distribution $\mathcal{P}(y_x(t + \Delta t, y_y(t + \Delta t)|y_x(t), y_y(t))$ represents the conditional probability distribution, determined under the condition that the considered particle is located at $(y_x(t), y_y(t))$ at the time t. Then the drift $D^{(1)}_{x,y}$ and diffusion coefficients $D^{(2)}_{x,y}$ can be determined as transport coefficients from this distribution.

The distribution in x-direction is obtained by tracing $\mathcal{P}(y_x, y_y)$ over the y-direction. Analogous, the distribution in y-direction is determined. The n-th momentum of y_i yields

$$\langle y_i^n \rangle = \int y_i^n \mathcal{P}(y_i)\, \mathrm{d}y_i, \tag{6.18}$$

where the diffusion coefficients are related to the growth of the mean-squared displacement $\hat{\sigma}_i^2 = \langle y_i^2 \rangle - \langle y_i \rangle^2$. Due to the symmetry of the dynamics in x- and y-direction the drift $D_i^{(1)}$ vanishes in both directions.

At the top of Figure 6.19, the time evolution of the mean-squared displacement $\hat{\sigma}_i^2$ in x- and y-direction is shown on the basis of numerical data. $\hat{\sigma}_i^2$ grows linearly in time, so that a normal diffusive behavior according to

$$\hat{\sigma}_i = 2D_i^{(2)} t \tag{6.19}$$

can be assumed, where the diffusion constant is given by

$$D_i = \lim_{t \to \infty} \frac{1}{2t} \hat{\sigma}_i. \tag{6.20}$$

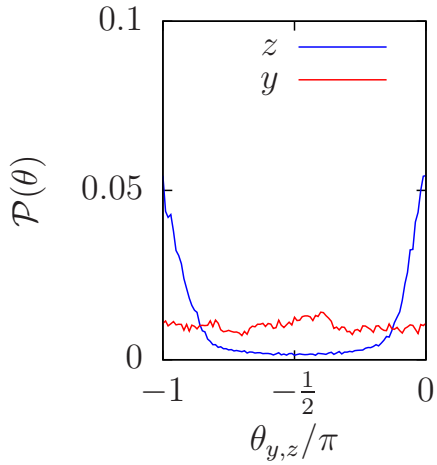

Figure 6.18.: Replot of Figure 6.8 to illustrate the context between diffusion constant $D_i^{(2)}$ and dumbbell rotations.

As reference diffusion coefficient $D_{\text{ref}} = v^2 t$ is defined via the intrinsic velocity $v = \dot{\gamma} a$ and time scale $t = \frac{1}{\dot{\gamma}}$

$$D_{\text{ref}} = \frac{\dot{\gamma}}{a^2}. \tag{6.21}$$

The linear growth of $\hat{\sigma}_i$ is only valid in a range, where the motion of tracer particles in the bulk flow is not influenced by wall effects preventing the tracer particles to penetrate the walls. Therefore, the mixing velocity in terms of the diffusion constant $D_i^{(2)}$ is measured only within the range of a linear growing mean-squared displacement.

It seems surprising that the numerically determined diffusion constants in the two directions do not differ from each other, since the driving forces act only in the x, z-plane and force the dumbbells to flips along the x-direction. That is correct, if the dumbbell is perfectly aligned along the x-axis. When the angle θ_y is enclosed by the dumbbell axis and the x-direction in the x, y-plane, the coupling force $\boldsymbol{f}^p \propto (\cos(\theta_y), \sin(\theta_y, 0)$ forces the dumbbell to flip along this direction $(\cos(\theta_y), \sin(\theta_y), 0)$. Figure 6.18 illustrates the uniform distribution of θ_y. Since the transport of liquid is coulped to the dumbbell rotations, the inhomogenity in x- and y-direction vanishes, although it appears for uncoupled beads, where the diffusion constant in x-direction is always larger than the one along the y-direction.

The rescaled numerically determined diffusion constants for dumbbells and

for uncoupled beads within a variation of the volume fraction Φ are shown in parts *a*) (for the x-direction) and *b*) (for the y-direction) of Figure 6.19. Besides the vanishing inhomogenity the illustrated data points indicate the growth of the diffusion constants with increasing volume fraction, even if the volume fraction $\Phi > \Phi^*$ indicates a semi dilute regime. Once two beads are connected to a dumbbell, the diffusion constant increases again, where the data illustrated for Weissenberg numbers $W = 0.1$ (blue), $W = 1$ (red), and $W = 10$ (magenta) reveal a dependence due to elastic effects.

Even though the Lyapunov exponents (Cf. Section 6.5) and the diffusion coefficients actually measure the same, they have different properties. Thus, statements about the mixing velocity in dependence of Φ, $\hat{R}$, and W can only be made if the diffusion coefficients are considered. What are the conceptual differences?

Actually, the only difference is that the Lyapunov spectrum addresses the stability in the vicinity of a reference trajectory only qualitatively. By re-selecting new neighboring trajectories after an interval Δt, the quantitative analysis of perturbed trajectories inside the entire channel is interupted, although the reference trajectory itself may cover the total channel. In order to detect only the possibility of mixing, this method is adequate. In contrast, the determination of diffusion coefficients addresses to the dynamics of a plurality of such reference trajectories, thus containing information on the mixing velocity. This is the reason, why the Lyapunov spectrum does not change beyond Φ^*, where the mixing velocity in terms of $D_i^{(2)}$ continues to rise. The same applies to the analysis of the diffusion coefficients $D_i^{(2)}$ as a function of the dumbbell length $\hat{R}$, as illustrated in Figure 6.19*c*). A torque acts on each dumbbell yielding the angular momentum $\boldsymbol{L} = \boldsymbol{r} \times \boldsymbol{v}$, i. e., the longer the dumbbell the faster the two beads move during the executed half-turns. Then the tracers near the beads move correspondingly faster, increasing the diffusion constants $D_i^{(2)}$ with increasing $\hat{R}$.

That a more detailed investigation of the mixing properties in dependence of the Weissenberg number W is justified can be seen in Figure 6.19*a*) and Figure 6.19*b*), where the highest diffusion constants $D_i^{(2)}$ are reached for small Weissenberg numbers and thus hard spheres. The data plotted in Figure 6.19*d*) show the diffusion coefficient $D_i^{(2)}$ for a suspension of $N = 60$ dumbbells in

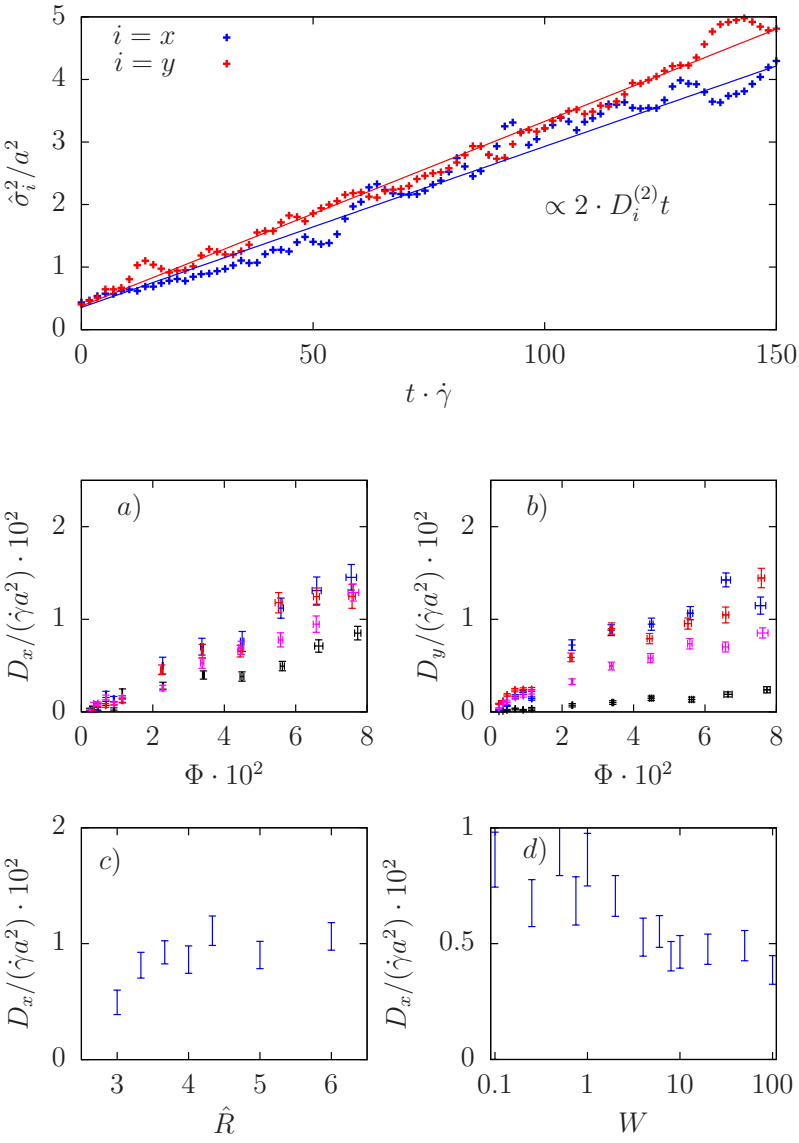

Figure 6.19.: Top: Mean-squared displacement of the tracer distribution in x- and y-direction for a suspension of $N = 90$ dumbbells with $W = 0.1$ and $\hat{R} = 3.33$. The mean-squared displacement grows linearly in time. Bottom: Numerically determined diffusion constants in *a*) x- and *b*) y-direction for $\hat{R} = 3.33$ in dependence of the volume-fraction Φ. The different colors refer to Weissenberg numbers $W = 0.1$ (blue), $W = 1$ (red), and $W = 10$ (magenta). Uncoupled beads are represented by the black data points. *c*) Diffusion constant in dependence of $\hat{R}$ and *d*) illustrates the dependence of $D_i^{(2)}$ on the Weissenberg number.

the range of $W = 0.1$ to $W = 100$. The observation of the decrease in the diffusion coefficient described above is confirmed. Note that the limiting case of uncoupled beads is given by $W = \infty$ and the diffusion constant converges towards the corresponding value of $D^{(2)}$.

Observing large mixing abilities at low Weissenberg number W is a contradictory result to all expectations and experimental observations [67, 69]. One would expect that the mixing rate increases due to the increasing dumbbell deformations, exactly in the opposite direction, before it tends to the limit of uncoupled beads for very large Weissenberg numbers W. With this expectation one tends to forget that the dynamics is overdamped, i. e., the bead-induced flow structures are damped quasi-instantaneously with $1/r^3$, when they are apart by the distance r from the bead. Therefore, the decreasing diffusion coefficient with increasing Weissenberg number confirms the statement that the perturbation are strictly coupled to the dumbbell dynamics since the rotational frequency ν decreases for soft springs.

6.7. Rheology in dumbbell suspensions

Unlike the previous sections, which discussed the destabilizing effects of the dumbbells on the flow field, in this section the rheology of the dumbbell suspension in dependence of the parameters Φ, W, and $\hat{R}$ is investigated. For this purpose, the beads are uniformly distributed in the entire channel, where in the case of dumbbell suspensions in addition the orientations are uniformly distributed. The considered quantity is the time-averaged change of the viscosity $\Delta\bar{\eta}$ (Cf. Eq. (5.21))

$$\Delta\bar{\eta} = \langle \Delta\eta(t) \rangle_t = \left\langle \frac{\eta^{\text{eff}} - \eta_0}{\eta_0} \right\rangle_t , \tag{6.22}$$

resulting from numerical simulations with the Fluid-Particle-Dynamics method.

Einstein has derived the linear dependence of the viscosity η^{eff} on the volume-fraction Φ in the diluted regime [47, 48], which has been extended to a quadratic dependence on Φ^2 by Bachelor and Green [27] as well as Felderhoff and Cichocki [35] for the semi-diluted regime, taking into account the non-negligible

bead-bead interaction

$$\eta^{\text{eff}} = \eta_0 \left[1 + w_1\Phi + w_2\Phi^2 + \mathcal{O}\left(\Phi^3\right)\right]. \tag{6.23}$$

The pre-factors have been determined to $w_1 = 2.5$ [47, 48] and $w_2 = 5.0$ [35] or $w_2 = 5.2$ [27], but it has been shown that in strong confined suspensions of unconnected spheres these pre-factors change [37]. Also the effect of different object shapes on the viscosity was analyzed [75].

According to Eq. (6.23) a linear relation between $\Delta\bar{\eta}$ and the volume-fraction Φ is expected for a dilute suspension of uncoupled spheres. This is validated by varying the number of suspended particles between $m = 4$ and $m = 180$, which correspond to volume-fractions from $\Phi = 0.00230 \pm 0.00002$ to $\Phi = 0.09826 \pm 0.00165$. The relative viscosity change is presented in Figure 6.20 (red). It can be seen that the linear relation $\Delta\bar{\eta} \propto \Phi$ holds up to about $\Phi^* = 0.05$. Beyond Φ^* the effects of hydrodynamic interaction between the beads become stronger, represented within the quadratic term in Φ entering Eq. (6.23). The data-points for suspensions of uncoupled beads are reproduced very well by Eq. (6.23).

In Section 5.4 it was shown that the contribution of a single dumbbell to the viscosity change $\Delta\bar{\eta}$ deviates significantly from the contribution of uncoupled beads only during the passage of configurations perpendicular to the streamlines with $\theta \approx -\frac{\pi}{2}$.

Because these configurations are very rare particularly in the dilute regime, a difference between the effective viscosity $\Delta\bar{\eta}$ can hardly be discerned in Figure 6.20, where $\Delta\bar{\eta}$ is illustrated in dependence of the volume fraction Φ for uncoupled beads (red), dumbbells of length $\hat{R} = 3.33$ (blue), and $\hat{R} = 6.66$ (green).

The increase of the effective viscosity $\Delta\bar{\eta}$, whether as a function of the volume fraction Φ or the Dumbbell length $\hat{R}$, is explicable, if the length l is introduced as

$$l = a\left(\frac{4\pi}{3\Phi}\right)^{\frac{1}{3}}, \tag{6.24}$$

which represents the mean distance of uncoupled beads. For distances $l < l^* = l(\Phi^*) \approx 5.1a$ the hydrodynamic interaction between suspended beads becomes significant so that the first linear increase of $\Delta\bar{\eta} \propto \Phi$ changes to

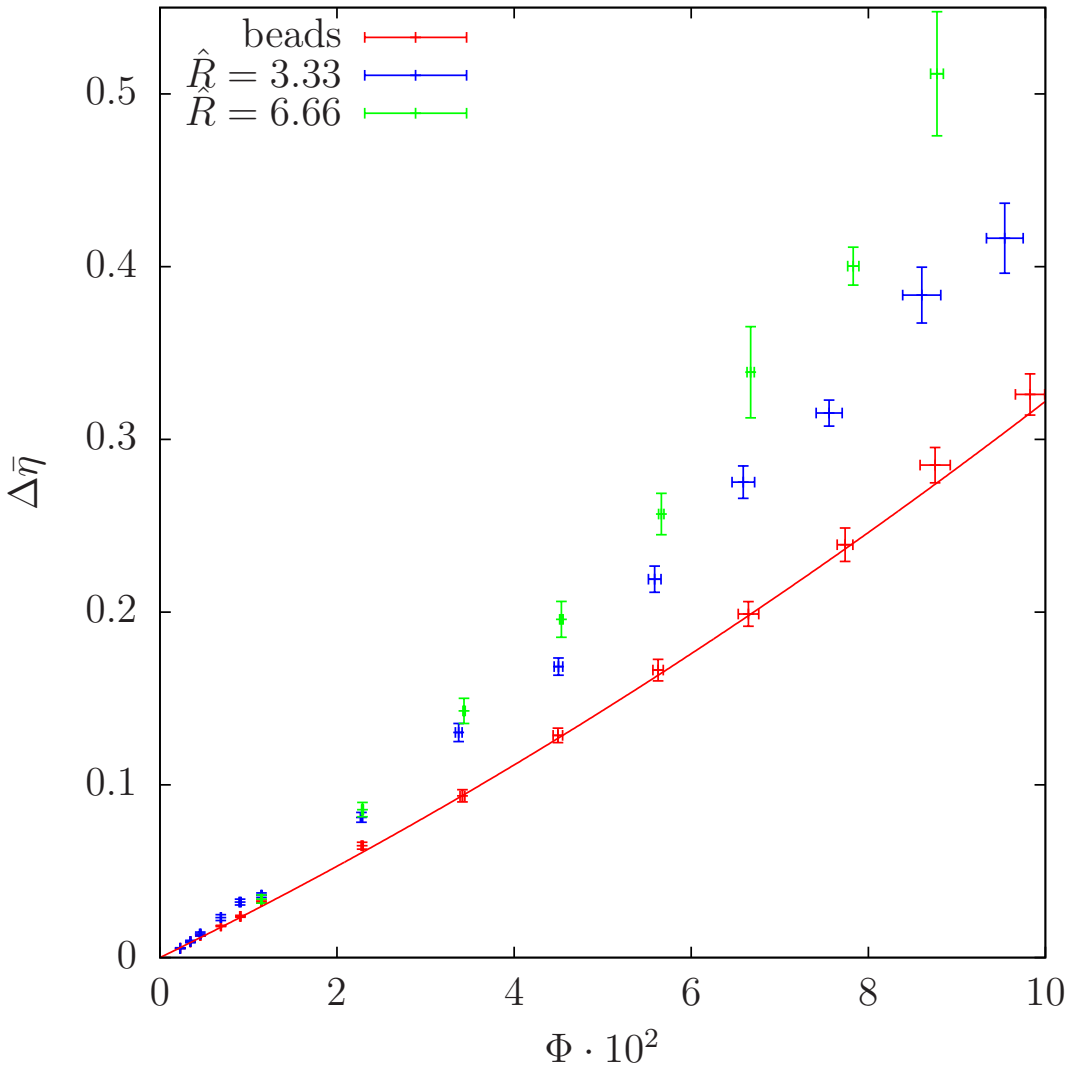

Figure 6.20.: The averaged viscosity $\Delta\bar{\eta}$ as a function of the volume fraction Φ. The red data points represent suspensions of uncoupled beads, where in blue and green suspensions of dumbbells with Weissenberg number $W = 0.1$ are shown. These two series differ in the ratio of dumbbell length to radius $\hat{R} = 3.33$ (blue) and $\hat{R} = 4.33$ (green). The solid line marks the analytical result of Einstein, Bachelor and Green given by Eq. (6.23).

a quadratic dependence of $\Delta\bar{\eta} \propto \Phi^2$ with the known prefactors from [27, 47, 48](Cf. Figure 6.20. In addition, this figure illustrates the increase of the effective viscosity $\Delta\bar{\eta}$ for dumbbells in the semi-dilute regime $\Phi > \Phi^*$ in dependence of their length $\hat{R}$.

On the one hand, this is attributed to the increase of suspended dumbbells, which adopt configurations around $\theta \approx -\frac{\pi}{2}$. On the other hand, the direct coupling forces between the two dumbbell forming beads extend the superposed flow structures around the beads. Since the two respective beads are directly connected within the distance $\hat{R}$, the average distance l, as given in Eq. (6.24), between two beads that influence each other only via the hydrodynamic interaction decreases when $\hat{R}$ becomes large.

Taken together, this means that an increase of the number of suspended particles in terms of Φ, combined with the extension of dumbbells in terms of $\hat{R}$ leads to an increased overlap of flow structures around the dumbbells, which in turn increases the effective viscosity $\Delta\bar{\eta}$ since these structures push reinforced liquid towards the walls, where the effective viscosity is determined. Therefore, the illustrated curves for dumbbellls of length $\hat{R} = 3.33$ (blue) and $\hat{R} = 6.66$ (green) lay clearly above the red reference curve of uncoupled beads. The increase of the contribution to $\Delta\bar{\eta}$ as a function of the relative dumbbell-length $\hat{R}$ is shown in Figure 6.21 in more detail. The illustrated data is obtained for a fixed volume-fraction $\Phi \approx 0.06$. In this example, the contribution is enhanced by about 20 percent as compared to the bead contribution.

In the same manner one can ask how the elasticity of dumbbells in terms of the Weissenberg number W contributes $\Delta\bar{\eta}$. Therefore, on the right side of Figure 6.21, $\Delta\bar{\eta}$ is illustrated for Weissenberg numbers W in the range of $W_{\min} = 0.1$ and $W_{\max} = 100$ for a volume fraction of $\Phi = 0.06$. It is noticeable that the spring elasticity generates two plateaus of $\Delta\bar{\eta}$, one for hard springs and one for soft ones, connected by a transition region around $W \approx 1$ with a decrease of $\Delta\bar{\eta}$ by about 10%. According to Section 5.4 with Figure 5.9 and Figure 5.11,the difference is attributed to the slowdown of dumbbell rotations within an enhancement of the Weissenberg number W. The two plateaus occur due to the following effects:

For small Weissenberg numbers W the dumbbell deformations remain small and relax instantaneously. This ensures that for $W \ll 1$ the liquid transport

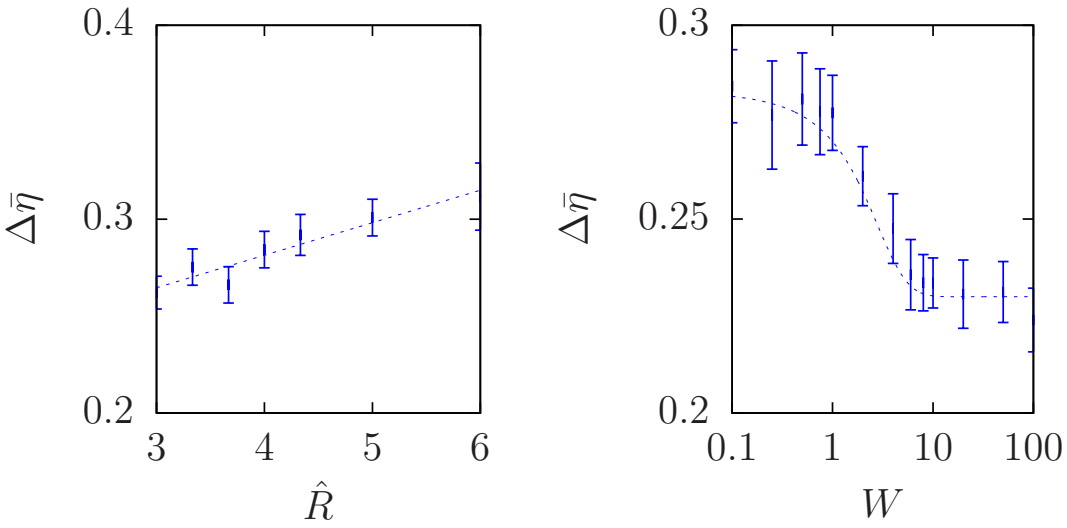

Figure 6.21.: The relative viscosity change $\Delta\bar{\eta}$ as a function of the dumbbell length $\hat{R}$ for fixed $W = 0.1$ (left) and as function of W for fixed $\hat{R} = 4$ (left).

of the dumbbells is executed within a hardly changing effect on the effective viscosity $\Delta\bar{\eta}$. The lack of compensation arises at $W \approx 1$. The two dumbbell beads can more and more be considered as uncoupled objects with increasing Weissenberg number W. The effective viscosity decreases. However, the second plateau obtained by very soft dumbbells $W \gg 1$ provides values of $\Delta\bar{\eta}$, which stay enhanced in comparison to the value of uncoupled beads. That is associated to the FENE-springs (Cf. Eq. (5.2)), which restricts the two beads to a maximum distance independent of the Weissenberg number W. If the bead distance reaches the range of this maximum distance, a torque is generated, which keeps the dumbbell motion across the streamlines alive. Again, a pattern of motion occurs, barely changing within variations of the Weissenberg number W.

6.8. Conclusions and Outlook

In this chapter, the dynamics of a sheared suspension of elastic dumbbells was systematically analyzed using the Fluid-Particle-Dynamics method. In particular, the occurrence of turbulent structures at low Reynolds numbers

was investigated in dependence of the number of suspended particles in terms of the volume fraction Φ, depending on their length $\hat{R}$ and their elasticity expressed by the Weissenberg number W.

It has been found that the time-dependent perturbations, which are necessary for the occurence of turbulence, are given by vortices in the direct vicinity of the beads. Due to the high viscosity in the system, these structures can not detach from the dumbells expressed in the correlation length $\Lambda_i \approx 4a$, which remains on the order of the bead radius a. Nevertheless the flow structures induce an irregular dumbbell dynamics and the system can be considered as turbulent.

There are some similarities between the turbulence presented within this work and inertial turbulence at high Reynolds numbers or elastic turbulence, as it is described in [120, 68, 69]. Here, the effective mixing process should be mentioned, expressed in a positive Lyapunov exponent, but also the decay of the power spectrum $P(\nu)$ following the scaling law

$$P(\nu) \propto \nu^b, \tag{6.25}$$

where $b = -3.5$ indicates the dissipation of energy from fast rotating structures along dumbbell rotations with small frequences. This type of energy conversion occurs in every turbulent system. If one compares this determined exponent with the one occuring within the range of $b = -3.3$ to $b = -3.8$ for elastic turbulence [69, 120], a coincidence of these two types of turbulence is found.

Nevertheless, there are serious differences to both types of turbulence mentioned above. As well as inertial turbulence, the transition to elastic turbulence takes place via subcritical bifurcations. However, the onset of the quantity-dependent turbulence described here occurs suddenly, as mediated by the structural instability of the parallel configuration of a dumbell to the shear lines for $\theta = 0$.

It is astonishing that very small numbers of suspended particles are already sufficient for an unpredictable dynamics. The question is whether the irregularity in the dilute regime is really turbulent, since only a small part of the channel volume in the center is mixed, which takes place also very slowly while the rest of the channel is not affected by the perturbing flow structures. The dilute regime is in any case that regime in which an increase of the irregu-

lar behavior can be observed before the turbulence has fully developed in the semi-dilute regime.

An original question of this work was whether the elastic instability can be reproduced within a simple dumbbell model. The answer to this is clearly no and can be seen either in Figure 6.19, where the mixing of the fluid in dependence of the dumbbell elasticity is analysed within the determination of the diffusion constant $D^{(2)}$, or in Figure 6.21, where the effective viscosity is plotted against the Weissenberg number.

It is not uncommon that the diffusion constant, which is directly coupled to the fluctuations in the velocity field $\tilde{\boldsymbol{u}}$, and the effective viscosity increases simultaneously. It is intuitively clear that a system that underlies higher fluctuations produces a higher resistance expressed in a higher effective viscosity. Mathematically, this is expressed by the so-called Reynolds stress tensor σ_{Re}

$$\sigma_{\mathrm{Re}} = \langle \tilde{\boldsymbol{u}}\tilde{\boldsymbol{u}} \rangle. \tag{6.26}$$

The equivalence of the two variables is not the main point, which consists in the fact that there does not appear a critical Weissenberg number W_c, which seperates an ordered from a turbulent regime as long as the considered suspended particle is a dumbbell. In this kind of suspensions the behavior seems to be reversed to the onset of elastic instabilities described in [69, 120], which indicate the turbulent regime for high Weissenberg numbers W. Therefore, a simple dumbbell is unsuitable to satisfactorily describe elastic instabilities due to the mentioned structural instability. Nevertheless, the simulations have shown that the connection of beads to build elastic particles constitutes a significant difference between the dynamics of coupled and uncoupled beads, where at least the extension of the dumbbells results in an increase in the effective viscosity and the mixing in terms of the diffusion constant $D^{(2)}$. Ultimately, the question remains open whether a minimization of the structural instability allows access to a closer examination of possible elastic instabilities.

Certainly, the dynamics of bead-spring chains is structurally stabilized within the extension to $3, 4, ...$ beads per chain, since the destabilizing effect on a bead in the chain interior is canceled by the interaction with two adjacent spheres. Besides the minimization of structural instabilities, the extension to a chain enables the consideration of additional degrees of freedom, which are related to deflections of the now flexible chain.

Unfortunately, an extension of the chain involves fundamental considerations about the expansion of the simulation range. In this chapter, the simulations took place on a $61 \times 61 \times 61$ grid with mesh size $\delta = 1$. The radius of a bead is $a = 3\delta$ and the usual dumbbell diameter is $r_0 = 10\delta$. An extension around each additional bead extends the suspended object by $r_0 = 10\delta$. The limits of the channel are reached very quickly. One could think about the reduction of the bead radius a, which should not be done for two reasons:

1. A certain radius is required for a accurate resolution of a bead on the grid.

2. Even if the instability is called elastic, the real perturbation is caused by the structures around the beads. In addition, these are reproduced inaccurately when the balloon solution is reduced.

Thus, only an increase of the simulation box will help. For this task one should ask whether there are possibilities to speed up the time-consuming simulation method, since the average time a simulation on the $61 \times 61 \times 61$ box already cost 1.5 weeks.

The last question aimed at minimizing the structural instability of a dumbbell. However, the turbulence described in this work can also be seen as a reference system for shear induced turbulence at low Reynolds numbers. The perturbations of the laminar flow field consist in vortex structures, which result from bead rotations with constant rotation velocities due to the constant shear rate. Not every flow profile generates constant rotational movements within the entire channel range. Thus, the range of excited frequencies by the external flow is broadened as soon as the shear flow is replaced by a pipe flow.

Even though conceptually little will change, since the instability of the dumbbell is maintained, the behavior of the system can quantitatively change expressed,e. g., in the determined power spectrum, mixing properties and the effective viscosity. These changes can also lead to a different behavior depending on the Weissenberg number W and certainly the dumbbell length $\hat{R}$ because a functional dependency of the shear rate $\dot{\gamma}(x)$ on the position x introduces another non-linearity into the system. There are no limits to the introduction of geometrical nonlinearities. For example, with a certain amount of programming effort, the question can be raised about the influence of curved

streamlines on the dynamical behavior inside the channel.

Part II.

Expansion of a cloud of swimmers

7. Forage: A self-diffusve process

Microswimmers like the alga *Chlamydomonas reinhardtii* or the bacterium *Escherichia coli*, which are illustrated in Figure 7.1, are biological examples of swimmers moving at micrometer-scales. In contrast to a human swimmer or fish, using the thrust for an effective locomotion, all inertial effects are damped quasi instantaneously. According to [131], an E. coli bacterium comes to the scale of 10^{-10}m as soon as it stops the propulsion. This leads to some conceptional differences in the dynamics the swimmers perform implying fluid motions.

As a living object, a biological microswimmer is dependent on an effective foraging. The alga C. reinhardtii produces food by means of photosynthesisis. Each cell has an eyespot that enables the cell to detect light from outer light sources. Such a source represents a preferred direction of movement and the propulsion along this direction is called *phototaxis* [154]. The bacterium E. coli is able to detect chemical gradients via a sensoric system enabling the cell to provide *chemotaxis* [22, 23].

In fact, every living swimmer follows an outer gradient for foraging, where also magnetotaxis is observed. The search for food follows the same principles independent on the specific swimmer type. The cell provides propulsion within an intrinsic duration τ, where it covers a distance $l_0 = v_0\tau$ called persistence length with v_0 being the mean velocity of the swimmer. After this "run" the swimmer uses the eyespot or sensors to measure its orientation towards the light source or chemical gradient. Subsequently, a descision is made whether the swimmer changes the direction completely within a reorientation process, when disadvategeous areas are reached, or it maintains more or less its direction of motion with only small deviations around the preferred direction of the detected gradient.

The propulsion together with the reorientation lead to a random walk of each

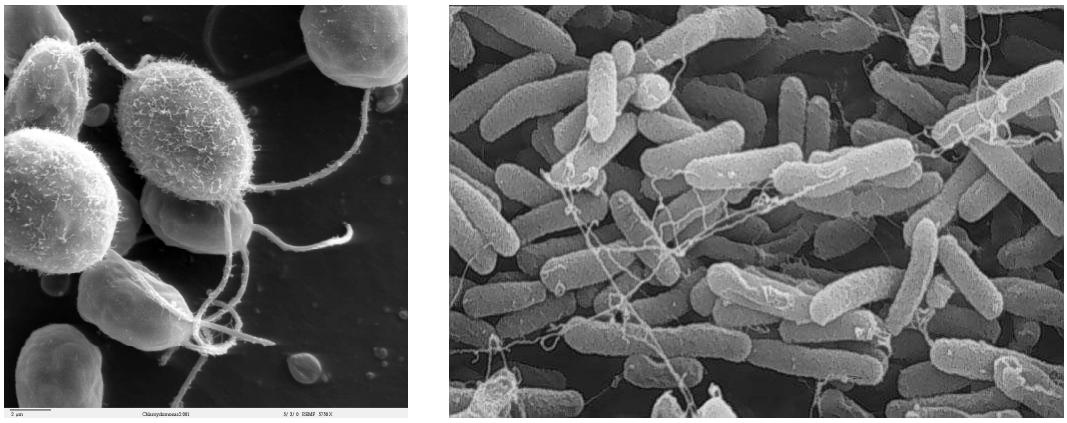

Figure 7.1.: Replot of Figure 1.3 illustrating *Chlamydomonas reinhardtii* (left) [3] and *Escherichia cioli* (right) [4].

swimmer, where in contrast to thermal diffusion the forage-induced random walk does not obey a fluctuation-dissipation theorem determining the strength of noise due to its dependence of inner-celular decisions, which take a small amount of time. In the model reorientations are assumed to happen instantaneously. Instead, the fluctuations depend on specific parameters, which may vary from swimmer to swimmer. These are the velocity v_0 and reorientation time τ, but also angles θ enclosed by the orientation $\boldsymbol{e}_r$ of a swimmer and a preferred axis $\hat{\boldsymbol{e}}_z$ and ϕ enclosed by the old $\boldsymbol{e}_r$ and new $\boldsymbol{e}_r$ direction of motion influence the diffusive dynamics of the swimmer.

In this chapter the propulsive dynamics of the swimmer is described before the diffusive contribution to the displacement of isolated, non-hydrodynamically interacting swimmers is discussed.

7.1. Equations of motion in the low Reynolds number regime

The dynamics of an incompressible fluid is described by the Navier-Stokes equation along with the incompressibility condition

$$\rho\left(\partial_t \boldsymbol{u}(\boldsymbol{x},t) + \boldsymbol{u}(\boldsymbol{x},t)\cdot\nabla\boldsymbol{u}(\boldsymbol{x},t)\right), \;=\; -\nabla p(\boldsymbol{x},t) + \eta\nabla^2\boldsymbol{u}(\boldsymbol{x},t) + \boldsymbol{F} \quad (7.1)$$

$$\nabla\cdot\boldsymbol{u}(\boldsymbol{x},t) \;=\; 0, \quad (7.2)$$

where $\boldsymbol{u}(\boldsymbol{x},t)$ denotes the local flow field, $p(\boldsymbol{x},t)$ is the pressure and $\boldsymbol{F}$ refers to the outer forces. ρ and η represent the constant fluid density and dynamic viscosity. The introduction of appropriate characteristic length scale L and velocity U as well as time $T = L/U$ yields the rescaled dimensionless Navier-Stokes equation

$$\mathrm{Re}\left(\partial_{t'}\boldsymbol{u}' + \boldsymbol{u}'\cdot\nabla'\boldsymbol{u}'\right) = -\nabla' p' + \nabla'^2\boldsymbol{u}' + \boldsymbol{F}' \tag{7.3}$$

with the Reynolds number $\mathrm{Re} = \frac{\rho}{\eta}UL$. The occuring effects in the dynamics of a fluid can be attributed either to inertial effects due to the nonlinear advective term $\boldsymbol{u}\cdot\nabla\boldsymbol{u}$ or friction in terms of $\nabla^2\boldsymbol{u}$. The Reynolds number measures the importance of inertial contributions against friction.

A CR-cell consists of a nearly spherical cell body of radius $a \approx 1\mu$m. Using the values $U \approx 120\mu$m for the swimming velocity, $\rho = 1000\mathrm{kg/m}^3$ for the density, and $\eta = 10^{-3}\mathrm{kg/m\ s}$ for the viscosity of water at 20°C, one can determine a value of the Reynolds number of $\mathrm{Re}_{CR} \approx 10^{-4} \ll 1$. In this case, the partial derivative ∂_t and the advective term $\boldsymbol{u}\cdot\nabla\boldsymbol{u}$ on the left hand side of Eq. (7.1) can be neglected and Eq. (7.1) can be replaced by the linear and time-independent Stokes equation

$$0 = -\nabla p + \eta\nabla^2\boldsymbol{u} + \boldsymbol{F}. \tag{7.4}$$

Since Eq. (7.4) is time-independent, it is also symmetric under time-reversal. For swimming at low Reynolds numbers that directly implies that if a swimmer departs its propelling stroke into a forward and backward motion, which only differ in their direction of execution, it would reach the initial position after a full stroke. In other words, a scallop that can swim at high Reynolds numbers by opening and closing the two shells, using the inertial rebound, only generates an oscillatory but no directed motion at low Re. This fact is known as the scallop theorem [131]. Additional degrees of freedom are required to break the time-reversal symmetry. Purcell has presented three linked elements that are able to propagate [131]. There are a variety of concepts that lead to an effective propulsion, which may be based on three spheres [116] or the variation of sphere sizes [135]. Further concepts of swimming in the low Re regime are presented in [104]. Brenner:1981 The linearized Stokes equation Eq. (7.4) can be solved analytically for an unbounded system [75]:

$$\boldsymbol{v}(\boldsymbol{x}) = \int \mathcal{H}(\boldsymbol{x}-\boldsymbol{x}')\cdot\boldsymbol{F}(\boldsymbol{x}')\,\mathrm{d}^3\boldsymbol{x}'. \tag{7.5}$$

with $\mathcal{H}(\boldsymbol{r})$ denoted as the Oseen tensor [119]

$$\mathcal{H}_{ij} = \frac{1}{8\pi\eta r}\left(\delta_{ij} + \frac{r_i r_j}{r^2}\right) \qquad \text{for} \quad i \neq j \tag{7.6}$$

and the diagonal elements

$$\mathcal{H}_{ij} = \frac{1}{6\pi\eta a}. \tag{7.7}$$

This tensor mediates the hydrodynamic interaction (HI) between the points $\boldsymbol{x}'$, where the force $\boldsymbol{F}$ acts on the fluid and the point $\boldsymbol{x}$, where this force generates a velocity perturbation $\boldsymbol{v}(\boldsymbol{x})$. Eq. (7.6) shows a slow decay with $1/r$ so that the HI is long-ranged.

7.2. Forces generated by a flagellum

The main strategy microswimmers use to break the time-reversal symmetry of Eq. (7.4) relies on the anisotropic friction coefficents $\zeta_\parallel$ and $\zeta_\perp$ of a long rod, pulled through the surrounding liquid with a force $\boldsymbol{F} = F\hat{\boldsymbol{e}}$ parallel ($\parallel$) or perpendicular ($\perp$) to the rod-axis.

This rod may be partitioned in a chain of touching spheres with radius a [40]. For the i-th sphere the equation of motion can be written as

$$\dot{\boldsymbol{x}} = \frac{\boldsymbol{F}_i}{\zeta} + \sum_{i \neq j} \mathcal{H}(\boldsymbol{x}_i - \boldsymbol{x}_j) \cdot \boldsymbol{F}_j. \tag{7.8}$$

In the continuum limit, where $s \in [-L/2; L/2]$ denotes the contour line along the rod, this equation can be rewritten [72]

$$\dot{\boldsymbol{x}}(s) = \frac{1}{3\pi\eta}\boldsymbol{f}(s) + \int \mathcal{H}(\boldsymbol{x}(s) - \boldsymbol{x}(s') \cdot \boldsymbol{f}(s')\,\mathrm{d}s', \tag{7.9}$$

where $\boldsymbol{f}(s) = \frac{F}{L}\hat{\boldsymbol{e}}$ is the force-density along the rod axis. Mechanisms in which individual spheres crystalize to rods are called *shish kebab models* in the polymer science [74, 153].

Now the friction coefficients for the motion of the rod parallel and perpendicular to its axis are defined as

$$\boldsymbol{F} = \zeta_\parallel \boldsymbol{v}_\parallel + \zeta_\perp \boldsymbol{v}_\perp. \tag{7.10}$$

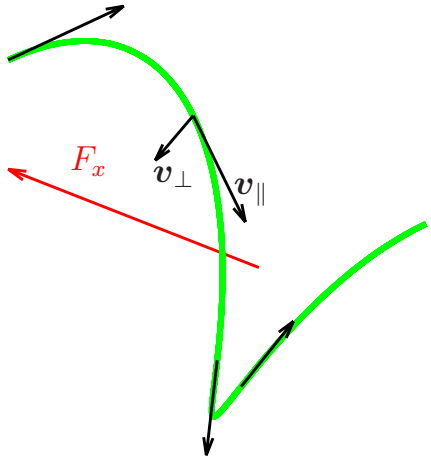

Figure 7.2.: A helical shaped fagellum generates a force parallel to the direction of motion with help of anisotropic friction coefficient parallel and perpendicular to the rod axis.Perpendicular conributions average out

To calculate the two coefficents $\zeta_\parallel$ and $\zeta_\perp$ from Eq. (7.9) the special case of a rod situated along the x-axis is considered. The averaged rod velocity $\boldsymbol{v}_{\text{rod}} = \frac{1}{L}\int \dot{\boldsymbol{x}}\,\mathrm{d}s$ is then given by

$$\boldsymbol{v}_{\text{rod}} = F\left(\frac{\hat{\boldsymbol{e}}}{3\pi\eta L} + \frac{\hat{\boldsymbol{e}} + (\hat{\boldsymbol{e}}_x\cdot\hat{\boldsymbol{e}})\hat{\boldsymbol{e}}_x}{4\pi\eta L^2}\int_{2a}^{L}\frac{L-s}{s}\,\mathrm{d}s\right). \tag{7.11}$$

To prevent self-interaction the integral is cut off below $s < 2a$, corresponding to the diameter of the rod.

The scalar product equals $\hat{\boldsymbol{e}}_x\cdot\hat{\boldsymbol{x}} = 1$ for a parallel drag force and $\hat{\boldsymbol{e}}_x\cdot\hat{\boldsymbol{x}} = 0$ in perpendicular direction, so that the pre-factors differ by a factor of two, i. e.,

$$\zeta_\perp = \frac{4\pi\eta L}{\ln(L/2a)}, \quad \zeta_\perp = 2\zeta_\parallel. \tag{7.12}$$

On the right hand side of Figure 7.1 a EC-bacterium is shown. This type of swimmer rotates its flagella counterclockwise. Thereby all flagella form a helix and synchronize to a bundle leading to the propulsion. The motorprotein forces the flagellum to rotate around the helix axis so that each flagellum can be described by a propagating wave with

$$\boldsymbol{x} = [x, A\sin(kx-\omega t), A\cos(kx-\omega t)] \tag{7.13}$$

with amplitude A, frequency ω, and wave number k. A segment of the rod at position x then moves with the velocity $\boldsymbol{v}(x)$

$$\boldsymbol{v} = \partial_t \boldsymbol{x} = A\omega \left[(0, -\cos(kx - \omega t), \sin(kx - \omega t)\right]. \tag{7.14}$$

The local tangent vector $\boldsymbol{t}$ is given by

$$\boldsymbol{t} = [(1, Ak\cos(kx - \omega t), -Ak\sin(kx - \omega t))] \tag{7.15}$$

where the velocity can be split in $\boldsymbol{v}_\parallel = \frac{(\boldsymbol{v}\cdot\boldsymbol{t})}{t}\hat{\boldsymbol{t}}$, and $\boldsymbol{v}_\perp = \boldsymbol{v} - \boldsymbol{v}_\parallel$, with the parallel component given by

$$\boldsymbol{v}_\parallel = -\frac{A^2\omega k}{1 + A^2k^2}\hat{\boldsymbol{t}} \tag{7.16}$$

with the unit tangent $\hat{\boldsymbol{t}} = \frac{\boldsymbol{t}}{t}$. According to Eq. (7.10) the force F_x generated along the direction of swimming is obtained by averaging Eq. (7.16) along the helix axis

$$F_x = \frac{\zeta_\parallel - \zeta_\perp}{L} \int \frac{A^2\omega k}{1 + A^2k^2}\,\mathrm{d}x. \tag{7.17}$$

The perpendicular force contributions vanish, so that F_x is the net force of propulsion executed by a flageullum (Cf. Figure 7.2. For small amplitudes A, the integral yields

$$F_x = \frac{1}{2}(\zeta_\parallel - \zeta_\perp)A^2\omega k. \tag{7.18}$$

The result of Eq. (7.18) presented here differs from the reality, since non-linear shapes of the flagellum especially at small distances x to the cell body are neglected, where the flagellum is anchored. Nevertheless, it shows the importance of $\zeta_\perp \neq \zeta_\parallel$ for an effective propulsion at low Reynolds numbers. In addition, Eq. (7.18) shows some intuitive results on swimming, where the generated force is enhanced linearly with increasing frequency ω of flagella rotations and wave number k of helical whorls of the flagellum and quadratic with increasing amplitude of the propagating wave [104, 49]. Also the alga Chlamydomonas reinhardtii uses the difference between $\zeta_\parallel$ and $\zeta_\perp$ for purposes of propulsion even if their stroke resembles that of the human breast stroke. The generation of forces during this movement pattern is described in [21].

7.3. Force-dipoles and velocity of isolated swimmers

Most swimmers in the low Reynolds number regime move autonomously, i. e., they generate the acting forces, e. g., by the beat of a flagellum with a propagating helical wave. Thereby the averaged force $\boldsymbol{F}(\boldsymbol{x}+\boldsymbol{p}) = -F_0\hat{\boldsymbol{e}}$ acts at a distance $\boldsymbol{p} = p_0\hat{\boldsymbol{e}}$ from the cell nucleus, pulling or pushing in the direction of motion. This force is balanced by the drag force $\boldsymbol{F}(\boldsymbol{x}) = F_0\boldsymbol{e}$ acting on the cell nucleus at $\boldsymbol{x}$.

Ultimately, the driving motor forces and friction generate a force-dipole $F_0\boldsymbol{p}$ with a net-force of zero on the cell-body [87, 104]. In the biological word two types of dipolar swimmers can be observed, where experimental confirmations on the generated flow-field were provided for E. coli and C. reinhardtii by Dresher et. al [45, 44]. The far-ranging flow field is illustrated in Figure 7.3 and looks similar for both types of a force dipole. The main difference is the flow direction, where for a puller in the direction of motion $\hat{\boldsymbol{e}}$ an attractive flow occurs, whereas, in the perpendicular direction the flow is pushed away leading to repulsion. For pushers the situation is reversed.

Mathematically one obtains the dipolar flow field from the Oseen tensor Eq. (7.6). With a dipole of strength $D = F_0 p$ located arround $\boldsymbol{x}_0 \pm \frac{1}{2}\boldsymbol{p}$ one obtains the fluid velocity $\boldsymbol{v}(\boldsymbol{x})$ at the position $\boldsymbol{x}$

$$\boldsymbol{v}(\boldsymbol{x}) = \frac{D}{8\pi\eta r^2}\left(-1 + 3(\hat{\boldsymbol{e}}_r \cdot \hat{\boldsymbol{e}})^2\right)\hat{\boldsymbol{e}}_r \tag{7.19}$$

after an expansion to order p/r with $r = |\boldsymbol{x} - \boldsymbol{r}_0|$ and $\hat{\boldsymbol{e}}_r = \boldsymbol{r}/r$. In contrast to a monopolar flow field, which decays as $1/r$, the dipolar field decays faster with $1/r^2$ from the center of the dipole.

On the one hand, the force-dipole yields the propagation, on the other hand the long-range behavior of the generated flow field superposes with the self-generated velocity. This hydrodynamic interaction leads to collective effects in the dynamics of several micro-swimmers, where the different directions of the flow around pushers and pullers yield some characteristic differences, which are discused in Chapter 8

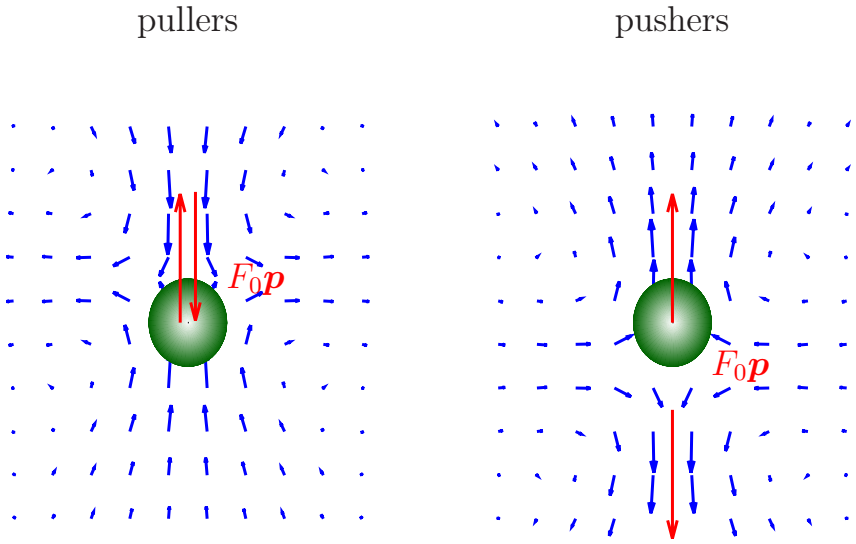

Figure 7.3.: left: Flow field generated by a puller. The force dipole attracts fluid from the front and back. This water flows away perpendicular to the orientation (Blue arrows). Right: pushers attract fluid from besides the swimmer, which is pushed away in the direction of orientation.

Propagation with force dipoles

As observable we choose a characteristic point $\boldsymbol{x}$ of the swimmer, such as the center of the spherical cell-body. If this is pulled or pushed with a constant force $F_0\hat{\boldsymbol{e}}$ through the surrounding liquid, it moves with the constant velocity $\boldsymbol{u}_x = F_0/(6\pi\eta a)\mathcal{I}\cdot\hat{\boldsymbol{e}}$, where a denotes the radius. But the motor force $-F_0\hat{\boldsymbol{e}}$ generated within a distance $\boldsymbol{p} = p\hat{\boldsymbol{e}}$ with $p > a$ from the cell enters into the equation of motion via the Oseen tensor Eq. (7.6). The swimmer, no matter if a pusher or puller then moves with the constant velocity

$$\dot{\boldsymbol{x}} = \boldsymbol{v}_0 = \frac{(2-3\frac{a}{p})F_0}{12\pi\eta a}\hat{\boldsymbol{e}}. \tag{7.20}$$

For $p = 2a$ we obtain

$$\boldsymbol{v}_0 = \frac{F_0}{24\pi\eta a}\hat{\boldsymbol{e}}. \tag{7.21}$$

The propulsion in the force-dipole model with vanishing net force is thus realized by the different mobility matrices coupling the two forces to the cell-body.

Far field and hydrodynamic interaction between two swimmers

Considering the dynamics of several swimmers one swimmer i moves in the flow field generated by all other ones $j \neq i$. The equation of motion for the i-th swimmer then reads

$$\boldsymbol{x}_i = \boldsymbol{v}_{0,i} + \tilde{\boldsymbol{v}}_i, \tag{7.22}$$

where $\tilde{\boldsymbol{v}}_i$ contains the perturbed hydrodynamic interaction, given by all other swimmers [165]

$$\tilde{\boldsymbol{v}} = \sum_{j \neq i} \mathcal{H}_t(\boldsymbol{x}_i - \boldsymbol{x}_j) \cdot \boldsymbol{F}_j - \sum_{j \neq i} \mathcal{H}_t(\boldsymbol{x}_i - \boldsymbol{x}_j - \boldsymbol{p}_j) \cdot \boldsymbol{F}_j, \tag{7.23}$$

with the force $\boldsymbol{F}_j$ generated by the j-th swimmer and $\mathcal{I}$ denoting the identity matrix. In the mobility matrix $\mathcal{H}_t(\boldsymbol{\varrho})$ the Oseen tensor Eq. (7.6) is replaced by the Rotne-Prager tensor given by

$$\mathcal{H}_t = \begin{cases} \frac{1}{8\pi\eta\varrho}\left(\left(1+\frac{2a^2}{3\varrho^2}\right)\mathcal{I} + \left(1-\frac{2a}{\varrho^2}\right)\frac{\boldsymbol{\varrho}\boldsymbol{\varrho}}{\varrho^2}\right), & \text{for} \quad \varrho > 2a \\ \frac{1}{6\pi\eta a}\left(\left(1-\frac{9\varrho}{32a}\right)\mathcal{I} + \frac{3\varrho}{32a}\frac{\boldsymbol{\varrho}\boldsymbol{\varrho}}{\varrho^2}\right) & \text{for} \quad \varrho < 2a. \end{cases} \tag{7.24}$$

This tensor bypasses the singularities for $\varrho \to 0$ occuring in the Oseen-tensor by treating the cases $\varrho > 2a$ and $\varrho < 2a$ seperately. In the limit $\varrho \to 0$ this tensor reaches the matrix with the Stokes-friction coefficient in the diagonal entries.

When an isolated swimmer moves with constant velocity in a specified direction of motion $\hat{\boldsymbol{e}}$, the forces $\boldsymbol{F}$ generated by other swimmers at a distance $\boldsymbol{r}$ generate a torque $\boldsymbol{T}$ acting on the considered swimmer

$$\boldsymbol{T} = \boldsymbol{\varrho} \times \boldsymbol{F}. \tag{7.25}$$

These torques induce a swimmer rotation at an angular velocity $\boldsymbol{\omega} = \dot{\theta}\hat{\boldsymbol{e}}$ and the oientation of a swimmer alters according to

$$\dot{\hat{\boldsymbol{e}}} = \boldsymbol{\omega} \times \hat{\boldsymbol{e}}. \tag{7.26}$$

There is a Rotne-Prager tensor, which connects the torque $\boldsymbol{T}$ to the angular velocity $\boldsymbol{\omega}$ via $\boldsymbol{\omega} = \mathcal{H}_r \cdot \boldsymbol{T}$. This Rotne-Prager tensor for rotations can be written as [165]

$$\mathcal{H}_r = \begin{cases} -\frac{1}{16\pi\eta\varrho^3}\left(\mathcal{I} - 3\frac{\boldsymbol{\varrho}\boldsymbol{r}}{\varrho^2}\right), & \text{for} \quad \varrho > 2a \\ \frac{1}{8\pi\eta a^3}\left(\left(1-\frac{27\varrho}{32a}+\frac{5\varrho^3}{64a^3}\right)\mathcal{I} + \frac{9\varrho}{32a} - \frac{3\varrho^3}{64a^3}\frac{\boldsymbol{\varrho}\boldsymbol{\varrho}}{\varrho^2}\right) & \text{for} \quad \varrho < 2a. \end{cases} \tag{7.27}$$

In Figure 7.3 the two different types of propelling force-dipoles of a *pusher* and *puller* are shown. The blue vectors indicate the direction and strength of the flow field in the surrounding fluid. The two force-dipoles only differ in the position of the propelling force in the front or in the back. This small difference leads to a quite different dynamical behavior within a suspension of interacting swimmers. The flow field around pushers cause a particle-particle attraction perpendicular to the swimming direction and they repell each other in the direction of motion. This attractive effect ensures a stable collective movement of swimmers moving in parallel directions leading to clustering. This strong impact of the hydrodynamic interaction is not found in the case of pullers, where the situation is reversed. The repulsive flows perpendicular to the direction of motion favour an isolated single particle dynamics of quasi-non-interacting swimmers.

7.4. Modeling the diffusive swimmer dynamics

A biological swimmer needs energy for the propulsive motion and to keep alive. For example, the alga Chlamydomonas is able to perform photosynthesis [169]. For finding optimal light-flooded places, an eyspot enables the cell to detect intensity gradients of the irradiating light. Cells like E. coli or B. subtilis perform chemotaxis in a similar way with the help of detectors for chemical gradients inside the cell membrane [23]. It is also known that there are bacteria, which detect magnetic fields for foraging [39]. The phenomenology of the resulting motions of phototaxis, chemotaxis, and magnetotaxis etc. is the same:

The cell moves in one direction $\boldsymbol{e}_i$ within a *run*. After the run it detects the increase or decrease of, e. g., the nutrient concentration. If the concentration decreases, the swimmer decides to initiate a sequence of flagella motions to change its orientation in arbitrary direction. This process is called *tumbling*. For E. coli the different states of motion during the tumbling stte have been investigated by Darnton et al. [36]. Elsewise the swimmer holds its direction of motion.

The phenomenon of chemotaxis can be described by a set of partial differential equations for the cell density and concentration of chemicals [96]. In

this model the generation and destruction rates of nutrients, as well as the diffusivity and mortality rate of the cells can be considered. What this model does not consider, is the hydrodynamic interaction between the cells. In order to describe the impact of hydrodynamic particle-particle interaction on chemo- or phototactic cells, in this section the diffusive dynamics of swimmers is analysed by replacing the swimmer density by a particle-based description of the dynamics. Chemo- or phototactic effects are taken into account by limiting the reorientation range of each swimmer within specified distributions. First, the dynamics is analysed without taking into account the hydrodynamic particle-particle interaction.

The dynamics of $N = 500$ swimming objects with spherical cell-body with radius a at the positions $\boldsymbol{x}_i(t)$ are described by Eq. (7.22), where hydrodynamic interaction $\tilde{\boldsymbol{v}}$ is not taken into account for the first. Then the dynamics of each swimmer reduce to the motion of a sphere with radius $a = 1$ with constant velocity $v_0 = 10$ towards the orientation vector $\hat{\boldsymbol{e}}_i$ if not stated otherwise

$$\dot{\boldsymbol{x}}_i = v_0 \hat{\boldsymbol{e}}_i. \tag{7.28}$$

The isolated swimmers perform a movement without any variation of orientation within one run of duration τ. It has been found experimentally that this time is exponential distributed

$$\mathcal{P}(\tau) = \frac{1}{\bar{\tau}} \exp\left\{-\frac{\tau}{\bar{\tau}}\right\} \tag{7.29}$$

with the averaged run time $\bar{\tau}$. This averaged time represents one system parameter and may vary between $\bar{\tau}_0 = 5\,\mathrm{d}t$ and $\bar{\tau} = 10,000\,\mathrm{d}t$ in the presented simulations with the time step of integration $\mathrm{d}t = 10^{-3}$. A C. reinhardtii cell with $a = 0.5\,\mu$m moves with $v_0 \approx 120\,\mu\frac{\mathrm{m}}{\mathrm{s}}$, i. e., one swimmer propagates its diameter within $\tau_0 = a/v_0 \approx 0.1\,\mathrm{s}$. This time τ_0 can be defined as a second characteristic time, where a swimmer can be influenced by deterministic effects such as the hydrodynamic interaction. As dimensionless parameter the ratio between τ_0 and $\bar{\tau}$ measuring deterministic against diffusive effects

$$R_\tau = \frac{\tau_0}{\bar{\tau}} \tag{7.30}$$

is defined. Note that shortening the runtime $\bar{\tau}$ results in an increase of R_τ. The shorter the time $\bar{\tau}$, the more often reorientations take place. This means

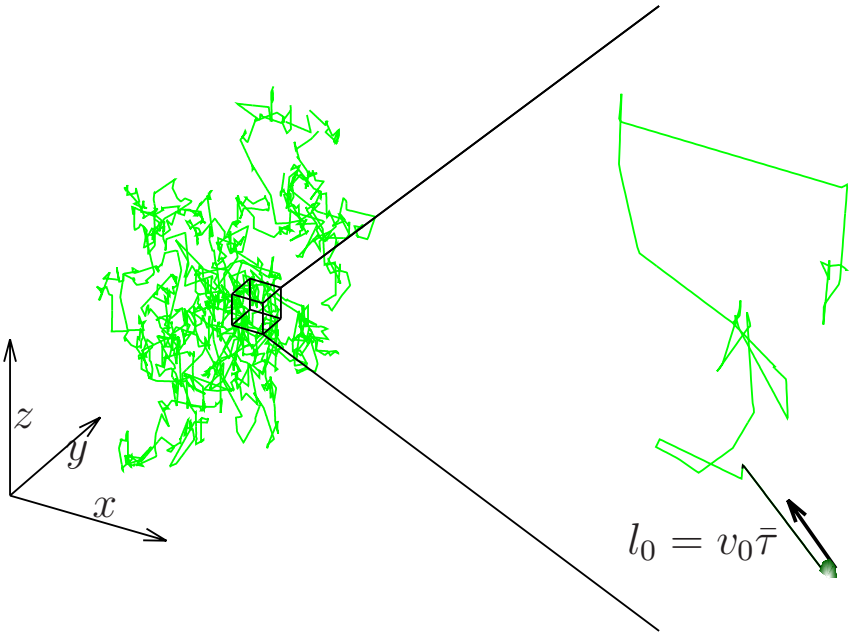

Figure 7.4.: Illustration of a random-walk with persistence length l_0 performed by a swimmer of velocity v_0. The random swimmer reorients after an average the time $\bar{\tau}$.

that the higher this ratio R_τ, the more diffusive is the character of the described dynamics. C. reinhardtii cells reorient on average every second, so that $R_\tau(CR) \approx 10$, i. e., a swimmer covers the persistence length $l_0 = 20\,a$ within one run (cf. Figure 7.4).

After each run a tumble is executed within a comparatively short time. In this work it is assumed that these reorientations occur instantaneously. For an equal distribution of new orientations $\boldsymbol{e}_i(t')$ with $t' > t$ the mean orientation $\langle \boldsymbol{e}_i \rangle$ and correlation $\langle \boldsymbol{e}_i(t) \cdot \boldsymbol{e}_j(t') \rangle$ can be assumed as

$$\langle \hat{\boldsymbol{e}}_i \rangle = 0 \tag{7.31}$$

and

$$\langle \boldsymbol{e}_i(t) \cdot \boldsymbol{e}_j(t') \rangle = \delta_{ij} \exp\left\{ -\frac{|t - t'|}{\bar{\tau}} \right\}. \tag{7.32}$$

By these reorientations a random-walk is generated, yielding a self-driven diffusive dynamics of the swimmers. Self-driven means that the reorientation is not driven by thermal fluctuations, driving the diffusion in terms of a fluctuation-dissipation theorem, where fluctuationing forces $f(t)$ entering a

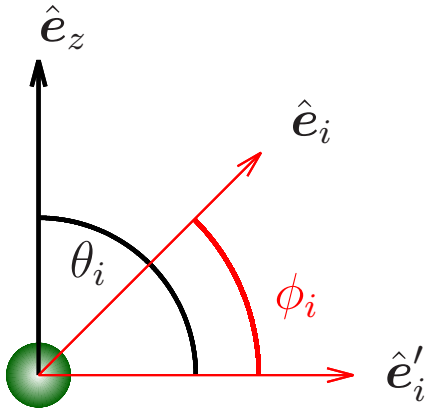

Figure 7.5.: The two angles θ_i and ϕ_i determining the new direction of motion.

Langevin equation

$$m\ddot{x}(t) + 6\pi\eta a\dot{x}(t) + f(t) \tag{7.33}$$

measured in terms of the temperature T are coupled to the fluctuating force $f(t)$ via the dissipation-fluctuation-theorem

$$\langle f(t)f(t')\rangle = \frac{2kT}{\eta}\delta(t-t') \tag{7.34}$$

with the Boltzmann constant k and viscosity η. Such a theorem does not exist for the present swimmer dynamics. The diffusivity depends rather on intrinsic quantities like the velocity v_0, the running time τ_0 and the distribution of adopted angles within the reorientation.

The reorientation changes the old orientation of the i-th swimmer $\hat{\boldsymbol{e}}_i = \hat{\boldsymbol{e}}_i(t)$ to a new direction of motion $\hat{\boldsymbol{e}}'_i = \hat{\boldsymbol{e}}_i(t')$ with $t' > t$. As illustrated in Figure 7.5 two angles θ_i and ϕ_i are defined. θ_i denotes the angle between the orientation of a swimmer $\hat{\boldsymbol{e}}_i$ and a prefered direction of motion $\hat{\boldsymbol{e}}_z$, in which the concentration of nutrients increases or in which a light source is positioned. ϕ_i denotes the angle between the old ($\hat{\boldsymbol{e}}'_i$) and new ($\hat{\boldsymbol{e}}_i$) direction of motion.

The reorientations happen quickly and in the simulations they are assumed to take place instantaneously. it is possible that within the short time of the biological process a swimmer can not reach every angle on the unit sphere. The furthest possible angle between the new and old direction $\hat{\boldsymbol{e}}_i$ and $\hat{\boldsymbol{e}}'_i$ of motion is given by $\phi_0 = \pi$. Then the swimmer would continue propelling in opposite direction. The parameter $\alpha \in [0;1]$ is defined as $\phi_{\max} = \alpha\pi$, where

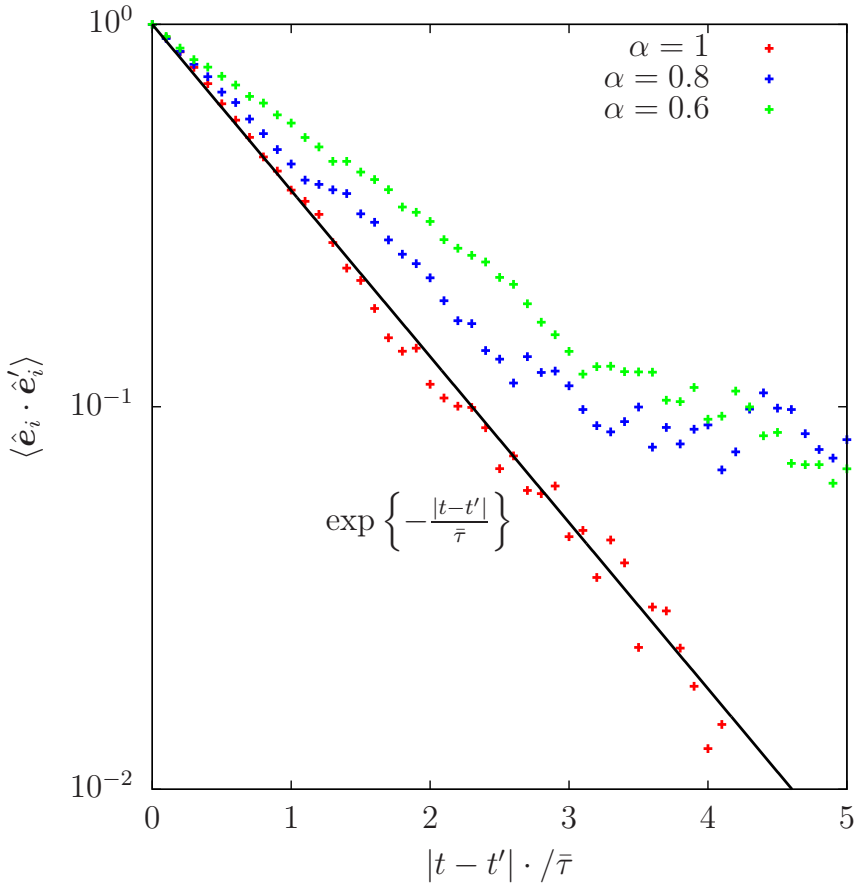

Figure 7.6.: The autocorrelation-function $\langle \hat{\boldsymbol{e}}_i \cdot \hat{\boldsymbol{e}}'_i \rangle$ for several values of α.

$\phi_{\max}$ denotes the maximum angle that can be covered within one reorientation. The angle ϕ_i is assumed to be equally distributed between $\phi_i = 0$ and $\phi_i = \alpha\pi$ in the simulations. $\alpha = 1$ means that the swimmer might reorient on the whole unit sphere, whereas $\alpha = 0$ means in fact no reorientation and thus diffusion.

Up to this point the modeling has been described that enters directly the simulation of the dynamics of a number of $N = 500$ micro-swimmers. Since two simulations can differ from each other due to the stochasticity of the reorientations, it is useful to provide a statistical description of the directions $\hat{\boldsymbol{e}}_i$. It is possible to make analytical statements on the statistical moments of $\boldsymbol{e}_i$ similar to the analytical solving of a Langevin equation [137].

Each swimmer moves towards its initial direction of motion, where this direction is arbitrary. Figure 7.6 shows that the parameter α enters the exponential correlation-function

$$\left\langle \hat{\boldsymbol{e}}_i \cdot \hat{\boldsymbol{e}}'_j \right\rangle = \delta_{ij} \exp\left\{ -\frac{\alpha|t - t'|}{\tau_0} \right\} \tag{7.35}$$

and prolongs the time where the orientations $\hat{\boldsymbol{e}}_i$ and $\hat{\boldsymbol{e}}'_i$ are correlated. Note that the correlation Eq. (7.35) is a result of the selected angular distributions with $phi_i\ in[0;\ alpha\ pi]$. It is not explicitly specified in the simulations.

Biological swimmers may orient themselves towards external light sources or alternatively chemical sources, in which case a preferential direction of motion can be identified. Without restriction, the z-axis is defined as this direction. The angle θ_i denotes the angle between the new orientation $\hat{\boldsymbol{e}}'_i$ and $\hat{\boldsymbol{e}}_z$. This angle is Gauss distributed with a standard deviation $\sigma = \beta\pi$. For small values of $\beta \to 0$, directions of motion with small deviations around $\hat{\boldsymbol{e}}_z$ occur. The angle θ_i is limited to the intervall $\theta_i \in [0; \pi]$. For an increasing standard deviations with $\beta > 0.5$ the Gauss distribution thus merges more and more into an equal distribution, which is reached for $\beta > 1$. The observed distribution of z-components of the orientation vector for different values of β is shown in Figure 7.7.

By varying the distribution around the z-direction the mean value of orientations changes. While for $\beta > 1$ a uniform distribution leads to an average angle $\langle\theta\rangle = \frac{\pi}{2}$ and thus $\langle\hat{e}_z\rangle = \cos(\frac{\pi}{2}) = 0$, this angle θ is linearly reduced for $\beta \to 0$. The mean direction of swimmers can be well described by the fit

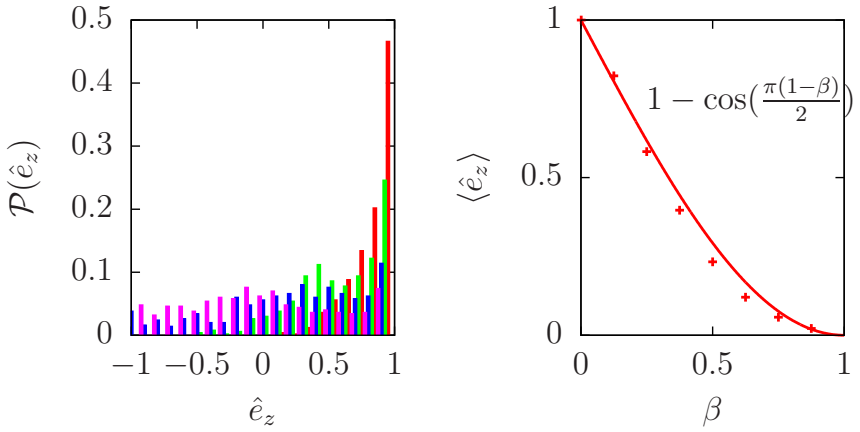

Figure 7.7.: Left: Distribution of the z-components of the directions of motion $\hat{\boldsymbol{e}}_1$, ..., $\hat{\boldsymbol{e}}_N$ for $\beta = \frac{1}{8}$ (red), $\beta = \frac{1}{4}$ (green), $\beta = \frac{1}{2}$ (blue), and $\beta = 1$ (magenta).Right: Mean value of direction of motion in z-direction versus β. The data points fit using $f(\beta) = 1 - \cos\left(\frac{\pi(1-\beta)}{2}\right)$ in the range of $\beta \in [0; 1]$.

function:

$$\langle \hat{\boldsymbol{e}}_i \rangle = 1 - \cos\left(\frac{\pi(1-\beta)}{2}\right) \hat{\boldsymbol{e}}_z. \tag{7.36}$$

When $\beta < 1$, as shown in Figure 7.7 on the right, the swimmers show a preferred direction of motion. To prevent the drift of swimmers towards a preferrential direction, the two parameters may be chosen as $\alpha = 1$ and $\beta = 1$ as reference for reorientations on the entire unit sphere.

8. Dispersion of a boundless cloud of swimmers

After the introduction of force dipoles within Chapter 7 to describe the hydrodynamic interaction between micro-swimmers, as well as after the description of simulation principles for the reorientation of these swimmers, both effects are linked within this chapter to describe the dispersion of a initially Gauss distributed cloud of swimmers to which both effects have an influence. The description of biased random walks for chemo- or phototactic micro-swimmers leads to a Fokker-Planck equation for the distribution of the swimmers [73]. That the probability distribution under non-linear effects, such as the hydrodynamic interaction, can change its shape is also known [121].

This work deviates from the description of a cloud as a probability distribution for the position r and concentration in terms of the volume fraction Φ. Rather, particle-based simulations of the dispersion of such a cloud are presented in this chapter. The aim of these simulations is to explain the dispersion of the cloud by the effects of the individual particle dynamics which is subject to hydrodynamic interaction, and to identify differences between pullers and pushers.

In addition to parameters, such as the volume fraction Φ, position r, standard deviation σ and center $\boldsymbol{\mu}$ which are related to the distribution of swimmers, also quantities like the distance $\boldsymbol{\varrho}$ and the distance between the nearest neighbors λ coupled to the hydrodynamic interaction (cf. Eq. (7.24) and Eq. (7.27) play an essential role (cf. Figure 8.1). Before the complete dynamic system is considered, first the dispersion without hydrodynamic interaction is investigated, to provide a reference for the dispersion with hydrodynamic interaction.

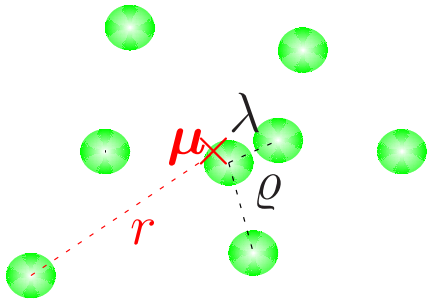

Figure 8.1.: Sketch of a cloud of swimmers with the defined distances ϱ between two swimmers, λ the distance between next neighbors, and r the distance between a swimmer and the center point $\boldsymbol{\mu}$.

8.1. Definition of the volume fraction

The initial distribution $\mathcal{P}(\boldsymbol{x})$ of the positions $\boldsymbol{x}$ of the $N = 500$ swimmers is assumed to be a Gaussian curve, where the initial orientations are determined corresponding to the distributions presented in Section 7.4. The Box-Müller method is used to determine the initial position $\boldsymbol{x}(t_0)_i$ of the i-th swimmer with a Gauss distributed distance r_i to the center of mass coordinate $\boldsymbol{\mu}$ defined as

$$\mu_\alpha = \frac{1}{N} \sum_i^N x_{\alpha i} \tag{8.1}$$

with $\alpha = x, y, z$. The course of the individual trajectories can differ from simulation to simulation, so it is justified to perform a statistical treatment of the dynamics of N swimmers. In addition to the center of mass μ_α (cf. Eq. (8.1)), the standard deviation σ_α is defined as

$$\sigma_\alpha^2 = \frac{1}{N} \sum_i^N (x_{\alpha i} - \mu_\alpha)^2 \tag{8.2}$$

In Section 7.3 it was shown that the hydrodynamic interaction in terms of the Rotne-Prager tensor $\mathcal{H}$ depends on the distance ϱ_{ij} between the interacting swimmers i and j. First of all, the volume fraction Φ is introduced, which links the distance ϱ_{ij} between the swimmers to the distribution.

Without restriction, the statement is correct that the averaged distance $\bar{\varrho}$ increases as soon as the standard deviation σ increases. By means of σ, the

spherical reference volume $V_S = \frac{4}{3}\pi\sigma^3$ covered by swimmers can be introduced. Each swimmer itself covers a volume of $V_s = \frac{4}{3}\pi a^3$ so that the volume fraction can be defined as

$$\Phi = \frac{NV_s}{V_S} = \frac{Na^3}{\sigma^3} \tag{8.3}$$

In simulations, the initial volume fraction Φ_0 can be set. The following results have been obtained with $\Phi_0 = 0.1$ so that the initial standard deviation σ, which determines the initial distribution is given by

$$\sigma = \sqrt[3]{\frac{Na^3}{\Phi}}. \tag{8.4}$$

The positions $x_i(t)$ are determined via an iterated integration of Eq. (7.28) using Euler steps taking into account the specifications of the reorientation process, so that the distribution of positions $\mathcal{P}(\boldsymbol{x}, t)$ can be obtained time-resolved in three dimensions. Therefore, the variance σ_α^2 (cf. Eq. (8.2)) and the volume fraction $\Phi(t)$ (Cf. Eq. (8.3)) are time-dependent quantities.

Especially in those cases with $\beta \to 0$ the dispersion of the cloud happens in an inhomogeneous fashion. Thus, the time-dependent volume fraction $\Phi(t)$ is defined as the ratio between the volume of the N swimmers and the volume $V_S = \frac{4}{3}\pi\sigma_x\sigma_y\sigma_z$. The volume fraction $\Phi(t)$ yields:

$$\Phi(t) = \frac{Na^3}{\prod_\alpha \sigma_\alpha(t)} \qquad \text{, with } \alpha = x, y, z. \tag{8.5}$$

Figure 8.2 shows the temporal behavior of the volume fraction Φ for a set of $N = 500$ swimmers with $v_0 = 10$, but different mean durations $\bar{\tau}$ of one run. After an initial regime without noticable change of Φ the cloud starts to disperse and the volume fraction decreases following a scaling behavior

$$\Phi(t) \propto t^\gamma, \tag{8.6}$$

with $\gamma = -\frac{3}{2}$ in the long time limit.

For long $\bar{\tau}$ one observes an intermediate regime with $\gamma = -3$. The exponents are obtained under the following considerations on the lengths σ_α. For $\bar{\tau} \to \infty$ the swimmers do not reorient, so that each swimmer moves according to Eq. (7.28). The position $\boldsymbol{x}_i$ at time t is then simply obtained via

$$\boldsymbol{x}_i(t) = \boldsymbol{x}_i(0) + \int \mathrm{d}t\, v_0 \hat{\boldsymbol{e}}_i = v_0 t \boldsymbol{e}_i \tag{8.7}$$

and the variance σ_α^2 around the center coordinate μ_α is given by:

$$\sigma_\alpha^2 = \langle (x_\alpha - \mu_\alpha)^2 \rangle = \langle x_\alpha^2 \rangle - \langle x_\alpha \rangle^2. \tag{8.8}$$

Here and in the following the brackets $\langle x \rangle = \frac{1}{N} \sum_i^N x_i$ have the meaning of averaging over all swimmers. The mean value μ_α and σ_α at time t can now be expressed with help of the propagation of each swimmer, as for the mean orientation and correlation-function Eq. (7.35) and Eq. (7.36). One can write:

$$\mu_\alpha = \langle x_\alpha(t) \rangle = \langle x_\alpha(0) \rangle + \langle \int \mathrm{d}t v_0 \hat{e}_\alpha \rangle. \tag{8.9}$$

At this point the inhomogenety, which is controlled by the parameter $\beta < 1$, enters the growth process of the cloud within a propagation of the center point in a linear manner, and the mean value along the z-axis is given by

$$\mu_z(t) = \langle x_z(0) \rangle + v_0 t \left(1 - \cos\left(\frac{\pi(1-\beta)}{2} \right) \hat{\boldsymbol{e}}_z \right), \tag{8.10}$$

where along the x and y-direction $\mu_\alpha = \langle x_\alpha(0) \rangle$ no propagation occurs.

The dispersion is described by the growth of σ_α^2 and thus the meansquared displacement $\langle x_\alpha^2 \rangle$, which reads

$$\langle x_\alpha^2 \rangle = \left\langle \int \mathrm{d}t \, \mathrm{d}t' x_{\alpha i}(t) x_{\alpha i}(t') \right\rangle = \left\langle x_{\alpha i}^2(0) + \frac{v_0^2}{3} \int \mathrm{d}t \, \mathrm{d}t' \, \hat{e}_i(t) \cdot \hat{e}_i(t') \right\rangle. \tag{8.11}$$

The last expression corresponds to the correlation-function given by Eq. (7.35). For short $|t - t'| \ll \tau_0/\alpha$ the exponential function yields $\exp\{-\alpha |t-t'|/\bar{\tau}|\} = 1$. The integration of Eq. (8.11) then yields a short-time regime with $\langle x_\alpha^2 \rangle \propto t^2$. The volume fraction decreases with t^{-3}, where the occurence of this regime depends on the initial extension $\langle \boldsymbol{x}^2(0) \rangle$ of the cloud and $\bar{\tau}$ (cf. Figure 8.2.

The integration of the exponential function for large $|t - t'| \gg \bar{\tau}/\alpha$ gives $\bar{\tau}/\alpha$ and thus the total varriance reads

$$\sigma_\alpha^2 = \left\langle x_{\alpha i}^2(0) + \frac{v_0^2}{3} \int \mathrm{d}t \, \mathrm{d}t' \, N \exp\left\{ -\alpha \frac{|t-t'|}{\tau_0} \right\} \right\rangle = \left\langle x_{\alpha i}^2(0) + N \frac{v_0^2 \bar{\tau}}{3\alpha} t \right\rangle. \tag{8.12}$$

Thus, the volume fraction scales as $\Phi \propto t^{-\frac{3}{2}}$ in the diffusive regime. The decay of Φ in dependence of the time t, as illustrated in Figure 8.2 can be split in three parts:

First an initial regime without a noticalble change of Φ, which may be followed by a decay with $\gamma = -3$ for long $\bar{\tau}$ and $t \ll \bar{\tau}/\alpha$. This regime can be

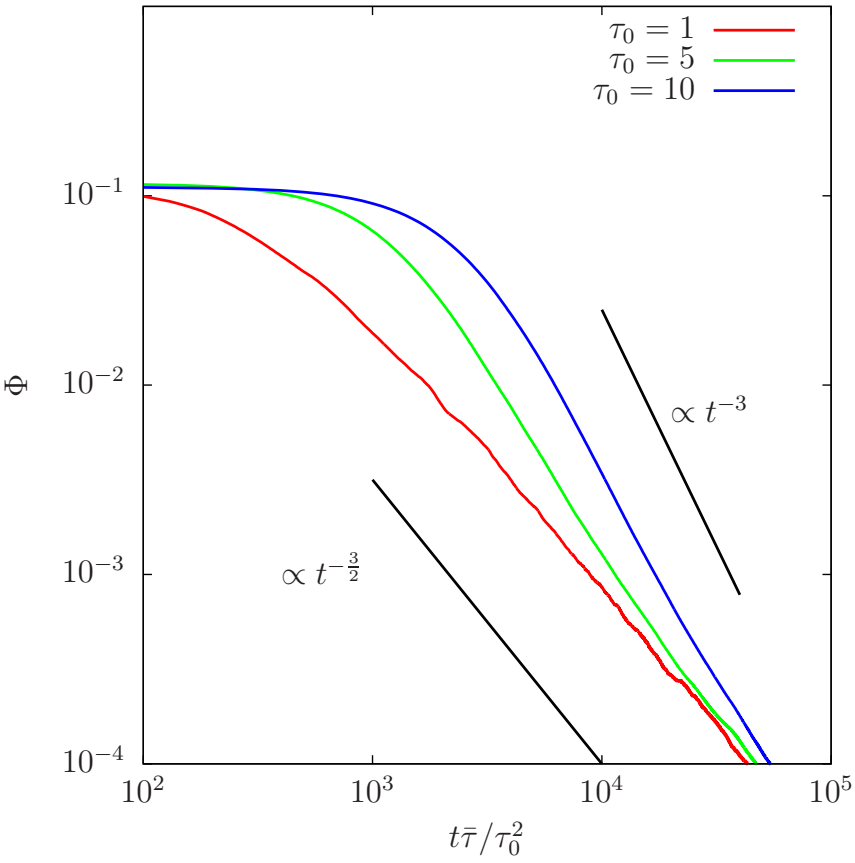

Figure 8.2.: Volume fraction Φ for a cloud of $N = 500$ swimmers with $v_0 = 10$ and different durations $\bar{\tau}$ of a run. For long times $\bar{\tau}$, the scaling law of dispersion changes from t^{-3} to $t^{-\frac{3}{2}}$ as a result of the transition from the ballistic to the diffusive regime.

attributed to a ballistic regime, in which the swimmers have not reoriented, but have propagated an appreciable distance. For long times $t \gg \bar{\tau}/\alpha$, the swimmers reach the diffusive regime containing swimmer reorientations. Then, the decay of Φ transiates from Φ^{-3} to $\gamma \propto -\frac{3}{2}$.

These scaling laws are universial,i. e., independent of the velocity v_0 and the mean reorientation time $\bar{\tau}$. However, the rate of dispersion depends very well on these parameters. It is essential that a swimmer, reorienting quickly swims small distances within the short time $\bar{\tau}$, contributes less to the dispersion than a swimmer having a long intrinsic reorientation time $\bar{\tau}$. On the other hand a fast swimmer with a high velocity v_0 only needs a short time $\tau_0 = a/v_0$ to cover the swimmer radius a. On the first view it seems astonishing that this time τ_0 enters quadratically entering the velocity v_0 (Cf. Figure 8.2). By means of Eq. (8.12) a characteristic time T scale for the dispersion process can be determined, which depends only on the velocity v_0, radius a, and reorientation $\bar{\tau}$ given as

$$T = \alpha v_0^2/a^2/\bar{\tau} = \alpha \tau_0^2/\bar{\tau}. \tag{8.13}$$

This time corresponds to the time one swimmer needs to cover its body length in the presence of reorientations under the consideration of reorientations. In the following sections this time T is used to rescale temporal dependencies of the dispersion process.

8.2. Moments of the distribution

Instead of following the growth of the total distribution $\mathcal{P}(\boldsymbol{x}, t)$ of swimmers with proceeding time, the swimmer dynamics can be investigated by following the trajectories $\boldsymbol{x}_i(t)$ starting at the initial positions $\boldsymbol{x}_i(0)$. The previously described random-walk (cf. Section 7.4) of the swimmers cause a diffusive dynamics dependent on v_0, and $\bar{\tau}$, but also on α and β. In numerical simulations and direct experimental observations of a cloud of biological swimmers, the progress of a distribution $\mathcal{P}(\boldsymbol{x}(t))$ of swimmer positions is analysed. An initial Gaussian distribution $\mathcal{P}(\boldsymbol{x}(0))$ decays following a Fokker-Planck equation [137]

$$\partial_t \mathcal{P}(\boldsymbol{x}(t)) = \nabla \cdot \left(D^{(1)} \mathcal{P} + \nabla D^{(2)} \right) \mathcal{P}(\boldsymbol{x}(t)), \tag{8.14}$$

with the drift- and diffusion-term $D^{(1)}$ and $D^{(2)}$, where the first term represents a propulsion of the mean value of the cloud and the second one describes the

diffusive dispersion. The description of the cloud dynamics via Eq. (8.14) and Eq. (3.4) including the reorientation mechanism is equivalent. The cofficients $D^{(1)}$ and $D^{(2)}$ can be interpreted as Kramers-Moyal coefficients, defined as [137]

$$D^{(n)}(\boldsymbol{x},t) = \frac{1}{n!t}\langle(\boldsymbol{x}(t)-\boldsymbol{x}(0))^n\rangle \tag{8.15}$$

where $\langle(\boldsymbol{x}(t)-\boldsymbol{x}(0))^n\rangle$ denotes the n-th conditional moment

$$\langle(\boldsymbol{x}(t)-\boldsymbol{x}(0))^n\rangle = \int \mathrm{d}\boldsymbol{x}\,(\boldsymbol{x}(t)-\boldsymbol{x}(0))^n\mathcal{P}(\boldsymbol{x}(t)). \tag{8.16}$$

The conditional moments are obtained from numerical simulations of Eq. (3.4). The diffusion around the center point of the cloud is given by

$$D^{(2)} = \frac{1}{2t}\left(\langle(x(t)-x(0))^2\rangle - \langle x(t)-x(0)\rangle^2\right). \tag{8.17}$$

Up to second order the expressions for $\langle\boldsymbol{x}^n\rangle$ are known from Eq. (8.9) and Eq. (8.12) in dependence of v_0, $\bar{\tau}$, α and β. The terms due to drift $D^{(1)}$ and diffusion $D^{(2)}$ are given by

$$D^{(1)} = v_0\left(1-\cos\left(\frac{\pi(1-\beta}{2}\right)\right)\hat{\boldsymbol{e}}_z \tag{8.18}$$

$$D^{(2)} = \frac{1}{3}\frac{v_0^2\bar{\tau}}{\alpha} \tag{8.19}$$

Figure 8.3 shows the evolution of the diffusive regime, characterized by $D^{(2)}$ for long times $t \gg \bar{\tau}/\alpha$. This stationary state arises after the transition from the inital ballistic motion, where the mean squared displacement grows with t^2 while the first reorientations have not taken place. After these reorientations the correlation-function $\langle\boldsymbol{e}_i\cdot\boldsymbol{e}_i'\rangle$ decays below $1/e \approx 0.4$ at the time $\bar{\tau}/\alpha$ (Cf. Figure 7.6), where this corresponds exactly to the time after which the diffusive regime occurs.

From Eq. (8.18) and Eq. (8.19) it can be seen that variations of the parameter β have an effect on the propagation of the cloud in terms of a drift towards a preferred direction, where the parameter α affects only the diffusivity. Figure 8.4 shows $D^{(1)}$ and $D^{(2)}$ as a result of a numerical study in dependence of the parameter β is shown, determined for each direction x, y and z. It is astonishing that the diffusive dynamics remains homogeneously along all three directions with a common diffusion coefficient $D^{(2)} = \frac{1}{3}\frac{v_0^2\tau_0}{\alpha}$ above $\beta = 0.5$. Below this value the preferrence of the z-direction is reflected in the break

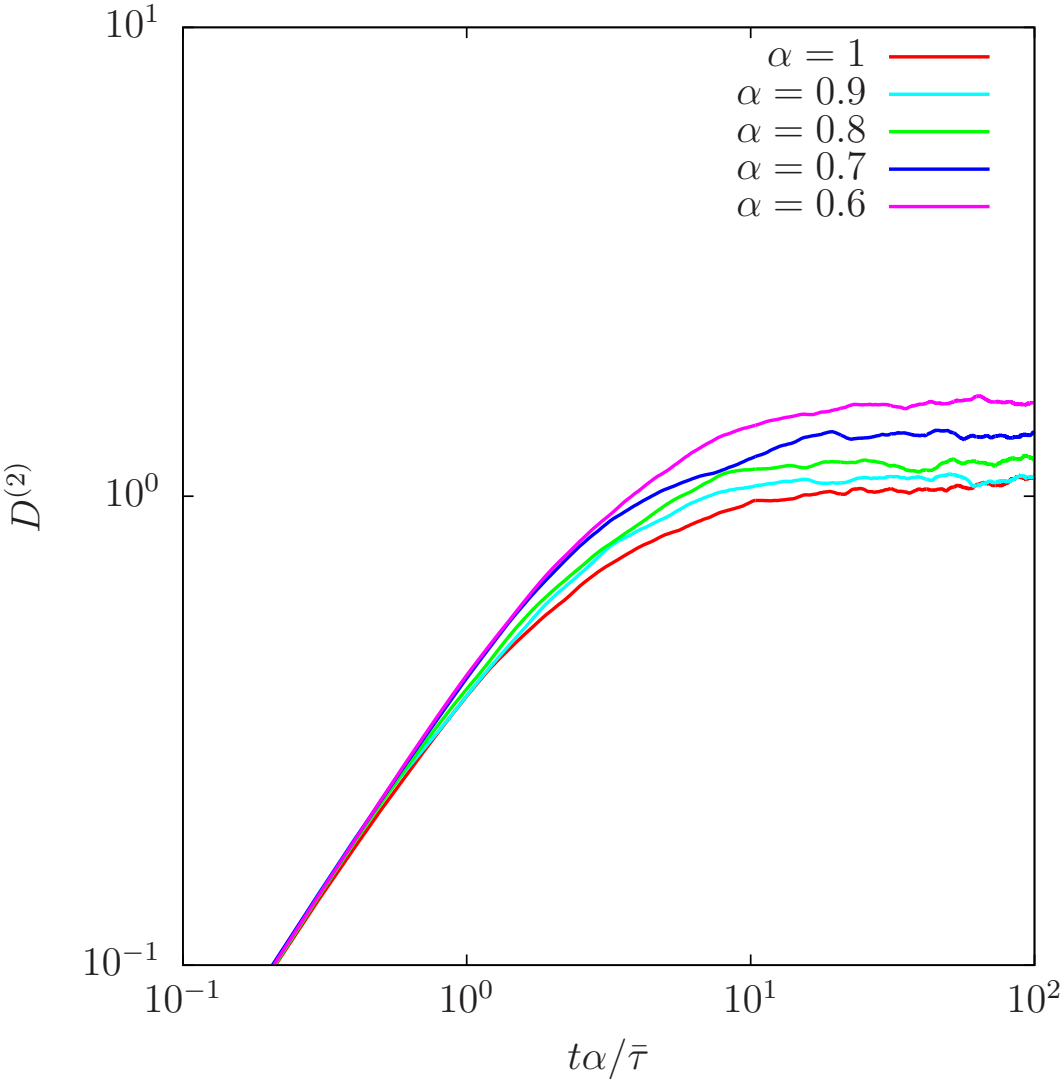

Figure 8.3.: The diffusion coefficient for $v_0 = 10$, $\bar{\tau} = 1$ and $\beta = 1$, but different values of α. The diffusive regime appears for times $t\alpha/\bar{\tau} > 10$.

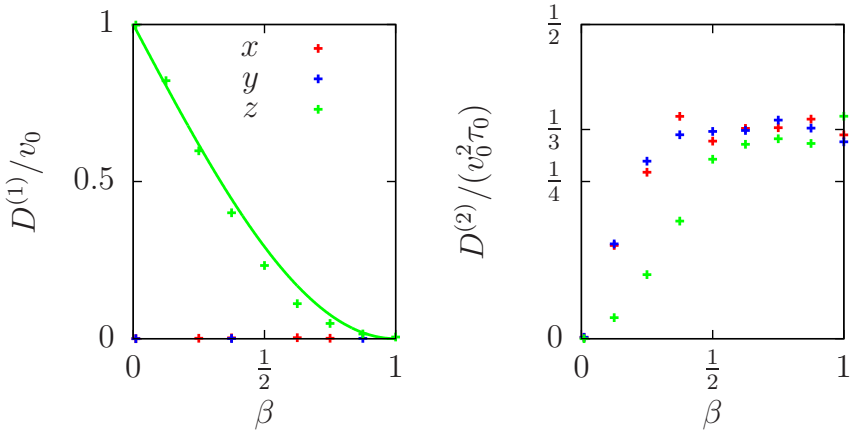

Figure 8.4.: Numerical study on the drift-coefficent $D^{(1)}$ (left) and diffusion coefficient $D^{(2)}$ (right) in dependence of the parameter β. The homogeneous diffusion is broken below $\beta < 0.5$, where different coefficients $D^{(2)}$ occur in x-,y-, and z-directions. For $\beta = 0$ no diffusive broadening of the swimmer distribution occurs.

of homogenity. Also, below $\beta < 0.5$ the range of adopted orientations has shrinked, so that the diffusion coefficent $D^{(2)}$ in all three directions decreases until no reorientations take place for $\beta = 0$ and thus no diffusion occurs, with $D^{(2)} = 0$.

8.3. Dispersion with Hydrodynamic Interaction

The velocity of each individual swimmer is generated by propelling motions, which generate a flow field around the swimmer. This field is described by means of force-dipoles, as introduced in Eq. (7.20). Two different types of swimmers, called *pushers* and *pullers*, exist in the biological world. In the theoretical description the force dipoles only differ in the sign of the propelling forces. Around the swimmers a flow field $\tilde{\boldsymbol{v}}$ is generated, which decays as r^{-2} with distance r from swimmer j. A swimmer i at the distance r from swimmer j is influenced by just this flow field, its motion is influenced by perturbations from all other swimmers.

The fact that the different sign in the propelling forces leads to a totally different interactive processe in the cloud of pushers and pullers is illustrated

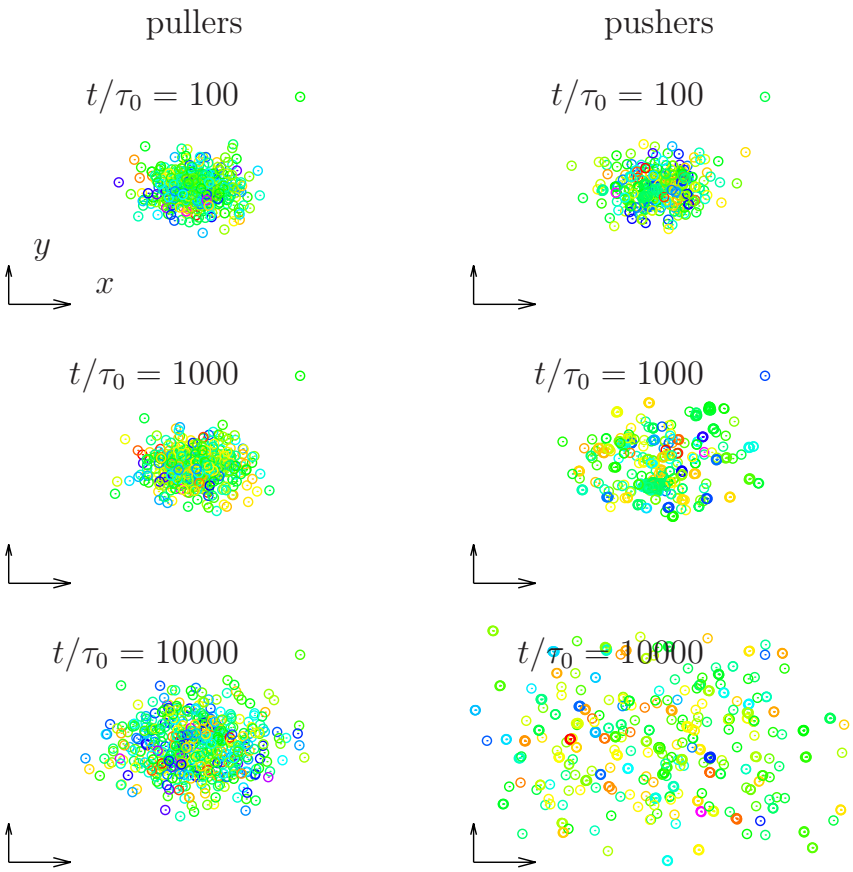

Figure 8.5.: Snapshots of a cloud of $N = 500$ swimmers with $v_0 = 10$, $\bar{\tau} = 0.01$, $\alpha = 1$ and $\beta = 1$ after different times t. The cloud on the left consists of pullers, analogous the right figures illustrate slouds of pushers. In the latter case the growth occurs much faster for long times. In colors the position z-direction is indicated.

in Figure 8.5, This figure shows snapshots of $N = 500$ swimmers with the same parameters at different times t. The only difference between the illustrations on the left and right is the swimmer type, where the clouds on the left (right) consist of pullers (pushers). One can see that the dispersion process for pushers occurs much faster than for pullers.

The big difference between the dynamics of pullers and pushers can be seen in Figure 8.6. Here the distribution of the distance λ between the swimmer i and its next neighbor j is shown:

$$\lambda = \min(\varrho_{ij}), \tag{8.20}$$

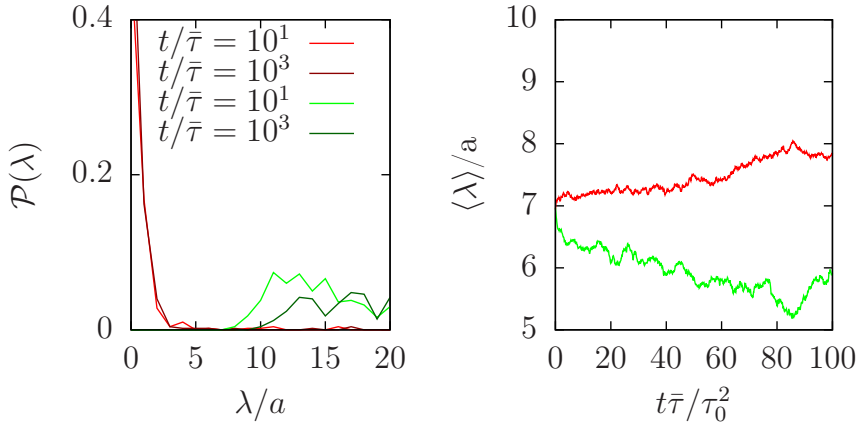

Figure 8.6.: Left: Distribution of the distance λ between next neighbors for pushers (red) and pullers (green) for $\tau_0 = 0.01$ and $v_0 = 10$ at different times. Where pushers tend to cluster with a constant distribution preferring small distances, the distribution shifts to high vallues with increasing time for pullers. On the right hand side the temporal developement of the mean-vallue of λ indicates the approach of pushers, where pullers tend to repell each other.

with $\varrho_{ij} = \sqrt{(\boldsymbol{x}_i(t) - \boldsymbol{x}_j(t))^2}$ for fixed i and $j \in [0, N]$, but $j \neq i$. The left hand side shows the distribution $\mathcal{P}(\lambda)$ of the distance between next neighbors for pullers (red) and pushers (green). The main difference is that the mean distance between pullers tends to grow, whereas the attraction of pushers perpendicular to their orientation leads to clustering, as indicated by a preference of small distances between neighboring swimmers. This tendency of attraction between pushers can also be seen on the right, where the mean value $\langle\lambda\rangle$ is plotted. Due to the decay of hydrodynamic interaction with r^{-2} (Cf. Eq. (7.19)) the collective effects in a suspension of swimmers are mainly carried by the pairwise interaction between next neighbors. Hence, it can happen that local clusters occur that are stable for long time windows, where swimmers support each other with a collective velocity higher than v_0. This will lead to an increase of the mean velocity as sketched in Figure 8.5.

The dynamic simulations of $N = 500$ swimmers with $v_0 = 10$ with reorientations after $\bar{\tau}$ include hydrodynamic interaction $\tilde{v}$ between each pair of

swimmers given by Eq. (7.23) with Eq. (7.24)

$$\tilde{\boldsymbol{v}} = \sum_{j \neq i} \mathcal{H}_t(\boldsymbol{x}_i - \boldsymbol{x}_j) \cdot \boldsymbol{F}_j - \sum_{j \neq i} \mathcal{H}_t(\boldsymbol{x}_i - \boldsymbol{x}_j - \boldsymbol{p}_j) \cdot \boldsymbol{F}_j. \tag{8.21}$$

In addition each force generated by swimmer j induces a torque on the swimmer i, where the total torque $\tilde{\boldsymbol{\omega}}$ is given by:

$$\tilde{\boldsymbol{\omega}} = \sum_{j \neq i} \mathcal{H}_r(\boldsymbol{x}_i - \boldsymbol{x}_j) \cdot \boldsymbol{F}_j - \sum_{j \neq i} \mathcal{H}_r(\boldsymbol{x}_i - \boldsymbol{x}_j - \boldsymbol{p}_j) \cdot \boldsymbol{F}_j. \tag{8.22}$$

The full equations of motion are given by:

$$\dot{\boldsymbol{x}}_i = v_0 \boldsymbol{e}_i + \tilde{\boldsymbol{v}}, \tag{8.23}$$

$$, \dot{\boldsymbol{e}}_i = \tilde{\boldsymbol{\omega}} \times \boldsymbol{e}_i. \tag{8.24}$$

In Eq. (7.27) and Eq. (7.24) $\mathcal{H}_r(\boldsymbol{\varrho})$ and $\mathcal{H}_t(\boldsymbol{\varrho})$ are given and the force $\boldsymbol{F}_j = F_0 \boldsymbol{e}_j$ is coupled to the velocity v_0 via Eq. (7.21):

$$F_0 = \varepsilon 24 \pi \eta a v_0, \tag{8.25}$$

with a parameter ε introduced to later enabling the decoupling between the propulsive motion with v_0 and the hydrodynamic interaction. For the moment this parameter is set to $\varepsilon = 1$. The analysis of the cloud growth under hydrodynamic interaction is provided in the same way as in the case of free dispersion without hydrodynamic interaction. The difference now is that the full dynamical equations are not solvable analytically for a number of $N = 500$ swimmers. Therefore, Eq. (8.24) and Eq. (8.24) are solved numerically.

The investigations are started with a homogeneous distribution of swimmer orientations with $\alpha = 1$ and $\beta = 1$, so that no drift of the total cloud occurs. The refference diffusion-constant is given by

$$D_0 = v_0^2 \bar{\tau} / \alpha, \tag{8.26}$$

if a three-dimensional dynamics is considered.

The interest lies on the effect of hydrodynamic interactions on the diffusion coefficient of the cloud. As an initial guess, on dimensional grounds one may expect the hydrodynamic interaction, which depends on the volume fraction Φ, to enter like

$$D^{(2)} = \langle v_0 \hat{\boldsymbol{e}}_i + \tilde{\boldsymbol{v}}(\Phi) \rangle^2 \tau_0 / \alpha. \tag{8.27}$$

The main question at this point is, how the hydrodynamic interaction influences the diffusion coefficient $D^{(2)}$?

As initial condition a volume fraction of $\Phi \approx 0.1$ prescribed as well as a constant intrinsic velocity $v_0 = 10$. In Figure 8.7 the diffusion coefficient $D^{(2)}$ against the time t is illustrated for pullers (left) and pushers (right). In both cases the red line shows the data for an average running time $\bar{\tau} = 1$ with the ballistic regime for small times t. There is no difference between these two curves and also the differences to the diffusive dynamics without hydrodynamic interaction vanish for such large $\bar{\tau}$. The effect of hydrodynamic interaction with the differences between pullers and pusher become visible if $\bar{\tau}$ is reduced (cf. the curves for $\bar{\tau} = 0.05$ and $\bar{\tau} = 0.1$) .

The vanishing effects for long run times $\bar{\tau}$ can be explained as follows: The hydrodynamic interaction shows attractive as well as repulsive parts for both swimmers. It is known that especially those parts of the hydrodynamic interaction perpendicular to the swimmer orientation predominate the collective dynamics (Cf. [49, 104] implying that pullers are repelled from each other by the hydrodynamic interaction decreasing with with ϱ^{-2}. In long runs with $\tau_0/\bar{\tau} = 10$ the interactive effects get lost at the early stages of the ballistic regime. Further, pushers with $\tau_0/\bar{\tau} = 10$ do not show visible differences to the free dispersing case, although an attractive interaction leads to long-lasting cooperative effects between the swimmers. Also this swimmer type underlies a repulsive interaction along the direction of motion. Considering two pushers i and j interacting with each other,simultaneously to the attraction of the two swimmers are more and more repelled by the repulsive parts of the hydrodynmic interaction. Both swimmer types have in common that for long times the repulsion predominates dispersing the swimmers and decreasing their hydrodynamic interaction. Compared to $\bar{\tau}$ this happens that fast in the case of $\tau_0/\bar{\tau} = 10$,so that no difference to the free dispersion occurs.

In both cases the effects of hydrodynamic interaction appear when the reorientation rate $1/\bar{\tau}$ is increased drastically. The other graphes shown in Figure 8.7 belong to running times $\tau_0/\bar{\tau} = 1$ (blue), $\tau_0/\bar{\tau} = 0.5$, and $\tau_0/\bar{\tau} = 0.1$. By reducing the run times the removal of swimmers from each other is interrupted with each reorientation, so that the effect of hydrodynamic interaction persists for longer times. For pullers, which repell each other anyways one

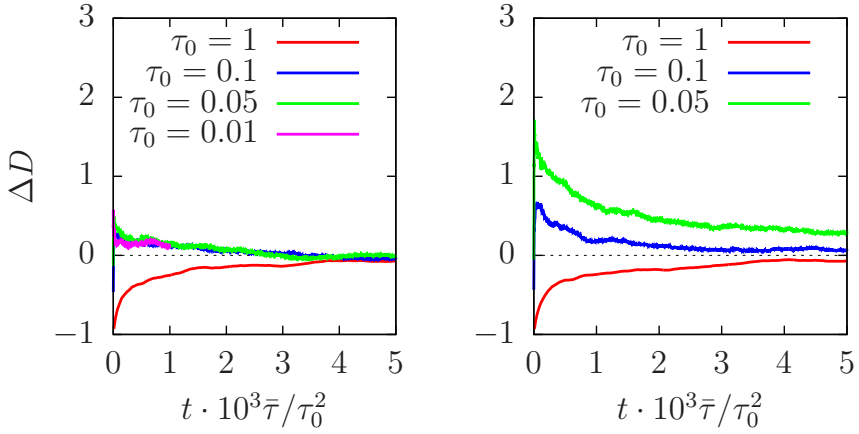

Figure 8.7.: Relative diffusion coefficient ΔD in swimmer suspensions with an initial volume fraction $\Phi = 0.1$ and intrinsic velocity $v_0 = 10$, but different run times τ_0. Left:suspension of pullers. Right: suspension of pushers.

would expect an increase of the diffusion coefficient of interacting swimmers decreasing to the reference diffusion constant of non-interacting swimmers. Figure 8.7 shows this behavior of the diffusion coefficient $D^{(2)}$. For pushers the diffusion coefficient $D^{(2)}$ enhances similar to the case of pullers. The main difference is that with increasing ratio $\tau_0/\bar{\tau}$ the diffusion coefficient $D^{(2)}$ tends to grow to high values.

To identify the hydrodynamic interaction in the diffusion coefficient ΔD is defined as the relative increase of the coefficient $D^{(2)}$ compared to D_0

$$\Delta D = \frac{D^{(2)} - D_0}{D_0}. \tag{8.28}$$

With the plot of the relative diffusion coefficients ΔD in Figure 8.7 it is shown that, no matter which swimmer type is considered, hydrodynamic interaction increases the diffusion coefficient $D^{(2)}$ is enhanced ($\Delta D > 0$) for small $\bar{\tau}$, so that the individual swimmer is faster in the collective as an isolated one. Figure 8.7 however does not allow to relate the hydrodynamic interaction is not able to couple the hydrodynamic interaction to the growth of the cloud directly.

Figure 8.8 shows the decrease of the time dependent volume fraction of clouds consisting of pullers (green) and pushers (blue) starting with an initial volume fraction $\Phi = 0.1$. The comparison with the red curve corresponding

to the case of free dispersion shows that only pushers disperse with increased velocity, whereas hydrodynamic interactions of pullers have no influence although the diffusion coefficient $D^{(2)}$ is initially increased for the illustrated data of suspensions of swimmers with velocity $v_0 = 10$ and reorientations after $\bar{\tau} = 0.01$ on average.

The growth of the cloud of swimmers in general is a self-interactive process, i. e., the distribution and the type of suspended particles have an impact on the growth of the swimmer distribution. With the diffusion coefficient $D^{(2)}$ or even better the deviation ΔD from the case of free dispersion a quantity is known that measures directly the impact of hydrodynamic interaction on the growth of the cloud. However, the volume fraction Φ measures the averaged distance between the interacting particles and thus represents a measurement of the strength of hydrodynamic interaction between the swimmers.

Growth of clouds of pushers

The illustrated graphs of ΔD in Figure 8.9 against the volume fraction Φ shows that for quickly reorienting pushers the enhancement ΔD does not depend on Φ for a long range of Φ leading to very diluted regimes. The illustrated data shows that the averaged distances between the swimmers increase very fast, as indicated by the enhanced diffusion coefficient $\Delta D > 0$. One would assume that ΔD would decrease with increasing distance between the swimmers acorrding to the decreasing hydrodynamic interaction in dependence of the decreasing volume fraction Φ, but the hydrodynamic interaction remains constant except for fluctuations arround an average strength $\tilde{v} \approx v_0$.

The cloud dispersionwith constant collective velocity can be explained as follows: The cloud of $N = 500$ swimmers can be departed in subdivisions of 3 or 4 swimmers with small particle-particle distance. These clusters reach far distances from each other within the stable collective dynamics indicated in the fast decrease of the volume fraction Φ.

The reference diffusion coefficient is a function of v_0, α, and $\bar{\tau}$ and thus one would expect the same dependencies that the relative coefficient $\Delta D = (D^{(2)} - D_0)/D_0$, but the expected dependence on reorientations in terms of $\bar{\tau}$ does not occur. This can be seen in Figure 8.9, where all curves of ΔD coincide

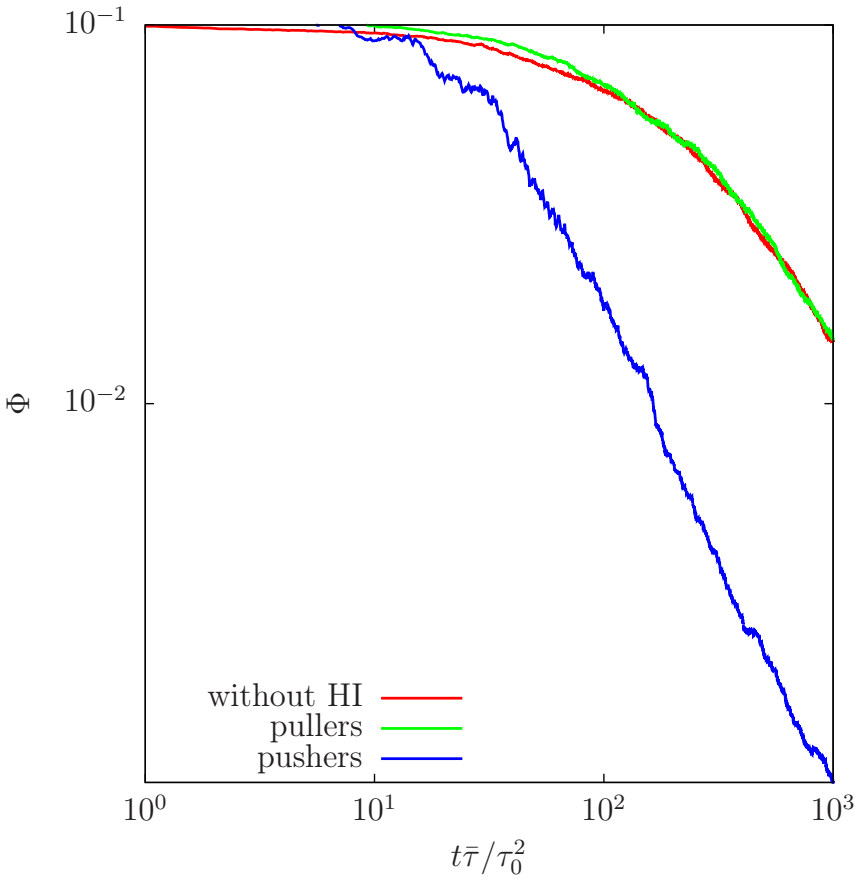

Figure 8.8.: The temporal development of the volume fraction Φ of swimmer suspensions with $v_0 = 10$ and $\bar{\tau} = 0.01$. For this set of parameters the hydrodynamic interaction has an impact on the diffusion coefficients $D^{(2)}$. The red curve represents data of non-interacting swimmers, where the green curve represents pullers and the blue graph illustrate data obtained ,for pushers.

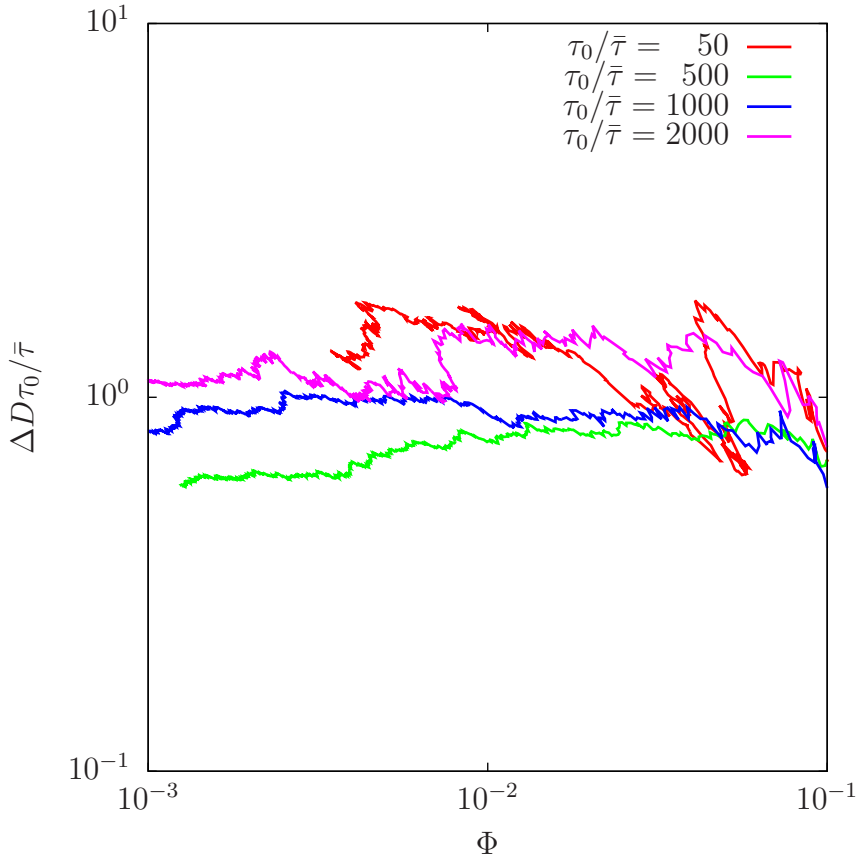

Figure 8.9.: The increase ofthe relative diffusion coefficients ΔD against the volume fraction Φ for several vallues of v_0 and $\bar{\tau}$. The collapse of the curves after the multiplication by $\tau_0/\bar{\tau}$ indicates that the velocity of the individual swimmers, and thus the cloud dispersion, is not directly related to the diffusion process.

when ΔD is rescaled with $av_0 = D_0\tau_0/\bar{\tau}$ instead of $D_0 = \alpha v_0^2\bar{\tau}$, so that the effect of reorientations vanishes effectively in ΔD wich can be interpreted as an enhanced collective velocity of swimmers affecting the dispersion. The fact that ΔD is effectively independent of $\bar{\tau}$ is a result of clustering and thus an effect of hydrodynamic interactions. In Figure 8.6 it was shown that despite the reorientations pushers tend towards a constant probability distribution of the nearest neighbors although the dispersion advances reducing volume fraction Φ. If the distance λ between adjacent swimmers remains constant, there are also no variations in the hydrodynamic interaction $\tilde{v}$ that occurs in ΔD.

The distance $\lambda = 2\,a$ is a minimum distance for interacting swimmers. With Eq. (7.19) the averaged flow-contribution in a distance $2a$ around one swimmer lies arround $\tilde{v} \approx 0.8v_0$. The enhancement of the diffusion coefficient ΔD lies betwenn $\Delta D = 2.0av_0$ and $\Delta D = 2.5av_0$. Together with Figure 8.6 one can assume that subgroups of two or three swimmers build clusters initially, which stay stable and lead to a fast dispersion of the cloud.

Growth of clouds of pullers

While a suspension of pushers show an increased dispersion in terms of ΔD (cf. Figure 8.9), a suspension of pullers with the same parameters shows no noticable differences in the temporal dependence of Φ (Cf. Figure 8.8). By plotting ΔD directly against the volume fraction Φ the task now is to identify the influence of hydrodynamic interaction between pullers within the cloud dispersion. The graphs of ΔD against Φ for several values of the intrinsic parameters $\bar{\tau}$ and v_0 are illustrated in Figure 8.10.

While clusters in suspensions of pushers change the distribution $\mathcal{P}(\boldsymbol{x})$, leading to a constant interactive impact on the dynamics, the hydrodynamic interaction between pullers decreases with decreasing volume fraction Φ and increasing particle-particle distance λ. In the dilute regime the hydrodynamic interaction increases the veocity of each particle on average, as reflected in the enhanced diffusion coefficient. This repulsion between swimmers does not change the distribution of swimmer positions itself. For this reason, ΔD is a function of the volume fraction Φ, assuming

$$\Delta D = A\Phi^B. \tag{8.29}$$

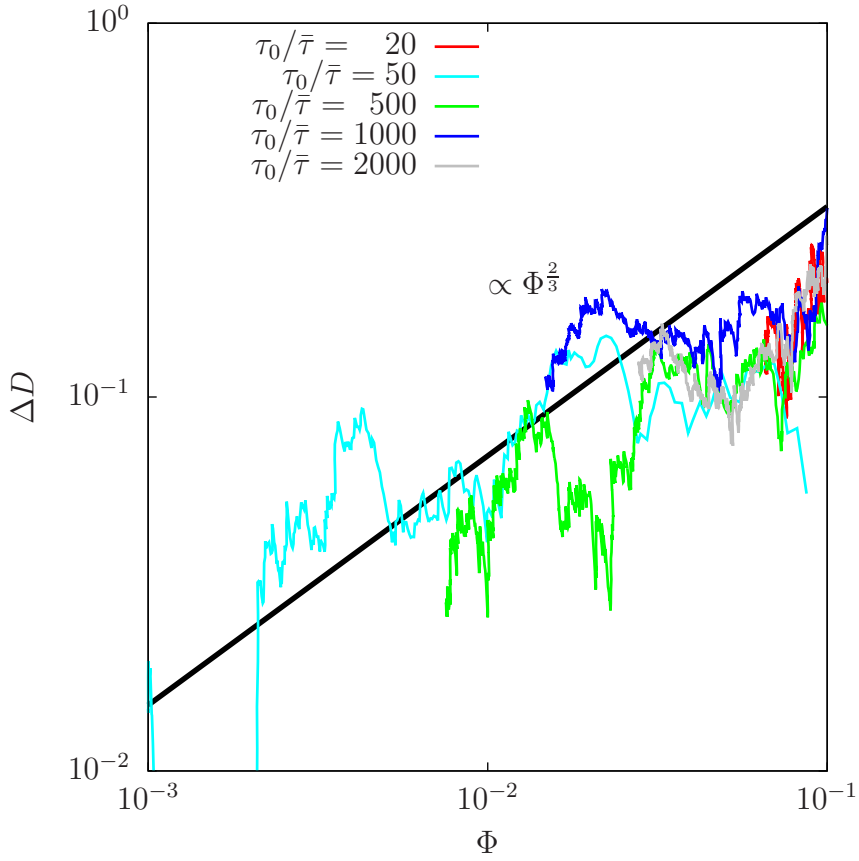

Figure 8.10.: The diffusion coefficient ΔD plotted against the volume fraction Φ for several suspensions of pullers with different v_0 and τ_0. ΔD decays proportional to $\Phi^{\frac{2}{3}}$.

A and B denote parameters, which can be determined by fits to the data shown in Figure 8.10, where all graphs decay with an averaged exponent $B = \frac{2}{3}$ for decreasing volume fraction Φ.

The relative diffusion coefficient ΔD for puller suspensions depends on the growing mean particle-particle distance λ, so that the interactive impact depends on v_0 and $\bar{\tau}$ via $D_0 = \alpha v_0^2 \bar{\tau}$. With this rescaling the collaps of all data-series to the generalized curve from Figure 8.10 occurs. The effects of swimmer interaction are about 20% for a volume fraction of $\Phi = 0.1$, which decay further to 1% for $\Phi = 0.001$ in a dilute suspension. The presented investigations have been made for swimmers, which reorient in an arbitrary direction with $\alpha = 1$ and $\beta = 1$.

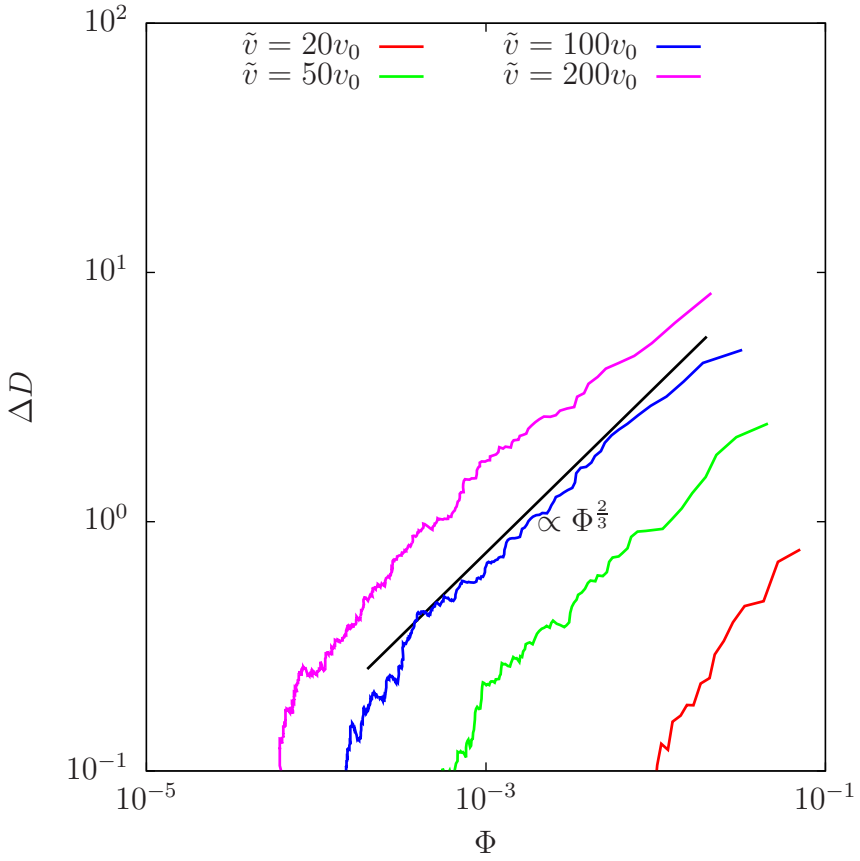

Figure 8.11.: The relative diffusion coefficient ΔD in dependence of Φ for several amplifing values of $\epsilon > 1$. The scaling law $\Phi^{\frac{2}{3}}$ can be attributed to the hydrodynamic interaction between pulers.

Although $B = \frac{2}{3}$ already results from fits of the obviously very noisy curves in Figure 8.10, this result is not particularly convincing after a pure look at Figure 8.10. In order to attribute this result to hydrodynamic interactions, the parameter ϵ in Eq. (8.25) is increased which determines the amplification of hydrodynamic interaction compared to the self-propulsion of the swimmers.

Figure 8.11 illustrates ΔD in dependence of the volume fraction Φ. Only beyond an amplification $\epsilon = 20$ an appreciable increase of ΔD is observed, which grows quadratically with ϵ since the resultant interactive velocity $\tilde{v}$ depends linearly on ϵ. The increase of hydrodynamic interaction, which enters via summation of all contributions into the single particle dynamics, has the effect that with increasing ϵ the diffusive character of the dynamics loses more

and more its dependence in the dense regime around $\Phi = 0.1$. As illustrated in Figure 8.11 wone can identify a critical volume fractions $\Phi_c(\epsilon)$, where hydrodynamic interaction only play a subordinate role in the collective dynamics for $\Phi < \Phi_c$. Above this volume fraction $\Delta D \propto \Phi^{\frac{2}{3}}$ is obtained no matter which value for the amplification is set.

It seems as if $B = \frac{2}{3}$ is a universal law for the dispersion of puller suspensions, which can be attributed to the hydrodynamic interaction between the swimmers. However, in order to detect the effect of the hydrodynamic interaction, without the loss in the ballistic regime quickly re-orientaing swimmers are required.

Phototaxis and hydrodynamic interaction

A valid question is, whether parameter variations have a significant impact on the cloud dispersion. Especially for $\beta \to 0$, the reorientation vanishes and the initially spherical cloud of interacting pullers, as illustrated in Figure 8.12, disperses inhomogeneously due to the attractive and repulsive components of the hydrodynamic interaction in different directions. In this section the influence of the parameters α and β on the dispersion are clarified.

In a first step, the parameter α is varied between $\alpha = 1$ (corresponding to reorientations on the full unity sphere) and $\alpha = 0.5$, indicating that the old ($\boldsymbol{e}_i$) and new ($\boldsymbol{e'}_i$) direction of motion cover a maximum angle of $\phi = \frac{\pi}{2}$ within one reorientation. In Figure 8.13 it can be seen that a reduction of the maximal covered angle results in a reduction of hydrodynamic interaction, where below $\alpha = 0.6$ no interactive effects can be identified for the chosen parameters corresponding to a time-ratio $\tau_0/\bar{\tau} = 0.02$. This decrease of the hydrodynamic interaction is not surprising, if one recalls that the hydrodynamic interaction for a given volume fraction Φ remains identical, where the reference coefficient $D_0 = v_0^2\bar{\tau}/\alpha$ increases with decreasing α. interaction

Interesting phenomena occur if the parameter converges to $\beta \to 0$. β is related to the covered angle between z-direction and direction of motion and $\beta = 0$ means that reorientations only take place if the swimmer was previously diverted from the hydrodynamic interaction with others. But first, between $\beta = 1$ and $\beta = 0.5$ the reduction of β induces an increasing drift term $D^{(1)}$

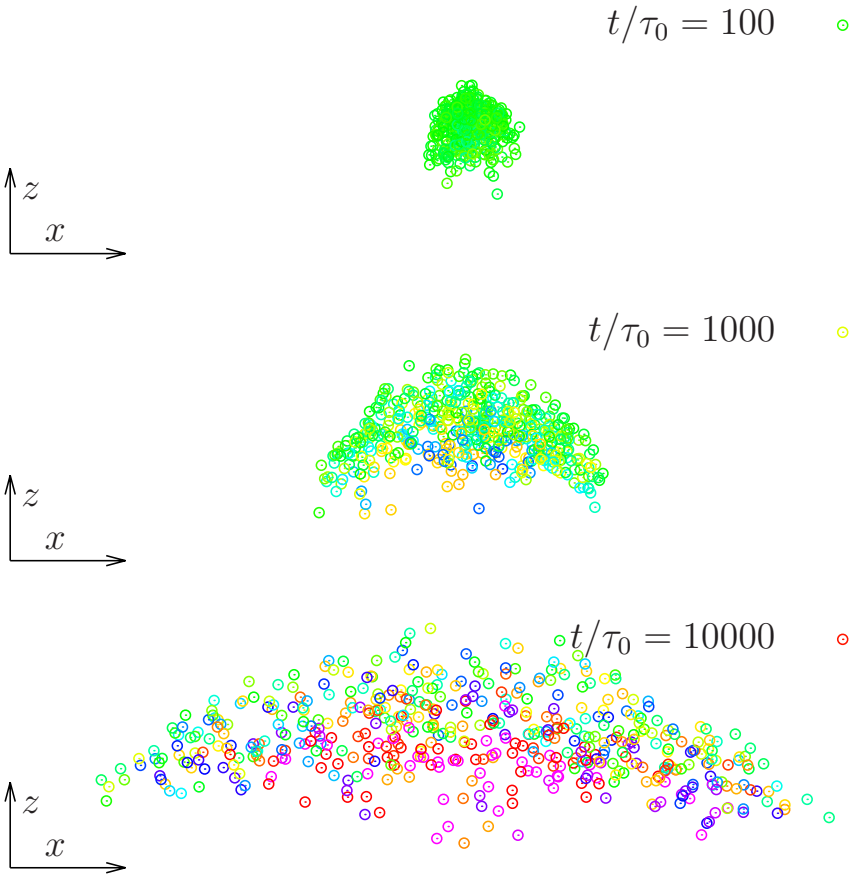

Figure 8.12.: Snapshots of $N = 500$ pullers aligned towards the z-direction at every reorientation at different time steps.

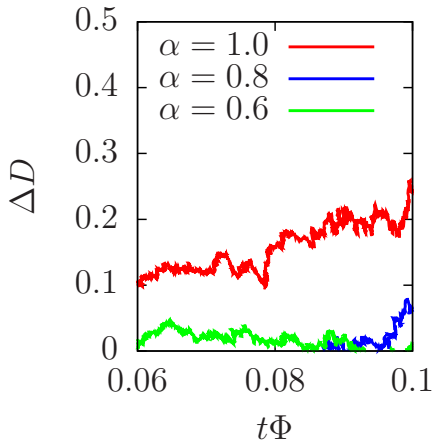

Figure 8.13.: Impact of hydrodynmic interaction ΔD on the diffusion coefficient against volume fraction Φ for $\alpha = 1, \alpha = 0.8$, and $\alpha = 0.6$.

without having an influence on the diffusion term $D^{(2)}$ because for $\beta \in [0.5; 1]$, the distribution of the directions of motion $\boldsymbol{e}_i$ is hardly different from a uniform distribution.

Only below $\beta = 0.5$ all swimmers orient themselves measurably towards the z-direction. Especially these configurations emphasizes the attractive and repulsive character of the interaction, where the pure diffusive dynamics more and more retreats (Cf. Figure 8.4). The growing inhomogenity with decreasing β is shown in Figure 8.14. In this figure the aspect ratio of cloud radii A defined as

$$A = \sigma_x/\sigma_z \tag{8.30}$$

is plotted against time for $\beta = 0.5$, $\beta = 0.25$, $\beta = 0.125$, and $\beta = 0$. In all four cases the dynamics starts with a spherical distribution with $A = 1$. Whie $\beta = 0.5$ does not show a variation of A except for fluctuations, all other values of β induce a relative decrease of σ_z against σ_x due to the increasing attraction along the z-direction accoompanied by the increasing repulsion in perpendicular directions.

The cloud dispersion for $\beta = 0$, as illustrated in Figure 8.12, represent a special case since it is only caused by hydrodynamic interaction with vanishing diffusive contributions (cf. Figure 8.4), where $D^{(2)} = 0$ means that no dispersion occurs. The interaction-driven dynamics can nevertheless be characterized in terms of the diffusion coefficient $D_z^{(2)}$, i. e., the preferred direction of motion and $D_r^{(2)}$ in the perpendicular r-direction with $r = \sqrt{x^2 + y^2}$. These diffusion coefficients are illustrated on the right part of Figure 8.14, where the red curve represents the diffusive motion in z-direction according to the attractive hydrodynamic interaction. On the other hand the green curve represents a direct measurement of the repulsive parts in r-direction.

In the initial stages of high volume fractions Φ the cloud is a spherical entity, which tightens in z-direction with a constant hydrodynamically mediated diffusion coefficient $D^{(2)}$. Within the cloud contraction the swimmers arrange in configurations, which can be characterized by the extreme case of two swimmers orienting towards the z-direction, but with a body-to-body connection line perpendicular to the z-orientation, where only the repulsive contributions act. A perfect configuration of swimmers in one plane is not achieved, but in Figure 8.14 it can be seen on the one hand that the attractive effect of the

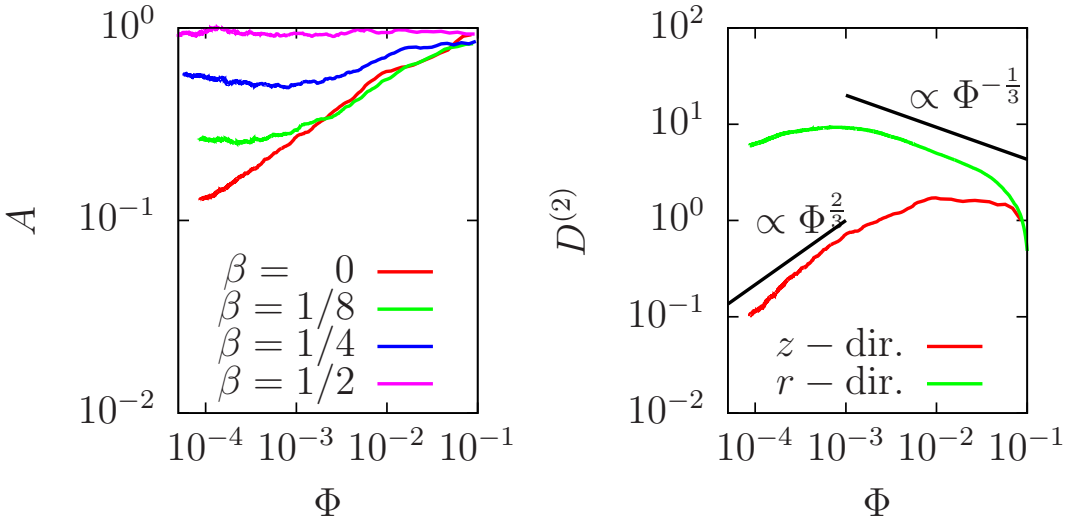

Figure 8.14.: Left: Aspect ration $A = \sigma_x/\sigma_z$ for reorientations with $\beta = 0.5$ (magenta). The aspect ratio reduces with decreasing β illustrating the growing dynamical inhomogenity. Right: The "hydrodynamic" diffusion coefficient $D^{(2)}/D_0 R_\tau$ in z-direction and r-direction for $\beta = 0$.

hydrodynamic interaction diminishes when a minimum of the aspect ratio A is obtained. On the other hand the diffusion coefficient in z-direction decreases for low volume fractions Φ, when the compressing dynamics has come to an end. From Figure 8.14 one can also see that the repulsive contribution in terms of $D_r^{(2)}$ increases within this first compressing phase of the dynamics, before also these contributions decrease due to increasing distances $\boldsymbol{\varrho}$ between the swimmers at small volume fractions Φ. Figure 8.14 shows that the decrease as well as the increase of $D^{(2)}$ in dependence of Φ can be decribed via a scaling law with exponents B being multiples of $\frac{1}{3}$. The repulsive parts grow with

$$D_r^{(2)} \propto \Phi^{-\frac{1}{3}} \tag{8.31}$$

in this initial regime at high volume fractions Φ, whereas the attractive contributions decay with

$$D_z^{(2)} \propto \Phi^{\frac{2}{3}}. \tag{8.32}$$

Note that $D_r(2) > D_z^{(2)}$. This is a relict of the dominant repulsive hydrodynamic interaction between pullers. Both diffusion coefficients $D_z^{(2)}$,$D_r^{(2)}$ as well as ΔD for a suspension of homogeneously reorienting swimmers decay or

increase with scaling exponents proportional to $\frac{1}{3}$. These scaling laws can be viewed as characteristics of the hydrodynamic interaction.

8.4. Conclusion and Outlook

In this chapter the dispersion of a distribution called *cloud* consisting of swimmers is investigated by means of particle-based simulations. As described in Chapter 7, such a swimmer reorients from time to time and is able to interact hydrodynamically with other swimmers within the cloud. The hydrodynamic interaction can be described by force dipoles, where dependent on the direction of the two forces F_0 the two cases of a *puller* and *pusher* occur. The distribution of the swimmer orientation during the reorientation process called *tumble* are defined by two parameters α, related to the angular velocity within the tumbling motion, and β, describing the distribution around a preferred direction of motion, as selected by the swimmers in the context of *chemo-* or *phototaxis*. The dispersion of the cloud is analyzed systematically in dependence of α and β, as well as the velocity v_0 and mean time of a run $\bar{\tau}$.

The reference case of a stochastic motion without hydrodynamic interaction can be described as self-propelled diffusion. This is characterized by an initial ballistic regime for short periods t with an increases of the mean-squared displacement $\langle x^2 \rangle \propto t^2$, which changes into a diffusive regime with a diffusion constant $D^{(2)} = v_0 \bar{\tau}/\alpha$. In particular, the ability of chosing a completely new orientation on the unit sphere associated with α affects the diffusion constant, which increases the less a swimmer is able to deviate from the old direction in the course of its reorientation. If the parameter $\beta \to 0$ is changed, e. g., the orientation of swimmers towards the z-direction is preferred. In the course of phototaxis, swimmers move towards a light source placed along this direction, leading to a drift term $D^{(1)} \neq 0$.

Considering the same diffusion process for hydrodynamically interacting micro-swimmers, the question is how the diffusion coefficient change in the case of pushers or pullers? The hydrodynamic interaction between two swimmers depends not only on their relative orientation. The averaged strength of the interaction depends on the distance ϱ with $1/\varrho^2$, which can be related to the standard deviation σ of the cloud. Therefore, the dependence of $D^{(2)}$ on

Φ is analyzed in Chapter 8. It turns out that the hydrodynamic interaction increases the diffusion coefficients in both cases. However, the coefficient is always larger for pushers even though the swimmers remove faster from the center. In the case of pullers, $D^{(2)}$ decays $\propto \Phi^{\frac{2}{3}}$ towards low volume-fractions $\Phi \to 0$. An enhancement of the hydrodynamic interaction has shown that this scaling law can be attributed to the hydrodynamic interaction.

But why is the diffusion coefficient $D^{(2)}$ constantly increased in the case of pushers? This can not be understood by just consulting the distribution of the swimmer distance to the center point, but by considering the distribution of the distances λ between the next neighboring swimmers. For pushers, this distribution converges towards a constant distribution preferring small distances λ. Therefore, although a dispersion of the total cloud takes place, the swimmers form subgroups, in which they move with an increased collective velocity, as a result of the hydrodynamic interaction.

If the distribution of possible angles for reorientations is limited by decreasing α, one can conclude that the effect of the hydrodynamic interaction on the dispersion decreases. This happens due to the fact that with decreasing α, the swimmers have less and less the possibility to change their direction of motion through tumbling, leading to a faster divergence of the distribution accompanied by a fast decrease of the hydrodynamic interaction.

The effects of the hydrodynamic interaction may also get lost, if the mean time $\bar{\tau}$ of runs is large compared to $\tau_0 = a/v_0$. Then, the swimmers of the cloud reach such large distances, so that the hydrodynamic interaction does not play a role within the diffusive regime.

Inhomogeneities in the dispersion occur when $\beta = 0$. Then, the dynamics is only influenced by the hydrodynamic interaction, which effects are reflected in the diffusion coefficients $D_r^{(2)}$ and $D_z^{(2)}$. Also in this case, the coeffizients $D_\alpha^{(2)}$ depend on the volume-fraction Φ, where the attractive and repulsive effects grow or decay with Φ^B, where the exponent B is a multiple of $\frac{1}{3}$, which seems to be a characteristic scaling law for the dispersion in the presence of hydrodynamic interaction.

One question that may arise is whether the dispersion of swimmers can be controlled, e. g., by external flows. Experiments and simulations have

revealed the effect of self-focusing of a continuous jet of swimmers in a pipe-flow [91, 110]. First simulations within this work have shown that a finitely extended cloud of phototactic pullers can also be stabilized by the application of an external pipe-flow. Since the swimmers reorient towards the z-direction after some time, they break off the rotational movements, as mediated by the external flow. On the average, the swimmers are thus subject to the repulsive effect, as mediated by the hydrodynamic interaction. The swimmers push each other into outer regions of the flow channel, where they are turned towards the channel center by the flow vorticity. This results in a circulating movement similar to a convection flow, whereby the cloud of swimmers remains compact for low flow velocitiy. If the latter is increased, a critical point exists at which the cloud is split into smaller subgroups. However, further simulations are required to further characterize this transition.

Bibliography

[1] H. Leonard, *http://hermanleonard.com/index.php/gallery/1/1/20/Print* (accessed 5th of September 2016).

[2] L. daVinci, *http://www.leonardodavinci.net/studies-of-water-passing-obstacles-and-falling.jsp* (accessed 9th of September 2016).

[3] J. V. Moroney, A. R. Ynalvez, *http://ripe.illinois.edu* (accessed 5th of November 2016).

[4] S. Owens, *http://http://commtechlab.msu.edu* (accessed 6th of November 2016).

[5] S. I. Abdelkhalik and R. B. Bird, *RHEOLOGY OF LOPSIDED-DUMBBELL SUSPENSIONS*, Appl. Sci. Res. **30**, 269 (1975).

[6] F. Alarcón and I. Pagonabarraga *Spontaneous aggregation and global polar ordering in squirmer suspensions*, J. Mol. Liq. **185**, 56 (2013)

[7] G. P. Alexander and J. M. Yeomans, *Dumbbell swimmers*, Europhys. Lett. **83**, 34006 (2008).

[8] G. P. Alexander, C. M. Pooley, and J. M. Yeomans, *Scattering of low-Reynolds-number swimmers*, Phys. Rev. E **78**, 045302 (2008).

[9] G. P. Alexander, C. M- Pooley, and J. M. Yeomans, *Hydrodynamics of linked sphere model swimmers*, J. Phys. Condens. Matter **21**, 204108 (2009).

[10] M. M. Alfonso and D. Vincenzi, *Nonlinear elastic polymers in random flow*, J. Fluid Mech. **540**, 99 (2005).

[11] K. H. Alfsen and J. Frøyland, *Systematics of the Lorenz Model at* $\sigma = 10$, Phys. Scr. **31**, 15 (1985).

[12] W. Alt, *Biased Random walk models for chemotaxis and related diffusion approximations*, J. Math. Biol. **9**, 147 (1980).

[13] I. S. Aranson, A. Sokolov, J. O. Kessler, and R. E. Goldstein, *Model for dynamical coherence in thin films of self-propelled microorganisms*, Phys. Rev. E **75**, 040901(R) (2007).

[14] J. Argyris, G. Faust, M. Haase, and R. Friedrich, *Die Erforschung des Chaos* (Springer, Berlin, Heidelberg, 2010).

[15] V. I. Arnol'd, *Gewöhnliche Differentialgleichungen* (Springer, Berlin, 1980).

[16] M. Avila, A. P. Willis, and B. Hof, *On the transient nature of localized pipe flow turbulence*, J. Fluid Mech. **646**, 127 (2010).

[17] S. Ayyalasomayajula, A. Gylfason, L. R. Collins, E. Bodenschatz, and Z. Warhaft, *Lagrangian Measurements of Inertial Particle Accelerations in Grid Generated Wind Tunnel Turbulence*, Phys. Rev. Lett. **97**, 144507 (2006).

[18] E. Balkowsky, G. Falkovich, and A. Fouxon, *Intermittent Distribuion of Inertial particles in Turbulent Flows*, Phys. Rev. Lett. **86**, 2790 (2001).

[19] J. Bammert, S. Schreiber, and W. Zimmermann, *Dumbbell diffusion in a spatially periodic potential*, Phys. Rev. E **77** 042102 (2008)

[20] J. Bammert and W. Zimmermann, *Dumbbell transport and deflection in a spatially periodic potential*, Euro. Phys. J. E **28**, 331 (2009).

[21] P. V. Bayly, B. L. Lewis, E. C. Ranz, R, J. Okamoto, R. B. Pless, and S. K. Dutcher, *Propulsive Forces on the Flagellum during Locomotion of Chlamydomonas reinhardtii*, Biophys. J. **100**, 2716 (2011).

[22] H. C. Berg, *Random walks in biology* (Princeton University Press., Princeton, 1993).

[23] H. C. Berg and L. Turner, *Chemotaxis of bacteria in glass capillary arrays. Escherichia coli, motility, microchannel plate, and light scattering*, Biophys. J. **58**, 919 (1990).

[24] H. C. Berg, *E. coli in motion* (Springer, New York, 2003).

[25] T. Biben and C. Misbah, *Tumbling of vesicles under shear flow within an advected-field approach*, Phys. Rev. E **67**, 031908 (2003).

[26] R. B. Bird, C. F. Curtiss, R. C. Armstrong, and O. Hassager, *Dynamics of Polymeric Liquids I, II* (Wiley & Sons, New York, 1987).

[27] G. K. Batchelor and J. T. Green, *The determination of the bulk stress in a suspension of spherical particles to order c^2*, J. Fluid Mech. **56**, 401 (1972).

[28] F. Brady, A. S. Khair, and M. Swaroop, *On the bulk viscosity of suspensions*, J. Fluid Mech. **554**, 109 (2006).

[29] L. Cannavacciuolo and R. G. Wink1er, *Mesoscale simulations of polymer dynamics in microchannel flows*, Euro. Phys. Lett. **83**, 3 (2008).

[30] A. Celani, S. Musacchio, and D. J. Vincenzi, *Polymer Transport in Random Flow*, Stat. Phys. **118**, 531 (2005).

[31] M. Chertkov, I. Kolokolov, V. Lebedev, and T. Turitsyn, *Polymer statistics in a random flow with mean shear*, J. Fluid Mech. **531**, 251 (2005).

[32] U. K. Chaeng, D. Roy, J. H. Lee, and M. J: Kim, *Fabrication and magnetic control of bacteria-inspired robotic microswimmers*, Appl. Phys. Lett. **97**, 213704 (2010).

[33] A. T Chwang and T. Y.-T. Wu, *Hydromechanics of low-Reynolds-number flow. Part 1. Rotation of axisymmetric prolate bodies*, J. Fluid Mech. **63** 3, 607 (1974).

[34] L. H. Cisneros, R. Cortez, C. Domborowski, R. E. Goldstein, and J. O. Kessler, *Fluid dynamics of self-propelled microorganisms, from individuals to concentrated populations*, Exp. Fluids **43**, 737 (2007).

[35] B. Cichocki and B. U. Felderhof, *Short-time diffusion coefficients and high frequency viscosity of dilute suspensions of spherical Brownian particles*, J. Chem. Phys. **89**, 1049 (1988).

[36] N. C. Darnton, L. Turner, S. Rojevsky, and H. C. Berg, *On torque and tumbling in swimming Escherichia coli*, J. Bacteriol. **189** 1756 (2007).

[37] Y. Davit and P. Peyla, *Intriguing viscosity effects in confined suspensions: A numerical study*, Europhys. Lett. **83**, 6 (2008).

[38] P. Degond, A. Lozinski, and R. G. Owens, *Kinetic models for dilute solutions of dumbbells in non-homogeneous flows revisited*, J. Non-Newtonian Fluid Mech. **165**, 509 (2010).

[39] E. F. Delong, R. B. Frankel, and D. A. Bazylinski, *Multiple Evolutionary Origins of Magnetotaxis in Bacteria*, Science **259**, 803 (1993).

[40] M. Doi and S. F. Edwards, *The Theory of Polymer Dynamics* (Clarendon Press, Oxford, 1986).

[41] C. Domborowski, L. Cisneros, S. Chatkaew, R. E. Goldstein, and J. O. Kessler, *Self-Concentration and Large-Scale Coherence in Bacterial Dynamics*, Phys. Rev. Lett. **93**, 098103 (2004).

[42] J. Dunkel, S. Heidenreich, K. Drescher, H. H. Wensink, M. Bär, and R. E. Goldstein, *Fluid Dynamics of Bacterial Turbulence*, Phys. Rev. Lett. **110**, 228102 (2013).

[43] K. Drescher, K. C. Leptos, I. Tuval, T. Ishikawa, T. J. Pedley, and R. E. Goldstein, *Dancing Volvox: Hydrodynamic Bound States of Swimming Algae*, Phys. Rev. Lett. **102**, 168101 (2009). 2

[44] K. Drescher, R. E. Goldstein, N. Michel, M. Polin, and I. Tuval, *Direct Measurement of the Flow Field around Swimming Microorganisms*, Phys. Rev. Lett. **105** 168101 (2010).

[45] K. Drescher, J. Dunkel, L. H. Cisneros, S. Gangulya, and R. E. Goldstein,*Fluid dynamics and noise in bacterial cell–cell and cell–surface scattering*, Proc. Natl Acad. Sci. USA **108**, 10940 (2011).

[46] B. Eckhardt, T. M. Schneider, B. Hof, and J. Westerweel, *Turbulence Transition in Pipe Flow*, Annu. Rev. Fluid Mech. **39**, 447 (2007).

[47] A. Einstein, *Eine neue Bestimmung der Moleküldimension*, Ann. Phys. **19**, 289 (1906).

[48] A. Einstein, *Elementare Betrachtung über die thermische Molekularbewegung in festen Körpern*, Ann. Phys. **34**, 591 (1911).

[49] J. Elgeti, R. G. Winkler, and G. Gomper, *Physics of microswimmers - single particle motion and collective behavior: a review*, Rep. Prog. Phys. **78**, 056601 (2015)

[50] R. E. Eskridge and S. T. Rao, *Turbulent diffusion behind vehicles:Experimentally determined turbulence mixing parameters*, Atmos. Environ. **20**, 851 (1986).

[51] G. Falkovich, A. Fouxon, and G. Stepanov, *Accelaration of rain initiation by cloud turbulence*, Nature **419**, 151 (2002).

[52] G. Falkovich and A. Pumir, *Intermittent distribution of heavy particles in a turbulent flow*, Phys. Fluids **16** L47 (2004).

[53] G. Foffano, J. S. Lintuvuori, A. N. Morozov, K. Stratford, M. E. Cates, and D. Marenduzzo, *Bulk rheology and microrheology of active fluids*, Eur. Phys. J. E **35**, 10 (2012).

[54] G. K. Fraenkel, *Visco-Elastic Effect in Solutions of Simple Particles*, J. Chem. Phys. **20**, 642 (1952).

[55] R. Friedrich and J. Peinke, *Description of a Turbulent Cascade by a Fokker-Planck Equation*, Phys. Rev. Lett. **78**, 863 (1997).

[56] R. Friedrich and J. Peinke, *Approaching complexity by stochastic methods: From biological systems to turbulence*, Physics Reports **506**, 87 (2011).

[57] U. Frisch, *Turbulence - The Legacy of A. N. Kolmogorov*,(Cambridge University Press, Cambridge, 1995).

[58] A. Furukawa, D. Marenduzzo, and M. E. Cates,*Activity-induced clustering in model dumbbell swimmers: The role of hydrodynamic interactions*, Phys. Rev. E **90** 022303 (2014).

[59] W. Gao, X. Feng, A. Pei, C. R. Kane, R. Tam, C. Hennessy, and J. Wang, *Bioinspired helical microswimmers based on vascular plants*, Nano Lett. **14**, 305 (2014).

[60] X. Garcia, P. Peyla, and S. Rafaï, *Light Control of the Flow of Phototactic Microswimmer Suspensions*, Phys. Rev. Lett. **110**, 138106 (2013).

[61] M. Garcia, S. Berti, P. Peyla, and S. Rafaï, *Random walk of a swimmer in a low-Reynolds-number medium*, Phys. Rev. E **83**, 035301(R) (2011).

[62] S. Gerashchenko and V. Steinberg, *Statistics of tumbling of a single polymer molecule in shear flow*, Phys. Rev. Lett. **96**, 038304 (2006).

[63] F. Ginelli, P. Poggi, A. Turchi, H. Chaté, R. Livi, and A. Politi, *Characterizing Dynamics with Covariant Lyapunov Vectors*, Phys. Rev. Lett. **99**, 130601 (2007).

[64] I. O. Götze and G. Gompper, *Mesoscale simulations of hydrodynamic squirmer interactions*, Phys. Rev. E **82**, 041921 (2010).

[65] S. Ghorai and N. A. Hill, *Penetrative phototactic bioconvection*, Phys. Fluids **17**, 074101 (2005).

[66] S. Ghorai and N. A. Hill, *Gyrotactic bioconvection in three dimensions*, Phys. Fluids **19**, 054107 (2007).

[67] A. Groisman and V. Steinberg, *Elastic turbulence in a polymer solution flow*, Naturre **405**, 53 (2000).

[68] A.Groisman and V. Steinberg, *Efficient mixing at low Reynolds numbers using polymer additives*, Nature **410**, 905 (2001).

[69] A. Groisman and V. Steinberg, *Elastic turbulence in curvilinear flows of polymer solutions*, New J. Phys. **6**, 29 (2004).

[70] A. Gyr and A. Tsinober, *On the rheological nature of drag reduction phenomena*, J. Non-Neton. Fluid **73**, 153 (1997).

[71] Brian M. Haines,A. Sokolov, I. S. Aranson, L. Berlyand, and D. A. Karpeev, *Three-dimensional model for the effective viscosity of bacterial suspensions*, Phys. Rev. E **80**, 041922 (2009).

[72] L. Harnau, R. Winkler, and P. Reinecker, *Dynamic structure factor of semiflexible macromolecules in dilute solution*, J. Chem. Phys. **104**, 6355 (1996).

[73] N. A. Hill and D.-P. Häder, *A Biased Random Walk Model for the Trajectories of Swimming Micro-organisms*, J. Theor. Biol. **186**, 503 (1997).

[74] W. Hu, D. Frenkel, and V. B. F. Mathol, *Simulation of Shish-Kebab Crystallite Induced by a Single Prealigned Macromolecule*, Macromolecules **35**, 7172 (2002).

[75] J. Happel and H. Brenner, *Low Reynolds Number Hydrodynamics* (Prentice-Hall, Englewood Cliffs., 1981).

[76] J. P. Hernandez-Ortiz and M. Graham, *Transport and Collective Dynamics in Suspensions of Confined Swimming Particles*, Phys. Rev. Lett. **95**, 204501 (2005).

[77] V. Hessel, H. Löwe, and F. Schönfeld, *Micromixers - a review on passive and active mixing principles*, Chem. Eng. Sci. **60**, 2479 (2005).

[78] J. O. Hinze, *Turbulence 2nd edn.* (McGraw-Hill., 1975)

[79] B. Hof,C. W. H. van Doorne, J. Westerweel, F. T. M. Nieuwstadt, H. Faisst, B. Eckhardt, H. Wedin, R. R. Kerswell, and F. Waleffe, *Experimental Observation of Nonlinear Traveling Waves in Turbulent Pipe Flow*, Sience **305**, 1594 (2004).

[80] E. Hopf, *Abzweigung einer periodischen Lösung von einer stationären Lösung eines Differentialsystems*, Ber. Math.-Phys., Sächs. Akad. d. Wiss. Leipzig **94**, 1 (1942).

[81] E. Hopf, *A mathematical example displaying features of turbulence*, Commun. Pure Appl. Math. **1** 4, 303 (1948).

[82] C.-C. Huang, G. Sutmann, G. Gompper, and R. G. Winkler, *Tumbling of polymers in semidilute solution under shear flow*, Europhys. Lett. **93**, 54004 (2011).

[83] T. J. Hüttl and R. Friedrich, *Influence of curvature and torsion on turbulent flow in helically coiled pipes*, Int. J. Heat. FLuid **21**, 345 (2000).

[84] T. Ishikawa, G Sekiya, Y Imai, and T Yamaguchi, *Hydrodynamic Interactions between Two Swimming Bacteria*, Biophys. J. **93**, 2217 (2007).

[85] T. Ishikawa and T. J. Pedley, *The rheology of a semi-dilute suspension of swimming model micro-organisms*, J. Fluid Mech. **588**, 399 (2007).

[86] T. Ishikawa and T. J. Pedley, *Diffusion of swimming model micro-organisms in a semi-dilute suspension*, J. Fluid Mech. **588**, 437 (2007).

[87] T. Ishikawa, *Suspension biomechanics of swimming microbes* J. R. Soc. Interface **6**, 815 (2009).

[88] R. M. Jendrejack et al., *DNA Dynamics in a Microchannel*, Phys. Rev. Lett. **91**, 038102 (2003).

[89] J. Ji,R. Jiang, R. G. Winkler, and G. Gompper, *Mesoscale hydrodynamic modeling of a colloid in shear-thinning viscoelastic fluids under shear flow*, J. Chem. Phys. **135**, 134116 (2011).

[90] L. Jibuti, S. Rafaï and P. Peyla, *Suspensions with a tunable effective viscosity: a numerical study*, J. Fluid Mech. **693**, 345 (2012).

[91] L. Jibuti, L. Qi, C. Misbah, W. Zimmermann, S. Rafaï, and P. Peyla, *Self-focusing and jet instability of a microswimmer suspension*, Phys. Rev. E **90**, 063019 (2014).

[92] A. Kaiser, A. Peshkov, A. Sokolov, B. ten Hagen, H. Löwen, and I. S. Aranson, *Transport powerd by bacterial Turbulence*, Phys. Rev. Lett. **112**, 158101 (2014).

[93] K. Kamataka, T. Araki, and H. Tanaka, *Hydrodynamic selection of the kinetic pathway of a polymer coil-globule transition*, Phys. Rev. Lett. **13**, 108303(2009).

[94] V. Kantsler and V. Steinberg, *Transition to tumbling and two regimes of tumbling motion of a vesicle in shear flow*, Phys. Rev. Lett. **96**, 036001 (2006).

[95] R. Kekre, J. E. Butler, and A. J. C. Ladd, *Comparison of Lattice-Boltzmann and Brownian-dynamics simulations of polymer migration in confined flows*, Phys. Rev. E **82**, 011802 (2010).

[96] E. F. Keller and L. A. Segel, *Model for chemotaxis*, **30**, 225 (1971)

[97] A. N. Kolmogorov, *The Local Structure of Turbulence in Incompressible Viscous Fluid for Very Large Reynolds Reynolds number*, Dokl. Akad. Nauk SSSR, **30**, 299 (1941).

[98] A. N. Kolmogorov, *Refinement of previous hypotheses concerning the local structure of turbulence in a viscous incompressible fluid at high Reynolds number*, J. Fluid Mech. **13** 01, 82– 85 (1962).

[99] B. Kowalik and R. G. Winkler, *Multiparticle collision dynamics simulations of viscoelastic fluids: Shear-thinning Gaussian dumbbells*, J. Chem. Phys. **138**, 104903 (2013).

[100] T. C. B. Kwan and E. S. G. Shaqfeh, *Brownian dynamics simulations of the stress and molecular configuration of polymers in exponential and linearly-ramped shear flow*, J. Non-Newtonian Fluid Mech. **82**, 139 (1999).

[101] N. Küchler, H. Löwen, and A. M. Menzel, *Getting drowned in a swirl: Deformable bead-spring model microswimmers in external flow fields*, Phys. Rev. E **93**, 022610 (2016).

[102] L. D. Landau, *On the problem of turbulence*, C. R. Acad. Sci. UESS **44**, 311 (1944).

[103] R. G. Larson, *The Structure and Rheology of Complex Fluids* (Oxford University Press, New York, Oxford, 1999).

[104] E. Lauga and T. R. Powers, *The hydrodynamics of swimming microorganisms*, Rep. Prog. Phys. **72**, 096601 (2009).

[105] M. F. Linkman and A. N. Morozov, *Sudden Relaminarization and Lifetimes in Forced Isotropic Turbulence*, Phys. Rev. Lett. **115**, 134502 (2015).

[106] K. A. Liu and I. Lin, *Bacterial turbulence reduction by passive magnetic particle chains*, Phys. Rev. E **88**, 033004 (2013).

[107] I. Llopis and I. Pagonabarraga, *Hydrodynamic interactions in squirmer motion: Swimming with a neighbour and close to a wall*, J. Non-Net. Fluid Mech. **165** , 946 (2009)

[108] E. N. Lorenz, *Deterministic Nonperiodic Flow* J. Atmos. Sci. **20**, 130 (1963).

[109] R. A. Malevanets and R. Kapral, *Solute molecular dynamics in a mesoscale solvent*, J. Chem. Phys. **112** , 7260 (2000).

[110] M. Martin, A. Barzyk, E. Bertin, P. Peyla, and S Rafaï, *Photofocusing: Light and flow of phototactic microswimmer suspension*, Phys. Rev. E **93**, 051101(R) (2016).

[111] C. Misbah, *Vacillating breathing and tumbling of vesicles under shear flow*, Phys. Rev. Lett. **96**, 028104 (2006).

[112] A. N. Morozov and W. van Saarloos, *Subcritical Finite-Amplitude Solutions for Plane Couette Flow of Viscoelastic Fluids*, Phys. Rev. Lett. **95**, 024501 (2005).

[113] A. N. Morozov and D. Marenduzzo, *Enhanced diffusion of tracer particles in dilute bacterial suspensions*, Soft Matter, **10**, 2748 (2014).

[114] T. M2ücke, D. Kleinhans, and J. Peinke, *Atmospheric turbulence and its influence on the alternating loads on wind turbines*, Wind Energy **14**, 301 (2011).

[115] T. Mung, J. Y. Yoo, H. Choi, and D. D. Joseph, *Drag reduction by polymer additives in a turbulent channel flow*, J. Fluid Mech. **486**, 213 (2003).

[116] A. Najafi and R. E. Golestanian, *Simple swimmer at low Reynolds number: Three linked spheres*, Phys. Rev. E. **69**, 062901 (2004).

[117] R. W. Nash, R. Adhikari, J. Tailleur, and M. E. Cates, *Run-and-Tumble Particles with Hydrodynamics: Sedimentation, Trapping, and Upstream Swimming*, Phys. Rev. Lett. **104**, 258101 (2010).

[118] S. Newhouse, D. Ruelle and F. Takens, *Occurrence of strange AxiomA attractors near quasi periodic flows on T^m, $m \geqq 3$* Commun. Math. Phys. **64**, 35 (1979).

[119] C. W. Oseen(1910), *Über die Stokes'sche Formel, und über eine verwandte Aufgabe in der Hydrodynamik*, Arkiv för matematik, astronomi och fysik **vi**, 29 (1910).

[120] L. Pan, A. Morozov, C. Wagner, P. E. Arratia, *A nonlinear elastic instability in channel flows at low Reynolds numbers*, Phys. Rev. Lett. **110**, 174502 (2013).

[121] R. E. Pattle, *Diffusion from an instantaneous point source with a concentration-dependent coefficient*, Q. J. Mechanics Appl. Math. **12**, 407 (1959).

[122] C. S. Peskin,*The immersed boundary method*, Acta Numerica **11**, 479 (2002).

[123] P. Peyla, *Rheology and dynamics of a deformable object in a microfluidic configuration: A numerical study* Europhys. Lett. **80**, 34001 (2007).

[124] P. Peyla and C. Verdier, *New confinement effects on the viscosity of suspensions*, Europhys. Lett. **94**, 4 (2011).

[125] R. Peyret and T. Taylor, *Computational methods for fluid flow* (Springer, New York, 1990).

[126] H. Poincaré, *Science et méthode*, Ernest Flammarion, Paris (1908).

[127] M. Polin, I. Tuval, K. Drescher, J. P. Gollub, R. E. Goldstein1, *Chlamydomonas reinhardtii Swims with Two "Gears" in a Eucariotic Version of Run-and-Tumble Locomotion*, Science **325** 5939, 487 (2009)

[128] C. M. Pooley, G. P. Alexander and J. M. Yeomans, *Hydrodynamic Interaction between Two Swimmers at Low Reynolds Number*, Phys. Rev. Lett. **99**, 228103 (2007).

[129] R. Prabhakar and J. R. Prakash, *Multiplicative separation of the influences of excluded volume, hydrodynamic interactions and finite extensibility on the rheological properties of dilute polymer solutions*, J. Non-Newtonian Fluid Mech. **116**, 163 (2004).

[130] W. H. Press, S. A. Teukolsky, W. T. Vetterling, and B. T. Flannery, *Numerical Recipes in C*, (Cambridge Unversity Press, Cambridge, Port Chester, New York, Melbourne, Sidney, 1992).

[131] E. M. Purcell, *Life at low Reynolds number*, Am. J. Phys. **45**, 3 (1977).

[132] A. Puliafito and K. Turitsyn, *Numerical study of polymer tumbling in linear shear flows*, Physic D: Nonlinear Phenomena **211**, 9 (2005).

[133] D. O. Pushkin and J. M. Yeomans, *Fluid Mixing by Curved Trajectories of Microswimmers*, Phys. Rev. Lett. **111**, 188101 (2013).

[134] S. Rafaï, L. Jibuti, and P. Peyla, *Effective Viscosity of Microswimmer Suspensions*, Phys. Rev. Lett. **104**, 098102 (2010).

[135] O. Raz and J. E. Avron, *Swimming, pumping and gliding at low Reynolds numbers*, New J. Phys. **9**, 437 (2007)

[136] F. Rioual, T. Biben, and C. Misbah, *Analytical analysis of a vesicle tumbling under a shear flow*, Phys. Rev. E **69**, 061914 (2014).

[137] H. Risken, *The Fokker Planck equation* (Springer Berlin Heidelberg, 1996).

[138] S. D. Ryan, B. M. Haines, L. Berlyand, F. Ziebert, I. S. Aranson, *Viscosity of bacterial suspensions: Hydrodynamic interactions and self-induced noise*, Phys. Rev. E **83**, 0509048(R) (2011).

[139] D. Samanta, A. de Lozar, and B. Hof, *Experimental investigation of laminar turbulent intermittency in pipe flow*, J. Fluid Mech. **681**, 193 (2011)

[140] D. Samanta, Y. Dubief, M. Holzner, C. Schäfer, A. N. Morozovd, C. Wagner, and B. Hof, *Elasto-inertial turbulence*, PNAS **110**, 10557 (2013)

[141] M. Sano and Y. Sawada, *Measurement of the Lyapunov spectrum from Chaotic Time series*, Phys. Rev. Lett., **55**, 1082 (1985).

[142] D. Saintillan and M. J. Shelley, *Orientational order and instabilities in suspensions of self-locomoting rods*, Phys. Rev. Lett. **99**, 058102 (2007).

[143] D. Saintillan and M. J. Shelley, *Instabilities and pattern formation in active particle suspensions: kinetic theory and continuum simulations*, Phys. Rev. Lett. **100**, 178103 (2008).

[144] D. Saintillan and M. J. Shelley, *Instabilities, pattern formation, and mixing in active suspensions*, Phys. Fluids **20**, 123304 (2008).

[145] S. Schreiber, T. Fischer, and W. Zimmermann, *Hydrodynamic attraction and repulsion between assymetric rotors* New J. Phys. **12**, 073017 (2012).

[146] C. M. Schroeder, R. E. Teixeira , E. S. G. Shaqfeh,and S. Chu, *Dynamics of DNA in the flow-gradient plane of steady shear flow: observations and simulations*, Macromolecules **38**, 1967 (2005).

[147] J. E. Segall, M. D. Manson, and H. Berg, *Signal processing times in bacterial chemotaxis*, Nature **296**, 855 (1982).

[148] D. E. Smith, H. P. Babcock, and S. Chu, *Single-polymer dynamics in steady shear flow*, Science **283** , 1724 (1999).

[149] A. Sokolov, I, S. Aranson, J. O. Kessler, R. E. Goldstein, *Concentration Dependence of the Collective Dynamics of Swimming Bacteria*, Phys. Rev. Lett. **98**, 158102 (2007).

[150] A. Sokolov and I. S. Aranson, *Reduction of Viscosity in Suspension of Swimming Bacteria*, Phys. Rev. Lett. **103**, 48101 (2009).

[151] A. Sokolov, R. E. Goldstein, F. I. Feldchtein, and I. S. Aranson, *Enhanced mixing and spatial instability in concentrated bacterial suspensions*, Phys. Rev. E **80**, 031903 (2009).

[152] A. Sokolov and I. S. Aranson, *Physical Properties of Collective Motion in Suspensions of Bacteria*, Phys. Rev. Lett. **109**, 248109 (2012).

[153] R. H. Somania, L. Yanga, L. Zhub, and B. S. Hsiaoa, *Flow-induced shish-kebab precursor structures in entangled polymer melts*, Polymer **46**, 8587 (2005).

[154] R. L. Stavis and R. Hirschberg, *Phototaxis in Chlamydomonas reinhardtii*, J. Cell Biol. **59**, 367 (1973).

[155] D. Ruelle and F. Takens, *On the nature of turbulence*, Commun. math. Phys. **20**, 167 (1971).

[156] H. Tanaka and T. Araki, *Simulation method of colloidal suspensions with hydrodynamic interactions: Fluid particle dynamics*, Phys. Rev. Lett. **85**, 1338 (2000).

[157] G. I. Taylor, *Statistical Theory of Turbulence* (Proceedings of the Royal Society of London. Series A, Mathematical and Physical Sciences, 151(873):421, (1935).

[158] G. I. Taylor, *Analysis of the Swimming of Microscopic Organisms*, Proc. Roy. Soc. A **209**, 1099 (1951)

[159] R. E. Teixera, H. P. Babcock, E. S. G, Shaqfeh, and S. Chu, *Shear thinning and tumbling dynamics of single polymers in the flow-gradient plane*, Macromolecules **38**, 581 (2005).

[160] H. Tennekes and J. L. Lumley, *A First Course in Turbulence* (MIT Press, 1972)

[161] A. Tsinober *An Informal Conceptual Introduction to Turbulence*, (Springer, Dordrecht, Heidelberg, London, New York, 2009).

[162] P. T. Underhill, J. P. Hernandez-Ortiz, and M. Graham, *Diffusion and Spatial Correlation in Suspensions of Swimming Particles*, Phys. Rev. Lett. **100**, 248101 (2008).

[163] P. M. Vlahovska, T. Podgorski, and C. Misbah, *Vesicles and red blood cells in flow: From individual dynamics to rheology*, Comptes Rendue Physique **10**, 775 (2009).

[164] H. R. Warner Jr., *Kinetic theory and rheology of dilute suspensions of finitely extendible dumbbells*, Ind. Eng. Chem. Fundamen. **11**, 379 (1972).

[165] E. Wajnryb, K. A. Mizerski, P. J. Zuk, and P. Szymczak, *Generalization of the RotnePragerYamakawa mobility and shear disturbance tensors*, J. Fluid Mech. **731**, R3 (2013).

[166] K. Weissenberg, *A continuum theory of rheological phenomena*, Nature **159**, 310 (1947).

[167] C. M. White and M. G. Mungal, *Mechanics and Prediction of Turbulent Drag Reduction with Polymer Additives*, Annu. Rev. Fluid Mech. **40**, 235 (2008).

[168] R. G. Winkler, *Semiflexible polymers in shear flow*, Phys. Rev. Lett. **97**, 128301 (2006).

[169] G. B. Witman, *Chlamydomonas phototaxis*, Trends Cell Biol. **3** 11, 403 (1993).

[170] A. Wolf, J. B. Swift, H. L. Swinney, J. A. Vastano et al., *Determining Lyapunov exponents from a time series*, Physica D: Nonlinear phenomena **16**, 285 (1985).

[171] C. W. Wolgemuth, *Collective Swimming and the Dynamics of Bacterial Turbulence*, Biophys. J. **95**, 1564 (2008).

[172] H. Yang, G. Radons, and Holger Kantz, *Covariant Lyapunov Vectors from Reconstructed Dynamics: The Geometry behind True and Spurious Lyapunov Exponents*, Phys. Rev. Lett. **109**, 244101 (2012).

[173] Y. Yang, V. Marceau and G. Gomper, *Swarm behavior of self-propelled rods and swimming flagella*, Phys. Rev. E **82**, 031904 (2010)

[174] N. J. Zabusky, E. Segre, J. Deschamps, V. Kantsler, and V. Steinberg1 et al.,*Dynamics of vesicles in shear and rotational flows: Modal dynamics and phase diagram*, Phys. Fluids **23**, 041905 (2011).

[175] A. Zötl and H. Stark, *Nonlinear Dynamics of a Microswimmer in Poiseuille Flow*, Phys. Rev. Lett. **108**, 218104 (2012).

Danksagung

Eine Doktorarbeit soll eine über Jahre hinweg selbstständig angefertigte Arbeit sein. Ohne die motivierende Hilfe und den Austausch mit der Außenwelt ist ein solches Projekt jedoch nicht möglich. An dieser Stelle möchte ich die Gelegenheit nutzen einigen Menschen zu danken, die mich auf meinem Weg durch die letzten jahre sehr unterstützt haben.

Zunächst möchte ich Walter Zimmermann erwähnen, der mich in seine Arbeitsgruppe integrierte. Vanessa Weith, Jochen Bammert, Steffen Schreiber und André Foertsch gilt meine Dankbarkeit für viele physikalische Diskussionen rund um das Thema gelöster Teilchen in Flüssigkeiten.

Jochen Bammert und insbesondere Georg Freund seien hier voller Dankbarkeit für ihre Einarbeitung in numerische Methoden erwähnt, die mir das Arbeiten an meiner Dissertation sehr erleichtert hat. Georg ist leider viel zu früh von uns gegangen.

Markus Hilt möchte ich dafür danken, dass er jedes Problem rund um meine Computer in den Griff bekommen hat.

Mein ganz spezieller Dank gilt Diego Kienle. Seine moralische Unterstützung und fachliche Einschätzung der Arbeit haben mir über lange Durststrecken der letzten Jahre geholfen. Ich möchte ihm auch dafür danken meine Verbrechen an der englischen Sprache verfolgt zu haben.

Falko Ziebert möchte ich danken, für viele schön verlebte Stunden und biophysikalischen Diskussionen während DPG-Frühjahrstagungen und in Cargèse. Der Winter, in dem er während seiner Anstellung in Bayreuth einen großen Teil seiner Zeit bei uns verlebte, hat uns persönlich sehr bereichert.

Ich möchte auch Oliver Kamps und Uwe Thiele von der Universität Münster für ihre Einschätzungen meiner Arbeit auf dem Gebiet der Turbu-

lenz danken sowie für ihre Einladungen zu den Workshops auf der Zafern-Hütte im Algäu.

Den Professoren für Theoretische Physik Helmut Brand, Matthias Schmidt und Stefan Gekle möchte ich für ihren Rat und Zuspruch danken.

Knut Holtsträter möchte ich für den Lehrauftrag über die Bigband der Universität Bayreuth danken. Für immerhin zwei Jahre durfte ich so Erfahrungen im Leiten eines großen Klangkörpers sammeln. Außerdem hat er mir ein Schlagzeug beschafft, welches unter dem einen oder anderen Ausbruch schlechter Launen während Durststrecken zu leiden hatte.

Stefan Luschner möchte ich dafür danken, mir beigebracht zu haben dieses Schlagzeug zu bedienen.

Für ihre Ratschläge und ihr stets offenes Ohr möchte ich meinen Eltern Elisabeth und Winfried Greber ganz herzlich danken. Ihre Unterstützung während der Studienzeit haben meine Promotion erst ermöglicht.

Meine Schwiegereltern Gerhard und Renate Reichel dürfen in dieser Auflistung nicht fehlen. Ich möchte Ihnen ganz herzlich dafür danken, dass sie ihr grünes Paradies in Hoyerswerda für mich geöffnet haben. Im Sommer 2016 war die dort verlebte Zeit eine große Hilfe dieses Manuskript fertig zu stellen.

Mein größter Dank gebührt meiner Frau Ulrike Reichel-Greber. Sie hat dieses nicht enden wollende Abenteuer in Bayreuth zusammen mit mir durchgestanden, obwohl ich mit meinen Problemen rund um die Arbeit,... mit Sicherheit nicht pflegeleicht war. Unsere weiseste Entscheidung war die Anschaffung unserer beiden Hunde Isi und Bujo.

Eidestattliche Erklärung

Hiermit versichere ich an Eides Statt, dass ich die vorliegende Arbeit selbstständig verfasst und keine anderen als die von mir angegebenen Quellen und Hilfsmittel verwendet habe.

Weiterhin erkläre ich, dass ich die Hilfe von gewerblichen Promotionsberatern bzw. -vermittlern oder ähnlichen Dienstleistern weder bisher in Anspruch genommen habe, noch künftig in Anspruch nehmen werde.

Zusätzlich erkäre ich hiermit, dass ich keinerlei frühere Promotionsversuche unternommen habe.

Bayreuth, den 01.12.2016

Johannes Greber